ARO 25373.10-MS

2

THE OHIO STATE UNIVERSITY

A Fundamental Investigation into the Joining of Advanced Light Materials

W. A. Baeslack, III and L. Adler
Department of Welding Engineering

Army Research Office
Research Triangle Park, NC 27709-2211

Final Report

November 1991

TABLE OF CONTENTS

UNCLASSIFIED MASTER COPY - FOR REPRODUCTION PURPOSES

SECURITY CLASSIFICATION OF THIS PAGE

REPORT DOCUMENTATION PAGE

1a. REPORT SECURITY CLASSIFICATION
Unclassified

1b. RESTRICTIVE MARKINGS

2a. SECURITY CLASSIFICATION AUTHORITY

2b. DECLASSIFICATION / DOWNGRADING SCHEDULE

3. DISTRIBUTION / AVAILABILITY OF REPORT
Approved for public release;
distribution unlimited.

4 PERFORMING ORGANIZATION REPORT NUMBER(S)
RF Project 716625

5. MONITORING ORGANIZATION REPORT NUMBER(S)
ARO 25373.10-MS

6a. NAME OF PERFORMING ORGANIZATION
The Ohio State University
Research Foundation

6b. OFFICE SYMBOL (If applicable)
OSURF

7a. NAME OF MONITORING ORGANIZATION
U. S. Army Research Office

6c. ADDRESS (City, State, and ZIP Code)
1960 Kenny Road
Columbus, Ohio 43212

7b. ADDRESS (City, State, and ZIP Code)
P. O. Box 12211
Research Triangle Park, NC 27709-2211

8a. NAME OF FUNDING / SPONSORING ORGANIZATION
U. S. Army Research Office

8b. OFFICE SYMBOL (If applicable)

9. PROCUREMENT INSTRUMENT IDENTIFICATION NUMBER
DAAL03-88-K-0049

8c. ADDRESS (City, State, and ZIP Code)
P. O. Box 12211
Research Triangle Park, NC 27709-2211

10. SOURCE OF FUNDING NUMBERS

PROGRAM ELEMENT NO.	PROJECT NO.	TASK NO.	WORK UNIT ACCESSION NO.

11. TITLE (Include Security Classification)
A Fundamental Investigation into the Joining of Advanced Light Materials

12. PERSONAL AUTHOR(S)
W. A. Baeslack III and L. Adler

13a. TYPE OF REPORT
Final

13b. TIME COVERED
FROM 4/88 TO 10/91

14. DATE OF REPORT (Year, Month, Day)
1991 November 25

15. PAGE COUNT
230

16. SUPPLEMENTARY NOTATION
The view, opinions and/or findings contained in this report are those of the author(s) and should not be construed as an official Department of the Army position, policy, or decision, unless so designated by other documentation.

17. COSATI CODES

FIELD	GROUP	SUB-GROUP

18. SUBJECT TERMS (Continue on reverse if necessary and identify by block number)
welding, aluminum, titanium, powder metallurgy, rapid solidification, weldability, inertia-friction welding, linear-friction welding, laser welding, capacitor-discharge welding

19 ABSTRACT (Continue on reverse if necessary and identify by block number)

Research performed during this program investigated the fundamental, materials science aspects of joining advanced light materials, emphasizing the similar and dissimilar alloy joining of state-of-the-art dispersion-strengthened, elevated-temperature aluminum alloys, weld solidification/segregation effects on solid-state phase transformations in Al-Cu and Al-Cu-Li type alloys, and the application of advanced ultrasonic NDE techniques to evaluate the characteristics and quality of solid-phase welds between light materials.

The pulsed Nd:YAG laser welding process was shown to be highly effective in producing high-integrity fusion welds in a low-hydrogen content Al-8Fe-2Mo alloy. Detailed analytical-electron microscopy analysis showed that the extremely high solidification and cooling rates experienced during this process promoted the formation of a microstructurally refined, high-strength fusion zone microstructure, and that minimal dispersoid coarsening occurred in the weld heat-affected zone (HAZ). Transverse-weld oriented tensile joint efficiencies of

20. DISTRIBUTION / AVAILABILITY OF ABSTRACT
☐ UNCLASSIFIED/UNLIMITED ☒ SAME AS RPT. ☐ DTIC USERS

21. ABSTRACT SECURITY CLASSIFICATION
Unclassified

22a NAME OF RESPONSIBLE INDIVIDUAL
Dr. Andrew Crowson - Materials Science Div.

22b. TELEPHONE (Include Area Code)
(919) 549-0641

22c. OFFICE SYMBOL
ARO

DD FORM 1473, 84 MAR

83 APR edition may be used until exhausted.
All other editions are obsolete.

SECURITY CLASSIFICATION OF THIS PAGE
UNCLASSIFIED

essentially 100% were measured. Longitudinal-weld oriented bend testing showe excellent weld zone ductility with fracture occurring in the HAZ within the fusio zone of a previous pulse.

Transmission-electron microscopy studies of capacitor-discharge weld produced at high and low energy inputs in a high-hydrogen Al-Fe-Ce alloy showe complete melting at the weld interface and resolidification to an extremely fine, dendritic alpha-aluminum structure which exhibited high strength (join efficiencies of 100%). Analysis across the weld zones indicated the presence o extremely high temperature gradients and the essential absence of a weld HAZ.

The inertia- and linear-friction welding processes were demonstrated to be effective in the solid-phase joining of state-of-the-art dispersion-strengthene aluminum alloys, including Al-Fe-V-Si and Al-Fe-Mo-V alloy types. In-dept analytical-electron microscopy analysis was utilized to effectively characterize the influence of weld process type and welding parameters on the dispersoid ar grain structure across the weld interface. It was generally determined that th application of a sufficiently high axial force during welding minimized dispersoi and grain coarsening across the weld interface and thereby maximimized join efficiencies to levels approaching 90%. SEM fractographic studies related th weld interface microstructure with the resulting mechanical properties an fracture behavior.

Dissimilar inertia- and linear-friction welds were also generated between th dispersoid-strengthened aluminum alloys and both conventional ingot metallurg aluminum (2024-T351) and titanium alloys (CP, Ti-1100). Conventional light microscopy showed unique differences in the weld interface structure for variou dispersion-strengthened aluminum alloys which were attributed to differences i the elevated-temperature strengths of the alloys. AEM and electron-probe microanalysis revealed extensive mechanical mixing at the weld interface, with negligible evidence of interdiffusion. Mechanical testing showed high join efficiencies, over 80%, particularly in the inertia-friction welds produced a high axial force. Although high integrity welds between the dispersion-strengthened aluminum alloys and CP titanium were produced, higher elevate temperature strengths of the advanced titanium alloys (eg., Ti-1100) promote minimal interface deformation and marginal bonding.

The effect of elevated-temperature exposure on the structure and hardness o inertia-friction welds in Al-Fe-V-Si alloys was evaluated over a temperature ran from 425 to 575°C. Minimal dispersoid or grain coarsening was observed a temperatures up to 500°C, however, appreciable coarsening and softening was observed at higher temperatures. Higher temperature exposure further promoted th formation of coarse, equilibrium dispersoids.

AEM was utilized to study the influence of segregation during laser and gas tungsten-arc welding on subsequent solid-state phase transformations in Al-Cu an Al-Cu-Li type alloys. In the Al-Cu binary alloys, solidification-induce segregation was found to promote the formation of theta-prime in the vicinity o solidification substructure and grain boundaries, and its absence at the grai interiors. In Al-Cu-Li alloys (Al-2090), a similar response was observed in th as-welded and postweld-aged conditions, with T1 (Cu-containing) precipitati strongly influenced by solidification segregation, but the precipitation of Li-rich delta-prime to occur relatively uniformly across the fusion zone. In thi investigation, as-welded and postweld aged fusion zone and HAZ microstructure were related to their mechanical properties.

In conjunction with the materials joining studies, nondestructive evaluati of selected solid-phase welds was performed using advanced, ultrasoni spectroscopy techniques. These techniques were found highly effective in identifying discontinuities in dissimilar alloy inertia- and linear-friction welds produced between the dispersion-strengthened aluminum alloys and ingot metallur aluminum alloys, and in characterizing the width of the heat-and-deformation zo across the weld interface.

SUMMARY

Research performed during this program investigated the fundamental, materials science aspects of joining advanced light materials, emphasizing the similar and dissimilar alloy joining of state-of-the-art dispersion-strengthened, elevated-temperature aluminum alloys, weld solidification/segregation effects on solid-state phase transformations in Al-Cu and Al-Cu-Li type alloys, and the application of advanced ultrasonic NDE techniques to evaluate the characteristics and quality of solid-phase welds between light materials.

The pulsed Nd:YAG laser welding process was shown to be highly effective in producing high-integrity fusion welds in a low-hydrogen content Al-8Fe-2Mo alloy. Detailed analytical-electron microscopy analysis showed that the extremely high solidification and cooling rates experienced during this process promoted the formation of a microstructurally refined, high-strength fusion zone microstructure, and that minimal dispersoid coarsening occurred in the weld heat-affected zone (HAZ). Transverse-weld oriented tensile joint efficiencies of essentially 100% were measured. Longitudinal-weld oriented bend testing showed excellent weld zone ductility with fracture occurring in the HAZ within the fusion zone of a previous pulse.

Transmission-electron microscopy studies of capacitor-discharge welds produced at high and low energy inputs in a high-hydrogen Al-Fe-Ce alloy showed complete melting at the weld interface and resolidification to an extremely fine, dendritic alpha-aluminum structure which exhibited high strength (joint efficiencies of 100%). Analysis across the weld zones indicated the presence of extremely high temperature gradients and the essential absence of a weld HAZ.

The inertia- and linear-friction welding processes were demonstrated to be effective in the solid-phase joining of state-of-the-art dispersion-strengthened aluminum alloys, including Al-Fe-V-Si and Al-Fe-Mo-V alloy types. In-depth analytical-electron microscopy analysis was utilized to effectively characterize the influence of weld process type and welding parameters on the dispersoid and grain structure across the weld interface. It was generally determined that the application of a sufficiently high axial force during welding minimized dispersoid and grain coarsening across the weld interface and thereby maximimized joint efficiencies to levels approaching 90%. SEM fractographic studies related the weld interface microstructure with the resulting mechanical properties and fracture behavior.

Dissimilar inertia- and linear-friction welds were also generated between the dispersoid-strengthened aluminum alloys and both conventional ingot metallurgy aluminum (2024-T351) and titanium alloys (CP, Ti-1100). Conventional light microscopy showed unique differences in the weld interface structure for various dispersion-strengthened aluminum alloys which were attributed to differences in the elevated-temperature strengths of the alloys. AEM and electron-probe microanalysis revealed extensive mechanical mixing at the weld interface, with negligible

evidence of interdiffusion. Mechanical testing showed high joint efficiencies, over 80%, particularly in the inertia-friction welds produced at high axial force. Although high integrity welds between the dispersion-strengthened aluminum alloys and CP titanium were produced, higher elevated-temperature strengths of the advanced titanium alloys (eg., Ti-1100) promoted minimal interface deformation and marginal bonding.

The effect of elevated-temperature exposure on the structure and hardness of inertia-friction welds in Al-Fe-V-Si alloys was evaluated over a temperature range from 425 to 575°C. Minimal dispersoid or grain coarsening was observed at temperatures up to 500°C, however, appreciable coarsening and softening was observed at higher temperatures. Higher temperature exposure further promoted the formation of coarse, equilibrium dispersoids.

AEM was utilized to study the influence of segregation during laser and gas tungsten-arc welding on subsequent solid-state phase transformations in Al-Cu and Al-Cu-Li type alloys. In the Al-Cu binary alloys, solidification-induced segregation was found to promote the formation of theta-prime in the vicinity of solidification substructure and grain boundaries, and its absence at the grain interiors. In Al-Cu-Li alloys (Al-2090), a similar response was observed in the as-welded and postweld-aged conditions, with T1 (Cu-containing) precipitation strongly influenced by solidification segregation, but the precipitation of Li-rich delta-prime to occur relatively uniformly across the fusion zone. In this investigation, as-welded and postweld aged fusion zone and HAZ microstructures were related to their mechanical properties.

In conjunction with the materials joining studies, nondestructive evaluation of selected solid-phase welds was performed using advanced, ultrasonic spectroscopy techniques. These techniques were found highly effective in identifying discontinuities in dissimilar alloy inertia- and linear-friction welds produced between the dispersion-strengthened aluminum alloys and ingot metallurgy aluminum alloys, and in characterizing the width of the heat-and-deformation zone across the weld interface.

I. INTRODUCTION AND STATEMENT OF PROBLEM

Demanding goals for increased performance, reliability and affordability in advanced U.S. Army systems will mandate the increased utilization of light materials well into the twenty-first century. In recognition of this requirement, the DoD (including the respective service agencies and DARPA) has supported extensive research into the development of high-performance, light materials for a diversity of structural applications. Indeed, during the 1980's a virtual plethora of these materials were developed and evaluated to varying degrees, including ingot metallurgy and powder metallurgy Al-Li alloys, rapidly-solidified (RS), dispersion-strengthened aluminum alloys, RS magnesium alloys, continuous fiber and particulate-reinforced aluminum, titanium and magnesium metal-matrix composites, and alpha-two and gamma titanium-aluminide intermetallics. Although the many of these materials will not experience commercial exploitation, optimized derivative compositions representing nearly each one these alloy families are currently available on a semi-commercial or commercial basis which offer physical properties (eg., density, elastic modulus) and mechanical property combinations (eg., room and elevated-temperature strength, toughness, creep resistance) far superior to those exhibited by conventional light alloys. Although these materials will certainly not totally supplant conventional light alloys (eg., 5XXX aluminum alloys) in future Army systems, they will be critical to the design and development of many high-technology, performance-driven systems such as missiles, gas turbine-engines, etc.. Indeed, many of these materials are currently being evaluated in government and corporate IRAD-sponsored exploratory research and advanced development programs, and are being incorporated by designers into advanced military systems.

Since these novel materials are generally designed to exhibit highly-tailored mechanical and/or physical properties, and are more costly than conventional alloys, their most efficient use in structural applications will require effective integration with both conventional and dissimilar advanced alloys into monolithic structures [1]. Consequently, the ultimate utility of these materials in structural applications will be highly dependent on their fabricability, and more specifically on their capability to be effectively and economically joined. Although certain of these advanced alloys will be fusion weldable using conventional technologies, the majority will require the application of alternative, specialized joining processes and methodologies. Considering the unique and often complex physical metallurgy and processing associated with these materials, it is apparent that a fundamental understanding of exactly how these joining processes and methodologies influence joint integrity (ie., the presence of macroscopic defects and discontinuities), the evolution and nature of the metallurgical structure and correspondingly the joint mechanical properties must be developed.

In response to this requirement, the Army Research Office has supported research at The Ohio State University to investigate the materials science and engineering aspects of joining advanced light materials. During the past three years, significant contributions have been made regarding weld solidification phenomena, microstructure development during similar and dissimilar-alloy solid-phase welding (inertia- and linear-friction welding), segregation effects on solid-state phase transformation behavior in fusion welds, the development of structure/property/fracture relationships, and the application of advanced ultrasonic nondestructive evaluation (NDE) techniques for joint integrity and structure characterization.

The following sections provide a summary of important results determined in this three-year investigation. During this period, much of this research has been presented at national and international forums and published in the open literature. (Selected publications are provided in Appendix I.) The following section reviews pertinent results, concentrating on more recent experimental results which are currently under preparation for presentation and publication.

II. PRESENTATION OF IMPORTANT RESULTS

2.1 Materials Science Aspects of Joining RS Dispersion-Strengthened Aluminum Alloys

Dispersion-strengthened aluminum alloys produced by RS/PM technology represent an important class of high-strength aluminum alloys for elevated-temperature applications. These alloys are based on hyper-eutectic Al-Fe compositions (8-12 wt% Fe) with ternary and/or quaternary additions of molybdenum, cerium, vanadium, and silicon. RS/PM processing of these novel chemistries produces a unique microstructure consisting of submicron dispersoids in an extremely fine-grained (approximately one micron in average diameter) alpha aluminum matrix. The low interfacial energy between the dispersoid particles and the matrix, and the low solid-state diffusivity of transition elements in alpha aluminum provide minimal driving force for particle coarsening (ie., via Ostwald ripening), thereby promoting excellent particle stability and superior mechanical properties at temperatures up to 400°C in current generation alloys. In recent years, continued alloy development has markedly improved the mechanical properties of dispersion-strengthened aluminum alloys. In particular, advanced Al-Fe-V-Si alloys (eg., Al-8.5wt.%Fe-1.3wt%V-1.7wt%Si and Al-11.7wt%Fe-1.2wt%V-2.4 wt%Si) offer elevated-temperature strengths and stability far superior to both conventional aluminum alloys and earlier generation Al-Fe-Mo and Al-Fe-Ce alloys (2,3). High thermal stability of the sub-micron $Al_{13}(Fe,V)_3Si$ (body-centered cubic) dispersoids exhibited by the Al-Fe-Si-V alloys, and their spherical morphology, promote superior room and elevated-temperature strength while providing ductility, fracture toughness and fatigue properties comparable to those of conventional high-strength aluminum alloys.

As indicated above, the unique, "engineered" microstructures exhibited by RS, dispersion-strengthened aluminum alloys restrict their joining by conventional fusion welding processes and methodologies. Rather, the achievement of high joint efficiencies in these alloys requires the application of welding/joining processes and procedures which can "recreate" and/or "retain" across the weld region the unique, metastable base metal microstructures, thereby assuring high joint mechanical properties. During the past three years, research performed on the joining of these alloys has been fundamental in nature, directed principally toward developing an understanding of pertinent metallurgical phenomena associated with formation of the weld structure and its corresponding influence on mechanical properties. During the course of this research, the feasibility of achieving either of the basic joining requirements (ie., microstructure recreation and/or retention) has been demonstrated through the application and optimization of selected joining processes, detailed metallographic analysis of the base metal and joint regions, the determination of first-tier mechanical properties and fracture analysis. Fusion welding phenomena which have been studied include nucleation and growth phenomena during weld solidification, partially-melted and heat-affected zone formation, and the development of weld structure/property/fracture relationships. Solid-phase welding phenomena which have been studied for both similar and dissimilar-alloy compositions include the influence of welding process parameter effects on weld defect formation, the nature of the dispersoid and grain structures across the weld interface, and weld structure/property/fracture relationships. Alloys investigated have included Al-Fe-Ce, Al-Fe-Mo, Al-Fe-Mo-V and Al-Fe-V-Si types. Selected results from work performed during the past contract period are summarized below.

2.1.1 Pulsed Nd:YAG Laser and Capacitor-Discharge Welding

The electron beam weldability of low-hydrogen Al-8wt%Fe-2wt%Mo sheet was effectively demonstrated in earlier ARO-supported research at OSU (4-7). Although the presence of primary intermetallics within the fusion zone was not entirely suppressed (ie., a Zone B versus a Zone A microstructure was produced), the fine size of these intermetallics and the surrounding fine dendritic alpha microstructure promoted high hardnesses and correspondingly high joint efficiencies (above 75%) with moderate weld ductilities. TEM/SAD analysis of the weld fusion zone microstructures determined the fine, primary intermetallics to originate from the base metal (ie., unmelted or undissolved dispersoids) and to coarsen during solidification to an extent dependent on local cooling and solidification rates. It should be noted that slight dispersoid coarsening and microstructural softening in the electron beam weld HAZ's were also observed, although weld fracture consistently occurred in the fusion zone.

In the present program, pulsed Nd:YAG laser welding was shown to offer the potential for producing full-penetration welds in aluminum sheet material while promoting appreciably higher weld cooling rates (10^5-10^6 °C/s) and steeper temperature gradients across the weld zone (thereby minimizing dispersoid coarsening in the HAZ). Pulsed Nd:YAG laser welds were produced in low-hydrogen Al-8wt%Fe-2wt%Mo sheet using various pulsing parameters to vary the extent of pulse overlap (8,9). Figure 1 shows the transverse cross section and top surface of a Nd:YAG pulsed laser weld produced with significant pulse overlap, and reveals a white-etching fusion zone and a dark-etching HAZ at the interface with the previous fusion zone pulse. TEM analysis at various locations across the weld zone showed the presence of an extremely fine, spherical dispersoid distribution and fine dendritic alpha aluminum in the fusion zone. Near the fusion boundary (Fig. 2A), columnar alpha aluminum grains nucleated epitaxially from the base metal (which was confirmed via SAD and dark-field TEM analysis) and essentially entrapped unmelted/undissolved dispersoids which originated from the base metal. Nearer to the center of the fusion zone, shallower temperature gradients allowed the nucleation of dendritic alpha directly from the dispersoid growth centers (Fig. 2B).

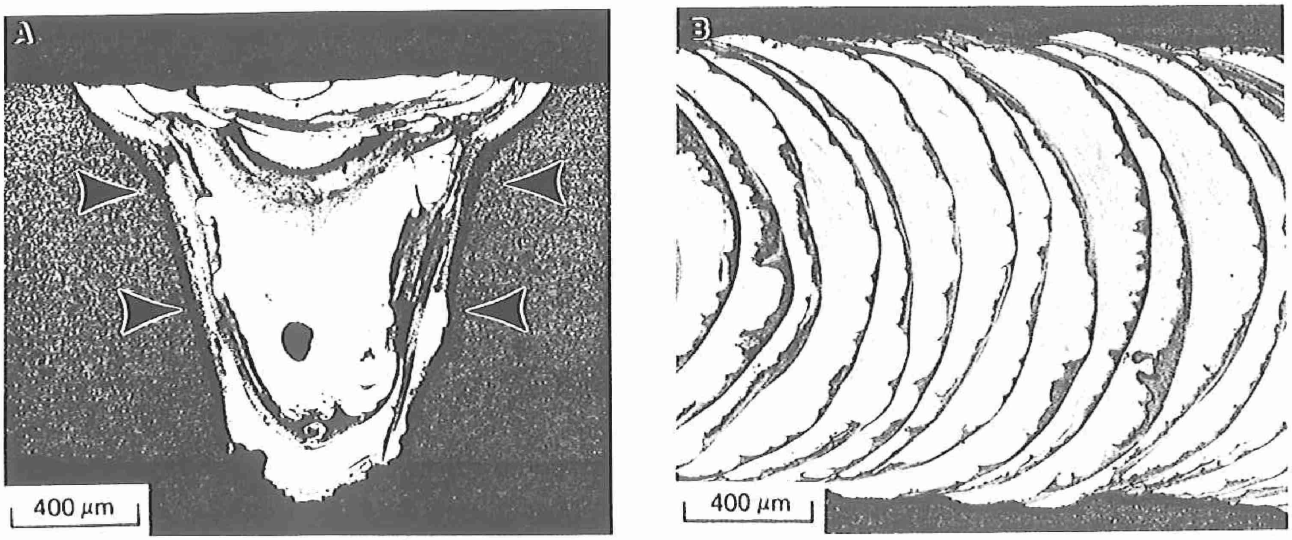

Fig. 1. Light micrographs of pulsed Nd:YAG laser weld in Al-8Fe-2Mo sheet showing (A) transverse section and (B) top surface. Arrows in (A) indicate locations of hardness traverses shown in Fig. 4.

Interestingly, in the HAZ formed in the previous pulse FZ, the dendritic structure transformed into a fine, acicular structure identified as equilibrium Al_3Fe (monoclinic) (Fig. 3C). Hardness traverses performed across the weld zone (Fig. 3) revealed

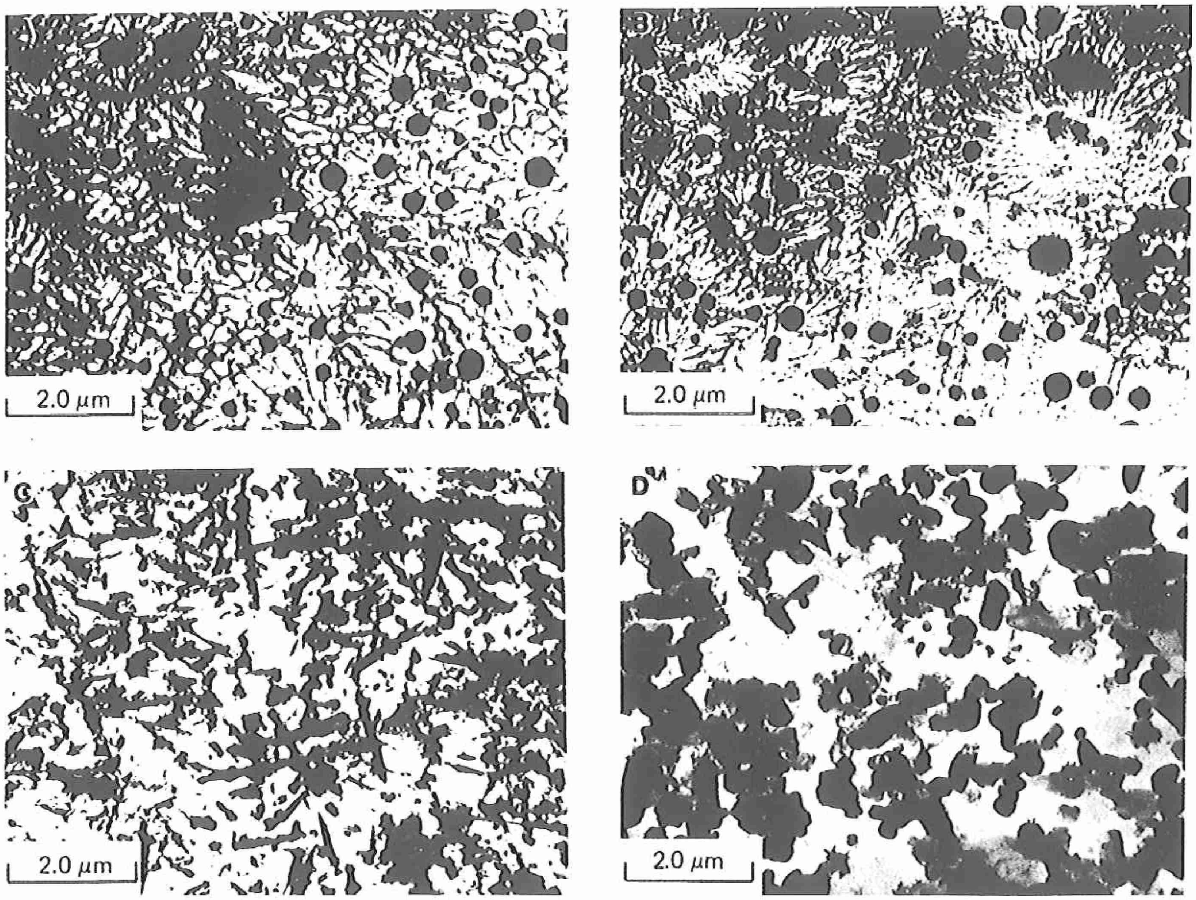

Fig. 2. TEM bright-field micrographs of pulsed Nd:YAG laser weld in Al-8Fe-2Mo: (A) fusion zone adjacent to fusion boundary; (B) center of FZ; (C) HAZ within FZ; (D) HAZ in base metal.

extremely high fusion zone hardnesses and an absence of hardness degradation across the HAZ's in the base metal or prior pulse, which was consistent with a measured 100% joint efficiency. Fracture during bend testing (which occurred at over 10% outer-fiber elastic + plastic strain) was associated with the HAZ in the prior fusion zone pulse (as shown in Fig. 4), presumably due a lower ductility in this region versus the surrounding regions because of the presence of acicular A_3Fe.

Microstructure examination and AEM compositional analysis was utilized to predict the solidification sequence experienced during Nd:YAG laser welding, which is schematically illustrated in the Al-Fe-Mo pseudo-binary phase diagram shown in Fig. 5. As shown, incomplete dissolution of the base metal dispersoids within the fusion zone promotes an effective, solidifying liquid chemistry (C_o') which is depleted in Fe and Mo versus the nominal alloy composition, (C_o), but which is still greater than the equilibrium eutectic composition. Despite the presence of an alpha aluminum substrate for epitaxial nucleation (ie., perfect wetting conditions), sufficient undercooling was experienced due to the extremely rapid weld cooling (down to $T_{E'}$ in Fig. 5) to promote solidification directly to alpha phase versus to primary intermetallics, as predicted from the equilibrium phase diagram. Coincident with the growth of the metastable alpha aluminum, the remaining melt is enriched with Fe and Mo and the composition of the melt ultimately reaches the composition of the metastable eutectic (point D), where it undergoes (metastable) eutectic

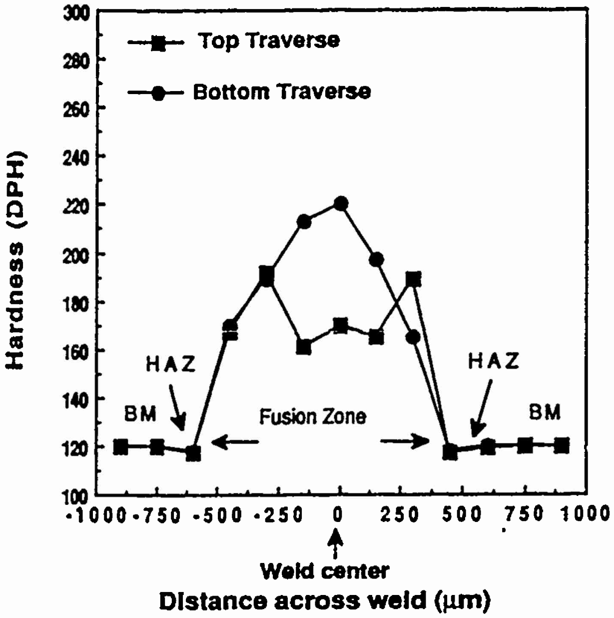

Fig. 3. Hardness traverses across pulsed Nd:YAG laser weld in Al-8Fe-2Mo (location of top and bottom traverses are shown in Fig. 2(A).

Fig. 4. Light micrograph showing fracture path on top surface of longitudinal-weld oriented bend specimen in Al-8Fe-2Mo. Arrow indicates direction of maximum stress during bend testing.

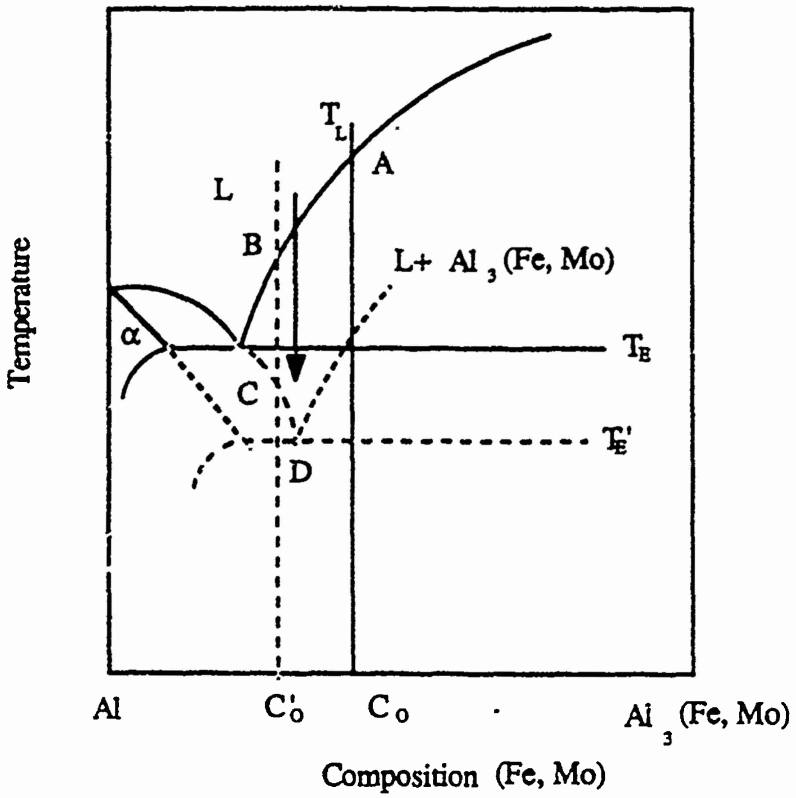

Figure 5. Schematic of $Al-Al_x(Fe,Mo)_y$ pseudo-binary phase diagram illustrating weld solidification sequence for pulsed Nd:YAG laser weld in Al-8Fe-2Mo.

solidification.

Based on the above analysis, it is apparent that evolution of the weld fusion zone microstructure in the RS dispersion-strengthened alloys is complex and markedly influenced not only by the weld solidification and cooling rate, but also by the thermal cycle and peak temperatures experienced within the molten fusion zone and the thermal stablity (ie., dissolution rate) of the base metal dispersoids.

Capacitor-discharge welding (initial-gap type) is a rapid-solidification/cooling rate fusion welding process which involves the axial impacting of cylindrical specimens under gravity and their subsequent arcing and melting by the discharge of a capacitor bank. During impact, the arc is extinguished, excess molten metal is expelled and rapid solidification occurs. Although more restrictive than energy-beam welding with regard to the component sizes and geometries which can be joined, the process offers the potential for joining RS dispersion-strengthened alloys which contain hydrogen levels too high to allow fusion welding without significant porosity formation.

In the previous study, capacitor-discharge welds were produced between cylinders of Al-8.4 wt%Fe-3.6 wt%4Ce using a fully-automated and instrumented welding system at the Oregon Graduate Center (10,11). The specimen tip geomety, drop weight and drop height were varied to effectively achieve different solidification and cooling rates within the weld fusion zone. As shown in Fig. 6, high quality, defect-free joints were produced using this process.

In the present study, AEM analysis across the weld zone (Fig. 7) produced at the highest pressure showed a completely Zone A microstructure comprised of dendritic alpha grains nucleating from the alpha base metal substrate and impinging at a weld centerline. An absence of primary intermetallics at the center of this fusion zone was indicative of the extremely high temperatures experienced at this location during welding. Consistent with microstructural analysis, mechanical property determination showed fusion weld zone hardnesses appreciably greater than that of the base metal and joint efficiencies of 100%.

2.1.2 Similar-Alloy 1.1.2 Similar Alloy Inertia- and Linear-Friction Welds

Despite a demonstrated capability to "recreate" an RS weld zone microstructure, the application of fusion welding techniques to many dispersion-strengthened aluminum alloys has been limited because of the inherently high hydrogen content of the alloys and associated formation of fusion zone and/or heat-affected zone porosity. Solid-phase joining processes offer an important alternative to the fusion welding of dispersion-strengthened aluminum alloys because both melting and solidification are avoided. Friction welding is a solid-state joining process that combines frictional heating generated at the faying surfaces with a high axial force to produce a metallic bond (12). The absence of melting at the interface during this process eliminates solidification-related discontinuities, such as porosity and cracking. In addition, the expulsion of surface contaminants and

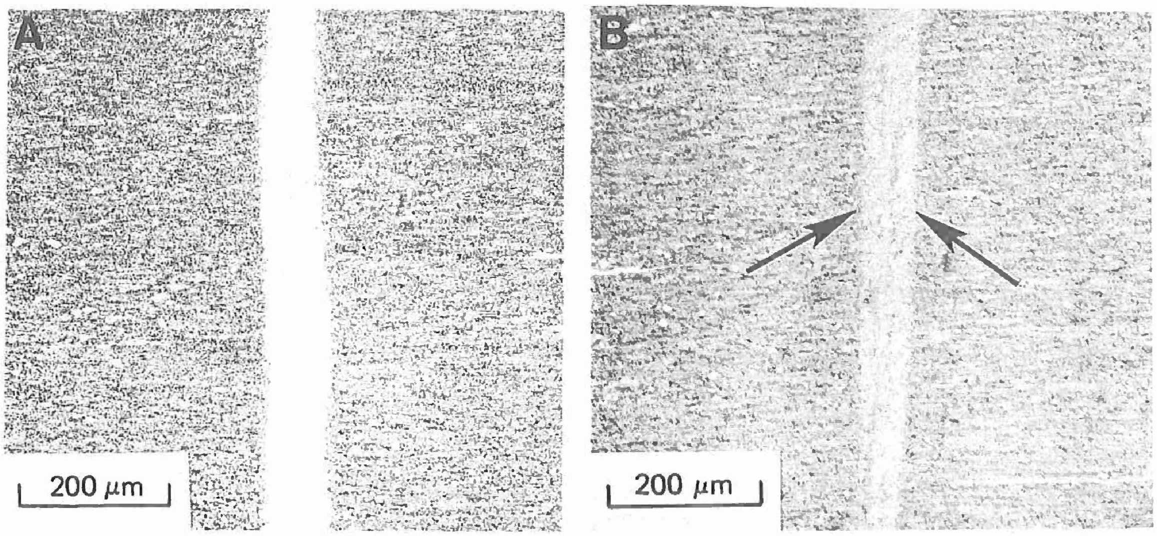

Fig. 6. Light micrographs of capacitor-discharge welds produced in Al-8Fe-4Ce which experienced (A) high and (B) moderate cooling rates.

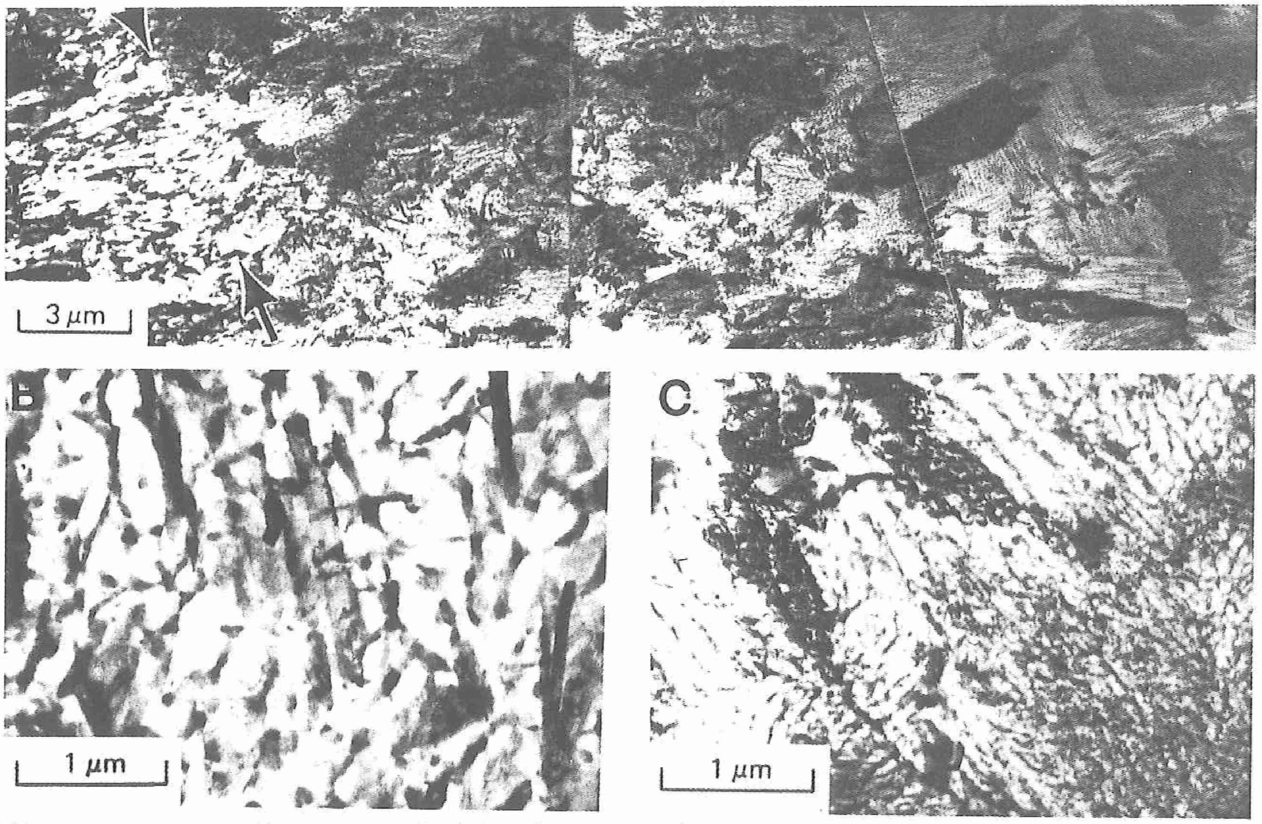

Fig. 7. TEM bright-field micrographs of capacitor-discharge weld produced in Al-8Fe-4Ce which experienced a high cooling rate: (A) microstructure traverse from unaffected base metal (left) to center of FZ (right); (B) edge of fusion zone at increased magnification; (C) center of fusion zone at increased magnification.

heat-and-deformation affected metal at the faying interfaces during the forging stage of the process promotes final coalescence between nearly unaffected base metals. Frictional heating of the workpieces is generally accomplished via rotational movement, thereby requiring a circular cross-section of at least one of the workpieces. Recent work at The Welding Institute in Cambridge, England has developed a linear-friction welding system in which heating at the weld interface occurs via relative linear (ie., translational) movement of the interfaces (13). This process is becoming more widely utilized in the U.S. due to its significant flexibility and applicability to non-axisysmmetric, non-circular workpieces.

Initial ARO-sponsored work by Hagey et al. (14) on high-hydrogen Al-Fe-Ce alloys found that high axial force significantly influences the macro- and microscopic characteristics of the weld zone, and the tendancy to form weld defects. They observed that the application of sufficiently high axial force promotes the formation of high-integrity, defect-free bonds which exhibit joint efficiencies exceeding 75%. Unfortunately, the limited spatial resolution of the light and scanning-electron microscopy techniques used in this initial study precluded effective microstructure characterization and therefore limited the development of structure/property/fracture relationships.

During the current contract period, extensive AEM was utilized to characterize both inertia-friction and linear-friction welds produced in Al-Fe-Mo-V (15) and Al-Fe-V-Si alloys (16-20). An understanding of the complex nature of deformation experienced in the vicinity of the weld interface and relationships between weld microstructures, mechanical properties and fracture behavior was developed.

Macroscopically, the heat-and-deformation-affected zone (HDZ) of both inertia- and linear-friction welds became narrower and more hourglass in shape with an increase in axial force. Extensive, high-temperature deformation during welding promoted a continuous reorientation of the directionally-oriented base metal macrostructures from perpendicular to parallel to the weld interface and a progressive microstructural transition from the heterogenous unaffected base metal to an increasingly homogenous microstructure at the center of the HDZ. This transition is shown in Fig. 8 for an inertia-friction weld produced in Al-12Fe-1.2V-2.4Si at high axial force. Light microscopy and AEM analysis revealed significant microstructural differences across the weld interfaces from the axial centerline to the weld outer periphery, which were related to differences in the thermal cycles and deformation experienced in these regions. Interestingly, evolution of the dispersoid and alpha-grain structures differed appreciably for the Al-Fe-V-Mo versus the Al-Fe-V-Si alloys. In an Al-9Fe-3Mo-1V alloy which contained relatively coarse base metal dispersoids, AEM analysis of the weld interface region revealed dispersoid fragmentation and therefore the generation of an effectively finer dispersoid structure in this region. This dispersoid refinement contributed in part to the higher hardness of this region.

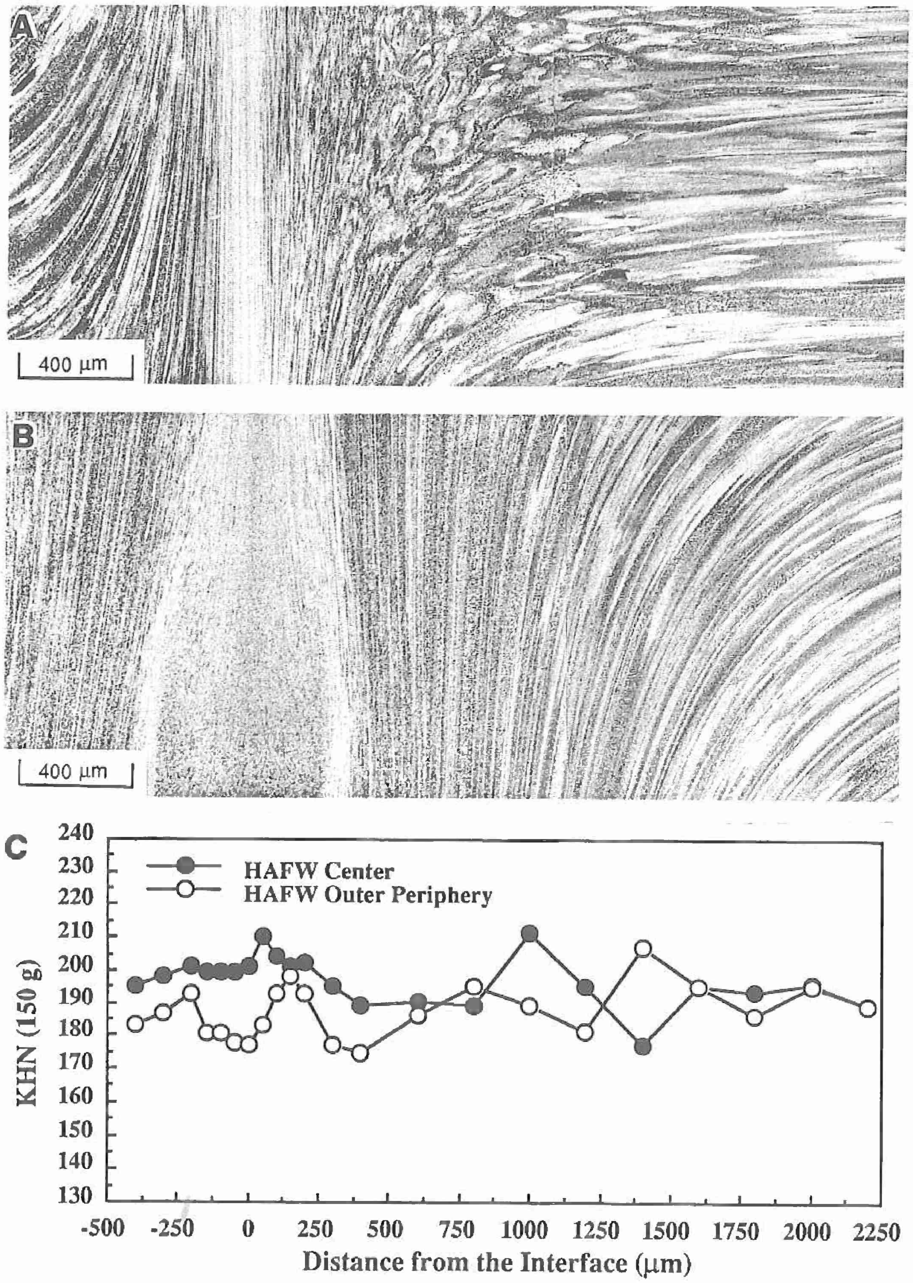

Fig. 8. Light micrographs of (A) center and (B) outer periphery regions and (C) corresponding hardness traverses for an inertia-friction weld produced in Al-12Fe-1.2V-2.4Si using high axial force.

apparent). Although similar microstructural homogenization was observed in both high and low axial force welds produced in Al-Fe-V-Si alloys (16-19), no evidence of fracture of the finer $Al_{13}(Fe,V)_3Si$ dispersoids was observed in these alloys. Analysis of a wide range of inertia-friction welds in both alloy systems revealed negligible evidence of dispersoid-coarsening, which was attributed to the rapid thermal cycles experienced during welding and to a lesser extent the expulsion of coarsened dispersoids out of the weld interface region as flash. This absence of dispersoid and alpha-grain coarsening (the alpha grains experienced dynamic recrystallization and their growth was prevented by the fine dispersoid structure) promoted negligible hardness losses across the weld interface in the welds produced at high axial force, as shown in Fig. 8.

Inertia-friction welds produced in both alloy types at lower axial force exhibited nonuniform deformation at the weld outer periphery which resulted in the formation of dispersoid-lean, coarse-grained regions with a hardness appreciably below that of the base metal. Light and TEM micrographs of this region are shown in Figure 9 for an inertia-friction weld produced in Al-12Fe-1.2V-2.4Si at low axial force (17). The application of sufficiently high axial force was found to eliminate the presence of this undesirable region.

Linear-friction welds produced in the Al-Fe-V-Si alloys exhibited microstructural transitions from the unaffected base metal to the center of the weld HDZ comparable to those of the

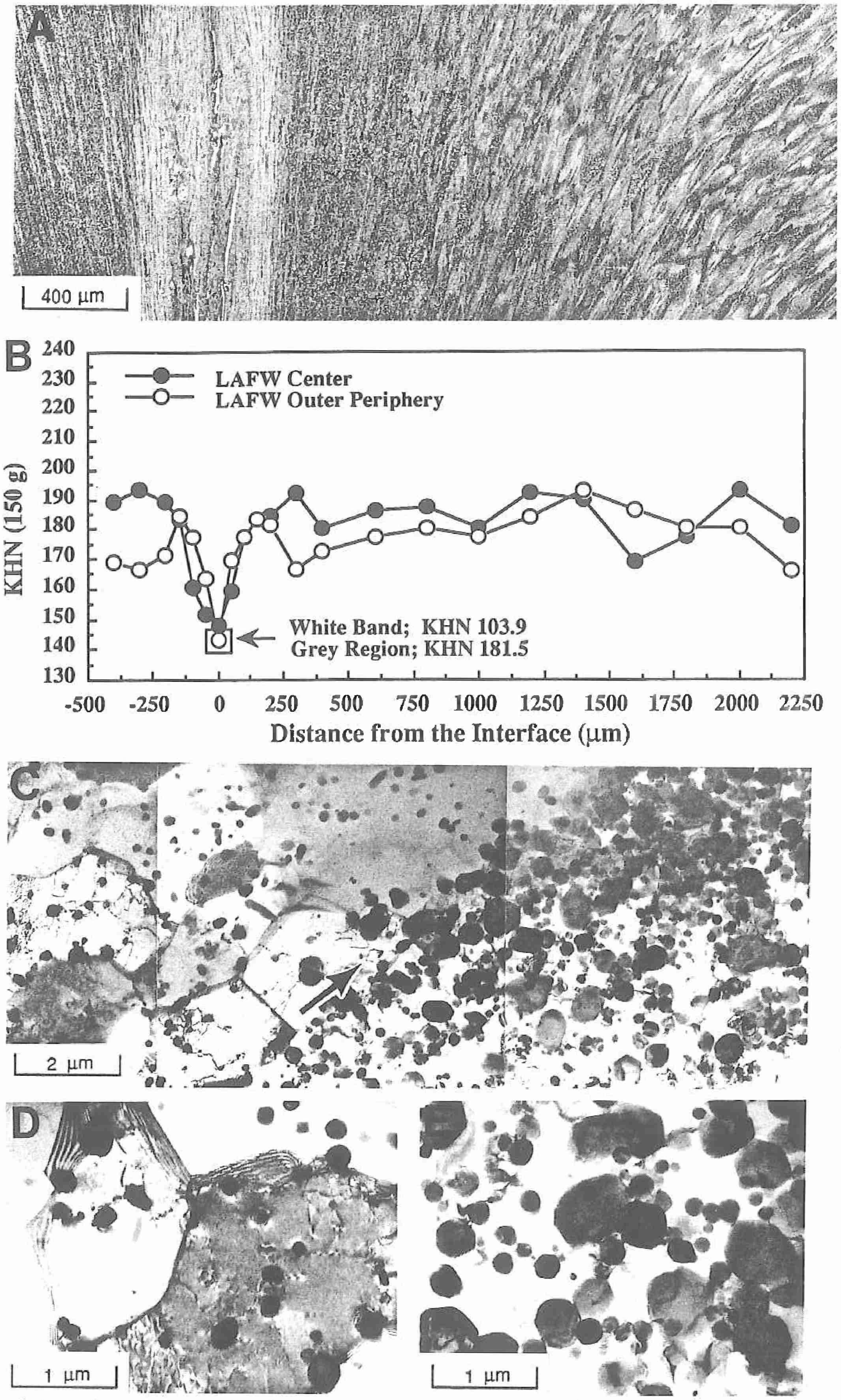

Fig. 9. Light micrograph (A) and corresponding hardness traverse (B) and TEM bright-field micrographs (C-E) at outer periphery for an inertia-friction weld produced in Al-12Fe-1.2V-2.4Si using low axial force.

inertia-friction welds (Figure 10A), but differed from the inertia-friction welds in showing evidence of dispersoid coarsening and elongation at the weld interface (Figure 10B)(18,19). This coarsening was attributed to the longer welding times experienced during the linear-friction versus inertia-friction welding processes, rather than to differences in the extent of expulsion during welding.

Results of transverse-weld oriented tensile testing were consistent for both weld types, indicating joint efficiencies exceeding 85% for welds produced at high axial force, and lesser values for specimens sectioned from the outer periphery of low axial force welds. Despite dispersoid coarsening at the weld interface, joint effiencies of the linear-friction welds were comparable to those of the high-axial force inertia-friction welds.

Extensive fractographic analysis showed failure to occur in the weld HDZ, and to be associated with the nature of deformation at the weld interface, with inertia-friction welds exhibiting a circumferential-outward deformation pattern while linear-friction welds exhibited a linear flow pattern.

2.1.3 **Dissimilar-Alloy Inertia- and Linear-Friction Welds**

As indicated above, the dissimilar joining of RS dispersion-strengthened aluminum alloys to conventional IM aluminum alloys and titanium alloys represents an important engineering goal, but presents challenging and complex process and metallurgical problems.

During the current research period, inertia-friction welds

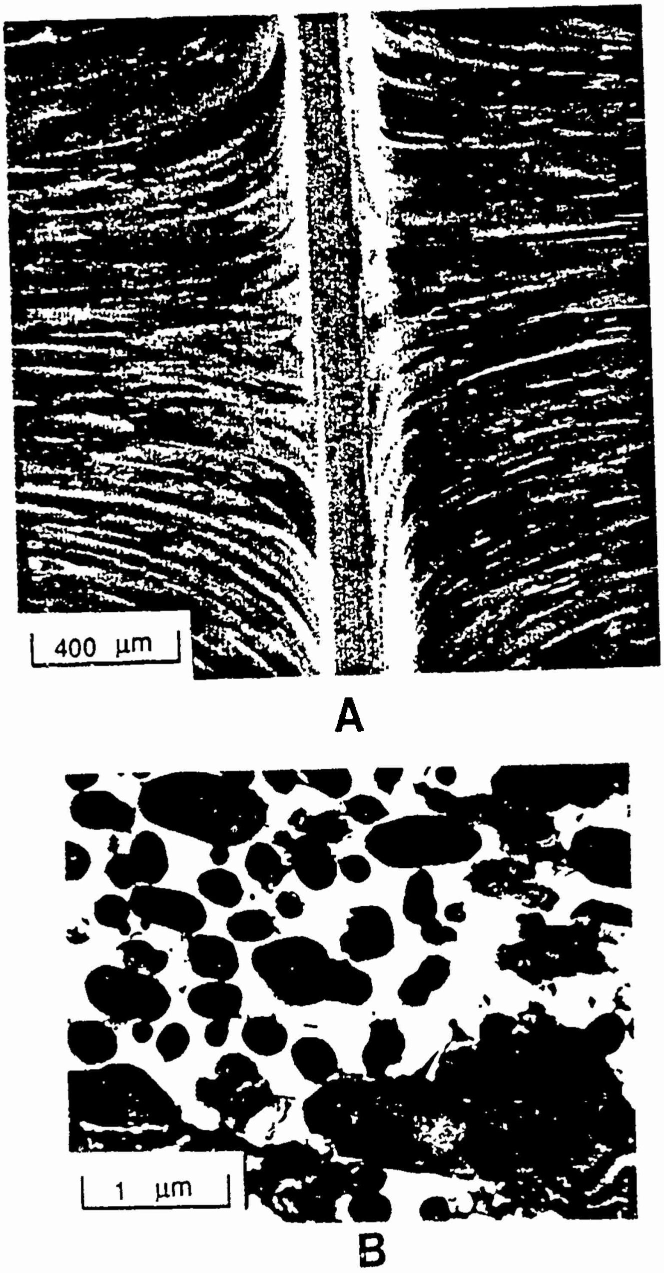

Fig. 10. Light micrograph (A) and TEM bright-field micrograph (B) at weld interface of linear-friction weld produced in Al-12Fe-1.2V-2.4Si.

were generated between Al-9Fe-3Mo-1V and IM-2024-T351 (Al-Cu) using a range of axial force levels. As expected, the weld flash originated principally from the IM-2024-T351, which was consistent with the lower elevated-temperature strength of this alloy. Detailed, systematic AEM at locations across the weld interface from the axial centerline to the outer periphery showed varying degrees of dynamic alpha grain recrystallization and the solutionizing of strengthening precipitates (S′) in IM-2024-T351 HDZ, negligible dispersoid and alpha grain coarsening in the Al-9Fe-3Mo-1V, and the occurrence of highly localized mechanical mixing between the two alloys at the weld interface. Evidence of this mechanical mixing is revealed for a low-axial force weld using AEM in Figure 11 and electron-probe microanalysis in Figure 12. Room-temperature transverse-weld tensile testing showed tensile strengths to range from between 85 and 90% of the RS/PM base metal strength, with fracture occurring principally in the Al-9Fe-3Mo-1V directly adjacent to the IM-2024-T351.

High-integrity dissimilar-alloy inertia- and linear-friction welds were also generated between IM-2024-T351 and Al-12Fe-1.2V-2.4Si and characterized in detail using light microscopy and AEM, room-temperature mechanical testing and fractographic analysis (18). Microstructural changes occurred predominantly in the IM-2024-T351, with mechanical mixing between the two alloys limited to an extremely narrow region across the weld interface. Transverse-weld tensile testing showed high joint efficiencies of

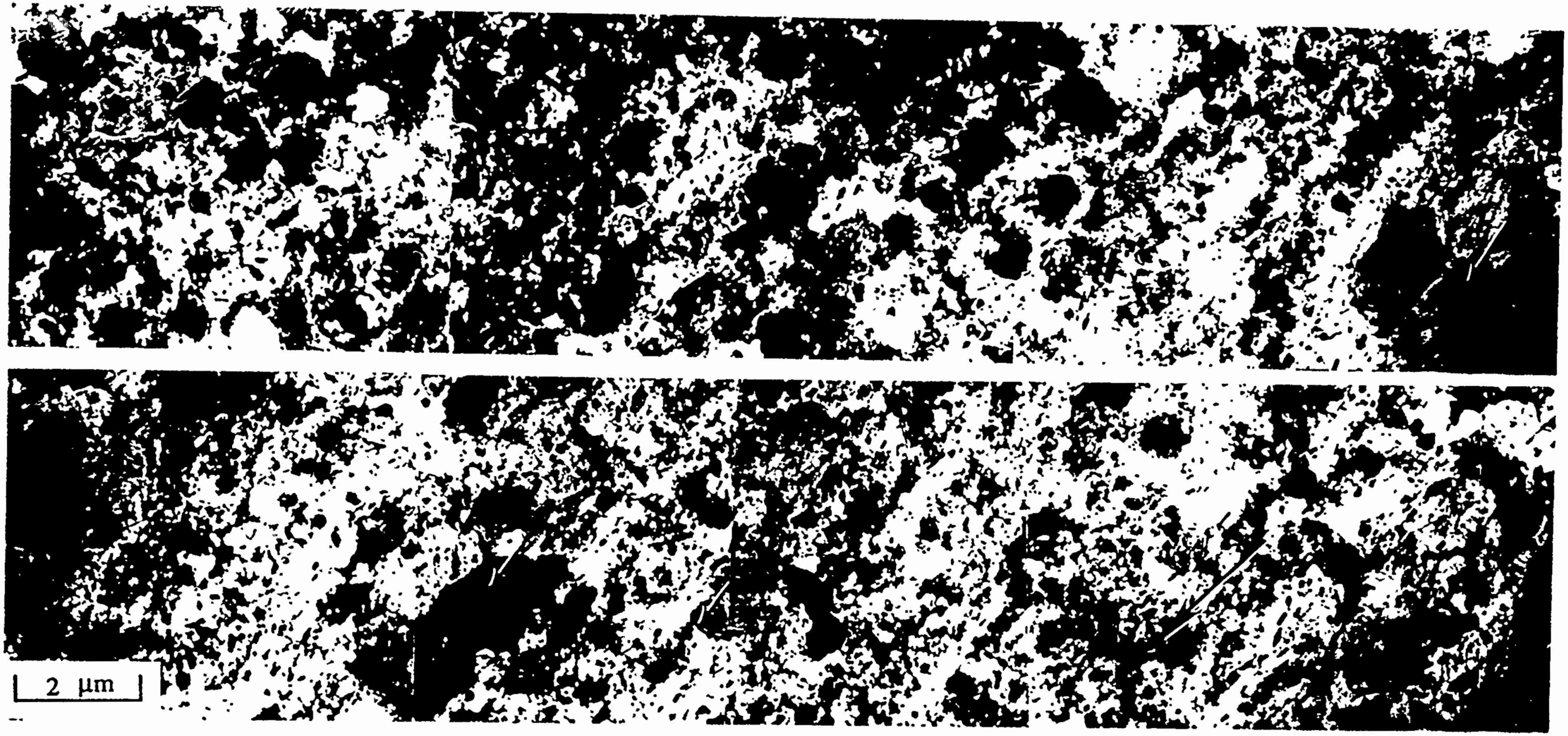

Fig. 11 TEM bright-field traverse across weld interface region at center of low-axial force inertia-friction weld between Al-9Fe-3Mo-1V and IM-2024-T351. Lower traverse is right side of top traverse. Left side of top traverse is Al-9Fe-3Mo-1V and right side of bottom traverse is IM 2024-T351. Large arrow indicates location of interface between mechanically mixed regions and IM 2024-T351.

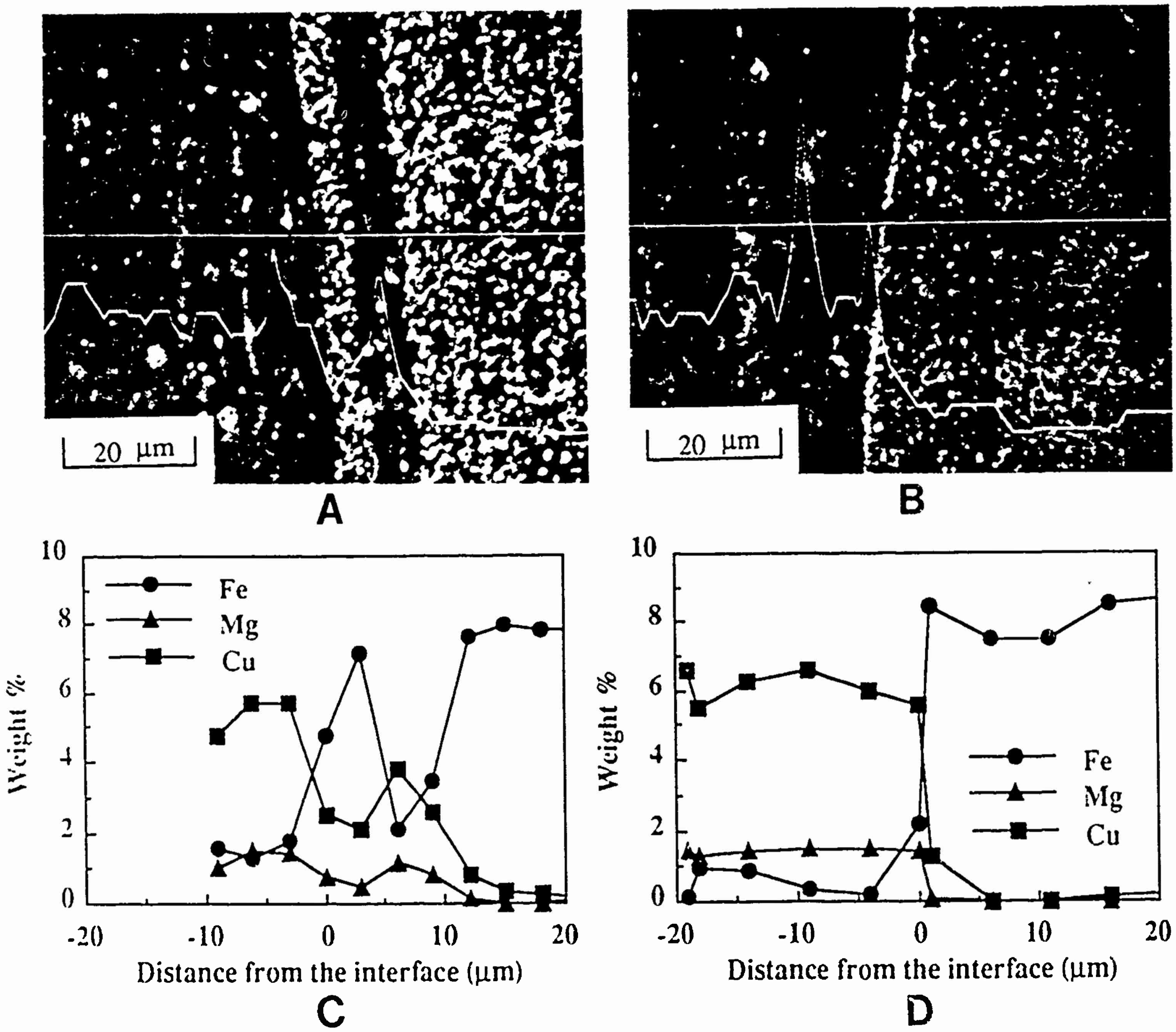

Fig. 12. EPMA traverses across low axial force inertia-friction weld interface produuced between Al-9Fe-3Mo-1V (right) and IM-2024-T351 (left). Straight lines in (A) and (B) are Cu K-alpha trace scans while (C) and (D) are results of point analysis.

95 and 85% (based on the IM 2024-T351 base metal strength) for the high axial force inertia-friction and linear-friction welds, respectively. Based on this analysis, it is anticipated that optimization of the linear-friction welding parameters would improve joint efficiencies to that comparable with optimum inertia-friction welds.

Inertia- and linear-friction welding studies were also performed on dissimilar-alloy joints produced between the RS/PM Al-Fe-V-Si alloys and Ti-1100 (an advanced, high-temperature ingot metallurgy alloy). Inertia-friction welds were produced on cylindrical specimens using a restraining ring around the lower strength aluminum in order to restrict its macroscopic deformation. Welds produced for a wide range of inertia, rotational velocity and axial force parameter combinations resulted in metallic bonds at the outer periphery (where relative velocity is highest) but incomplete bonding at the weld axial centerline. Appreciable deformation was experienced in the RS dispersion-strengthened alloy in a manner similar to that observed in similar alloy welds, while negligible evidence of microstructural change was observed in the high-temperature Ti-1100. Mechanical testing of the welds showed relatively low tensile strengths, which were attributed principally to incomplete bonding at the center of the weld, rather than the formation of a brittle titanium-aluminum intermetallic.

In an effort to achieve greater deformation in the titanium, and thereby promote enhanced bonding across the entire weld interface, a softer CP titanium alloy was inertia-friction welded to Al-12Fe-1.2V-2.4Si. As shown in Figure 13, macroscopic deformation occurred principally in the aluminum. Microscopic examination, however, revealed a region within the titanium which experienced deformation and apparent dynamic recrystallization of alpha titanium (HCP) grains. Deformation in the aluminum appeared comparable to that of the low-axial force similar alloy welds in these alloys, with dispersoid-free (white appearing) regions observed in the outer periphery. No evidence of a titanium-aluminum intermetallic was observed at the weld interface, although AEM of this interface is currently in progress. Hardness evaluation across the weld interface showed no degradation as compared to the unaffected base metals, and bend testing showed marginal ductility but evidence of complete metallurgical bonding across the entire weld interface. Considering the ease with which titanium alloys diffusion or inertia-friction weld, the results of this work are important in determining the potential of using softer interlayer materials to promote effective bonding of high-strength, elevated-temperature titanium alloys (eg., Ti-1100) to dispersion-strengthened aluminum.

2.1.4 Elevated-Temperature Exposure of Inertia-Friction Welds

Since dispersion-strengthened aluminum alloys are designed for application at elevated temperatures, the present program initiated work into evaluating the elevated temperature response of the inertia-friction weld zone, and comparing this response with that determined for the base metal region. In this work, which is presented in detail in Reference 22, inertia-friction welds

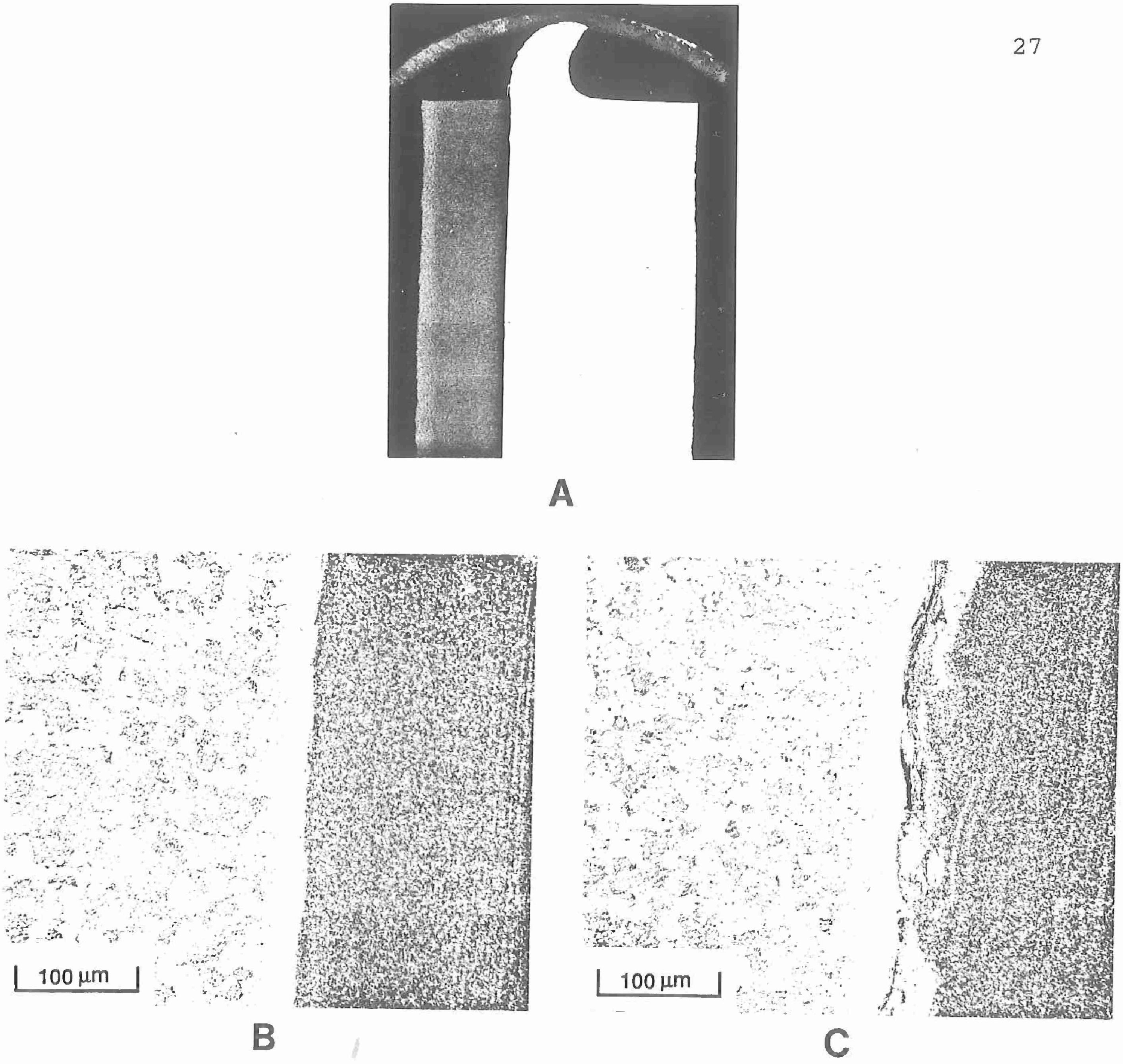

Fig. 13. Inertia-friction weld produced between Al-12Fe-1.2V-2.4Si (right) and CP titanium (left) at low axial force: (A) light macrograph; (B) light micrograph across interface at axial centerline; (C) light micrograph across interface at outer periphery.

produced in AA-8009 using a high axial force were exposed to temperatures of 425, 500 and 575 °C for times of 100, 200, 300 and 500 hours. The as-welded and thermally-exposed microstructures were characterized using light and transmission-electron microscopy and microhardness testing. Extensive quantitative metallography was performed using TEM (Hilliard's method) to characterize dispersoid and grain size distributions.

Results showed the occurrence of minimal dispersoid and grain coarsening at 425°C up to 500 hours (Figures 14 and 15). As shown in Figure 16, despite exhibiting a somewhat greater loss of hardness during thermal exposure versus the base metal and periphery region, it exhibited a higher absolute hardness than these regions after thermal exposure. Thermal exposure to 500°C promoted relatively little coarsening, however, an increase in the exposure temperature to 575°C promoted appreciable coarsening of the dispersoids and alpha grain structure, and the formation of extremely coarse, equilibrium Al_3Fe type dispersoids, as shown in Figure 17. The softening associated with this dispersoid and grain coarsening for specimens heat treated at 100 hours is shown in Figure 18.

2.2 Phase Transformations in Al-Cu and Al-Cu-Li Alloy Welds

The mechanical properties of fusion welds in high-strength, precipitation-hardened aluminum alloys are dependent to a large extent on the nature and kinetics of solid-state phase transformations (eg., solutionizing, reversion, and aging)

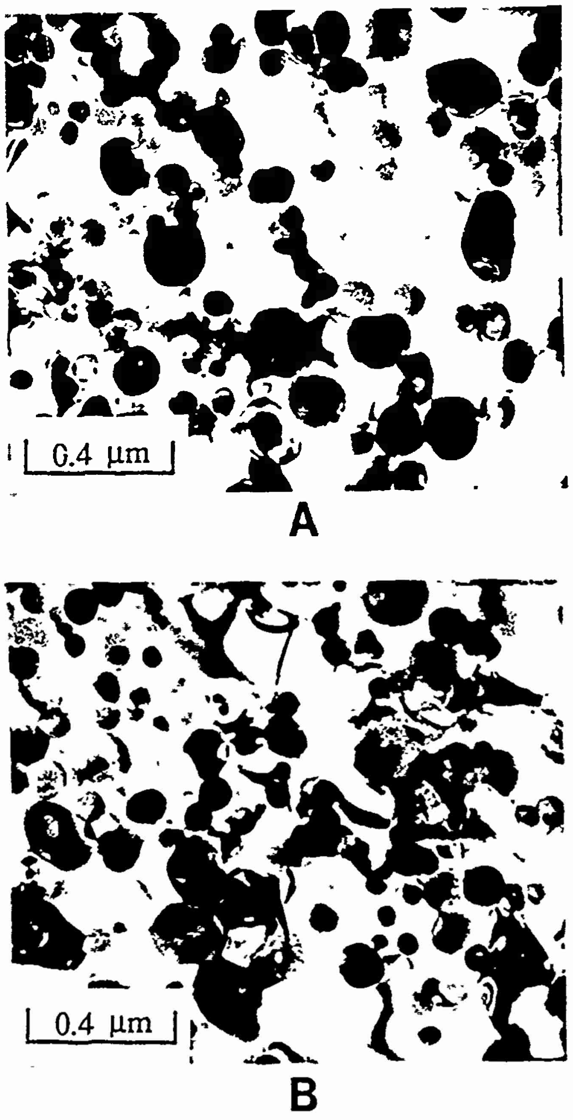

Fig. 14. TEM bright-field micrographs of the inner HDZ at the axial centerline for the AA-8009 IF weld and the base metal exposed at 425°C: (A) as-welded interface; (B) interface exposed for 500 hours.

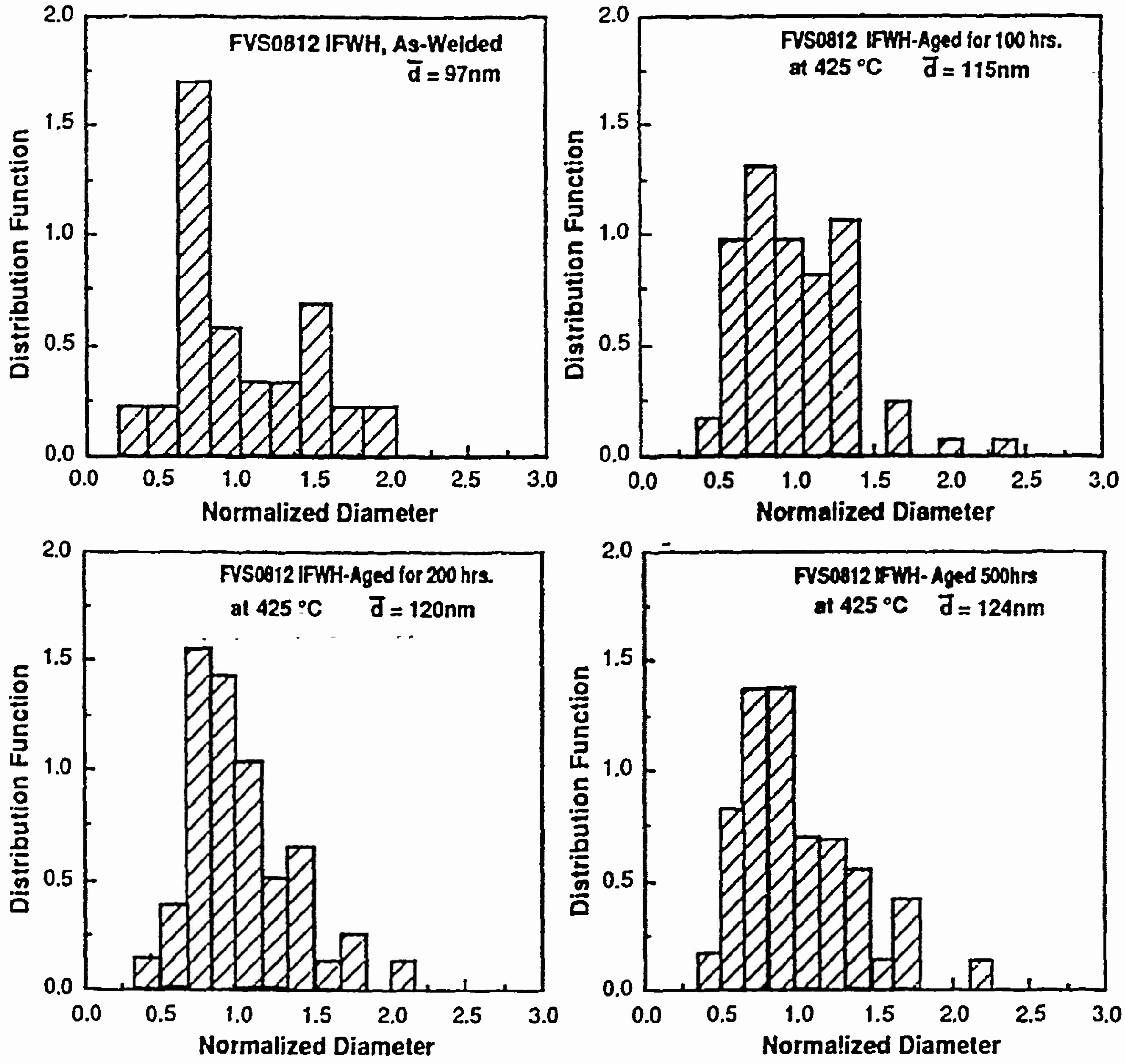

Fig. 15. Normalized distribution of dispersoids for the weld interface at the axial centerline for weld produced in AA-8009 welds exposed at 425°C.

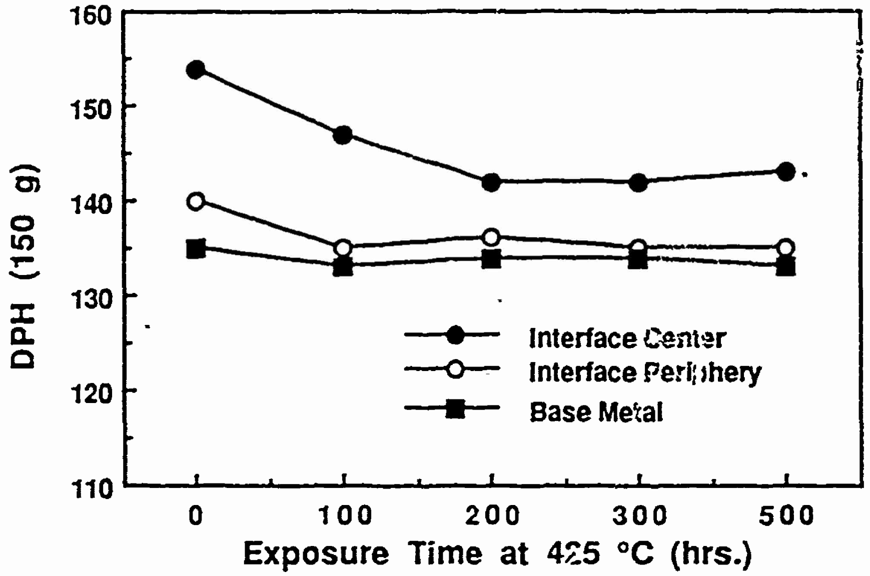

Fig. 16. Hardness versus exposure time for the base metal and central weld HDZ regions for inertia-friction weld produced in AA-8009 using high axial force.

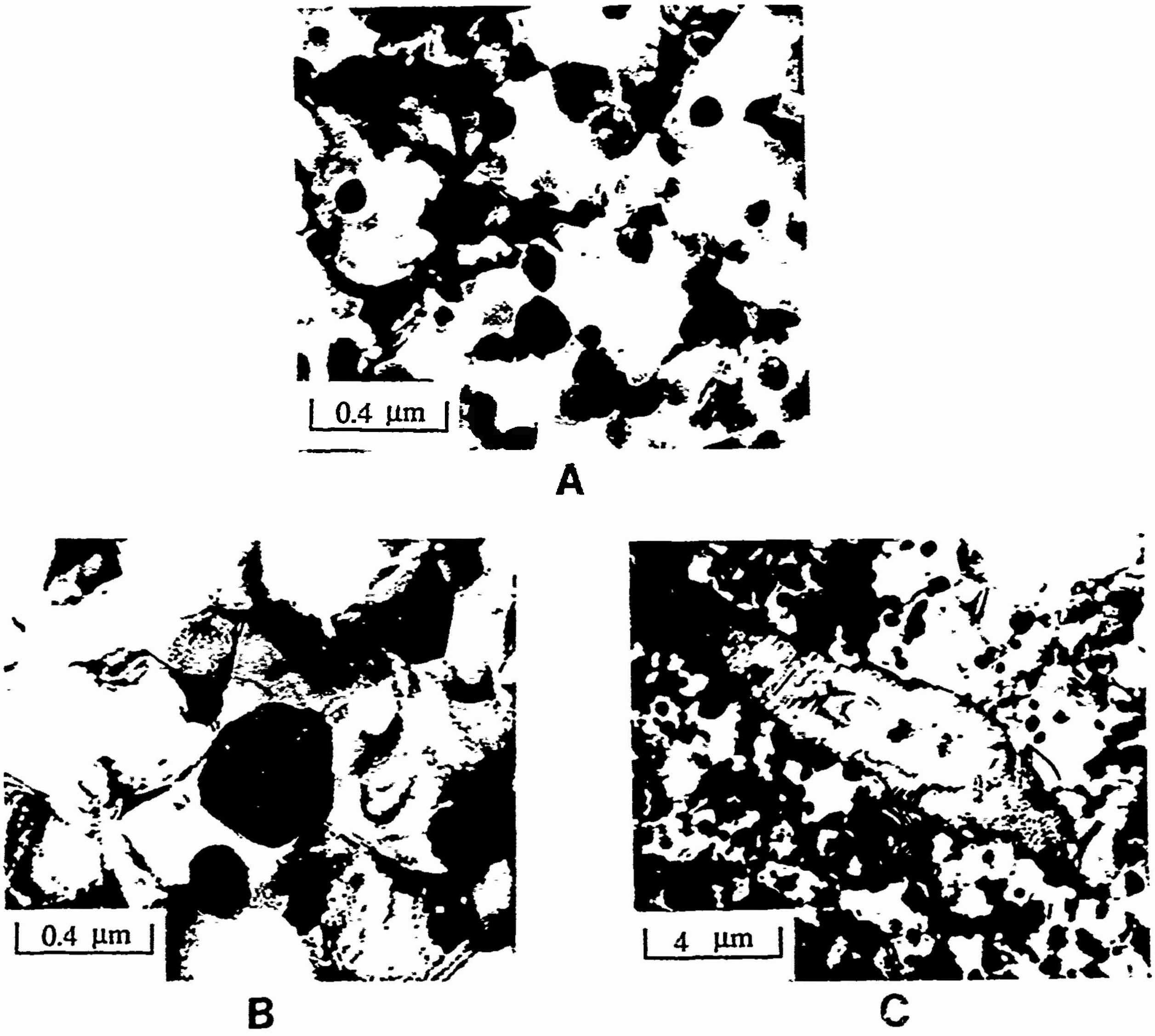

Fig. 17. TEM bright-field micrographs of the weld interface at the axial centerline for inertia-friction welds produced in AA-8009 and exposed to elevated temperatures for 100 hours: (A) 500°C; (B,C) 575°C.

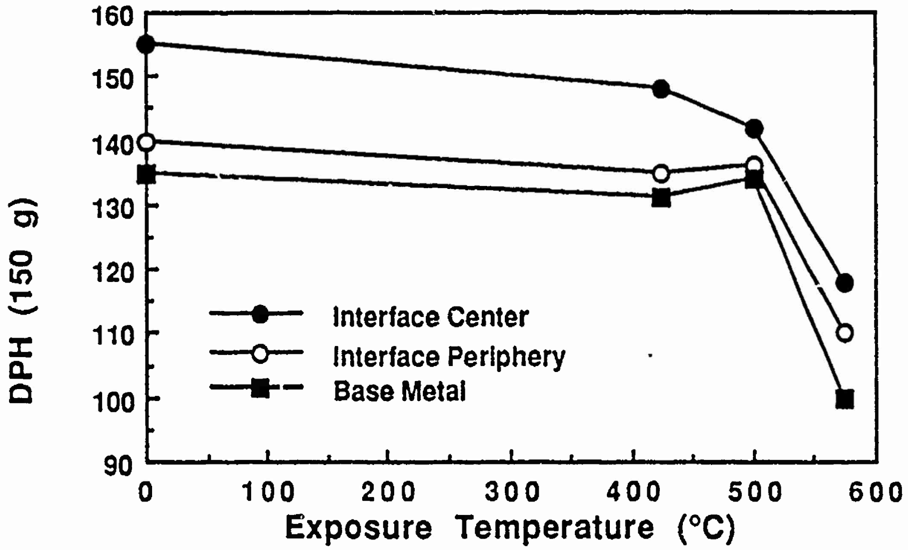

Fig. 18. Hardness versus exposure temperature in the base metal and weld region exposed for 100 hours.

experienced in the weld HAZ and fusion zone both during the welding process and subsequent postweld heat treatment. Although the limited spatial resolution of light microscopy precludes the effective analysis of these phase transformations, minimal AEM has been applied to characterize these complex phenomena. The limited AEM analysis performed to date has concentrated on the weld HAZ behavior. Studies by Dumolt (23) on GTA welds examined the nature of reversion in 2219 and overaging phenomena in 6061. More recently, Sunwoo et al. (24,25) used AEM to study thermal cycle effects on the microstructure of simulated GTA welds in the aluminum-lithium alloy 2090-T8 (Al-3Cu-2.2Li-0.1Zr (wt%). Their results indicated that dissolution of the delta-prime (Al_3Li), theta-prime (Al_2Cu) and T_1 (Al_2CuLi) strengthening phases present in the original base metal microstructure occurred at progressively higher temperatures, and that this dissolution promoted degradation in room and low-temperature mechanical properties. Work by the same authors on GTA and electron-beam weld fusion zone structures in 2090-T8 determined strengthening in the postweld aged condition to result principally from the presence of delta-prime, with the limited quantity and nonuniformity of T_1 (which was attributed to the solidification-segregation effects of Cu) reducing the contribution of this phase to precipitation strengthening.

ARO-sponsored work at OSU during the current period investigated in detail the microstructures and phase transformation behavior of GTA and laser welds in binary Al-Cu alloys and in the Al-Cu-Li alloy 2090-T8. The primary emphasis of this work was to investigate the influence of solidification-induced macro- and microsegregation effects on the precipitation response of the weld fusion zone both on weld cooling and at room temperature (ie., during auto- or natural aging) and during postweld heat treatment. It should be noted that this work is presently in final review for publication (26,27) and information and data obtained will only be summarized herein.

Initial work was performed on Al-2.5wt% and 6.0 wt% Cu binary alloys heat-treated to provide a base metal microstructure comprised of alpha aluminum and theta-prime. Light microscopy analysis of the weld fusion zone showed a typical dendritic alpha-aluminum solidification substructure with a divorced eutectic located at dendrite intersticies and grain boundaries. Detailed AEM (ie., TEM, STEM, SAD) analysis across the as-welded microstructure revealed a nearly precipitate-free alpha aluminum matrix with interdendritic Al_2Cu intermetallic located at both high and low-angle grain boundaries (Fig. 19). Occasional theta-prime precipitates were observed in regions surrounding the eutectic intermetallic which apparently forming during weld cooling or at room temperature Postweld aging at 190°C for 1, 4 and 16 hours promoted the heterogenous precipitation of theta-prime in the vicinity of eutectic intermetallic located at low-angle solidification subgrain boundaries, and along such boundaries which connected isolated islands of eutectic intermetallic. As shown in Figures 19B-D, an increase in aging time promoted an increase in coarseness of the theta-prime platelets. The almost constant width of the precipitate zone (4-5 microns) suggested that this region contained a critical minimum Cu content achieved during the final stages of interdendritic weld solidification, which is consistent with existing models for intercellular or interdendritic solidification segregation (28,29).

Following analysis of the Al-Cu binary alloys, detailed AEM was performed on autogenous GTA and CO_2 laser welds produced on 2090-T8E50 plate. Analysis of regions across the GTA and LW weld HAZ's in the as-welded condition indicated the occurrence of precipitate dissolution and growth phenomena appreciably more complex than that observed in the Al-Cu binary alloys and by Sunwoo (24) (which is consistent with the wider range of peak temperatures evaluated in the present study). Although space does not allow the

Fig. 19. GTA weld fusion zone in Al-2.5wt%Cu alloy: (A) TEM bright-field micrograph of as-welded microstructure, arrow indicates eutectic intermetallic; (B,C) TEM bright and dark-field micrographs of weld aged at 190°C/1 hr; (D,E) TEM bright and dark-field micrographs of weld aged at 190°C/16 hours.

details of these structures to be presented herein, an important observation was the existence of a soft, transition zone between the far and near-HAZ regions. In this region, which is shown in

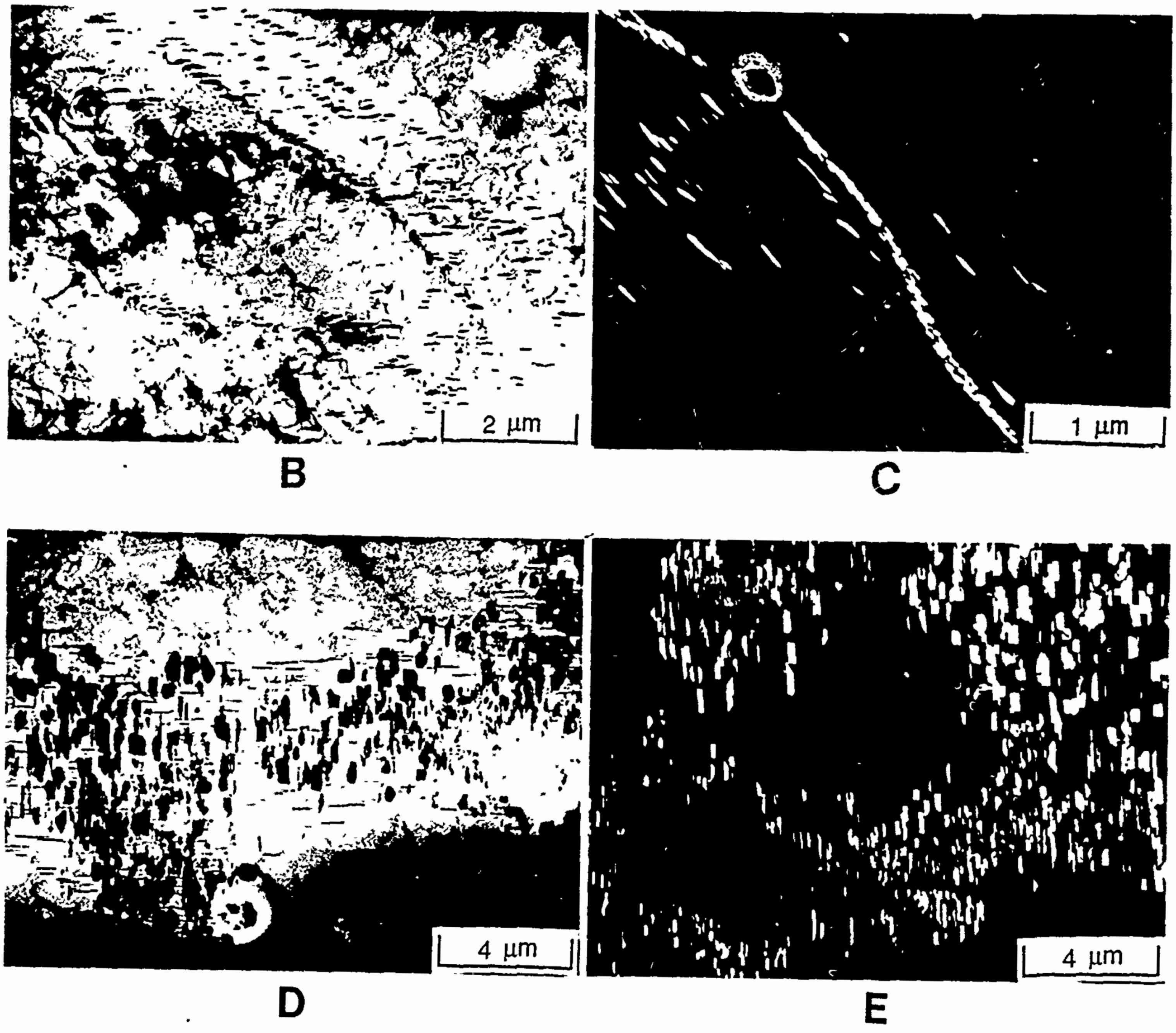

Fig. 9 (con't).

Figure 20, the original delta-prime reverted or resolutionized, the T_1 phase coarsened, and extremely fine delta-prime reprecipitated during weld cooling.

As indicated above, the objective of the current work was principally to evaluate the influence of solidification-induced segregation on precipitation effects in the weld fusion zone. Light microscopy of GTA welds in 2090-T8 revealed a dendritic alpha aluminum structure with interdendritic divorced eutectic (Fig. 21A). AEM analysis of this region revealed the presence of one eutectic type exhibiting an elongated morphology along alpha grain and subgrain boundaries and a second type exhibiting a more nodular morphology present within the alpha matrix, presumably at locations from which the grain boundary migrated following solidification. The presence of two eutectics, predicted to be comprised of alpha + T1 and alpha + TB (copper-rich), is consistent with solidification studies on 2090 by Chen et al. (30). SAD and dark-field imaging did reveal the presence of extremely fine, uniformly-distributed delta-prime throughout the alpha aluminum matrix (Fig. 21C). Postweld aging of the GTA weld fusion zone at 190°C promoted the nonuniform precipitation of T_1 platelets principally in the vicinity of the interdendritic eutectic (Fig. 22A), in a manner similar to the precipitation of theta-prime in the Al-Cu binary alloy. As shown in Figs. 22B-D, dark-field analysis revealed a noticible coarsening of the delta-prime precipitates, but their relatively uniform distribution across the alpha-aluminum matrix.

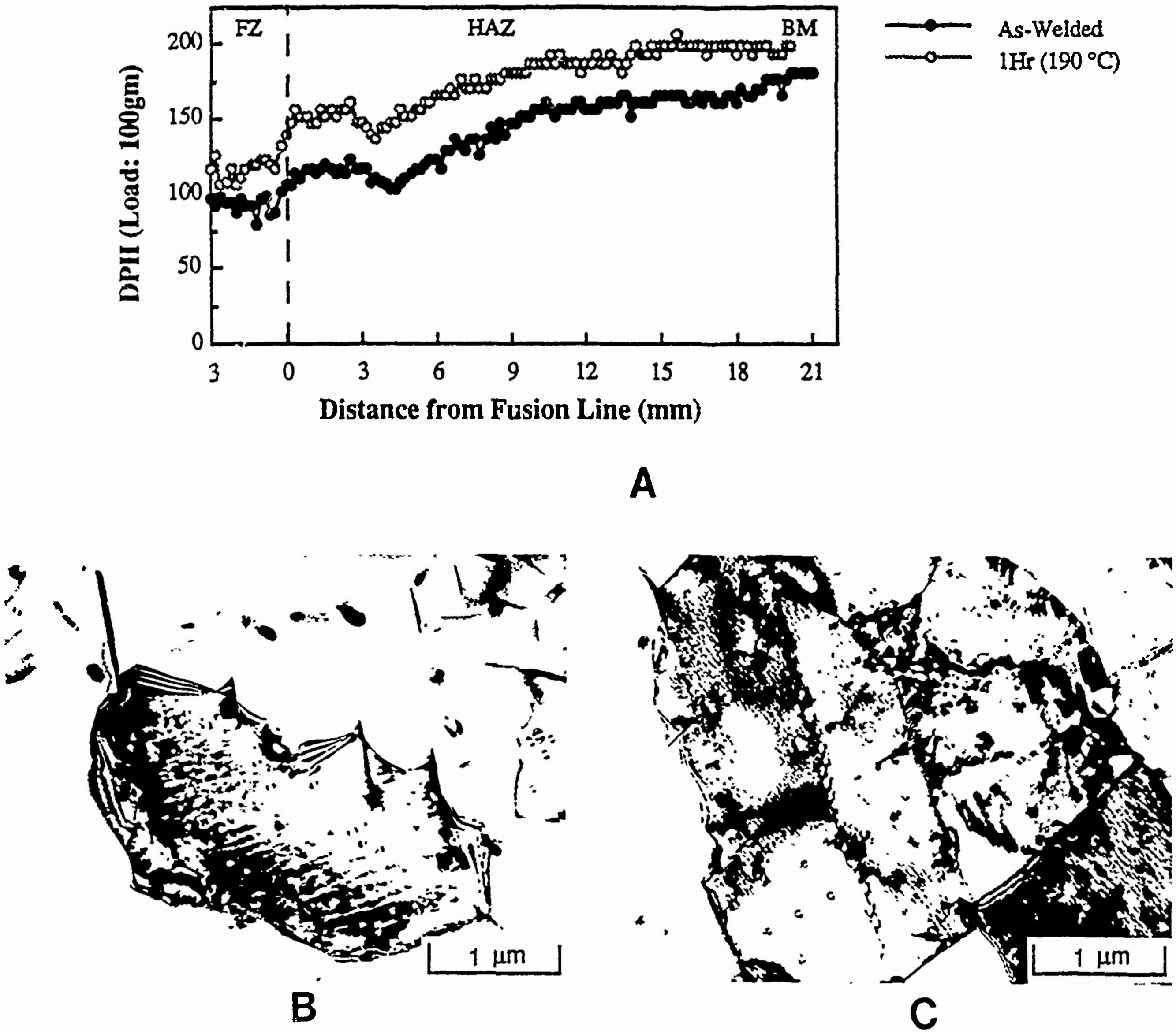

Fig. 20. GTA weld HAZ in 2090-T8: (A) hardness traverse across weld zone: (B,C) TEM bright-field micrographs showing grain boundary pinning by T_1 platelets.

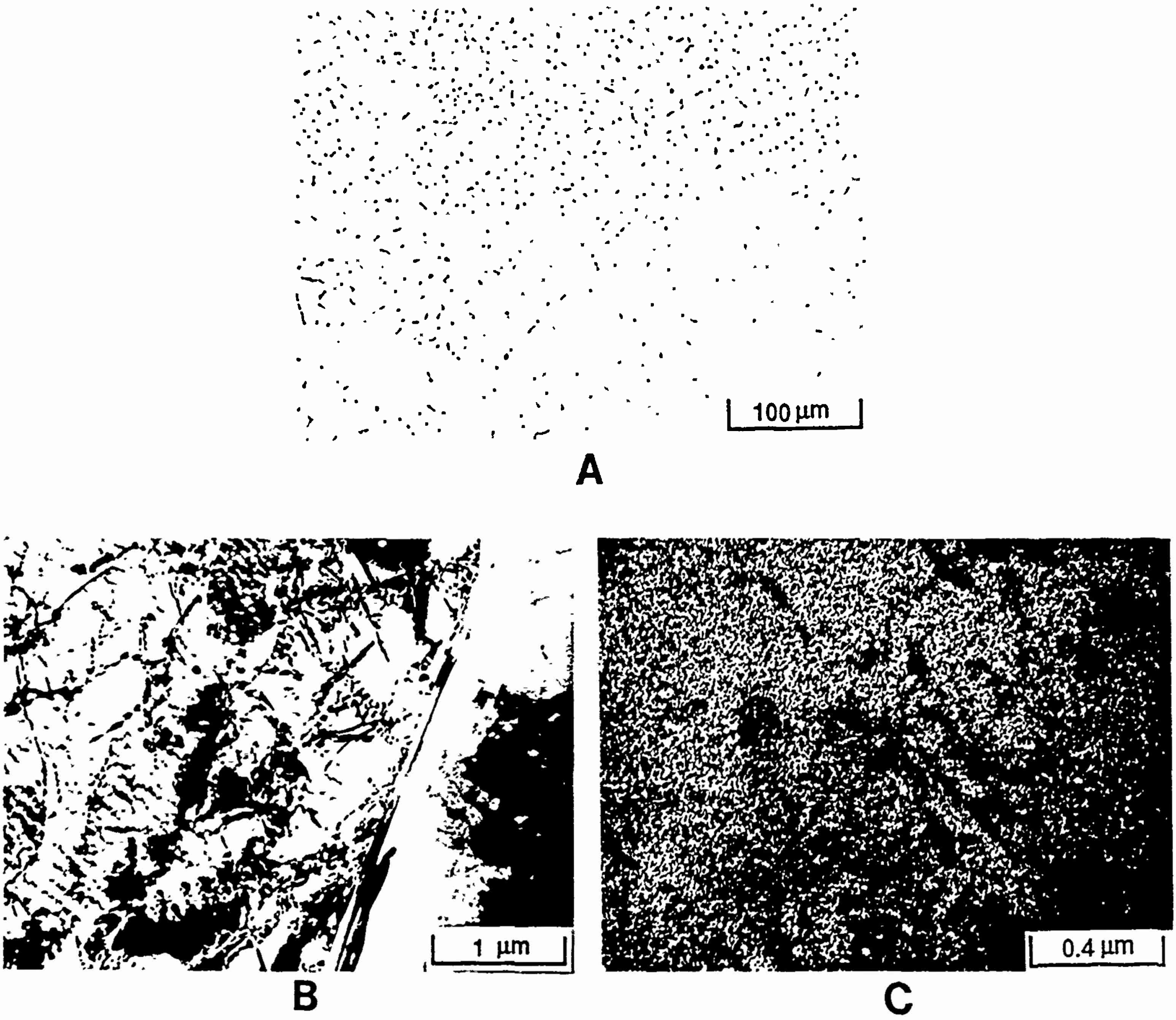

Fig. 21. GTA weld fusion zone (as-welded) in 2090-T8: (A) light micrograph; (B) TEM bright-field micrograph (arrow indicates eutectic intermetallic); (C) TEM dark-field micrograph showing delta-prime precipitates.

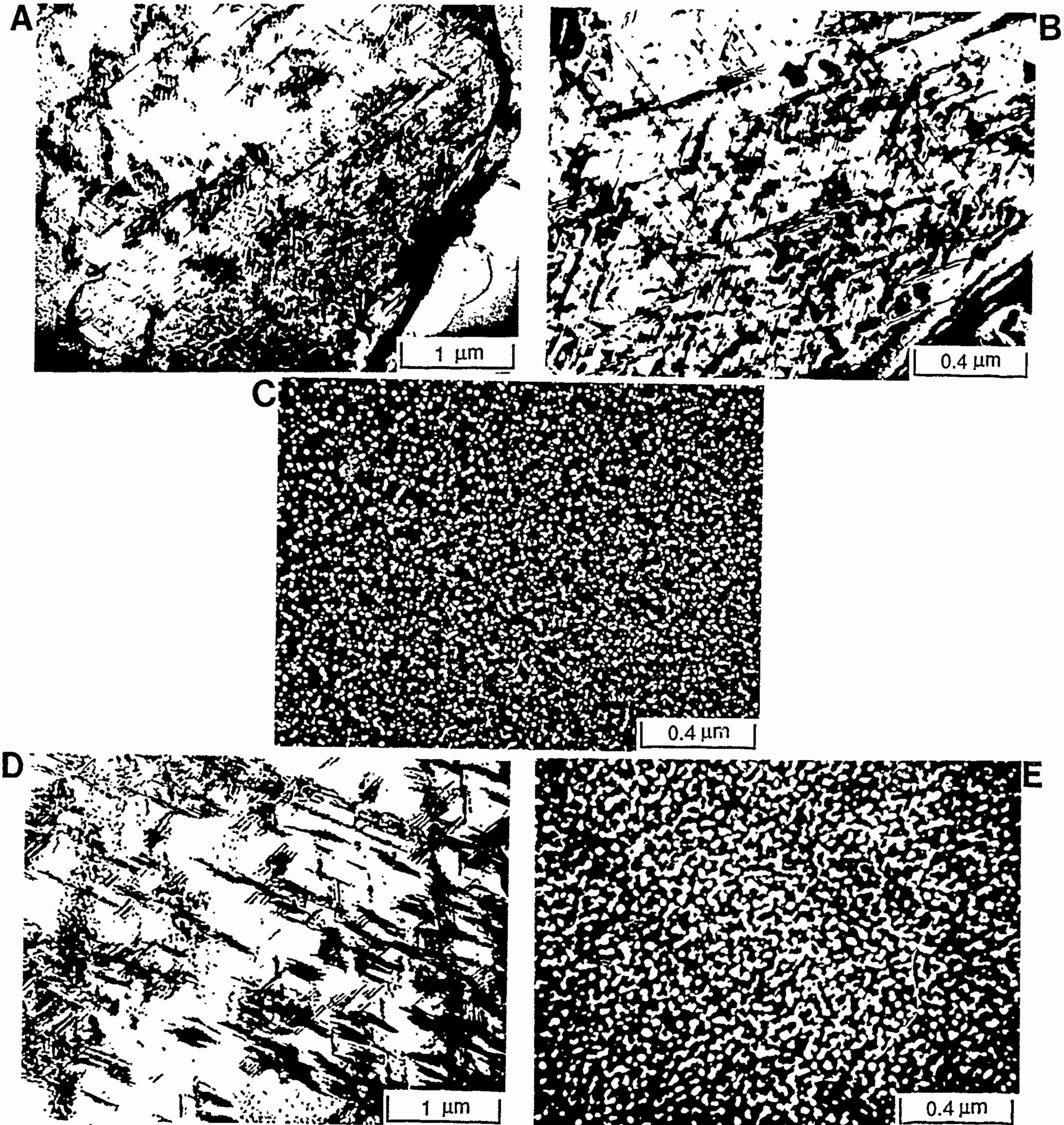

Fig. 22. GTA weld fusion zone in 2090-T8: (A,B) TEM bright-field and (C) dark-field micrographs of weld aged at 190°C/4 hr; (D) TEM bright-field and (E) dark-field micrographs of weld aged at 190°C/16 hours.

As expected, the laser weld fusion zone exhibited a much finer dendritic solidification substructure as compared to the GTA weld. Although not resolvable using TEM, SAD did indicate the presence of extremely fine delta-prime. Aging at 190°C for only one hour promoted the formation of T_1 and coarsening of the delta-prime. As in the GTA welds, the delta-prime was homogenously distributed, while the T_1 was located principally near solidification sub-grain boundaries. Figure 23 shows a high density of T_1 precipitates surrounding both binary and ternary eutectics for a laser weld fusion zone heat treated at 190°C/16 hours.

Correlation of as-welded and postweld heat-treated microstructures with hardness and tensile strength across the weld zone has been performed principally on the Al-2.5wt%Cu and 2090-T8 alloys. Generally, an increase in postweld heat treatment temperature promoted an increase in hardness and strength due to coarsening of the aging precipitates (overaging has not been observed for the time/temperature combinations evaluated to date). A detailed analysis of structure/property/fracture relationships is currently being completed for these alloy combinations under the current program.

2.4 Ultrasonic Analysis of Solid-Phase Welds in Advanced Aluminum Alloys

Ultrasonic nondestructive analysis (NDE) represents a technology critical to the effective implementation of both similar and dissimilar-alloy joints in advanced light materials. Conventional ultrasonic NDE evaluates reflected ultrasonic signal

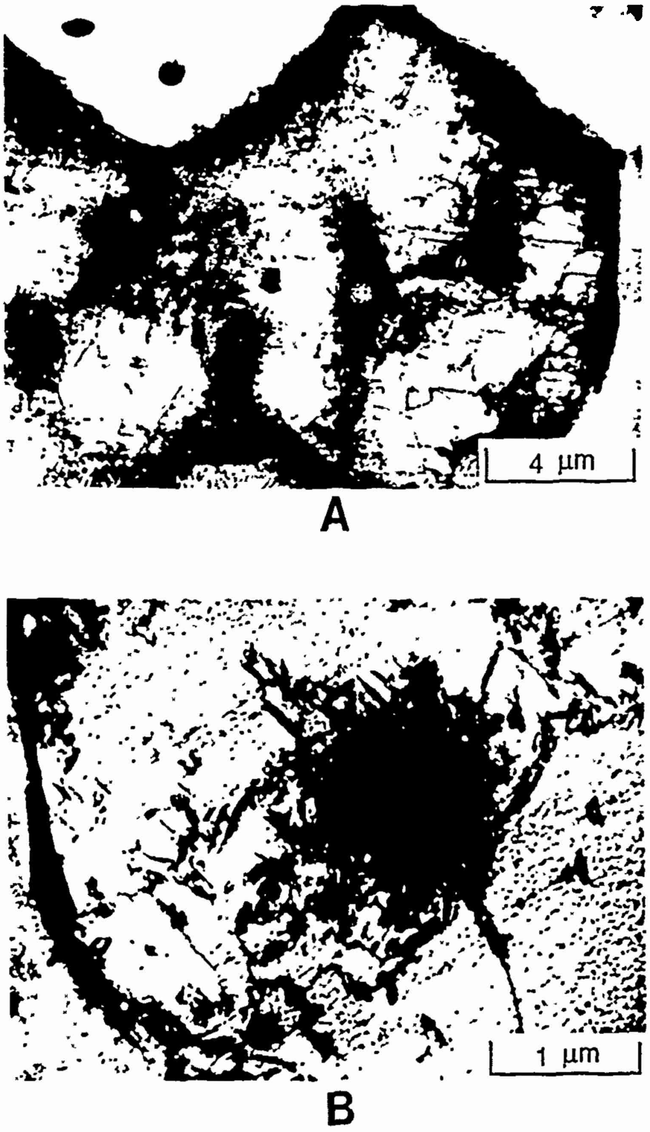

Fig. 23. TEM bright-field micrographs of CO_2 laser weld fusion zone in 2090-T8: (A) heterogenous formation of T_1 along alpha sub-grain boundaries; (B) heterogenous nucleation of T_1 around eutectic intermetallic within alpha matrix.

intensity (i.e., amplitude) in a time domain to obtain information regarding the location and size of defects and discontinuities in a material. Although the application of such conventional techniques (eg., the widely used "B" and "C" scan techniques) will continue to be significant, advanced ultrasonic NDE techniques continue to be developed which can provide greater resolution and accuracy versus conventional systems.

During the past decade, Adler and co-workers at OSU have developed ultrasonic spectroscopy analysis techniques in which a wide spectrum of frequencies are analyzed in order to characterize the nature of material discontinuities, structure, etc. The application of this technology to a wide range of materials, joint types and discontinuity types has demonstrated that such analysis can provide significantly greater information than conventional time-domain ultrasonic NDE systems.

Figure 24 shows a schematic illustration of the system utilized in the present ARO-supported program at OSU to characterize similar and dissimilar-alloy solid-phase welds produced in RS, dispersion-strengthened aluminum alloys. It consists of a system to generate, receive and amplify the ultrasonic signal and a signal analyzer to provide the required output. Signal analysis includes gating to isolate a particular acoustic signal, digitalizing of the signal, transforming from the conventional time to a frequency domain using a fast-Fourier transform (FFT) analysis, and finally signal deconvoluton to eliminate system frequency response. Selected samples of

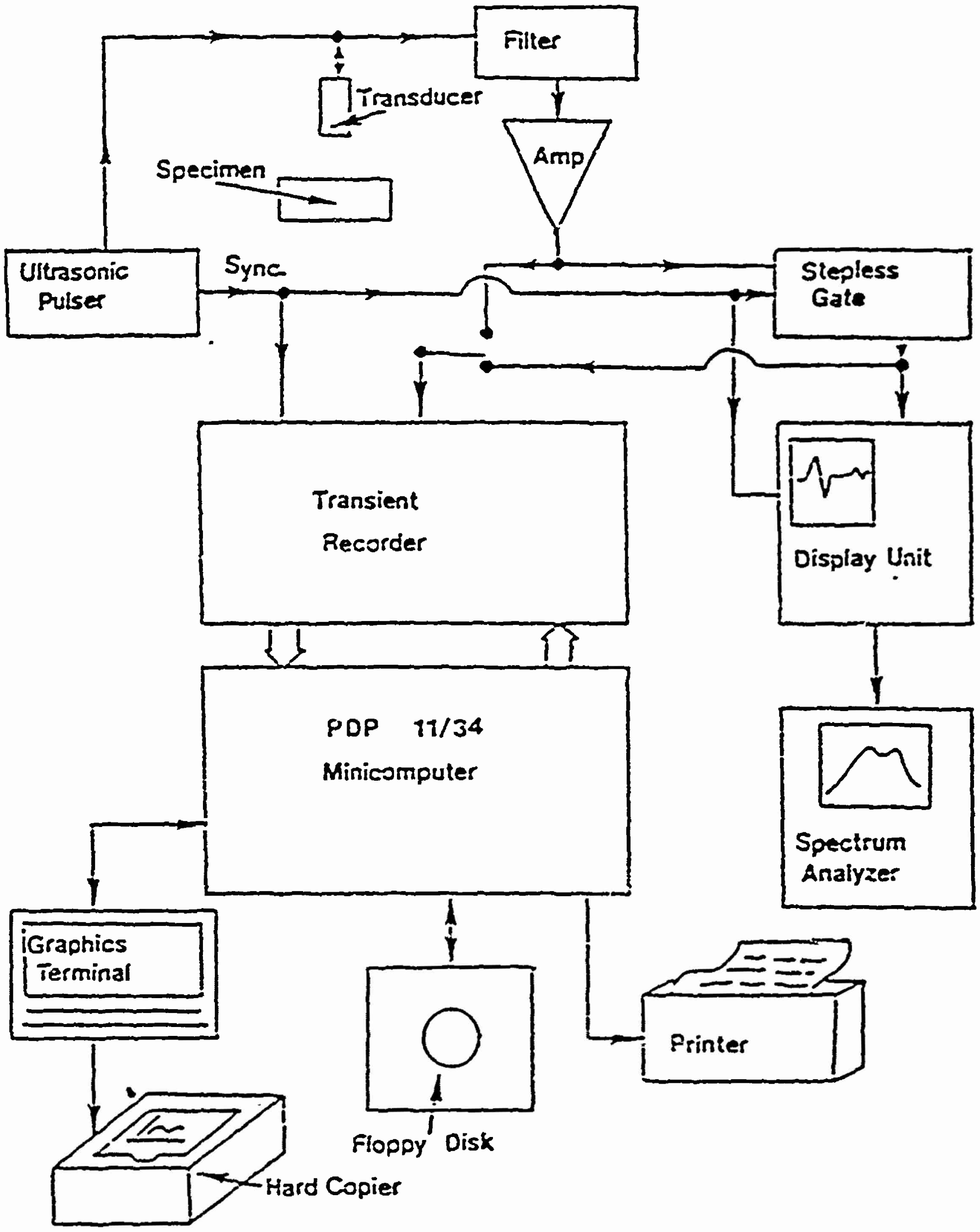

Fig. 24. Schematic illustration of OSU ultrasonic spectroscopy system.

how this system has been applied to the analysis of welds in light alloys are given below.

A symmetric reflection technique was applied to characterize the weld interface in dissimilar inertia-friction welds between Al-9Fe-3Mo-1V and IM-2024-T351. In this technique, reflection coefficients from both sides of the welded specimen were combined into symmetric and antisymmetric parts in order to facilitate better separation between possible boundary imperfections and the ideal boundary. Figure 25 shows a plot of reflection coefficient versus frequency for the dissimilar alloy weldment. R_1 and R_2 are the reflection coefficients with sound wave incidence from the IM and RS alloys respectively, R_s is the symmetric part of the reflection coefficient (ie., $R_s = (R_1 \div R_2)/2)$) and R_a is the antisymmetric part of the reflection coefficient (ie., $R_a = (R_1 - R_2/2)$. Depending on the acoustic impedance, Z, at the weld interface, cases of perfect bonding and a lack of bonding can be considered. For perfect bonding, $R_1 = - R_2$, and therefore R_s = zero. For lack of bonding, $R_s = -1$. In Figure 26, R_s is nearly zero across a wide range of frequencies, indicating good bonding, which was consistent with metallographic analysis and conventional "C" scan analysis. The significance of this analysis, versus the use of exclusively the "C" scan data, is that it is much more discriminating due to the range of frequencies examined, and also quantitatively more comparable to data obtained from other weldments.

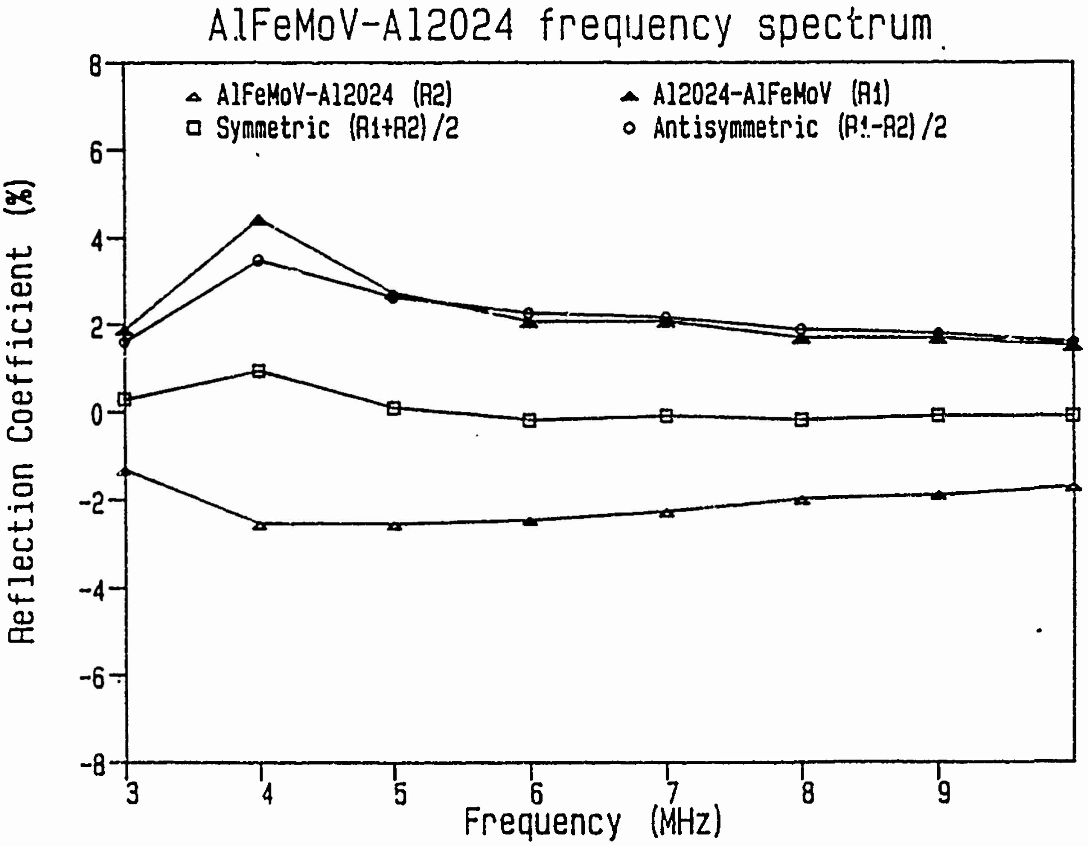

Fig. 25. Ultrasonic spectroscopy frequency spectrum generated for dissimilar-alloy inertia-friction weld produced between Al-9Fe-3Mo-1V and IM-2024-T351.

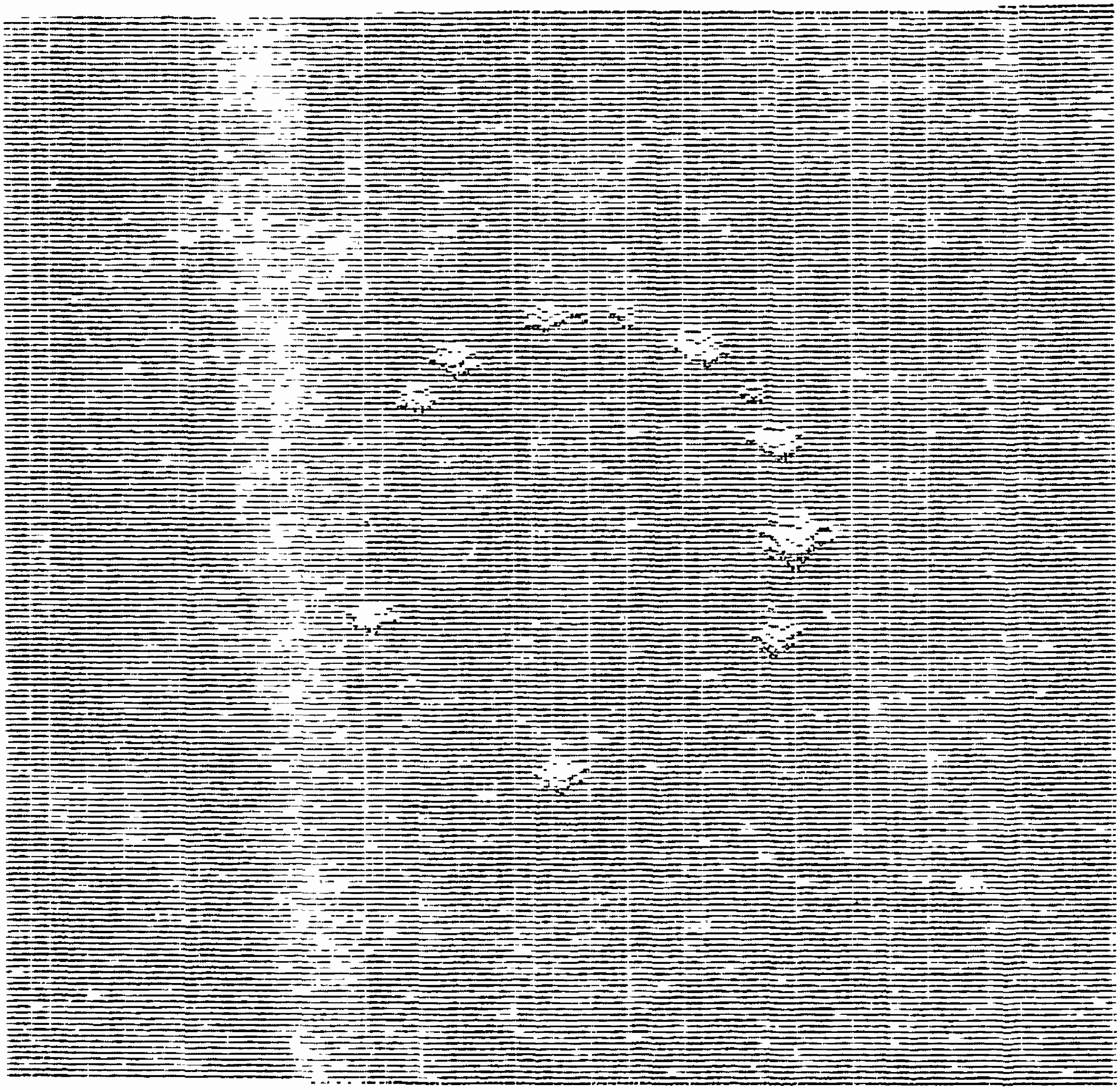

Fig. 26. Ultrasonic "C" scan image generated for dissimilar-alloy inertia-friction weld produced between Al-9Fe-3Mo-1V and IM-2024-T351.

Similar and dissimilar-alloy inertia- and linear-friction welds produced in the Al-Fe-V-Si alloys and IM-2024-T351 were characterized using conventional C-scan analysis, the generation of amplitude/position profiles from the axial centerline to the outer periphery, and reflection coefficient vs. amplitude curve generation. In general, results were very consistent with metallographic evaluation in showing only occasional discontinuities at the outer periphery, which were associated with flash formation. Interestingly, the reflection profile shown in Fig. 27 for a dissimilar inertia-friction weld indicated a change in weld quality from the center of the weld to the outer periphery, with an indication of the lowest bond quality at a midpoint between the weld axial centerline and outer periphery. This figure also reveals a lower amplitude associated with the high versus the low axial force welds, which indicates a higher integrity bond as indicated metallographically and through mechanical property evaluation. A similar difference in reflection coefficient amplitude is shown over a wide range of frequencies for these same welds in Figure 28.

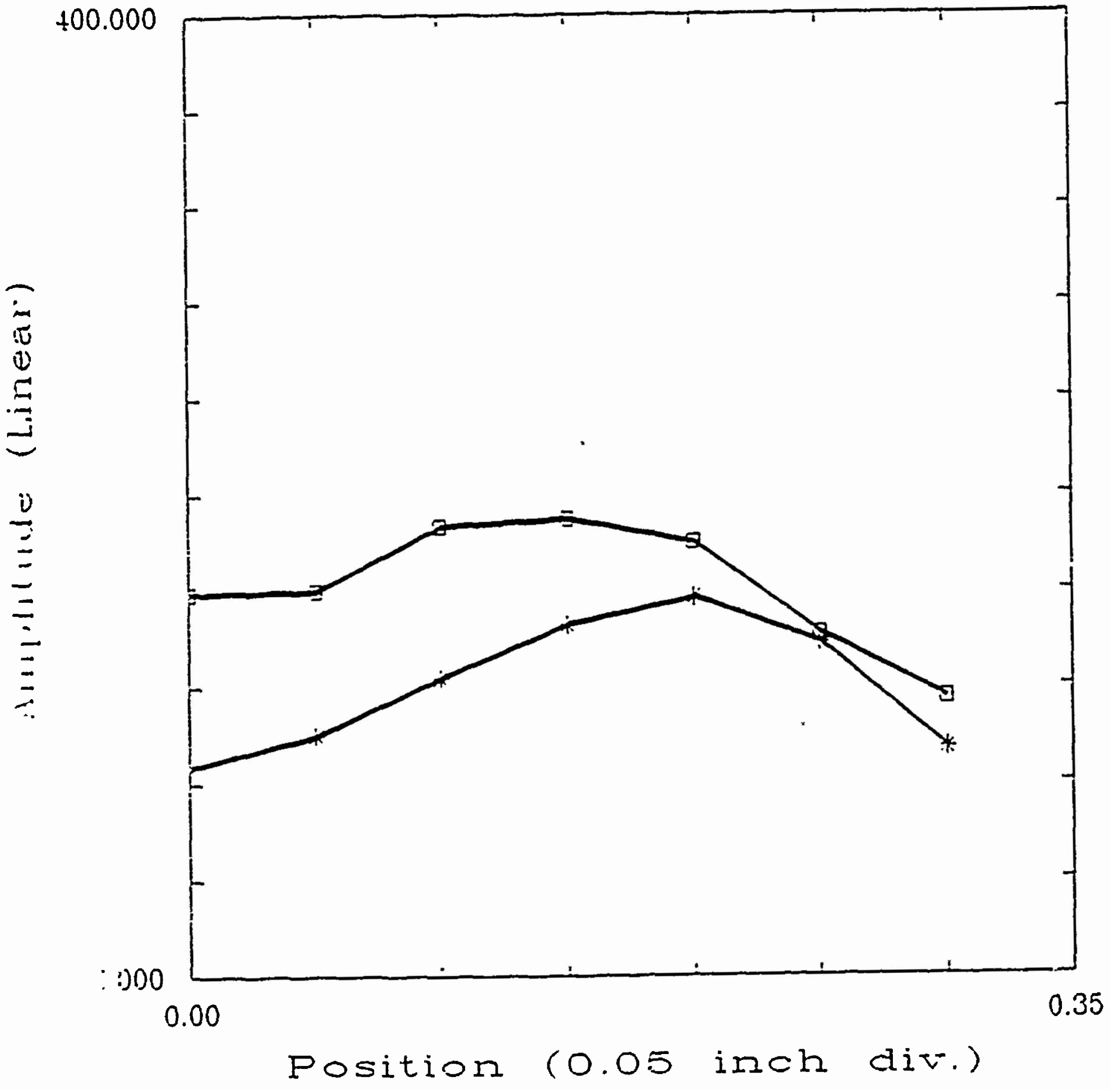

Fig. 27. Reflection profile from the interface of inertia-friction welds produced between Al-12Fe-1.2V-2.4Si and IM-2024-T351 at low axial force (squares) and high axial force (asterisks). Note the higher amplitude of the low axial force weld.

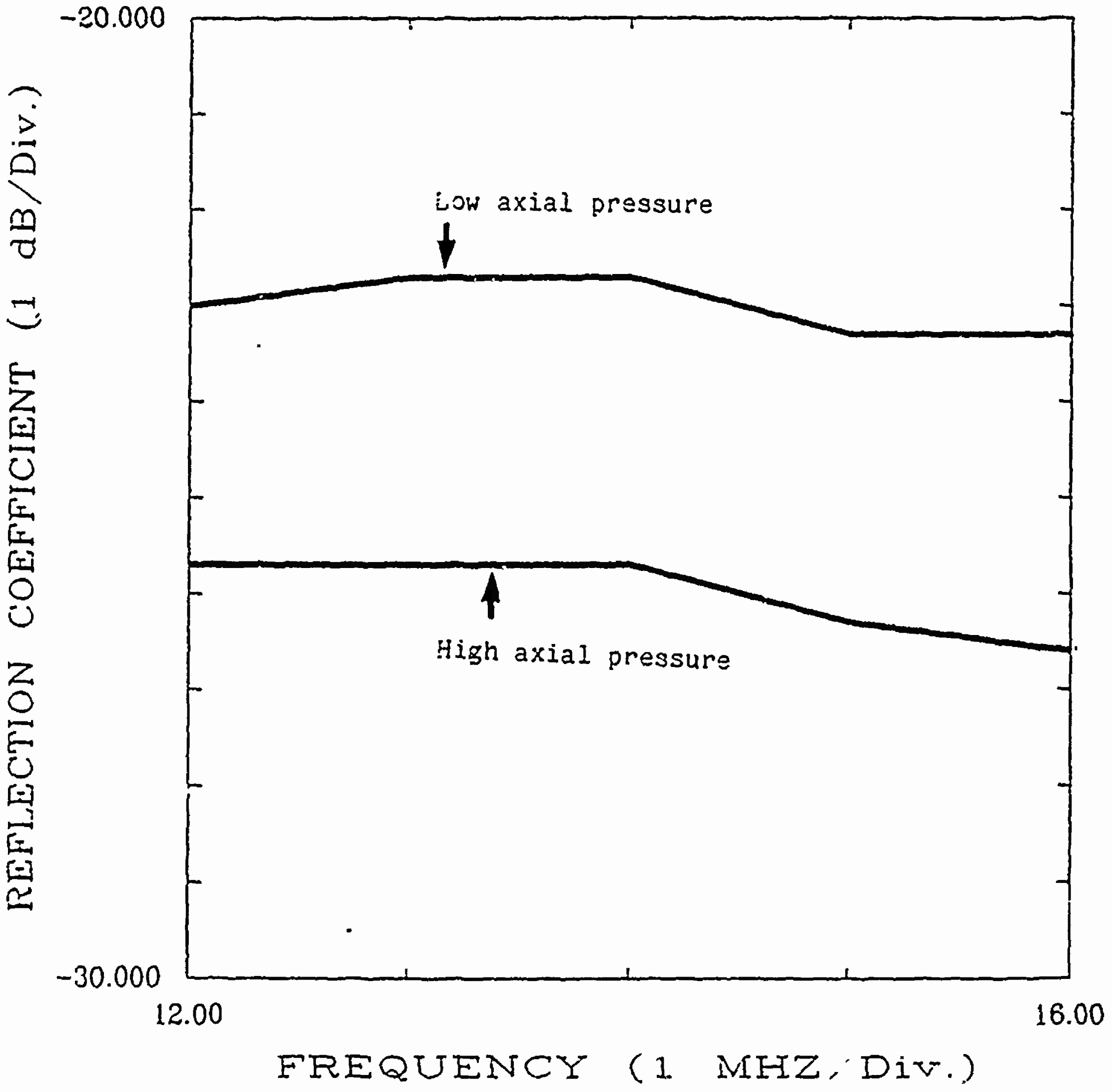

Fig. 28. Ultrasonic reflection curves for dissimilar inertia-friction welds between Al-12Fe-1.2V-2.4Si (same as shown in Fig. 27). The incident ultrasonic wave is longitudinal and the incident angle is normal (ie., perpendicular to the interface. Note that the curve with the lowest reflection is that for the weld produced using the highest axial force.

IV. REFERENCES

1. Eagar, T. W., "Challanges in Joining Emerging Materials," Department of Materials Science, Massachusetts Institute of Technology, Cambridge, Massachusetts (1991).

2. Das, S. K. and Davis, L. A., "High Performance Aerospace Alloys via RS Processing," Mats. Sci. and Eng., 98:1-12 (1988).

3. Skinner, D. J., "The Physical Metallurgy of Dispersion-Strengthened Al-Fe-V-Si Alloys," Dispersion Strengthened Aluminum Alloys, Y. Kim and W. Griffith, eds., TMS/AIME, Warrendale, PA, 181-197 (1988).

4. Baeslack, W. A. III and Krishnaswamy, S., "Electron-Beam Weldability of a Rapidly-Solidified, Powder Metallurgy Aluminum Alloy," International Trends in Welding Research, (S. A. David, ed.) ASM International, Materials Park, Oh, 357-362 (1987).

5. Krishnaswamy, S. and Baeslack, W. A. III, Electron-Beam Welding of Al-8Fe-2Mo," Mats. Sci. and Eng., 98:137-141 (1988).

6. Krishnaswamy, S. "Welding of a Rapid-Solidification/ Powder Metallurgy Al-8Fe-2Mo Alloy," Ph.D Dissertation, The Ohio State University, Columbus, Ohio (1989).

7. Baeslack, W. A. III, "Joining of Rapidly-Solidified, Powder Metallurgy Al-Fe-Ce Alloys," Proceedings of Second International SAMPE Metals and Metals Processing Conference, Dayton, Ohio (1988).

8. Krishnaswamy, S., and Baeslack, W. A. III, "Nd:YAG Laser Weldability of RS/PM Al-8Fe-2Mo Sheet," Recent Trends in Welding Science and Technology, (S. A. David, ed.) ASM International, Materials Park, Oh, 631-636 (1990).

9. Krishnaswamy, S. and Baeslack, W. A. III, "Metallography of a Pulsed Nd:YAG Laser Weld in a RS/PM Al-8Fe-2Mo Alloy," Materials Characterization, 24:331-353 (1990).

10. Baeslack, W. A. III, Hou, K. H. and Devletian, "Rapid Solidification Joining of a Powder Metallurgy Al-Fe-Ce Alloy," J. Mats. Sci. Lett. 7:944-954 (1988).

11. Baeslack, W. A. III, Hou, K. H. and Devletian, "Electron Microscopy of Rapidly-Solidified Weldments in a Powder Metallurgy Al-Fe-Ce Alloy," J. Mats. Sci. Lett. 8:716-720 (1989).

12. Wang, K. K., "Friction Welding," Welding Research Council Bulletin No. 204, Welding Research Council, New York, NY.

13. Nicholas, E. D., "Friction Welding of Non-Circular Sections With Linear Motion, Weld. Inst. Res. Report, #332 (1987).

14. Baeslack, W. A. III and Hagey, K. S., "Inertia Welding of Rapid-Solidification/Powder Metallurgy Al-Fe-Ce Alloys," Welding Journal, Research Supplement, **67**:139-155s (1988).

15. Hou, K. H., and Baeslack, W. A. III, "Electron Microscopy of Inertia-Friction Weldments in a Rapidly-Solidified Al-Fe-Mo-V Alloy," J. Mats. Sci. **25**:2642-2653 (1990).

16. Koo, H. H., Krishnaswamy, S. and Baeslack, W. A. III, "Solid-Phase Welding of a Rapidly-Solidified Dispersion-Strengthened Al-Fe-V-Si Alloy - FVS1212," Low Density, High Temperature Powder Metallurgy Alloys, (W. E. Frazier, J. Koczak and P. W. Lee, eds.), TMS/AIME, Warrendale, PA, 183-196 (1991)

17. Koo, H. H., Krishnaswamy, S. and Baeslack, W. A. III, "Characterization of Inertia-Friction Welds in a High-Temperature RS/PM Al-8.5Fe-1.3V-1.7Si Alloy (AA-8009), Materials Characterization, **26**:123-136 (1991).

18. Koo, H. H. and Baeslack, W. A. III, "Friction Welding of a Rapidly-Solidified Al-Fe-V-Si Alloy," submitted for publication in the Welding Journal Research Supplement.

19. Koo, H. H. and Baeslack, W. A. III, "Structure, Properties and Fracture of a Linear-Friction Weld in a Rapidly-Solidified Al-Fe-V-Si Alloy 8009," submitted for publication in Materials Characterization.

20. Koo, H. H., Sampath, K. and Baeslack, W. A. III, "Characterization of Inertia-Friction Welds Between a Rapidly-Solidified Al-Fe-Mo-V Alloy and IM 2024-T351," accepted for publication in Journal of Materials Science.

21. Koo, H. H. "Structure/Property/Fracture Relationships in Friction Welded Al-Fe Type Alloys," Ph.D. Dissertiation, in review (1991).

22. Koo, H. H. and Baeslack, W. A. III, "Thermal Exposure Effects on Friction Welds in a Dispersion-Strengthened Aluminum Alloy - AA-8009, in final review for publication in Materials Characterization.

23. Dumolt, S. D. , Ph.D. Dissertation, Carnegie-Mellon University, Pittsburg, PA (1983).

24. Sunwoo, A. J., Bradley, E. L. III, and Morris, J. W., Jr., "Effects of Heat-Affected Zone Peak Temperatures on the Microstructure and Properties of 2090 Al Alloy," Met. Trans. A., **21A**:2795-2804 (1990).

25. Sunwoo, A. J., and Morris, J. W., Jr., "Aging Characteristics of Electron Beam and Gas Tungsten-arc Fusion Zones in Al-Cu-Li Alloy 2090," Met. Trans. A, **22A**:903-913(1991).

26. Hou, J. and Baeslack, W. A. III, "HAZ Phase Transformations in GTA and Laser Welds in an Al-Li-Cu Alloy," in final review for submission to Journal of Materials Science.

27. Hou, J. and Baeslack, W. A. III, "Effect of Solute Segregation on the Precipitation Response in the Weld Fusion Zone of Al-Cu and Al-Cu-Li Type Alloys," in final review for submission to the Welding Journal Research Supplement.

28. Flemings, M. C., Solidification Processing, McGraw-Hill, New York (1974).

29. Brooks, J. A., and Baskes, M. I., "Weld Microsegregation Characterization and Modeling," Advances in Welding Science and Technology, (S. A. David, ed.,) ASM International, Materials Park, OH. (1986).

30. Chen, S. Lin, J. Chang, Y. and Chu, M. "Phase Equilibrium and Solidification of Al-Rich Al-Li-Cu Alloys, Light Metals-1990, (C. M. Bickert, ed.) 985-988 (1990).

IV. PROJECT PERSONNEL AND DEGREES GRANTED

A. S. Krishnaswamy, Ph.D. in Welding Engineering, 1989.

B. H. H. Koo, Ph.D. in Welding Engineering, 1991.

C. K. H. Hou, Ph.D. in Welding Engineering, to be granted in March, 1992.

V. TECHNICAL REPORTS AND PUBLICATIONS

5.1 Technical Reports

A. S. Krishnaswamy, "Weldability of a Rapidly-Solidified Al-Fe-Mo Alloy, Ph.D. Dissertation, Department of Welding Engineering, The Ohio State University, Columbus, Ohio (1989).

B. H. H. Koo, "A Metallurgical Investigation into the Friction Welding of Rapidly-Solidified, Dispersion-Strengthened Aluminum Alloys," Department of Welding Engineering, The Ohio State University, Columbus, Ohio (1991).

5.2 Publications (See Appendix I)

A. S. Krishnaswamy and W. A. Baeslack III, "Nd:YAG Laser Weldability of RS/PM Al-8Fe-2Mo Sheet," Recent Trends in Welding Science and Technology, S. A. David and J. Vitek, Eds. ASM International (1990) 631-636.

B. S. Krishnaswamy and W. A. Baeslack III, "Metallography of a Pulsed Nd:YAG Laser Weld in a RS/PM Al-8Fe-2Mo Alloy, "Materials Characterization, 24 (1990) 331-352.

C. K. H. Hou and W. A. Baeslack III, "Electron Microscopy of Rapidly-Solidified Weldments in a Powder Metallurgy Al-Fe-Ce Alloy," Journal of Materials Science Letters, 8 (1989) 716-720.

D. K. H. Hou and W. A. Baeslack III, "Electron Microscopy of Inertia-Friction Weldments in a Rapidly-Solidified Al-Fe-Mo-V Alloy," Journal of Materials Science, 25 (1990) 2642-2653.

E. H. H. Koo, K. Sampath and W. A. Baeslack III, "Characterization of Inertia-Friction Welds Between a Rapidly-Solidified Al-Fe-Mo-V Alloy and IM 2024-T351," Journal of Materials Science (in press).

F. H. H. Koo, S. Krishnaswamy and W. A. Baeslack III, "Solid-Phase Welding of a Rapidly-solidified Al-Fe-V-Si Alloy - FVS1212," Low Density, High Temperature Powder Metallurgy Alloys, W. E. Frazier, M. J. Koczak and P. W. Lee, Eds., TMS/AIME (1991) 183-196.

G. H. H. Koo, S. Krishnawamy and W. A. Baeslack III, "Characterization of Inertia-Friction Welds in a High-Temperature RS/PM Al-8.5Fe-1.3V-1.7Si Alloy (AA-8009)," Materials Characterization, 26 (1991) 123-136.

H. H. H. Koo and W. A. Baeslack III, "Structure, Properties and Fracture of a Linear-Friction Weld in Rapidly-Solidified Al-Fe-V-Si," Materials Characterization, (in press).

I. H. H. Koo and W. A. Baeslack III, "Friction Welding of a Rapidly-Solidified Al-Fe-V-Si alloy," Welding Journal, Research Supplement, (in review).

J. H. H. Koo and W. A. Baeslack III, "Elevated-Temperature Exposure Effects on Inertia-Friction Welds in Al-Fe-V-Si Alloy 8009," Journal of Materials Science Letters, (in review).

K. S. Krishnaswamy, T. Lienert and W. A. Baeslack III, "Nd:YAG Laser Weldability of RS/PM Al-8Fe-2Mo Sheet, Poster Presentation at 1990 IMS National Meeting. <u>Received First Prize in Graduate Student Class</u>.

L. H. H. Koo and W. A. Baeslack III, "Metallography of an Inertia-Friction Weld Between A Rapidly-Solidified Al-9Fe-3Mo-1V Alloy and IM-2024-T351," Poster Presentation at 1990 IMS National Meeting.

Appendix 1A

APPENDIX IA

S. Krishnaswamy and W. A. Baeslack III, "Nd:YAG Laser Weldability of RS/PM Al-8Fe-2Mo Sheet," Recent Trends in Welding Science and Technology, S. A. David, Ed., ASM International (1990) 631-636.

Presented at 2nd International Conference on Trends in Welding Research, Gatlinburg, Tennessee, 14-18 May, 1989.

Nd: Yag Laser Weldability of RS/PM Al-8Fe-2Mo Sheet

S. Krishnaswamy, W. A. Baeslack III
Department of Welding Engineering
The Ohio State University
Columbus, OH 43210, USA

T. J. Lienert
Sandia National Laboratories
Albuquerque, NM 87185, USA

Reprinted from
RECENT TRENDS IN WELDING SCIENCE AND TECHNOLOGY TWR'89
Proceedings of the
2nd International Conference on Trends in Welding Research
Gatlinburg, Tennessee, USA
14–18 May 1989

REPRINT

ASM INTERNATIONAL®
Materials Park, Ohio 44073

8903-021

SAN 204-7586
Printed in the United States of America

Nd: YAG LASER WELDABILITY OF RS/PM Al-8Fe-2Mo SHEET

S. Krishnaswamy, W. A. Baeslack III
Department of Welding Engineering
The Ohio State University
Columbus, OH 43210, USA

T. J. Lienert
Sandia National Laboratories
Albuquerque, NM 87185, USA

ABSTRACT

The microstructure, mechanical properties and fracture characteristics of a pulsed Nd: YAG laser weld in a rapid solidification/powder metallurgy (RS/PM) Al-8wt.% Fe-2.3wt.% Mo alloy have been investigated. Results showed the high power density but low total energy input associated with pulsed Nd: YAG laser welding to promote extremely rapid fusion zone (FZ) cooling rates in the vicinity of 10^5 °C/s. The weld FZ microstructure consisted primarily of submicron-sized spherical dispersoids in a matrix of fine dendritic-alpha aluminum. A dispersoid-coarsened heat-affected zone (HAZ) was also observed in the boundary between successive, overlapping melt zones. Transverse-weld tensile testing found fracture to occur in the unaffected base metal indicating 100% weld joint efficiency. Longitudinal-weld bend ductility testing revealed fracture initiation and propagation to be associated with the HAZ between successive melt zones at a bend ductility level only marginally below that of the base metal.

AL-8FE-2MO REPRESENTS A NEW FAMILY OF dispersion-strengthened aluminum alloys with an "engineered" microstructure produced via rapid solidification/powder metallurgy (RS/PM) processing [1-5]. These alloys are characterized by novel hyper-eutectic Al-Fe base compositions with ternary and/or quarternary additions of Mo, Ce, Ni and Si to improve dispersoid stability at elevated-temperatures. In these alloys, utilization of rapid cooling rates (in the range of 10^4 to 10^6 °C/s) suppresses the formation of primary intermetallic particles and instead promotes a solute supersaturated dendritic-alpha aluminum and/or micro-eutectic [2]. Subsequent consolidation and thermo-mechanical processing (TMP) treatments decompose the metastable as-solidified microstructural constituents and produce a high volume fraction of submicron-sized thermally stable dispersoids. The above microstructural features exhibit dispersion strengthening effects and consequently provide superior room-temperature and elevated-temperature mechanical properties [2, 4]. These high performance RS/PM Al-Fe-X alloys compete with Ti-6Al-4V alloy on a specific strength basis for use in several aerospace components operating at temperatures up to 315 °C [3-5].

If RS/PM Al-Fe-Mo type dispersion-strengthened alloys are to be utilized in structural applications, their efficient joining will be necessary. Considering the dependency of their superior mechanical properties on an "engineered" microstructure, it is apparent that joining techniques which can "recreate" and/or "retain" the unique microstructural characteristics of the base metal need to be utilized in order to achieve high joint efficiency. Among the fusion welding processes currently available to join aluminum alloys, high energy density processes such as electron beam (EB) and laser welding (LW) offer the greatest potential for achieving the above two microstructural goals. Recent weldability studies on Al-8wt.% Fe-2.3wt.% Mo (Al-8Fe-2Mo) determined that the high energy density and rapid cooling rates provided by EB welding generated an extremely fine FZ structure which exhibited a hardness and strength superior to that of the base metal [6]. However, the presence of a structurally coarse fusion boundary region (FBR) in these weldments served as a "weak-link" and promoted preferential failure with low ductility and a weld joint efficiency of 73%. Further EB welding investigations determined that the structurally coarsened FBR can be eliminated by using a lower weld energy input which promoted a steeper temperature gradient and a higher FZ cooling rate in excess of 10^4 °C/s [7]. These latter welds failed in the HAZ with acceptable ductility and an improved joint efficiency of 88%. Considering that an increased energy density could further increase the temperature gradient and cooling rate within the weld, and thereby enhance the FZ and HAZ microstructures, the present investigation was initiated in order to examine the microstructure, mechanical properties and fracture characteristics of a high energy density Nd: YAG pulsed laser weld in a RS/PM Al-8Fe-2Mo sheet.

EXPERIMENTAL PROCEDURE

The Al-8Fe-2Mo sheet utilized in this investigation originated from helium-atomized powder produced by Pratt and Whitney's rapid-solidification-rate (RSR) process [2, 4]. The inert atomization conditions produced spherically symmetric powder particles and also resulted in minimal oxidation and hydration of the powder particle surfaces. Subsequent to RSR processing, powder particles were compacted by direct consolidation, hot extruded into a billet and warm rolled into sheet 1.27 mm in thickness. The chemical composition of the as-received Al-8Fe-2Mo sheet was 8.0 wt.% Fe and 2.3 wt.% Mo with the residual hydrogen content below 1 ml/100 gm Al.

Autogenous Nd: YAG laser welds were produced with the weld longitudinal axis oriented parallel to the sheet rolling direction. The pulsed Nd:YAG laser welding conditions were optimized in order to produce a full-penetration, high depth-to-width ratio FZ. The optimized welding parameters were: 10 Hz pulsing rate, 5 ms pulse duration, 105 W (10.5 J/pulse) pulse power, 2.1 KW peak power, 2.54 mm/s (6 ipm) weld travel rate, 41.34 J/mm average energy input, 102 mm (4") focal length and argon shielding gas at a flow rate of 16.5 l/min. (35 cu. ft/hr). Subsequent to welding, the test coupons were evaluated using radiography to reveal possible weld defects such as cracks and porosity. Following radiographic examination, transverse and top sections of the weld coupons were mounted, polished and etched (Keller's reagent) for metallographic characterization using light microscopy.

Base metal and weldment microstructures were also characterized using thin foil transmission-electron microscopy (TEM). Thin foils for TEM characterization were prepared by the jet-electropolishing technique using a solution of 1 part nitric acid in 3 parts methanol at 20 V and at a temperature of -25 °C. Microstructure characterization was performed using a JEOL 200CX microscope operated at 200 KV. Additionally, energy dispersive spectrometer (EDS) analysis was performed using a Tracor-Northern TN 2000 system. A Cliff-Lorimer data analysis technique was utilized to obtain semi-quantitative compositions based on empirically determined K factors [8].

Base metal and weldment mechanical property evaluation included Vicker's diamond pyramid hardness (DPH) testing using a 500 gm load, transverse tensile testing (12.7 mm length and 3.2 mm width gage section) and longitudinal bend ductility testing. The longitudinal-weld bend ductility test was performed with the weld face in tension.

Fractography was performed on a Hitachi S-510 scanning-electron microscope (SEM) operated at 25 KV. Examination of the longitudinal weld bend coupon provided an "in-situ" comparative evaluation of the fracture in the FZ, HAZ and the unaffected base metal.

RESULTS & DISCUSSION

BASE MATERIAL CHARACTERIZATION - Light microscopy showed the as-received sheet to exhibit a uniform distribution of extremely fine, dark-etching dispersoid particles in a light-etching alpha aluminum matrix (Figure 1A). Dark-etching stringers were occasionally observed oriented parallel to the sheet rolling direction. These stringers appeared to originate from coarse powder particles which contained primary intermetallic particles [2], rather than from oxides present on powder particle surfaces.

TEM analysis of the base material microstructure revealed sub-micron dispersoids which varied significantly in size and morphology (Figure 1B). Although specific dispersoid types were not identified using electron diffraction techniques, EDS composition analysis indicated the coarser dispersoids to be Al_6Fe type, which is a metastable intermetallic previously reported in rapidly solidified Al-Fe-Mo and Al-Fe alloys [2, 9]. An alpha grain size of 1 to 2 µm was also indicated by bright and dark field imaging.

Mechanical property testing performed on the base metal found a hardness of 120 DPH, an ultimate tensile strength of 376 MPa (54.5 Ksi), a tensile elongation of 11% and a longitudinal bend ductility of 14 %.

WELD INTEGRITY - Radiographic examination of the welded coupons did not reveal indications of cracking. Although occasional spherical pores were observed within the FZ, the porosity levels were well within allowable limits for aerospace applications.

WELD STRUCTURE CHARACTERIZATION - Figures 2A & 2B show the macrostructure of the transverse and top sections of the pulsed Nd: YAG laser weld. As indicated, the FZ consisted of a light-etching microstructure with curvilinear bands of a dark-etching microstructure bounding successive melt zones. Light microscopy analysis of the light-etching region at increased magnification (Figures 3A and 3B) revealed extremely fine particles in an alpha aluminum matrix. Variations in the distribution of these dispersoid particles in the form of "swirls" appeared to be associated with convective fluid flow patterns experienced in the melt prior to solidification. The dark-etching regions observed at the boundaries between successive melt zones exhibited a smooth interface with the original melt zone and an irregular interface

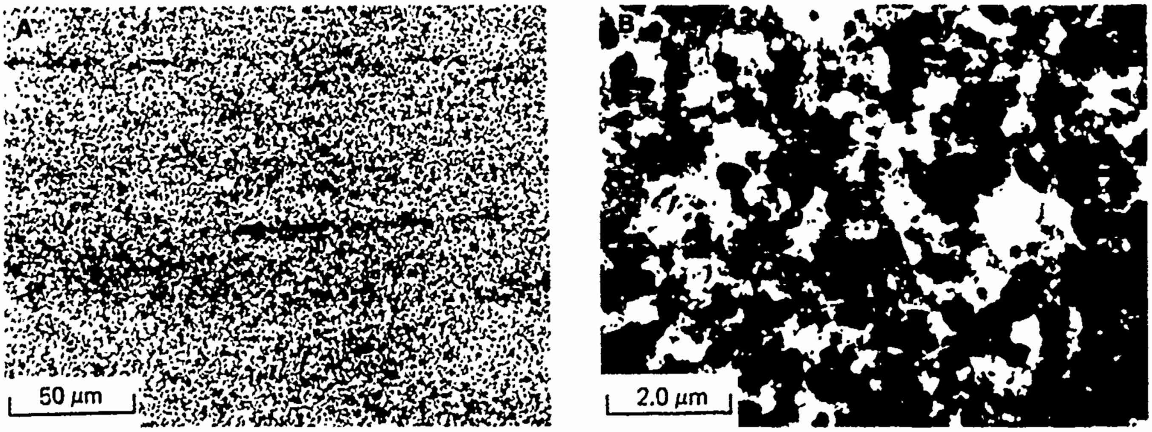

Figure 1: (A) Light micrograph and (B) TEM micrograph of RS/PM Al-8Fe-2Mo base metal.

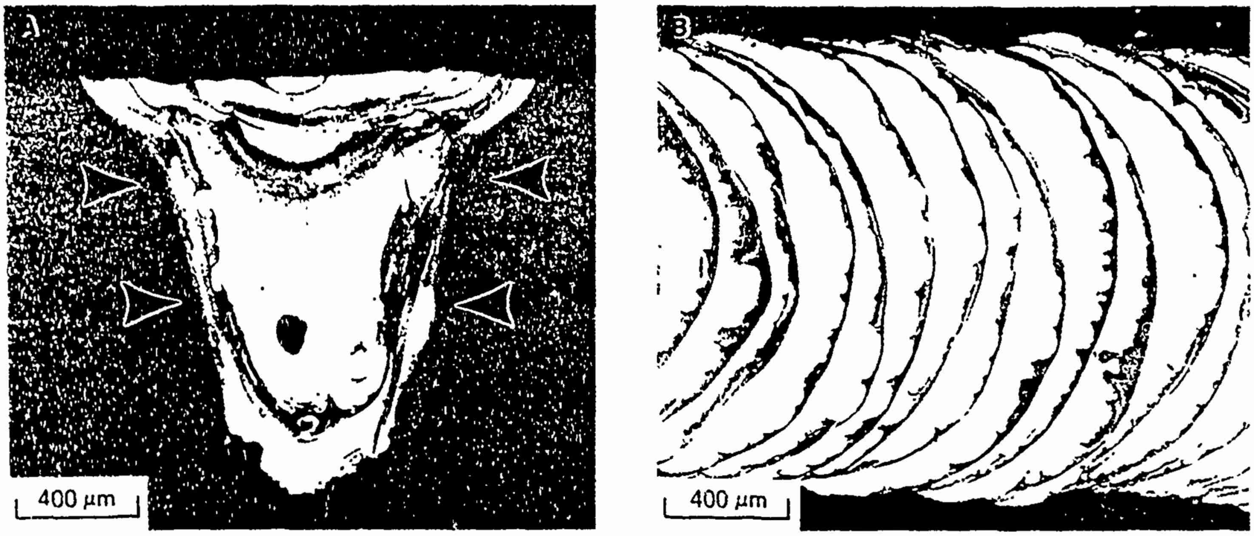

Figure 2: Light micrographs of pulsed Nd:YAG laser weld in Al-8Fe-2Mo showing (A) transverse section, (B) top surface. Arrows in (A) indicate locations of hardness traverses shown in Figure 5.

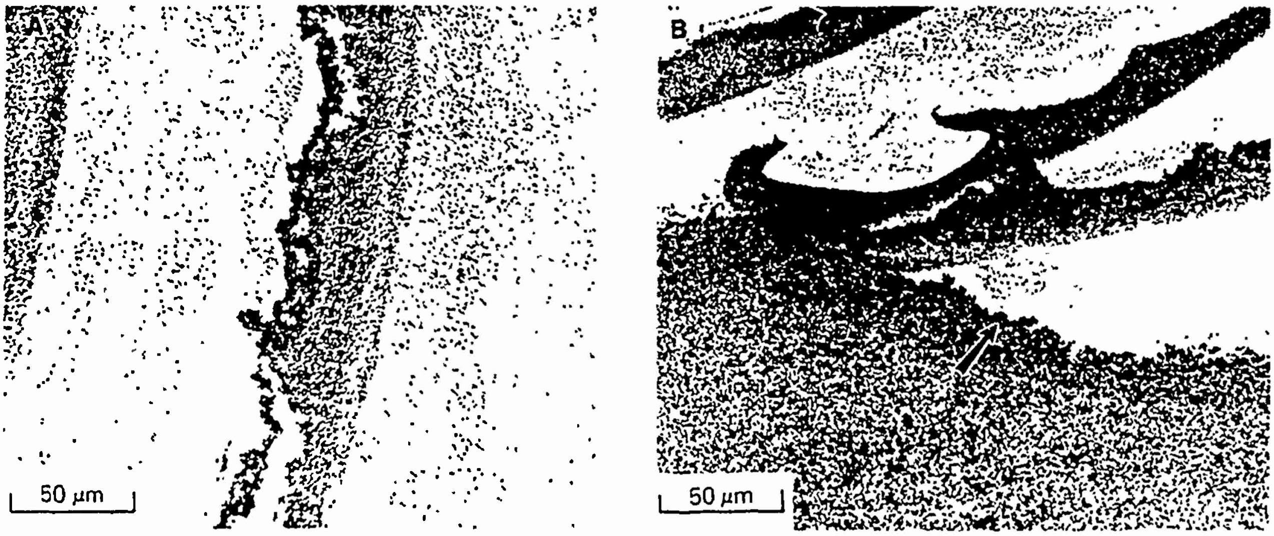

Figure 3: Light micrographs showing top surface of pulsed Nd:YAG laser weld in Al-8Fe-2Mo: (A) center of FZ, (B) fusion boundary (arrow).

bounding the subsequent melt zone. As shown in Figures 2B and 3B, the irregular boundary frequently exhibited a macroscopically "cusped" appearance, which was attributed to the nature of fluid flow within the molten weld pool. Analysis of this dark-etching structure at increased magnification suggested that it comprised of a HAZ on the side of the original melt zone and a FBR on the side of the subsequent melt zone. Solid-state dispersoid coarsening was evident within the HAZ, while in the FBR dispersoids coarsened in a stagnant region of molten alpha aluminum [6]. Evidence of a narrow, dark-etching band in the base metal directly adjacent to the FZ indicated a dispersoid-coarsened HAZ (Figure 3B).

TEM analysis of the weldment more clearly characterized the weld FZ and HAZ microstructures. As shown in Figures 4A and 4B, the FZ consisted of spherical intermetallics in a matrix of fine [illegible]itic alpha aluminum. EDS analysis indicated that the [illegible] intermetallics were the Al_6Fe type. The size and morphology of these intermetallics and their Al_6Fe type composition suggested that these particles originated from the base metal dispersoid particles. Based on this observation, it is apparent that the weld "fusion zone" was essentially a partially-melted region comprised of intermetallic particles dispersed in molten aluminum. Observed differences in the size and distribution of the intermetallics were attributed to the variations in the thermal conditions experienced within the molten weld pool, with dispersoids experiencing high temperatures dissolving more extensively than those in lower temperature regions. As shown earlier in the light micrographs (Figures 3A & 3B), convective currents within the FZ controlled the movement of dispersoids through these "high" and "low" temperature regions in the weld pool and thereby influenced their final size and distribution. Solidification of the weld pool initiated epitaxially from the fusion boundary, with columnar alpha-aluminum grains effectively "entrapping" the unmelted/undissolved dispersoids as solidification proceeded along a relatively steep temperature gradient. As shown in Figures 4A and 4B, solidification of the alpha aluminum matrix occurred to a cellular-dendritic substructure with fine intermetallics located in the last-to-solidify dendrite interstices. EDS

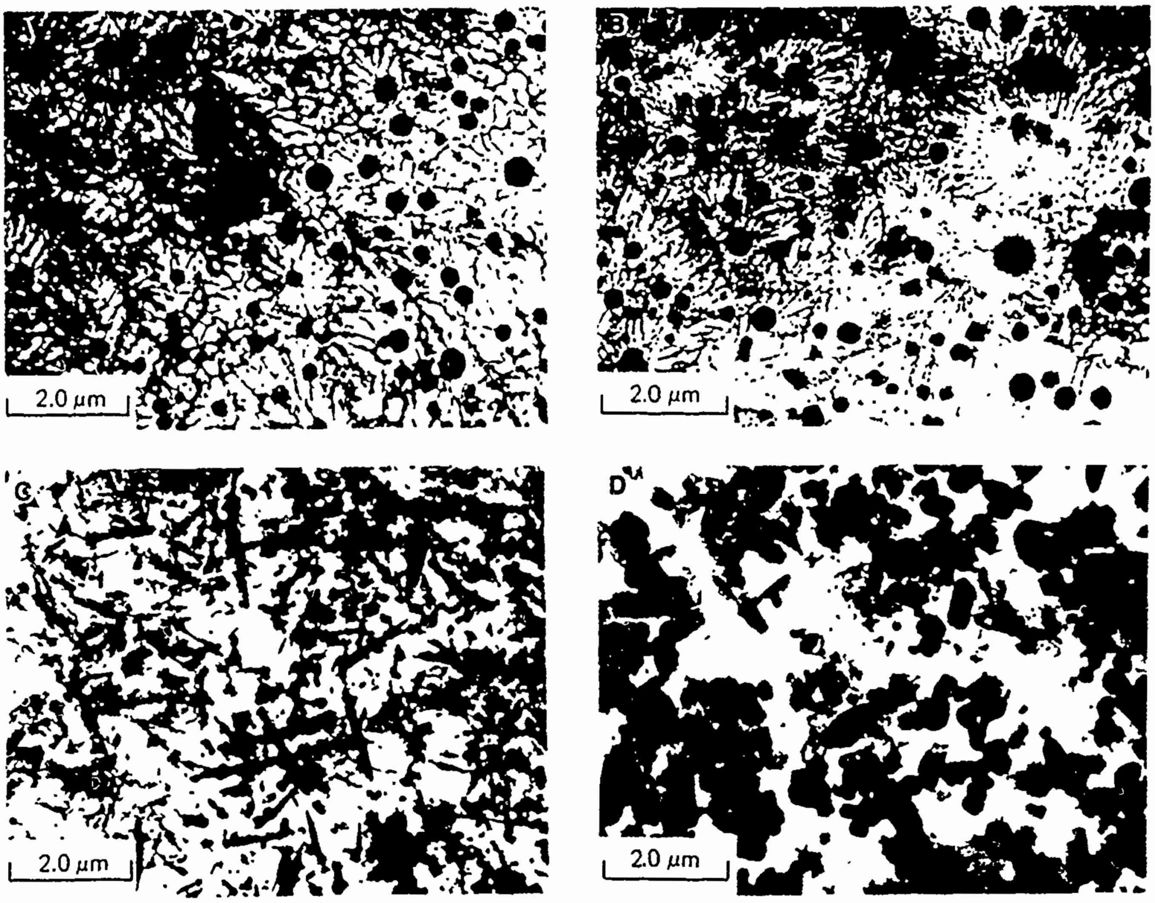

Figure 4: TEM micrographs of pulsed Nd:YAG laser weld in Al-8Fe-2Mo: (A) fusion zone adjacent to fusion boundary, (B) center of FZ, (C) HAZ within FZ, (D) HAZ in base metal.

semi-quantitative compositional analysis of the overall dendritic structure showed an Fe content of about 6wt.%, which was well beyond the eutectic composition of 1.8wt.% Fe [10] in binary Al-Fe systems (albeit Mo additions influence this composition to a limited extent). The solidification of this hyper-eutectic composition to primary alpha with an Fe content of about 0.85wt.% (versus a maximum equilibrium solid-solubility limit of 0.04 wt.% Fe [10] at the eutectic temperature) was attributed to the rapid cooling and solidification rates experienced within the pulsed laser weld. A comparison of the dendrite spacings with previous relationships between dendrite spacing and cooling rate in aluminum alloys [11, 12] indicated a Nd. YAG laser weld cooling rate of about 10^5 °C/s through the solidification temperature range. Nearer to the center of the FZ, where the temperature gradient became shallower, evidence of equiaxed growth was apparent. In this region, relatively coarse dendritic alpha-aluminum nucleated directly upon the spherical intermetallics.

Analysis of the HAZ in the FZ between successive laser pulses revealed the formation of acicular intermetallics believed to be Al_3Fe type [2, 9] in an alpha aluminum matrix (Figure 4C) Although occasional spherical intermetallics were also observed in this region, the cellular-dendritic solidification structure was essentially absent. During the laser weld thermal cycle, the extremely fine intermetallics at dendrite intersticies apparently underwent preferential dissolution in solid-state and thereby provided solute flux for the formation of acicular intermetallics. The supersaturated alpha aluminum matrix might have also provided additional solute flux for the formation of these acicular particles.

Figure 4D shows the TEM microstructure of the HAZ in the base metal directly adjacent to the FZ, and indicates only slight coarsening of the dispersoids versus the unaffected base metal (Figure 1B).

WELD PROPERTIES - Figure 5 shows hardness traverses at two locations across the transverse weld cross-section shown in Figure 2A. Consistent with the microstructural analysis, the hardness of the light-etching regions near the weld center was appreciably greater than that of the base material (220 versus 120 DPH). Hardness levels decreased to 170 DPH in the dark-etching boundary between successive pulse melt zones within the FZ due to appreciable coarsening of the dispersoids in this region. The hardness decreased to 118 DPH in the narrow HAZ in the base metal which was only marginally below that of the base metal.

Fracture of the transverse-weld oriented tensile specimens occurred in the unaffected base metal, indicating a 100% joint efficiency. Tensile properties of four tensile specimens averaged an ultimate tensile strength of 374 MPa (54.2 Ksi) and an elongation of 11%. The occurrence of fracture remote from the weld FZ, despite the presence of a HAZ exhibiting a lower hardness than the base metal, was attributed to the minimal width of the HAZ and the constraint effects of the surrounding higher strength

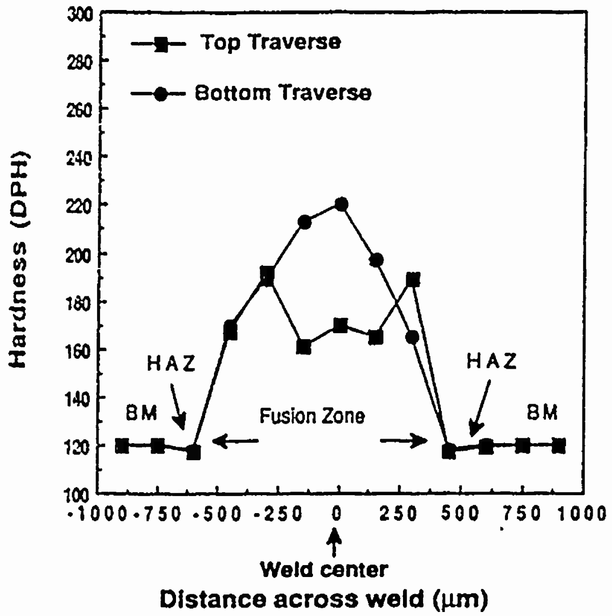

Figure 5: Hardness traverses across pulsed Nd:YAG laser weld in Al-8Fe-2Mo (location of top and bottom traverses are shown in Figure 2A).

microstructure. Longitudinal-weld bend ductility testing indicated a 11% bending strain at fracture initiation, which was only marginally below that of the base metal.

FRACTURE CHARACTERISTICS - Examination of the top surface of the fractured longitudinal-weld bend specimen (Figure 6) found the marginal reduction in bend ductility to be associated with the presence of the dispersoid-coarsened HAZ within the weld FZ. Although a specific crack initiation site could not be identified, crack propagation occurred principally along the smooth interface between the HAZ and the preceding pulse, rather than entirely through the coarsened HAZ or along the more irregular fusion boundary interface with the succeeding pulse. As shown in Figure 6, near the edges of the FZ the crack path deviated from the curvilinear boundary to a direction oriented perpendicular to the direction of maximum stress.

SEM fractographic analysis of the longitudinal-weld oriented bend specimen (Figure 7A) showed ductile-appearing fracture in the base metal regions which was consistent with the nucleation, growth and coalescence of microvoids in the interface between the dispersoid particles and the relatively soft alpha aluminum matrix. Although the macroscopic fracture path in the base metal indicated a texture parallel to the sheet rolling direction (Figure 7B), the size of the microvoids generally appeared to be uniform (Figures 7C). Fracture in the weld FZ also occurred in a ductile manner by void formation (Figures 7D). However, the size of the voids varied appreciably across the fracture surface. In some locations, voids were larger than those in the base metal (Figures 7E), which was consistent with the generally lower distribution of intermetallics in the FZ (i. e., compare Figures 1B and 3A). However, in other locations a void size finer than that observed in the base metal was found (Figures 7F), suggesting a possible influence from interdendritic intermetallic particles in promoting void nucleation. Clearly, the observed variations in void size across the FZ were consistent with variations in intermetallic distribution within this region.

Figure 6: Light micrograph showing fracture path on top surface of longitudinal-weld oriented bend specimen in Al-8Fe-2Mo. Arrow indicates direction of maximum stress during bend testing.

Analysis of the fracture initiation region at the top surface of the bend specimen (along the HAZ boundary within the FZ) revealed characteristics comparable to those observed in the fusion zone.

SUMMARY

The results of this investigation determined that the rapid cooling rates provided by pulsed Nd. YAG laser welding promoted a FZ microstructure comprised of submicron intermetallics in a matrix of fine dendritic alpha aluminum and minimal dispersoid coarsening in the base metal HAZ. The high strength of this FZ microstructure and the narrow width of the HAZ provided 100% joint efficiency. A dispersoid-coarsened microstructure in the HAZ at the boundary between successive melt zones served as a preferential fracture path during bend testing but promoted only a minimal loss in ductility.

ACKNOWLEDGEMENT

Research performed at The Ohio State University was supported by the Army Research Office under contract # DAAL03-88-K-0049. Work conducted at Sandia

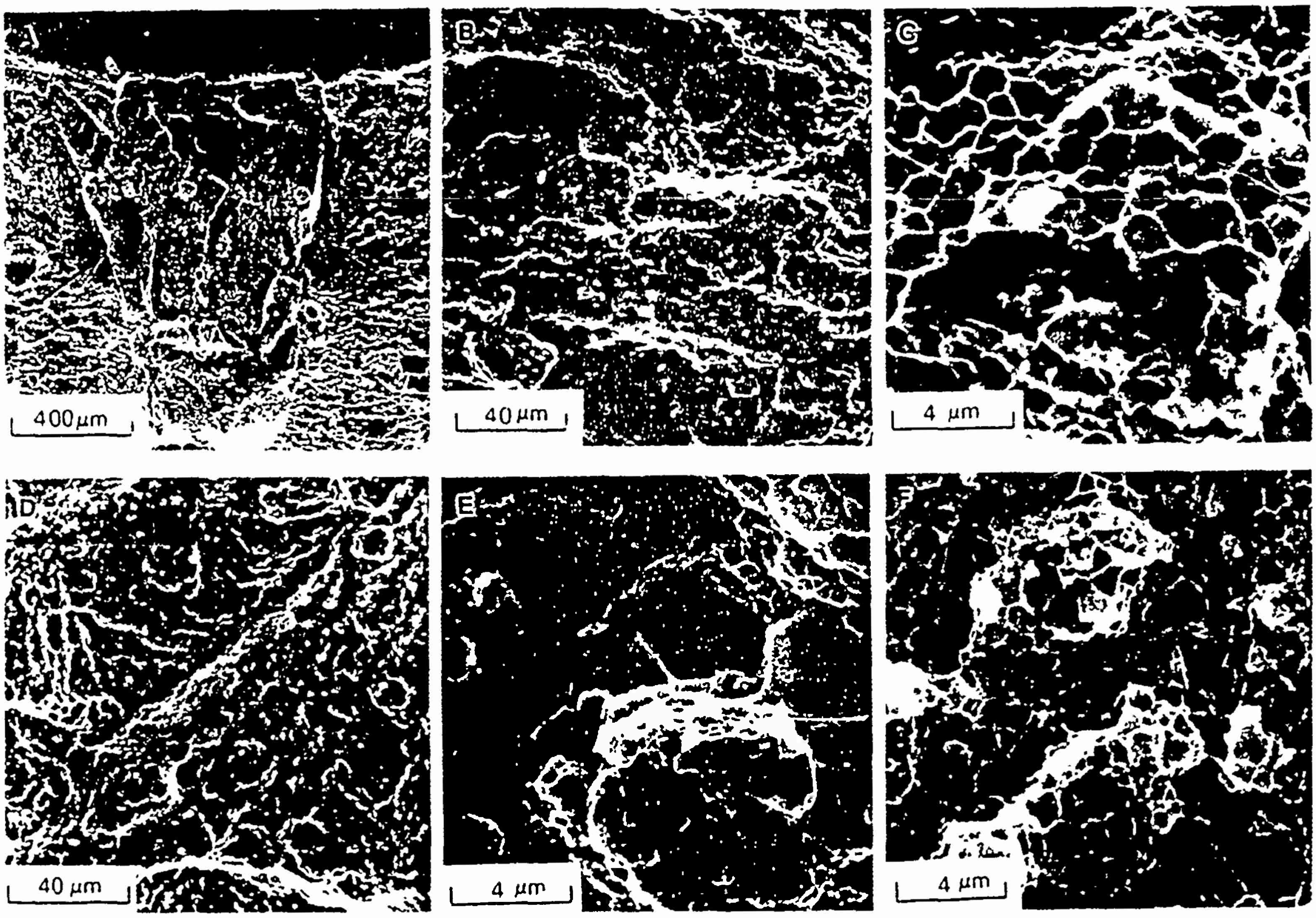

Figure 7. SEM fractographs of longitudinal-weld oriented bend specimen in Al-8Fe-2Mo· (A) fracture surface, (B, C) unaffected base metal, (D-F) fusion zone. Arrows in (A) indicate fusion boundary.

National Laboratories was supported by the Department of Energy under contract # DE-AC04-76DP00789. The authors also express appreciation to Mr. H. O. Colijn at the Central Electron Optics Facility, OSU for his assistance in STEM/EDS analysis.

REFERENCES

1) S. L. Langenbeck, W. M. Griffith, G. J. Hildeman and J. W. Simon, in "Rapidly Solidified Aluminum Alloys, STP 890," M. E. Fine and E. A. Starke, Jr. Eds. ASTM, PA, 410-22, (1986).

2) C. M. Adam and R. G. Bourdeau, in "Rapid Solidification Processing: Principles and Technologies II," R. Mehrabian, B. H. Kear and M. Cohen, Eds. Claitors Publishing, Baton Rouge, LA, 246-59, (1980).

3) C. M. Adam, in "Science and Technology of Undercooled Melts," P. R. Sahm, H. Jones and C. M. Adams, Eds. NATO-ASI Series, Martinus-Nijhoff Publishers, Dodrecht, 186-209, (1986).

4) C. M. Adam, in 'Rapidly Solidified Amorphous and Crystalline Alloys, Vol. 8," B. H. Kear, B. C. Giessen and M. Cohen, Eds. Elsevier Science Publishing Co. 411-22, (1982).

REFERENCES (Contd.)

5) C. M. Adam, in "Mechanical Behavior of Rapidly Solidified Materials,' S. M. L. Sastry and B. A. MacDonald, Eds. TMS, Warrendale, PA, 21-39, (1985).

6) W. A. Baeslack III and S. Krishnaswamy in "International Trends in Welding Research," S. A. David, Ed. ASM International, Metals Park, OH, 357-62, (1986).

7) S. Krishnaswamy and W. A. Baeslack III, Matls. Sci. & Engg. 98, 137-41, (1988)

8) M. H. Jacobs, A. G. Doggett and M. J. Stowell, J. Matls. Sci. 9, 1631-43, (1974).

9) P. Trebbia, "CLEDX: a stand alone program for quantitative X-ray analysis of thin films using the C-L procedure," to be published in a forthcoming issue of Ultramicroscopy

10) L. F. Mondolfo, Aluminum Alloys, Structure and Properties, Butterworths, London, 24, (1976)

11) H. Jones, "Rapid Solidification of Metals and Alloys," Monogr. 8, Institution of Metallurgists, London, 40-43, (1982).

12) G. R. Armstrong and H. Jones in "Proc conf Solidification and Casting of Metals,' Sheffield, The Metals Society, London, 454-59, (1979).

Appendix 1B

APPENDIX IB

S. Krishnaswamy and W. A. Baeslack III, "Metallography of a Pulsed Nd:YAG Laser Weld in a RS/PM Al-8Fe-2Mo Alloy," Materials Characterization, 24 (1990) 331-352.

Presented at 1991 ASM International Materials Congress in Cincinnati, Ohio.

MATERIALS CHARACTERIZATION 24:331–353 (1990)

Metallography of a Pulsed Nd:YAG Laser Weld in a RS/PM AL-8FE-2MO Alloy

S. KRISHNASWAMY AND W. A. BAESLACK III

Department of Welding Engineering The Ohio State University Columbus, OH 43210

The microstructure of a pulsed Nd:YAG laser weld in a rapid solidification/powder metallurgy (RS/PM) Al–8.0 wt.% Fe–2.3 wt.% Mo (Al–8Fe–2Mo) alloy was investigated using light microscopy, scanning electron microscopy (SEM) and transmission electron microscopy (TEM) techniques. This analysis revealed significant microstructure variations across the weld fusion zone (FZ). Near the fusion boundary, a light-etching FZ microstructure was observed to contain submicron dispersoids "entrapped" in a matrix of fine-sized dendritic alpha aluminum. At the center of the FZ, the presence of relatively coarse-sized intermetallic particles that served as growth centers for coarser dendritic alpha aluminum promoted a dark-etching microstructure. In the boundary between successive melt zones, both a heat-affected zone (HAZ) containing acicular dispersoids and a fusion boundary region (FBR) containing irregular-shaped particles in a coarse-grained dendritic alpha aluminum matrix were observed. A HAZ comprised of slightly coarsened dispersoids was also observed in the base metal bounding the FZ. Knoop hardness traverses across the FZ indicated a maximum hardness of KHN 260 in the light-etching FZ and a minimum hardness of KHN 135 in the HAZ between successive melt zones.

Introduction

Dispersion-strengthened aluminum alloys represent a new generation of Al–Fe base alloys produced via rapid solidification/powder metallurgy (RS/PM) processing [1, 2]. These alloys are based on novel hyper-eutectic Al–Fe base compositions with ternary and/or quarternary additions of Mo, Ce, Ni, Si, etc. RS/PM processing of these compositions produces an "engineered" microstructure consisting of a uniform distribution of submicron sized dispersoids in a fine-grained (1–2 μm) alpha aluminum matrix. The above microstructural features exhibit dispersion-strengthening effects and provide a density-corrected strength comparable to Ti-6Al-4V [3]. In view of possible significant improvements in thrust-to-weight ratio, these RS/PM Al–Fe base alloys are considered candidate

655 Avenue of the Americas, New York, NY 10010

1044-5803/90/$3.50

materials to replace Ti–6Al–4V in several aerospace components that operate at temperatures up to 315°C [4–6].

RS/PM PROCESSING

RS/PM processing essentially consists of two stages: 1) production of a rapidly solidified (RS) particulate, and 2) particulate consolidation. Rapid solidification processing (RSP) of hyper-eutectic Al–Fe base compositions suppresses the formation of coarse primary (intermetallic) particles and promotes the formation of a fine-grained, supersaturated alpha aluminum [7] and/or metastable micro-eutectic [3]. Subsequent solid-state consolidation and thermomechanical processing (TMP) treatments decompose the metastable as-solidified microstructural constituents and produce a high-volume fraction of submicron-sized dispersoids [8]. The type and morphology of the dispersoid particles are determined by the specific alloy composition, the RS conditions, and the particular TMP conditions employed. The ternary and/or quarternary alloy additions, which are characterized by low solid solubility and low solid-state diffusivity in aluminum [2], are particularly useful in reducing the interfacial energy or the lattice disregistry across the particle/matrix interface, thereby promoting the formation of thermally stable dispersoid particles [3]. The final microstructure may consist of both the stable, "nonshearable," incoherent (e.g., monoclinic Al_3Fe or $Al_{13}Fe_4$ type) acicular particles and metastable, "shearable," partially coherent, (e.g., orthorhombic Al_6Fe type) spherical or globular particles [3]. In the absence of significant solute flux, these submicron-sized particles resist elevated-temperature coarsening and remain thermally stable for long times, thereby maintaining dispersion-strengthening effects at elevated-temperatures.

WELDABILITY APPROACH

If these high performance RS/PM Al–Fe base alloys are to be utilized in structural applications, their efficient joining will be necessary. When one considers the relationships between the "engineered" microstructure and superior mechanical properties of the base metal, it is apparent that the weldability approach for these alloys must be oriented from a metallurgical perspective. With reference to fusion welding, the above weldability criterion for these alloys can be redefined as the ability of the welding process/condition to "recreate" a rapidly solidified microstructure in the fusion zone (FZ) and "retain" the microstructural characteristics of the base metal in the adjacent heat-affected zone (HAZ). Among the fusion welding processes currently available to join aluminum alloys, the high-energy density processes, such as electron beam (EB) and laser welding (LW), can be optimized to simultaneously produce steep temperature gradients, high solidification velocities, and rapid FZ cooling rates. Consequently, the above two processes offer possibilities for producing high-performance RS microstructures in the FZ while minimizing microstructural coarsening in the HAZ.

A previous investigation [9] involving microstructure characterization of a deep-penetration EB weld in a Al–8 wt.% Fe–1.7 wt.% Ni alloy found the occurrence of highly desirable metastable coupled eutectic microstructures near the fusion boundary. In the center of the FZ, the as-solidified microstructure exhibited coarse, equiaxed alpha aluminum grains that nucleated on large primary intermetallic particles. Recent weldability studies [10] involving a low-hydrogen Al–8 wt.% Fe–2.3 wt.% Mo (Al–8Fe–2Mo) revealed that a structurally coarse and mechanically weak fusion boundary region (FBR) was produced in EB welds made at high-energy inputs. Subsequent EB welding investigations [11] determined that the structurally coarsened FBR could be effectively eliminated at low-weld energy inputs that promoted steeper temperature gradients and higher FZ cooling rates in excess of $10^{4.5}$°C/s. However, in contrast with the microstructure of the as-RS Al–8Fe–2Mo particulates, the FZ microstructure of these EB welds exhibited coarse intermetallic particles that also showed evidence of appreciable growth.

OBJECTIVES

Considering that an increased energy density could decrease the total energy input and simultaneously increase the temperature gradient and cooling rate within the weld and thereby enhance both the FZ and HAZ microstructure, the present investigation was initiated with the following specific objectives:

1. Characterize the microstructures obtained in the FZ and HAZ of a pulsed, Nd:YAG laser weld in RS/PM Al–8Fe–2Mo sheet using several complementary metallographic/microscopy techniques.
2. Utilize the above microstructural information to understand the weld solidification behavior.

Experimental

The Al–8Fe–2Mo sheet utilized in this investigation originated from helium-atomized powder produced by Pratt and Whitney's rapid-solidification-rate (RSR) process [3]. In the RSR process, a rapidly spinning disk produces powder particles by centrifugal atomization [12]. The inert convective cooling conditions minimize oxidation and hydration of the powder particle surfaces and also produce spherically symmetric powder particles (Fig. 1). Subsequent to RSR processing, powder particles in select size range were compacted by direct consolidation, hot extruded into a billet, and warm rolled into sheet 1.27 mm in thickness. Compositional analysis of the as-received sheet indicated 8.0 wt.% Fe, 2.3 wt.% Mo and a residual hydrogen content below 1 mL/100 g Al.

Autogenous, pulsed Nd:YAG laser welds were produced with the weld longitudinal axis oriented parallel to the sheet-rolling direction. The welding conditions were optimized to maximize weld FZ cooling rate and HAZ temperature gradients and to produce a full-penetration, high depth-to-width ratio FZ. In order to allow detailed characterization of both the FZ solidification structure and the heat-affected region within the FZ, the weld travel rate was manually controlled to obtain about 15%–25% overlap between successive melt zones. The optimized welding parameters are shown in Table 1.

Subsequent to welding, light microscopy, scanning electron microscopy (SEM) and transmission electron microscopy (TEM) techniques were uti-

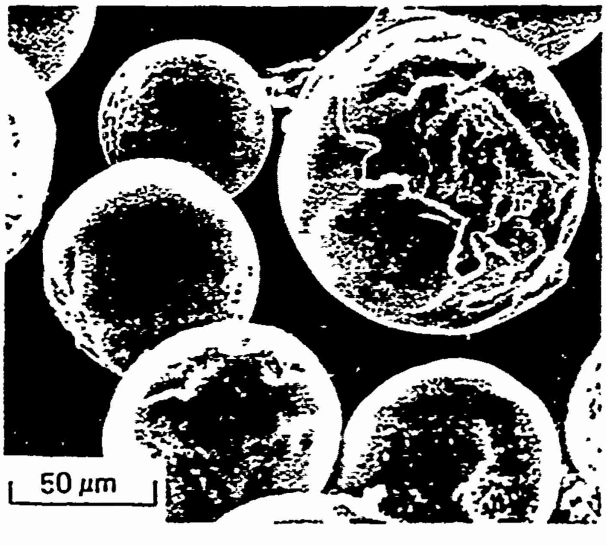

FIG. 1 SEM micrograph of Al–8Fe–2Mo powder particles produced by RSR atomization.

TABLE I
Optimized Pulsed Nd:YAG Laser Welding Conditions

Pulsing rate	10 Hz
Pulse duration	5 ms
Pulse power	230 W (23 J/pulse)
Peak power	4.6 KW
Power density	$\approx 2 \times 10^{4}$ W/mm^2
Focal length	102 mm (4")
Shielding gas	Argon
Gas flow rate	16.5 l/min (35 cu. ft/hr).

lized to characterize in detail the complex base metal. HAZ. and FZ microstructures and to demonstrate the complementary nature of these methods in evaluating the characteristics and origin of specific FZ and HAZ microstructures. The light and SEM analysis examined the transverse and top sections of the weld coupons. The weld sections were mounted in epoxy. ground to 600 grit emery and polished with a 3-μm diamond compound. Following final polishing with a colloidal silica suspension. the metallographic samples were etched with Keller's reagent. Specific FZ and HAZ microstructures were characterized using differential-interference contrast (DIC) light microscopy. Subsequently. the metallographic samples were vacuum-coated with a thin layer of carbon for microstructural characterization using SEM at higher magnifications. SEM examination was performed with ETEC Auto-scan SEM operating at 20 kV.

Base metal and weldment microstructures were also characterized using a JEOL 200CX TEM operated at 200 kV. Thin foils for TEM characterization were prepared by a twin jet-electropolishing technique using a solution of 1 part nitric acid in 3 parts methanol at 20 V and at a temperature of −25°C. Microstructure characterization mainly involved amplitude contrast imaging in bright field (BF) and dark field (DF) imaging conditions. Compositional data were obtained in the STEM mode. using a Tracor-Northern TN 2000 energy-dispersive spectrometer (EDS) system equipped with a beryllium window detector at 72° takeoff angle. A Cliff-Lorimer data analysis algorithm based on empirically determined K factors [13] was utilized to obtain semi-quantitative compositions from EDS data.

In addition to microstructure characterization. Knoop hardness (KHN) traverses were obtained from the top section of the weld coupon both transversely across the weld and along the longitudinal weld centerline.

Results and Discussion

BASE MATERIAL CHARACTERIZATION

Light microscopy analysis of the as-received Al–8Fe–2Mo sheet showed a uniform distribution of extremely fine, dark-etching dispersoid particles in a light-etching alpha aluminum matrix (Fig. 2a). Dark-etching stringers were also occasionally observed along the sheet-rolling direction. These stringers in the RS/PM base metal appeared to originate from coarse powder particles that contained primary intermetallic particles [3, 4] rather than from oxides formed on powder particle surfaces.

TEM analysis of the base material microstructure revealed both the size and morphology of the dispersoid particles and the alpha aluminum grain size. The submicron sized dispersoids exhibited either a spherical or an acicular morphology and ranged 0.2–0.6 μm in diameter or length (Fig. 2b). In view of the submicron size of these particles, the specific dispersoid types could not be identified using selected-area electron diffraction techniques. However, EDS compositional analysis indicated the spherical, coarse dispersoids to be enriched in both Fe (≈18 wt.% or 10.25 at.%) and Mo (≈8.3 wt.% or 2.75 at.%). These coarser particles were likely Al_6Fe type, which is a metastable, partially coherent, strengthening intermetallic previously reported in rapidly solidified Al-Fe-Mo and Al-Fe alloys [3, 14]. In contrast, EDS analysis of the acicular particles indicated a relative increase in Fe content (≈30 wt.% or 17.38 at.%) and a significant decrease in Mo content (≈1.5 wt.% or 0.52 at.%). These particles presumably belonged to the equilibrium Al_3Fe or $Al_{13}Fe_4$ type intermetallics, which formed an incoherent interface with the alpha aluminum matrix [3, 14]. Bright and dark field imaging indicated the alpha grain size to range between 1 and 2 μm. EDS analysis of the base metal alpha aluminum grains indicated supersaturation of both Fe (≈0.35 wt.%) and Mo (≈0.7 wt.%) relative to the equilibrium terminal solid solubility limit of both Fe (0.04 wt.%) and Mo (0.25 wt.%) in alpha aluminum [15, 16].

WELD STRUCTURE CHARACTERIZATION

Light Microscopy Examination

Figure 3a,b shows the macrostructure of the transverse and top sections of the pulsed Nd:YAG laser weld. Although the weld exhibited several microstructural transitions, these structures were characterized by two principal etching responses. A light-etching microstructure was observed

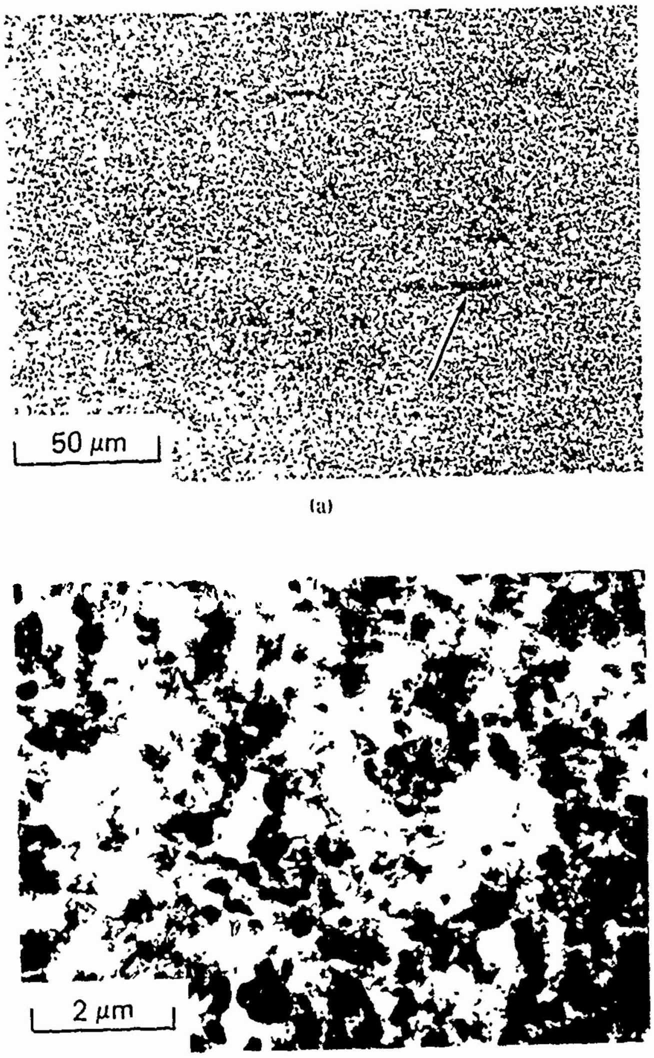

(b)

FIG. 2 (a) Light micrograph and (b) bright field TEM micrograph of RS/PM Al–8Fe–2Mo base metal. Arrow in (a) shows dark-etching stringers containing coarse intermetallic particles.

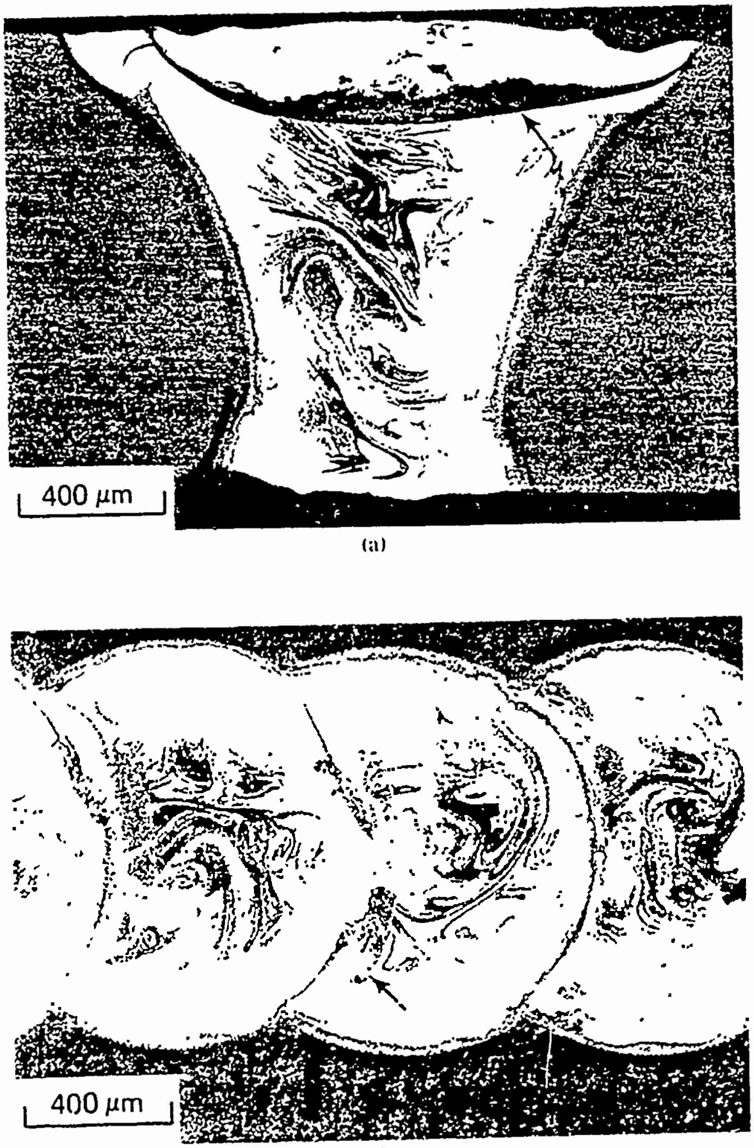

(a)

(b)

FIG. 3. Light micrographs of pulsed Nd:YAG laser weld in Al–8Fe–2Mo: (a) transverse section. (b) top surface. Small arrows indicate HAZ bounding successive melt zones. Dark-etching "swirl' correspond to dispersoid coarsened regions.

near the weld outer periphery. In contrast, dark-etching microstructures were observed at three different locations: in the center of the FZ, in a curvilinear band bounding successive melt zones and in the base metal directly adjacent to the FZ (Fig. 3a,b).

Light microscopy analysis of the light-etching FZ structure at increased magnification (Fig. 4a,b) revealed extremely fine particles in an alpha aluminum matrix. In contrast, the dark-etching central FZ structures consisted of relatively coarse-sized particles in an alpha aluminum matrix. Variations in the distribution of these particles in the form of "swirls" appeared to be associated with convective fluid flow patterns experienced in the melt prior to solidification. These "swirls" appeared to originate near the fusion boundary and move toward the weld center (Fig. 3a,b). The dark-etching regions in the curvilinear boundaries between successive melt zones exhibited a smooth interface bounding the preceding melt zone, and an irregular interface with the subsequent melt zone. Analysis of this dark-etching structure at increased magnification (Fig. 4a,b) suggested that it was comprised of a HAZ on the side of the original melt zone (smooth interface) and a fusion boundary region (FBR) on the side of the subsequent melt zone (irregular interface). The irregular boundary frequently exhibited a macroscopically "cusped" appearance, which provided evidence of a vigorous fluid flow within the molten weld pool.

The microstructural transitions in the boundary between successive melt zones became more apparent at still higher magnification (Fig. 5). In the dark-etching regions adjacent to the smooth boundary with the original melt zone (large arrow in the far right side of Fig. 5), a uniform distribution of randomly oriented fine-sized particles was observed. These dark-etching particles appeared to result from solid-state phase transformation. In contrast, the irregular boundary with the subsequent pulse exhibited coarse-sized, irregular-shaped particles in a light-etching matrix. In this region, the particles appeared to have coarsened in a stagnant region of molten alpha aluminum [10]. In both of these regions, the alpha aluminum matrix structure was essentially irresolvable using light microscopy. In addition to the microstructural transitions observed earlier in the boundary between successive melt zones, Fig. 5 also indicates the presence of several dark-etching equiaxed particles (small arrows) in the central FZ.

SEM Examination

In comparison to light microscopy, SEM analysis provided a clearer delineation of the morphology of the different types of dispersed particles in the FZ. In general, particles with three different morphologies, viz.,

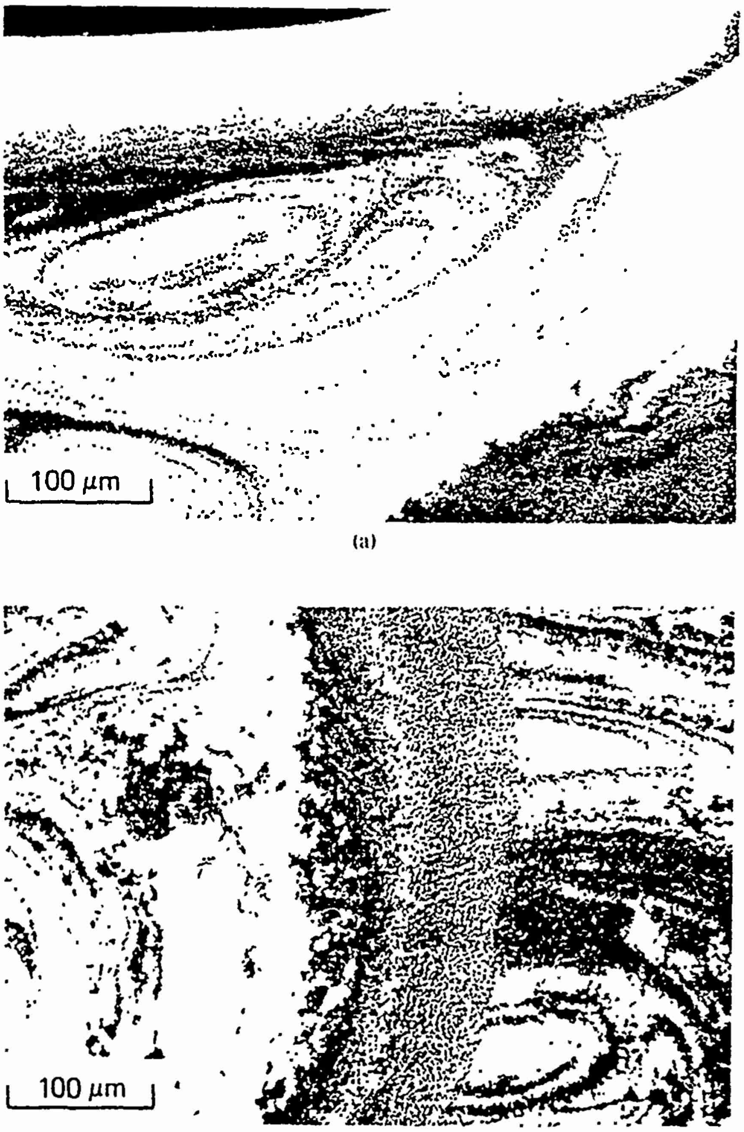

(a)

(b)

Fig. 4. Light micrographs of pulsed Nd:YAG laser weld in Al-8Fe-2Mo: (a) transverse section showing top corner of fusion zone; (b) top surface showing HAZ and FBR between successive melt zones.

FIG. 5. Light micrograph (differential-interference contrast) of pulsed Nd:YAG laser weld in Al–8Fe–2Mo showing boundary region between successive melt zones. Large arrow indicates boundary between HAZ and unaffected FZ of initial melt zone. Small arrows indicate equiaxed particles in the subsequent melt zone.

equiaxed, spherical, and irregular, were observed. Figure 6a shows the dark-etching "swirls," which essentially consisted of fine-sized equiaxed particles in an alpha aluminum matrix. In the region adjacent to the "swirl," the presence of several fine-sized and coarse-sized globular particles were observed. The relatively coarse-sized particles exhibited evidence of equiaxed growth. Equiaxed particles with side arms were observed more frequently in the central FZ (Fig. 6b). The long arms exhibited by these particles implied considerable growth during solidification. In addition to significant particle coarsening, the coarse structures also showed evidence of an alpha aluminum "halo" surrounding these large equiaxed particles. Evidently, the recalescence effects associated with the growth of these large particles contributed to the formation of coarser dendritic alpha microstructures around them. The dark-etching FBR between successive melt zones exhibited several irregular particles in a relatively coarse cellular-dendritic alpha aluminum matrix (Fig. 6c), while the adjacent HAZ contained predominantly fine-sized spherical particles in a relatively irresolvable alpha aluminum matrix (Fig. 6d). SEM analysis of the light-etching region near the weld outer periphery revealed a minimal distribution of fine-sized spherical particles (Fig. 7a). Evidence for the occurrence of epitaxial solidification normally associated with fusion welds was not readily observable in this region. SEM examination of the HAZ in the base material showed a uniform distribution of fine-sized particles (Fig. 7b) but did not reveal information on either the morphology of the particles or the grain size of the base metal alpha. Although the above SEM observations more clearly resolved the morphologies of the dispersed particles in the FZ as compared to light microscopy analysis,

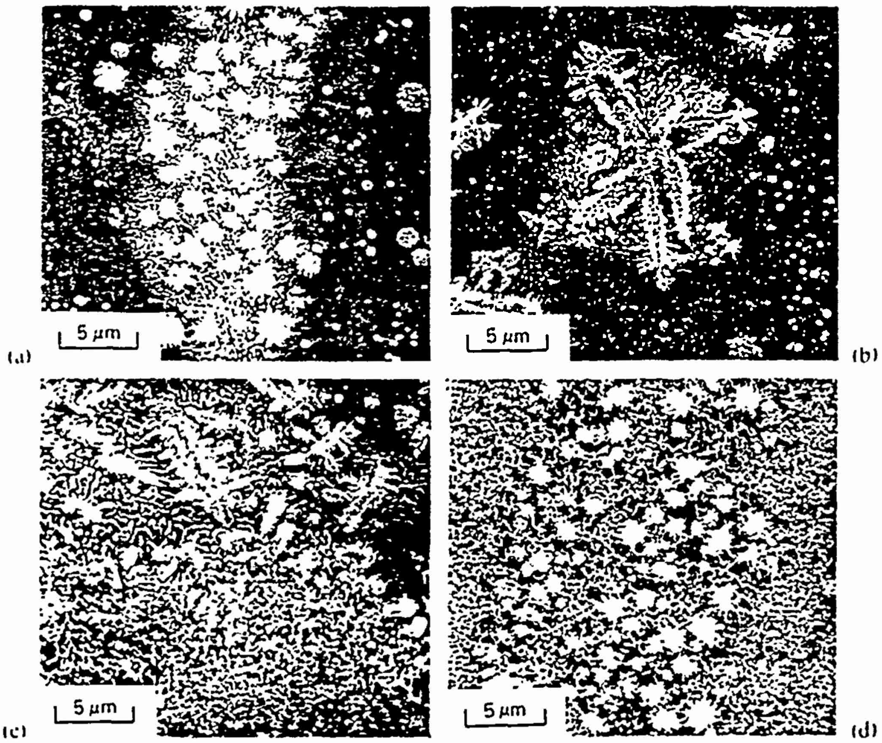

FIG. 6. SEM micrographs of pulsed Nd:YAG laser weld in Al–8Fe–2Mo: (a) dispersoid coarsened "swirl" at center of FZ; (b) coarse intermetallic within FZ; (c) FBR between successive pulses, arrow indicates fusion boundary; (d) HAZ within the preceding melt zone showing dispersoid coarsened "swirl."

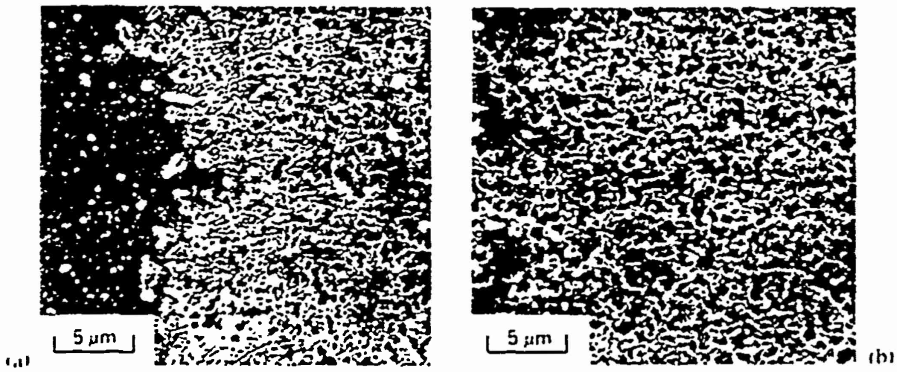

FIG. 7 SEM micrographs of pulsed Nd:YAG laser weld in Al–8Fe–2Mo: (a) FBR adjacent to base metal. (b) HAZ region.

the structure of the alpha aluminum matrix in both the base metal and FZ was nearly irresolvable.

TEM Examination

TEM analysis of the weldment provided increased resolution of the weld FZ and HAZ microstructures. The light-etching regions near the outer periphery of the weld (Figs. 3, 4) exhibited spherical particles in a matrix of fine-sized dendritic alpha aluminum (Fig. 8a). STEM/EDS analysis found these spherical particles typically contained 17.1 wt.% Fe (9.72 at.%) and 8.7 wt.% Mo (2.87 at.%), indicating Al_6Fe type intermetallics. The fine size and spherical morphology of these intermetallics and their Al_6Fe-type composition suggested that they originated from base metal dispersoid particles. The wide difference in the melting points of intermetallic particles and alpha aluminum tended to support the possible occurrence of unmelted/undissolved intermetallic particles in molten alpha aluminum. Based on this observation, it is apparent that the weld "fusion zone" was essentially a partially melted region comprised of unmelted/undissolved intermetallic particles dispersed in molten aluminum. Considering the nonequilibrium thermal conditions obtained within the molten weld pool, the observed variations in the size and distribution of the intermetallics were attributed to the variations in the local thermal conditions. Dispersoids that experienced high temperatures apparently dissolved more extensively than those in lower temperature regions. As shown earlier in the light micrographs (Fig. 3a,b), convective currents within the FZ controlled the movement of these dispersoids through the "high" and "low" temperature regions in the weld pool and thereby influenced their final size and distribution. Under these conditions, the solidification of the weld pool initiated epitaxially from base metal alpha in the fusion boundary (Fig. 8b). These epitaxially grown alpha aluminum grains effectively "entrapped" the unmelted/undissolved dispersoids as solidification proceeded along a relatively steep temperature gradient across the advancing solid–liquid interface. The presence of steep temperature gradients in this region promoted solidification of the melt to a columnar-dendritic substructure with fine intermetallics or solute rich particles partitioned to the last-to-solidify dendrite intersticies. EDS semi-quantitative compositional analysis of the overall dendritic structure showed ≈7 wt.% Fe and ≈2.2 wt.% Mo, which was well beyond the eutectic composition of 1.8 wt.% Fe [14] in binary Al–Fe systems (albeit Mo additions influence this composition to a limited extent). The solidification of this hyper-eutectic composition to primary alpha with ≈3.0 wt.% Fe (versus a maximum equilibrium solid-solubility of 0.04 wt.% Fe

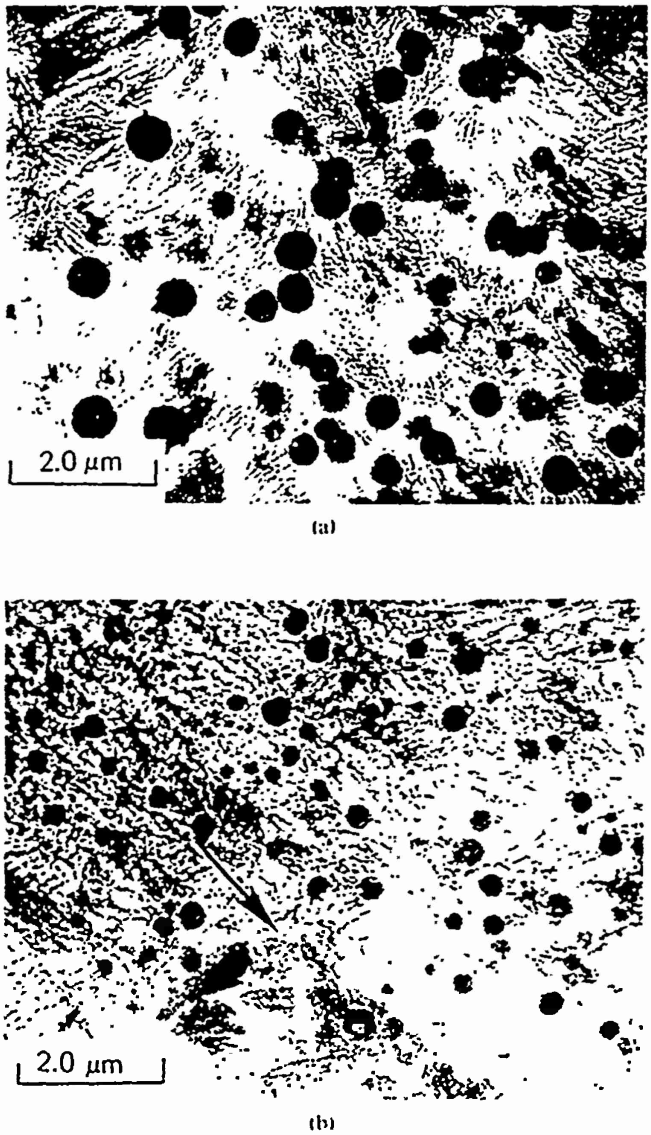

FIG. 8. Bright field TEM micrographs of pulsed Nd:YAG laser weld in Al-8Fe-2Mo: (a) FZ (light-etching regions in light micrographs). (b) FBR adjacent to base metal. (c) center of FZ (dark-etching in light micrographs). (d) FBR between successive laser melt zones Arrow in (b) indicates columnar-dendritic growth direction.

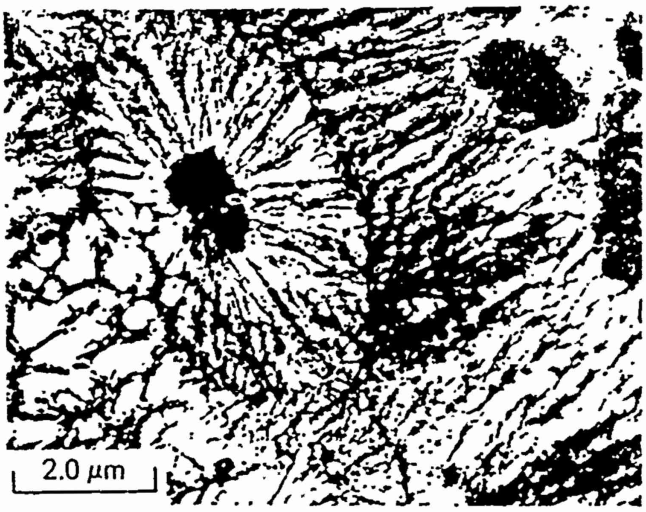

(c)

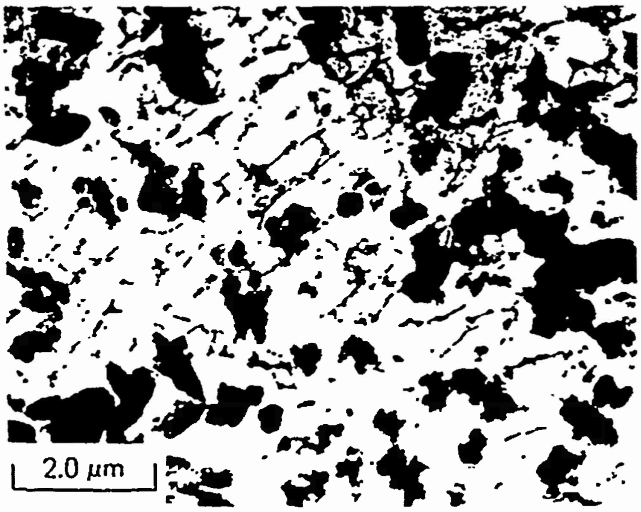

(d)

FIG. 8. (*Continued*)

[14] at the eutectic temperature) and ≈1.9 wt.% Mo was attributed to the rapid cooling and solidification rates experienced within the pulsed laser weld. Indeed, a comparison of the dendrite arm spacings with previous relationships between dendrite arm spacing and cooling rate in aluminum alloys [17, 18] indicated a Nd:YAG laser welding cooling rate in excess of 10^{5}°C/s through the solidification temperature range.

As shown in Fig. 8c, the central FZ exhibited relatively coarse-sized particles that nucleated dendritic alpha aluminum. STEM/EDS analysis of the coarse-sized particles revealed the composition as ≈23.8 wt.% Fe (14.1 at.%) and ≈8.25 wt.% Mo (2.8 at.%). These coarse-sized particles were presumably either Al_3Fe or $Al_{13}Fe_4$-type intermetallics originating from base metal dispersoid particles. Nearer to the center of the FZ, where the temperature gradient became shallower, the unmelted/undissolved base metal dispersoid (intermetallic) particles underwent equiaxed growth. EDS analysis of the alpha aluminum sheath ("halo") around these coarse particles indicated significant increases in solid-solubility of both Fe (≈4.67 wt.%) and Mo (≈2.1 wt.%). Interestingly, a comparison of the composition of the overall matrix structure (≈7 wt% Fe and ≈2.2 wt.% Mo) with that of the alpha-aluminum sheath suggested possible alpha-aluminum growth through solute partitioning. Since increased solid solubility of Fe in aluminum (obtained through rapid solidification processing) is known to decrease the lattice parameter of alpha aluminum [19], the decrease in lattice parameter of alpha aluminum can be expected to improve the lattice registry across the interface between the Al_3Fe or $Al_{13}Fe_4$ type intermetallic particle and the supersaturated alpha aluminum. Considering that a lattice disregistry of 10% or less between potential nucleant and alpha aluminum promotes nucleation of alpha aluminum [20], the improvement in lattice registry across the interface between the Al_3Fe or $Al_{13}Fe_4$ type intermetallic particle and the supersaturated alpha aluminum and the local thermal conditions may be considered responsible for promoting the formation of alpha aluminum "halo" around the intermetallic particle.

TEM analysis of the dark-etching FBR between successive laser pulses revealed both the irregular shape of the particles and the coarse size of the dendritic alpha aluminum matrix (Fig. 8d). EDS analysis indicated that the irregular particles typically contained 27.91 wt.% Fe (16.1 at.%) and 2.63 wt.% Mo (0.88 at.%), and suggested that these particles were the equilibrium Al_3Fe or $Al_{13}Fe_4$-type intermetallics. In comparison with the composition of the alpha aluminum matrix in the light-etching regions, the coarser as-solidified alpha aluminum dendrites in the FBR were considerably leaner in both Fe (≈0.6 wt.%) and Mo (≈1.6 wt.), suggesting that the coarsening of the equilibrium dispersoid particles occurred in molten alpha aluminum and depleted the remaining liquid of both Fe and Mo.

TEM analysis of the HAZ in the FZ between successive melt zones revealed the formation of submicron-sized acicular particles in an alpha aluminum matrix (Fig. 9a). It is interesting to note that SEM examination of this region (Fig. 6d) was inadequate in resolving the presence of these fine-sized acicular particles. EDS compositional analysis of the acicular particles revealed the composition to typically consist of 21.22 wt.% Fe (11.69 at.%) and 1.9 wt.% Mo (0.62 at.%). Although EDS analysis suggested that these particles might belong to the Al_7Fe-type intermetallic (isomorphous with the Al_7Cr), presence of such particles has not been previously reported in Al–Fe–Mo systems. Furthermore, in comparison with the spherical particles observed in the light-etching regions of the FZ, these acicular particles exhibited a higher Fe/Mo ratio, suggesting Al_3Fe type. During the laser weld thermal cycle, the extremely fine intermetallics or solute-rich particles formed by elemental segregation at the last-to-solidify dendrite intersticies apparently underwent preferential dissolution in solid-state and thereby provided solute flux for the formation of these acicular particles. The supersaturated as-solidified alpha aluminum matrix ($\approx$3.0 wt.% Fe and $\approx$1.9 wt.% Mo) might have also provided additional solute flux of the formation/growth of these intermetallic particles. Note that, together with a near-complete absence of the as-solidified dendritic structure, occasional spherical intermetallics with characteristic growth morphologies were also observed in this region. Figure 9b shows the TEM microstructure of the HAZ in the base metal directly adjacent to the FZ. Consistent with a slight reduction in dispersoid particle density versus the base material (Fig. 2b), only marginal coarsening of the dispersoid particles was observed.

HARDNESS EVALUATION

Figure 10 shows a plot of the hardness traverse across the top surface of the pulsed Nd:YAG laser weld. Consistent with the microstructural analysis, the laser weld exhibited a maximum hardness of KHN 260 in the fine-grained (light-etching) FZ region. The hardness of the FZ decreased progressively from the outer periphery towards the weld center. The minimum hardness (KHN 180) observed in the FZ was higher than the unaffected base metal (KHN 118). Despite the limited structural coarsening observed in the HAZ in the base metal, this region did not exhibit any drop in hardness. The marginal increase in hardness (relative to the base metal) observed in this region was attributed to the minimal width

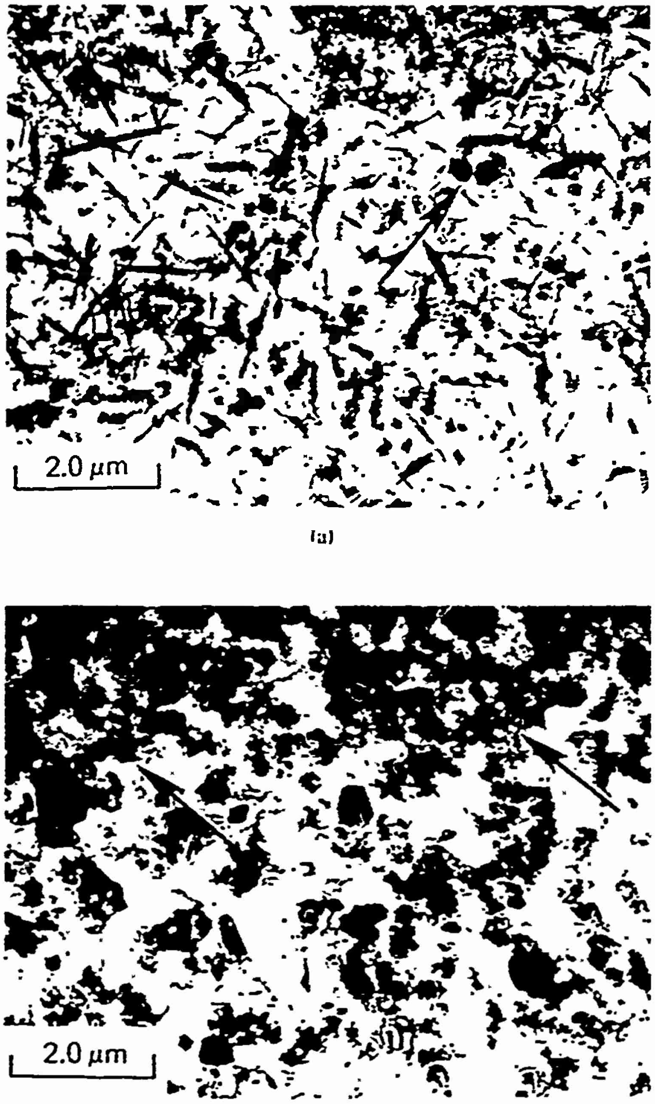

(a)

(b)

Fig. 9. Bright field TEM micrographs of HAZ in pulsed Nd:YAG laser weld in Al–8Fe–2Mo: (a) HAZ within FZ of preceding melt zone. (b) HAZ in base metal. Arrow in (a) indicates spherical intermetallic particles. Arrows in (b) indicate the boundary between HAZ and unaffected base metal.

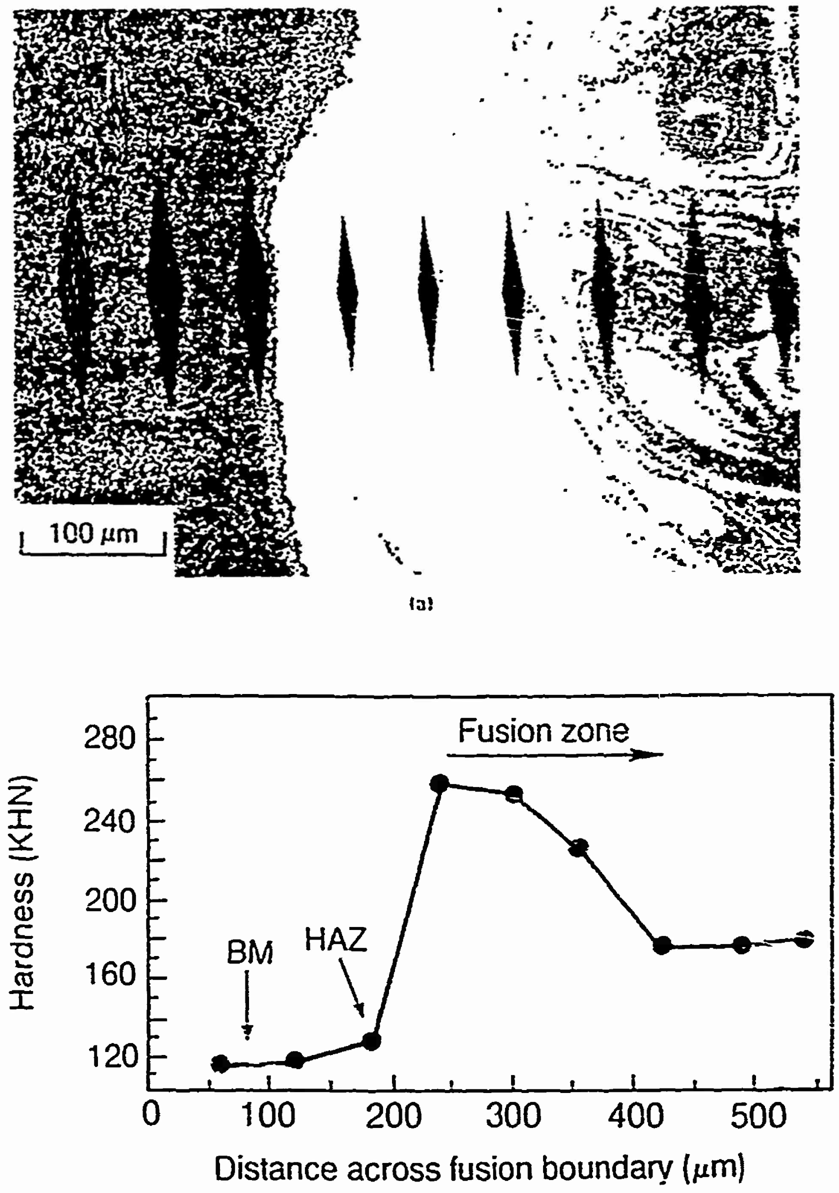

(a)

(b)

FIG. 10. Light micrograph of FBR in pulsed Nd:YAG laser weld in Al-8Fe-2Mo and corresponding Knoop hardness traverse using 200-g load.

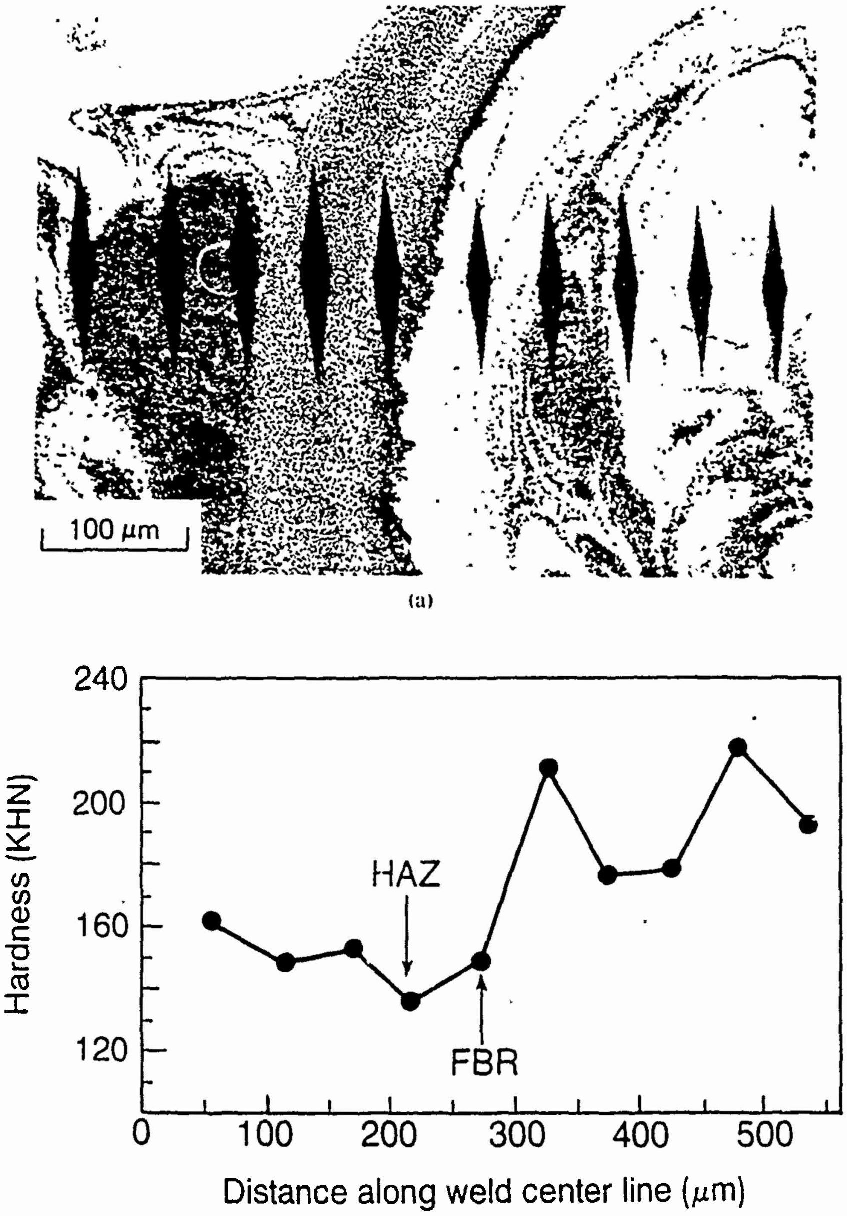

(a)

(b)

FIG. 11. Light micrograph of boundary between successive melt zones in pulsed Nd:YAG laser weld in Al-8Fe-2Mo and corresponding Knoop hardness traverse using 200-g load.

of the HAZ and the "constraint effect" of the surrounding high-strength microstructure.

The hardness traverse along the longitudinal weld centerline (Fig. 11) more clearly delineated the variation in hardness with the microstructural transitions observed in the FZ and in the boundary between successive melt zones. In agreement with the microstructural analysis, the dark-etching FZ regions exhibited a range of hardness, depending on the local size and distribution of the intermetallic particles. As shown, the hardness of the light-etching regions always far exceeded that of the dark-etching regions. A minimum hardness of KHN 135 was observed in the HAZ in the boundary between successive melt zones. In comparison with the hardness of the light-etching and dark-etching regions, the hardness of the HAZ represented approximately a 50% and 25% drop, respectively. The significant drop in hardness was attributed to the absence of the as-solidified fine dendritic substructure. The adjacent FBR exhibited a higher hardness of KHN 150 relative to the HAZ, the increase in hardness apparently originating from the strengthening effect of the fine interdendritic particles in the as-solidified microstructure.

Interestingly, results of a complementary weldability investigation [21] involving evaluation of mechanical properties of autogenous, full-penetration, pulsed Nd:YAG laser weld (41.34 J/mm average energy input) in Al–8Fe–2Mo sheet provided excellent correlation with the above metallographic analysis. Although use of a continuous travel rate produced a FZ exhibiting 70%–80% overlap between successive melt zones, transverse-weld tensile testing found fracture to occur in the unaffected base metal indicating 100% joint efficiency and a weld tensile strength in excess of 374 MPa (54.2 Ksi). Longitudinal-weld bend ductility testing revealed fracture initiation and propagation to be associated with the HAZ between successive melt zones with a bend ductility only marginally below that of the base metal (11% versus 14%).

Summary

The results of this investigation indicated that the pulsed Nd:YAG laser weld in RS/PM Al–8Fe–2Mo alloy exhibited four distinct microstructural regions characterized by two different etching responses. A light-etching FZ microstructure was observed near the outer periphery of the weld, while dark-etching microstructures were observed in the central FZ, the boundary between successive melt zones and a narrow HAZ with the base material. TEM analysis determined that the light-etching FZ structures consisted of spherical intermetallic particles "entrapped" in an extremely fine-grained, columnar-dendritic alpha aluminum matrix. In contrast, the dark-etching microstructures in the central FZ exhibited coarse intermetallic particles that also nucleated dendritic alpha aluminum. In the boundary between successive melt zones, both a HAZ containing acicular dispersoid particles and a FBR containing irregular-shaped dispersoid particles in a coarse-grained dendritic alpha aluminum matrix were observed. The specific microstructural transitions within the FZ were attributed to the presence of unmelted/undissolved base metal dispersoid particles and the local thermal conditions. The occurrence of a solute supersaturated alpha aluminum in the FZ and a dispersoid-coarsened microstructure in the HAZ in the boundary between successive melt zones may have implications on the long-term elevated-temperature stability of these microstructures.

The authors express appreciation to Mr. T. J. Lienert at Sandia National Laboratories, Albuquerque, New Mexico, for performing the Nd:YAG laser welds and to Mr. H. O. Colijn at the Central Electron Optics Facility, The Ohio State University (OSU), for his assistance in STEM/EDS analysis. Research performed at OSU was supported by the Army Research Office under contract #DAAL03-88-K-0049.

References

1. S. L. Langenbeck. W. M. Griffith. G. J. Hildeman and J. W. Simon. in *Rapidly Solidified Aluminum Alloys. STP 890* (M. E. Fine and E. A. Starke. Jr.. eds.). ASTM. PA (1986). pp. 410–422.
2. F. H. Froes. Y-W. Kim. and F. Hehman. *J. Metals* 39:8. 14–21 (1987).
3. C. M. Adam and R. G. Bourdeau. in *Rapid Solidification Processing: Principles and Technologies II* (R. Mehrabian. B. H. Kear and M. Cohen. eds.). Claitors Publishing. Baton Rouge. LA (1980). pp. 246–259.
4. C. M. Adam. in *Rapidly Solidified Amorphous and Crystalline Alloys.* Vol. 8 (B. H. Kear. B. C. Giessen. and M. Cohen. eds.). Elsevier Science Publishing Co.. New York (1982). pp. 411–422.
5. C. M. Adam. in *Science and Technology of Undercooled Melts* (P. R. Sahm. H. Jones. and C. M. Adams. eds.). NATO-ASI Series. Martinus-Nijhoff Publishers. Dodrecht (1986). pp. 186–209.
6. C. M. Adam. in *Mechanical Behavior of Rapidly Solidified Material* (S. M. L. Sastry and B. A. MacDonald. eds.). TMS. Warrendale. PA (1985). pp. 21–39.
7. J. H. Perepezko. in *Science and Technology of Undercooled Melts* (P. R. Sahm. H. Jones. and C. M. Adams. eds.). NATO-ASI Series. Martinus-Nijhoff Publishers. Dodrecht (1986). pp. 29–52.
8. J. E. Flinn. *Rapid Solidification Technology for Reduced Consumption of Strategic Materials.* Park Ridge. NJ. Noyes Publications (1985). pp. 64–93.
9. W. A. Baeslack III. *Metallography* 18:73–82 (1985).
10. W. A. Baeslack III and S. Krishnaswamy. in *International Trends in Welding Research* (S. A. David. ed.). ASM International. Metals Park. OH (1986). pp. 357–362.

11. S. Krishnaswamy and W. A. Baeslack III, *Ma. Sci. Eng.* 98:137–141 (1988).
12. S. J. Savage and F. H. Froes, *J. Metals* 36:4, 20–33 (1984).
13. P. Trebbia, *Ultramicroscopy*, 27:343–348 (1989).
14. M. H. Jacobs, A. G. Doggett, and M. J. Stowell, *J. Ma. Sci.* 9:1631–1643 (1974).
15. L. F. Mondolfo, *Aluminum Alloys: Structure and Properties*, London, Butterworths (1976), pp. 283–289.
16. L. F. Mondolfo, *Aluminum Alloys: Structure and Properties*, London, Butterworths (1976), pp. 329–331.
17. H. Jones, *Rapid Solidification of Metals and Alloys*, Monogr. 8, Institution of Metallurgists, London (1982), pp. 40–43.
18. G. R. Armstrong and H. Jones, in *Proc. Conf. Solidification and Casting of Metals*, The Metals Society, London (1979), pp. 454–459.
19. H. Jones, *Ma. Sci. Eng.* 5:1–18 (1969/70).
20. J. H. Perepezko and S. E. LeBeau, in *Aluminum Transformation Technology and Applications—1981* (C. A. Pampillo, H. Biloni, L. F. Mondolfo, and F. Sacchi, eds.), ASM, Metals Park, OH (1982), pp. 309–346.
21. S. Krishnaswamy, W. A. Baeslack III, and T. J. Lienert, Nd:YAG laser weldability of RS/PM Al-8Fe-2Mo sheet, *Proceedings of the Second International Conference on Trends in Welding Research* (S. A. David and J. M. Vitek, eds.), ASM International, Gatlinburg, TN, 14–18 May (1989) in press.

Received July 1989; accepted October 1989.

Appendix 1C

APPENDIX IC

K. H. Hou and W. A. Baeslack III, "Electron Microscopy of Rapidly-Solidified Weldments in a Powder Metallurgy Al-Fe-Ce Alloy," Journal of Materials Science Letters, 8 (1989) 716-720.

JOURNAL OF MATERIALS SCIENCE LETTERS 8 (1989) 716–720

Electron microscopy of rapidly solidified weldments in a powder metallurgy Al–Fe–Ce alloy

W. A. BAESLACK III, K. H. HOU
Department of Welding Engineering, The Ohio State University, Columbus, Ohio 43210, USA

J. H. DEVLETIAN
Department of Materials Science and Engineering, Oregon Graduate Center, Beaverton, Oregon 97006, USA

Al-Fe-Ce alloys are rapid-solidification powder metallurgy (RS PM) products that offer significant advantages over conventional ingot metallurgy (IM) aluminium alloys for elevated-temperature applications [1]. These alloys are basically hypereutectic Al-Fe compositions with ternary additions of cerium and contain a total (Fe + Ce) solute content of 12 to 18 at %. Through rapid solidification, the formation of coarse, primary intermetallics is suppressed and solidification instead occurs to a primary α-aluminium structure. Subsequent powder consolidation and thermomechanical processing promote the formation of a high volume fraction (25 to 35%) of extremely fine thermally stable dispersoids in a matrix of submicrometre α-grains. This unique microstructure provides moderate to high room-temperature strength and excellent elevated-temperature mechanical properties up to 300° C.

Recent work by the authors [2] has demonstrated that capacitor-discharge welding can successfully generate high-integrity joints in Al-Fe-Ce alloys. The extremely rapid heating and cooling rates associated with this process allow the generation of a rapidly solidified fusion zone without degradation to the surrounding base-metal microstructure. In addition, the simultaneous application of pressure during fusion-zone solidification suppresses the formation of hydrogen-induced porosity. In the original study [2] the investigation of weld-zone solidification characteristics was limited by the exclusive use of light microscopy for microstructure characterization. The purpose of the present work was to characterize capacitor-discharge weld-solidification phenomena in greater detail through the use of transmission electron microscopy (TEM).

The initial-gap capacitor-discharge welding process involves the axial impacting of cylindrical specimens under gravity and their subsequent arcing and melting by the discharge of a capacitor bank. During impact the arc is extinguished, excess molten metal is expelled and rapid solidification occurs. In the present work both high and moderate cooling rate welds were produced between 6.4 mm diameter rods of Al-8.4 wt % Fe-3.6 wt % Ce (Al-8Fe-4Ce). Specific welding parameters and conditions are described elsewhere [2]. Representative weldments were carefully sectioned longitudinally at the axial centreline into slices 0.4 mm thick and were mechanically thinned on SiC paper down to about 0.125 mm. Discs of diameter 3 mm were punched from the foils in the unaffected base-metal and weld-zone regions and electropolished in a solution of 25% nitric acid and methanol at −30° C. Thin foils were examined in a Jeol 200CX scanning TEM operated at 200 kV.

The unique microstructures and mechanical properties exhibited by Al-Fe-Ce alloy product forms are highly dependent on the rapidly solidified microstructure of the atomized powder. Fig. 1 shows solidification structures of powder particles in a typical hot-pressed Al-Fe-Ce alloy [3]. Microstructures of the powder particles can be observed to transition from nearly featureless regions of partitionless, planar growth at their nucleation site (coarser particles may contain multiple nucleation sites) to cellular and cellular-dendritic structures of progressively increasing coarseness at their outer peripheries. This gradual transition in solidification mode and structural coarseness is attributed to the effect of recoalescence heating on reducing local cooling rates as solidification proceeds. As expected, the proportion of planar and fine cellular growth to coarser cellular-dendritic growth increases with powder fineness due to the higher cooling rates and associated higher degrees of undercooling experienced by the finer powder particles. TEM studies on powder particles have revealed the presence

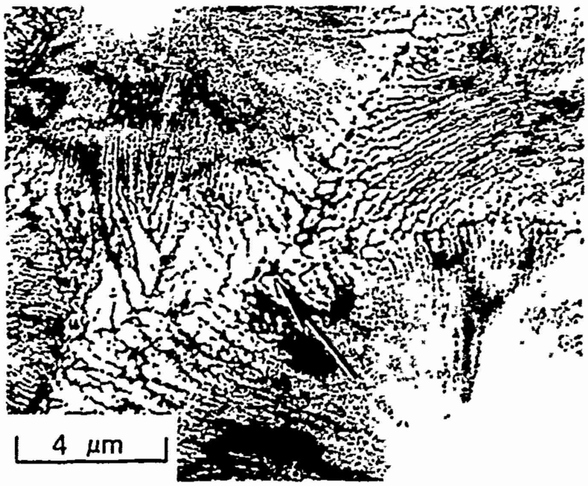

Figure 1 TEM bright-field micrograph of hot-pressed Al-Fe-Ce powder. The arrow indicates the intersection of three powder particles.

0261-8028/89 $03.00 + .12 © 1989 Chapman and Hall Ltd

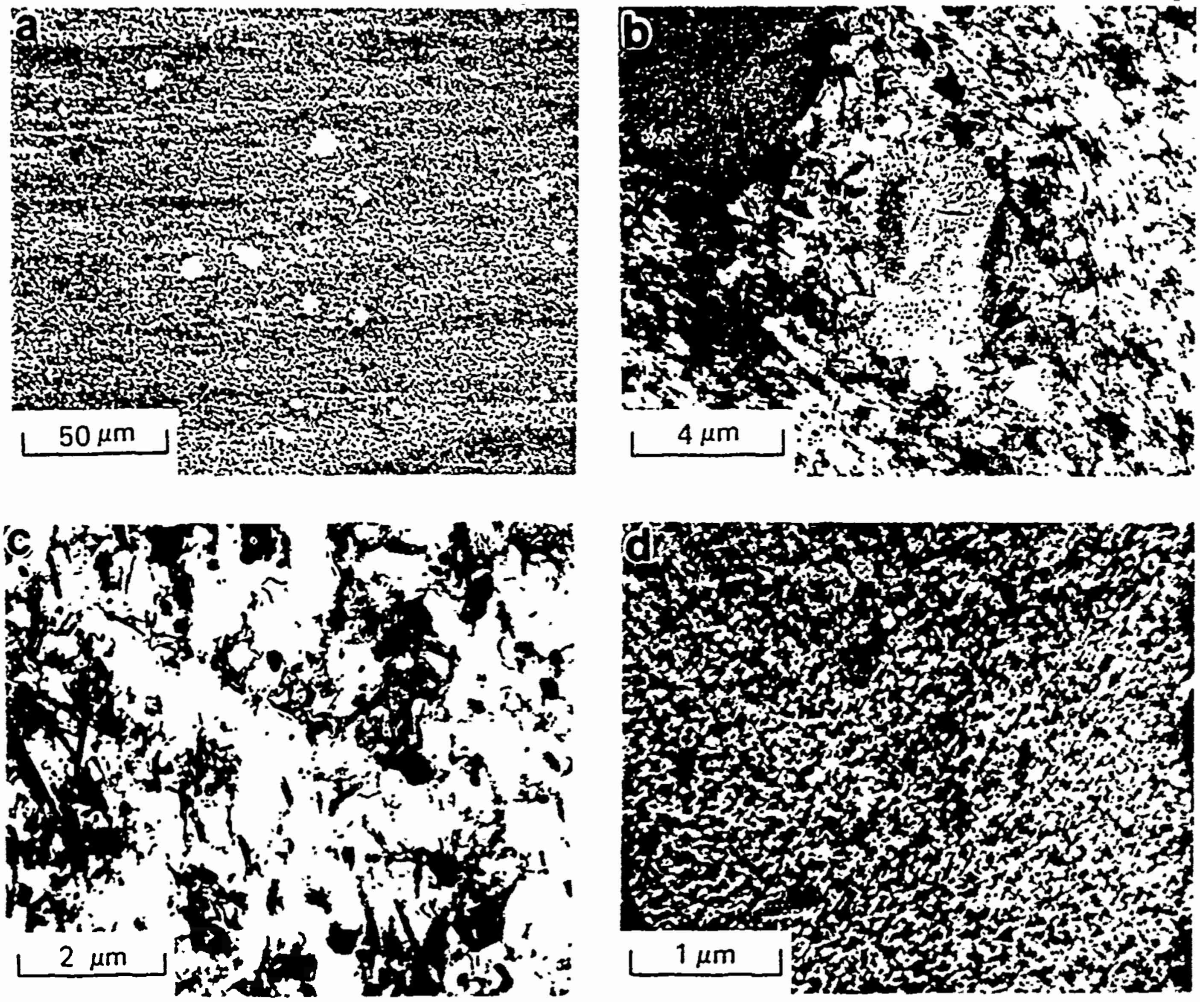

Figure 2 (a) Light and (b) to (d) TEM bright-field micrographs of Al–8Fe–4Ce extrusion.

of fine intermetallics at cell and dendrite boundaries ranging in size from 10 to 100 nm. Electron-diffraction analysis has determined that these intermetallics form during the final stages of rapid solidification [3].

Thermomechanical processing by extrusion breaks up the original powder particle microstructure, with higher extrusion temperatures and deformation levels promoting improved microstructural homogeneity. As shown in Fig. 2a, the extruded Al–8Fe–4Ce alloy studied in the present investigation exhibited good homogeneity and a light texture parallel to the extrusion direction. TEM examination of the dark-etching matrix showed a fine distribution of needle-like and globular intermetallics in a matrix of sub-micrometre α-aluminium grains (Figs 2b and c). Electron diffraction studies of these intermetallics have determined the needle-like phase to be $Al_{13}Fe_4$ and the globular phase to be $Al_{10}Fe_2Ce$ [3]. Also apparent in Fig. 2a are fine, featureless powder particles which retained their original spherical shape during extrusion. TEM analysis of these undeformed particles revealed an extremely fine, uniform distribution of intermetallics that formed in the solid state during compaction and thermomechanical processing (Figs 2b and d). The high hardness imparted to these powder particles by the fine intermetallics inhibited their deformation during hot-pressing and extrusion.

Light micrographs in Figs 3a and b illustrate weld regions of the high and moderate cooling rate capacitor-discharge welds, respectively. Optically the high cooling rate weld exhibited a predominantly featureless microstructure similar to featureless regions observed optically in the finer as-solidified powder [2]. In contrast, the moderate cooling rate weld exhibited a relatively uniform, dark-etching microstructure optically comparable with that observed in the coarser as-solidified powder. Based on the above discussion of powder particle microstructures, the high and moderate cooling rate fusion zones would be expected to exhibit planar or fine cellular and coarse dendritic solidification substructures, respectively. Both weld fusion zones were observed to contain occasional pores near the weld centreline and to exhibit hardnesses greater than that of the unaffected base metal [2].

The TEM bright-field micrograph in Fig. 4a shows a microstructure traverse across the high cooling rate capacitor-discharge weld zone from the unaffected base metal to the fusion zone centreline. Analysis of the base-metal region directly adjacent to the fusion boundary (indicated by arrows) revealed no evidence of intermetallic or α-grain coarsening. The absence of a weld heat-affected zone (HAZ) was attributed to the extremely rapid thermal cycle experienced in this

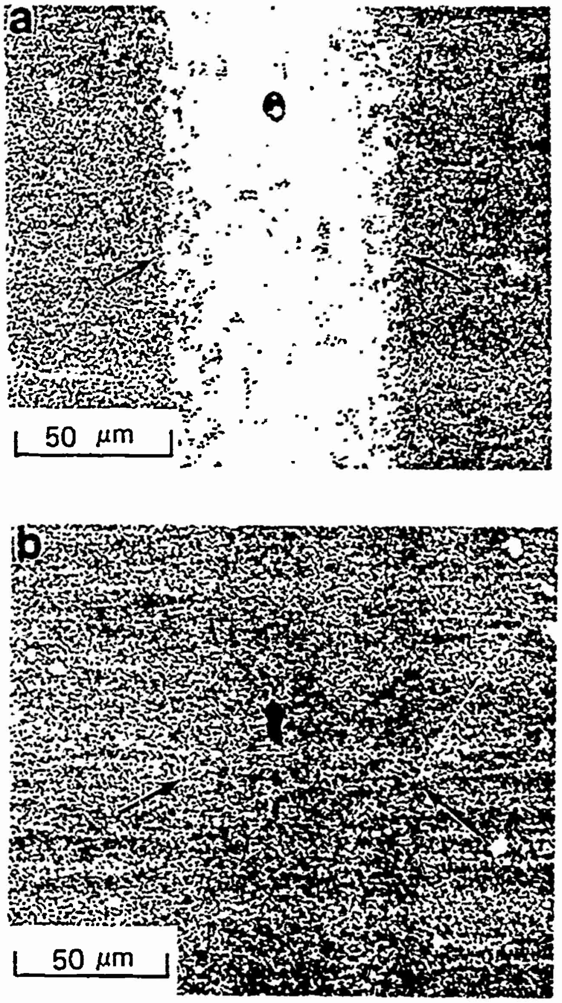

Figure 3 Light micrographs of capacitor-discharge weld fusion zones produced with (a) high and (b) moderate cooling rates. The arrows indicate the approximate fusion boundaries.

region and the metallurgical stability of the microstructure, and was consistent with no measurable decrease in hardness across the weld zone [2]. Solidification of α-grains in the weld fusion zone initiated epitaxially on base-metal α-grains in a cellular-dendritic mode. The relative coarseness of the fusion zone grains, which exhibit relatively uniform dark or light contrast in Fig. 4a, confirmed the operation of an intense competitive growth process across the weld-fusion boundary. TEM bright-field analysis at increased magnification revealed the presence of poorly defined intermetallics at cellular-dendrite boundaries. Ring-type diffraction patterns produced by these intermetallics indicated that they formed during the final stages of solidification rather than in the solid state on cooling. Also apparent in Figs 4a and b are needle-shaped intermetallics located randomly throughout the dendritic α-matrix. Bright- and dark-field TEM analysis at increased magnification indicated that these coarse intermetallics originated from the base metal and remained unmelted during the weld thermal cycle, due to their appreciably higher melting temperature than the α-aluminium matrix (Fig. 4d). During fusion zone solidification these intermetallics coarsened slightly and were subsequently entrapped by the solidifying α aluminium grains. Similar primary intermetallics have been shown to serve as growth centres for α-aluminium grains in rapidly solidified and chill-cast Al–Fe alloys [4]. In the present study, however, the presence of several intermetallics within a single α-aluminium grain, the traversing of intermetallics across α-grain boundaries and an absence of α-"haloes" surrounding the intermetallics indicated that these particles did not serve as growth centres for the fusion-zone α-grains. As solidification proceeded from the edge toward the centre of the fusion zone, the α-grains became increasingly columnar (Fig. 4a), the solidification substructure gradually transitioned from coarse cellular-dendritic to fine cellular (Figs 4c and e) and the density of coarse intermetallics decreased. These microstructural changes were attributed to an increase in peak temperature, cooling rate and solidification rate as solidification proceeded toward the fusion-zone centreline.

Fig. 5a shows a microstructure traverse across a moderate cooling rate capacitor-discharge weld from the base metal to the fusion-zone centreline. As in the high cooling rate welds, fusion-zone solidification appeared to initiate on α-grains in the base metal and proceed inward toward the weld centreline. Solidification occurred by a cellular-dendritic growth mode which became increasingly fine toward the weld centreline. The presence of distinctly columnar α-grains was much less apparent in the moderate than in the high cooling rate welds, becoming clearly discernable only near the centre of the weld. As shown in Fig. 5a, needle-like intermetallics appeared uniformly throughout the entire fusion zone in a quantity and coarseness somewhat greater than that observed in the high cooling rate weld. Throughout most of the fusion zone, the intermetallics appeared to become entrapped by solidifying α-aluminium grains and to exert little influence on the α-grain structure. Near the fusion boundary, however, the observation of more-randomly oriented α-grains and solidification substructure boundaries suggested the possible nucleation of α-grains by the intermetallics (Figs 5b and c). The extent of such nucleation and its effect on the overall α-grain structure could not be clearly determined from the present analysis.

As shown in Fig. 4a, spherical pores were occasionally observed near the fusion-zone centreline for both weld types. The distinctly spherical shape of these pores confirmed their origin as hydrogen bubbles which became entrapped near the weld centreline during the final stages of solidification. No evidence of solidification shrinkage cavities, as suggested by light microscopy [2], was observed by TEM.

TEM studies performed on capacitor-discharge welds in Al-8Fe-4Ce were significant in revealing important details about weld-zone solidification not discernable with light microscopy. Although light microscopy showed relatively uniform fusion-zone microstructures, TEM revealed gradual transitions in the weld-zone solidification structure from the fusion boundary to the fusion-zone centreline. These microstructure transitions, which were most significant in the high cooling rate weld, involved the formation of an increasingly columnar α-grain morphology and the change from a coarse cellular-dendritic to finer

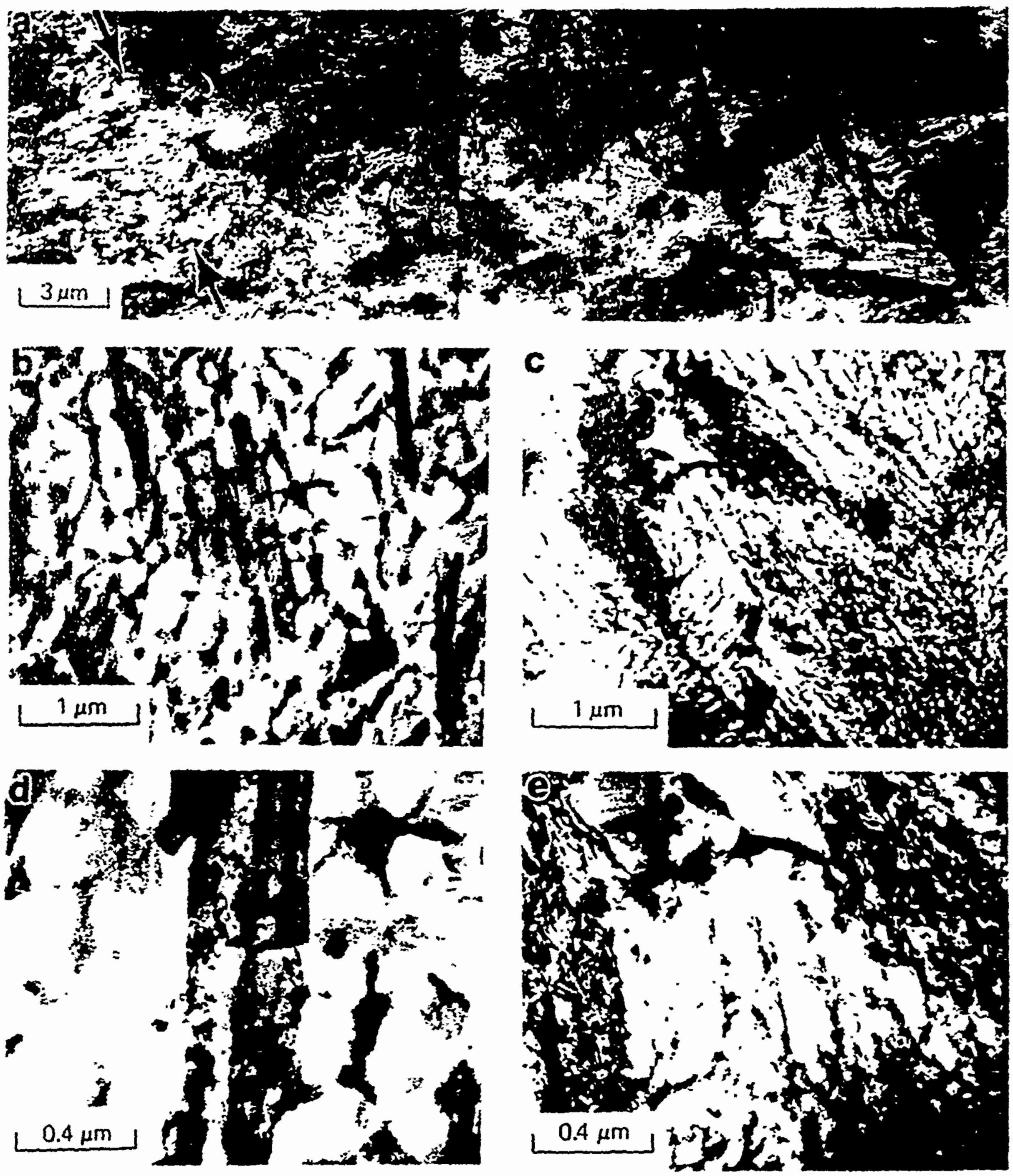

Figure 4 TEM bright-field micrographs of capacitor-discharge weld produced with high cooling rate. (a) Microstructure traverse from unaffected base metal (left) to centre of fusion zone (right). (b) and (d) edge of fusion zone at increased magnification. (c) and (e) centre of fusion zone at increased magnification.

cellular dendritic or cellular solidification substructures. It is of interest to note that this solidification substructure transition was the exact opposite of that observed in the powder particles, indicating significant differences in the nature of heat flow for these two solidification phenomena. TEM also revealed the presence of acicular intermetallics dispersed throughout both weld fusion zones which originated from the base metal. The rapid entrapment of these intermetallics during solidification of α-aluminium grains inward from the base-metal substrates appeared to minimize or preclude their serving as significant nucleation sites for α-aluminium grains.

Although solidification substructure type and coarseness varied with weld type and across the weld zone, it is significant to observe that the even the coarsest cellular-dendritic structure exhibited α-subgrain and interdendritic dispersoid sizes that were finer than that observed in the base metal. These observations were consistent with the higher hardness of both weld fusion zones than that of the base metal [2].

Acknowledgements

The authors are indebted to Dr G. J. Hildeman of ALCOA for providing the Al-Fe-Ce alloy. Appreciation is also expressed to Dr Y. W. Kim of the

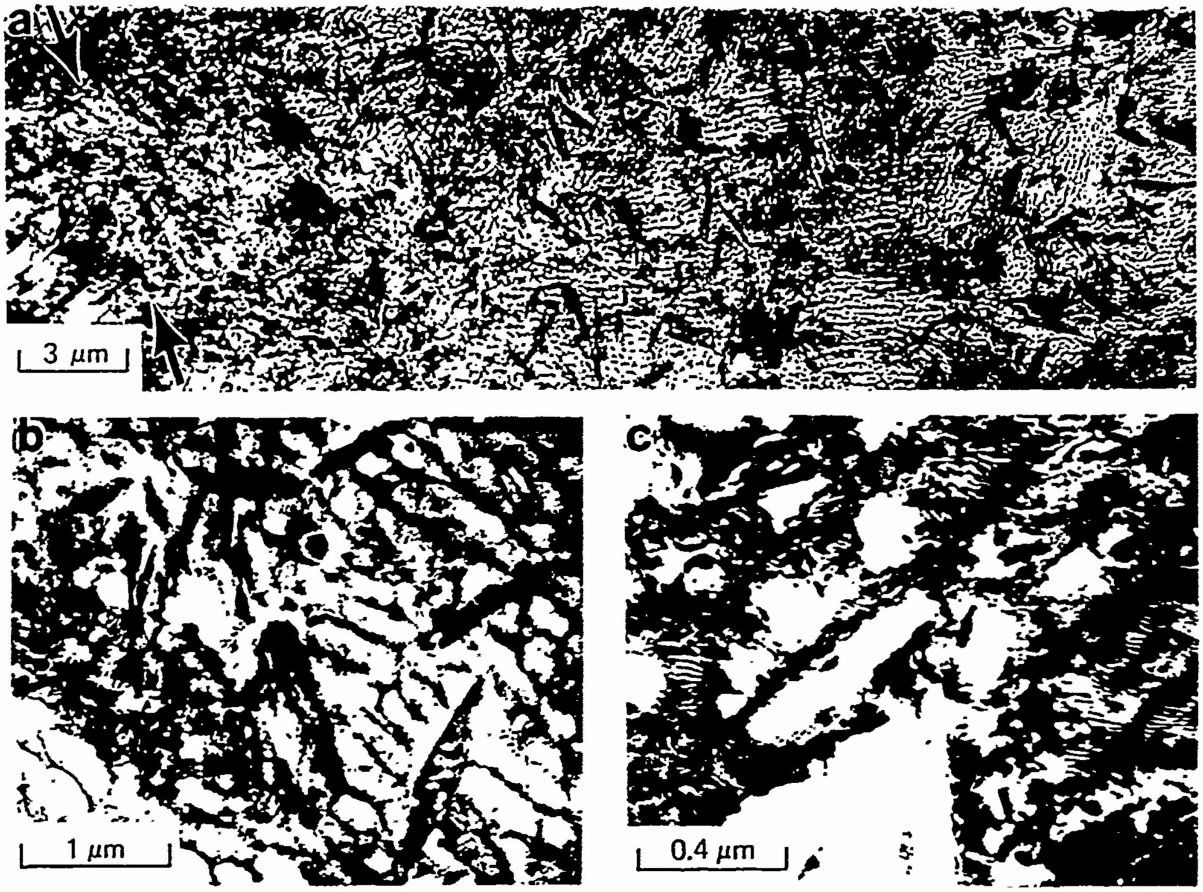

Figure [illegible] TEM bright-field micrographs of capacitor-discharge weld produced with moderate cooling rate. (a) Microstructure transverse from unaffected base metal (left) to centre of fusion zone (right). (b) and (c) edge of fusion zone at increased magnification.

Metcut-Materials Research Group at Wright-Patterson Air Force Base for providing the electron micrograph shown in Fig. 1. Work performed at the Ohio State University was supported by the Army Research Office under Contract No. DAAL03-88-K-0049.

References

1. S. L. LANGENBECK, W. M. GRIFFITH, G. J. HILDEMAN and J. W. SIMON, ASTM STP 890 (American Society for Testing and Materials, Philadelphia, Pennsylvania, 1986) p. 410.
2. W. A. BAESLACK, K. H. HOU and J. H. DEVLETIAN, *J. Mater. Sci. Lett.* 7 (1988) 944.
3. Y. W. KIM, "Dispersion Strengthened Aluminium Alloys" (The Metallurgical Society of AIME, Warrendale, Pennsylvania) in press.
4. H. JONES, *Mater. Sci. Eng.* 5 (1969) 1.

Received 2 November 1988
and accepted 5 January 1989

Appendix 1D

APPENDIX ID

K. H. Hou and W. A. Baeslack III, "Electron Microscopy of Inertia-Friction Weldments in a Rapidly-Solidified Al-Fe-Mo-V Alloy," <u>Journal of Materials Science</u>, 25 (1990) 2642-2653.

JOURNAL OF MATERIALS SCIENCE 25 (1990) 2642–2653

Electron microscopy of inertia–friction weldments in a rapidly solidified Al–Fe–Mo–V alloy

K. H. HOU, W. A. BAESLACK III
Department of Welding Engineering, The Ohio State University, Columbus, Ohio 43210, USA

The microstructures of inertia-friction weldments in a rapidly solidified, powder metallurgy Al–8.7Fe–2.8Mo–1V alloy were characterized using light and transmission electron microscopy. Extensive plastic deformation at the weld interface during the welding process was shown to fracture and disperse relatively coarse, spherical dispersoids present in the original base-metal microstructure, thereby resulting in a refined dispersoid size in this region. These fine dispersoids promoted an increase in hardness at the weld interface as compared to the unaffected base metal. Local regions of nonuniform interface deformation at the weld outer periphery resulted in a heterogeneous microstructure comprised of adjacent regions of high and low dispersoid density. The dispersoid-lean regions were characterized by appreciably coarsened alpha grains and a hardness well below that of the base metal. The greater extent of dispersoid-lean regions in welds produced with low axial force promoted preferential weld interface failure during three-point bend testing, while the near absence of these regions in welds produced with high axial force promoted failure in the unaffected base metal remote from the weld.

1. Introduction

Dispersion-strengthened aluminium alloys produced by rapid solidification/powder metallurgy (RS/PM) represent an important new class of materials for applications at elevated temperatures up to 350° C [1]. These alloys are basically hypereutectic Al–Fe compositions with ternary and quaternary alloying additions of cerium, molybdenum, silicon and vanadium to improve room-temperature strength and ductility and elevated-temperature creep properties. Through rapid solidification processing, the formation of coarse, primary intermetallics is suppressed and solidification instead occurs to primary alpha aluminium. Subsequent powder consolidation and thermo-mechanical processing promote the formation of a high volume fraction of thermally stable strengthening phases in a matrix of submicrometre alpha grains. This unique microstructure has been shown to provide high room-temperature strength and elevated-temperature mechanical properties previously not obtainable in conventional, ingot-metallurgy aluminium alloys [1]. The use of dispersion-strengthened RS/PM aluminium alloys in structural applications as potential replacements for conventional aluminium and titanium alloys will require their effective and economical joining. Unfortunately, the "engineered" microstructures exhibited by these alloys generally preclude their joining using conventional fusion welding techniques. Rather, joining processes must be utilized which can effectively "recreate" and/or "retain" in the weld region the unique microstructures upon which these alloys depend for their superior mechanical properties. Both fusion and solid-state joining processes have demonstrated a potential for achieving these goals. Such joining processes include electron-beam and laser welding [2–4], capacitor-discharge welding [5, 6] diffusion welding [7] and inertia-friction welding [8].

The successful fusion welding of RS/PM aluminium alloys requires rapid solidification and cooling rates which can prevent fusion zone solidification to undesirable, near-equilibrium microstructures and minimize microstructural coarsening and softening in the adjacent weld heat-affected zone. Electron-beam and laser welding studies on low hydrogen level RS/PM Al–8Fe–2Mo sheet have determined that the rapid solidification/cooling rates associated with these processes promote the formation of RS fusion zone microstructures exhibiting hardnesses and strengths superior to that of the base metal with minimal dispersoid coarsening in the heat-affected zone (HAZ). Joint efficiencies up to 100% have been achieved in Nd : YAG laser welds [4] which cool at rates approaching 10^5 °C sec^{-1}. Despite this capability to "recreate" an RS weld zone microstructure, fusion welding techniques have been applied with limited success to Al–Fe–X alloys because of the inherently high hydrogen content of RS/PM aluminium alloys and the associated formation of fusion zone porosity. Studies by the authors [5, 6] involving an RS/PM Al–Fe–Ce alloy containing a high hydrogen content have shown that high pressures experienced during fusion zone solidification in capacitor-discharge welds can prevent porosity formation while promoting the formation of an RS fusion zone. However, geometric and size

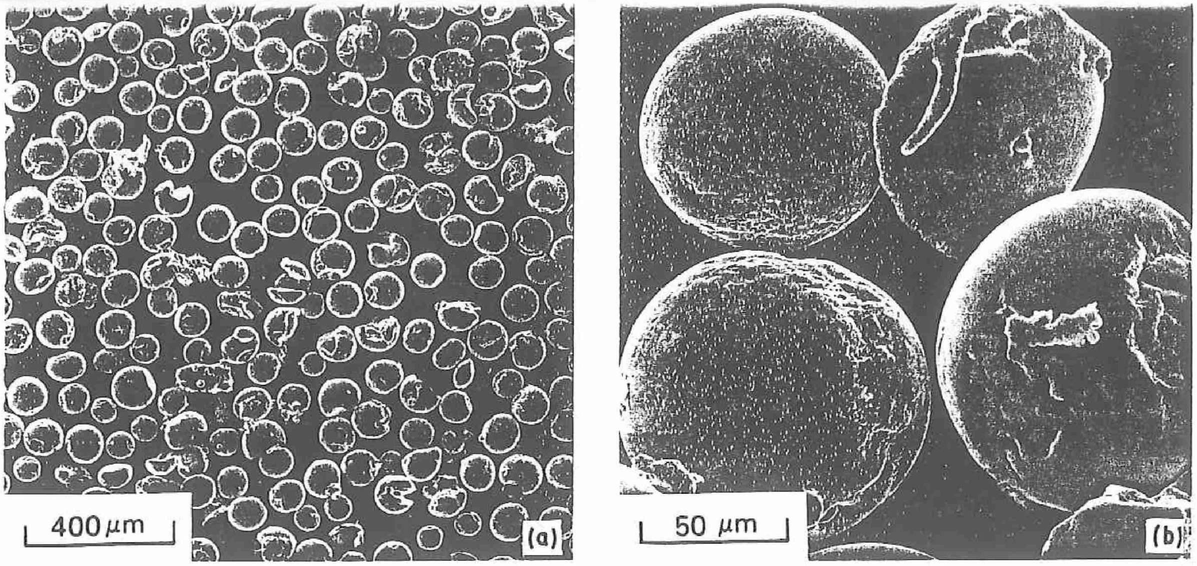

Figure 1 Scanning electron micrographs of Al-Fe-Mo-X rotary-atomized powder.

limitations of parts joined by this process restrict its utility.

Solid-state welding processes offer an important alternative to the fusion welding of Al-Fe-X alloys because both melting and solidification are avoided. Inertia-friction welding is a solid-state joining process that combines frictional heating generated at the faying surfaces with a high axial force to produce a metallic bond [9]. The general absence of melting at the interface during this process eliminates solidification-related discontinuities such as porosity and cracking. Also, the expulsion of surface contaminants and heat-and-deformation-affected metal at the weld faying interfaces during the forging stage of the process promotes final coalescence between nearly unaffected base materials. Inertia-friction welding studies on high-hydrogen content Al-Fe-Ce alloys [8] found that a high axial force promotes the formation of high-integrity, defect-free bonds which exhibit joint efficiencies exceeding 80%. Analysis of the weld interface region using light and scanning electron microscopy (SEM) revealed an extremely fine, complex microstructure which evolved from the complex nature of the thermal and mechanical conditions experienced during the steady state and final forging stages of the welding process. Unfortunately, the limited spatial resolution of the microscopy techniques utilized in this original study precluded thorough microstructure characterization and therefore limited the development of structure/property/fracture relationships.

The principal objective of the present study was to characterize in greater detail the weld interface microstructure of inertia-friction welds in a RS/PM Al-Fe-V-Mo aluminium alloy using thin-foil electron microscopy techniques.

2. Experimental methods

2.1. Materials

The chemical composition of the RS/PM Al-Fe-Mo-V alloy studied in the present investigation (in wt %) was Al-8.7Fe-2.8Mo-1.0V.

Powder production and processing were performed by Pratt and Whitney Aircraft using a rotary atomization (RSR) process [10]. Forced convective cooling with helium provided liquid droplet cooling rates of between 10^4 and 10^6 °C sec^{-1} and minimized surface oxide and hydrate formation. Fig. 1 illustrates the spherical powder particles typically produced with

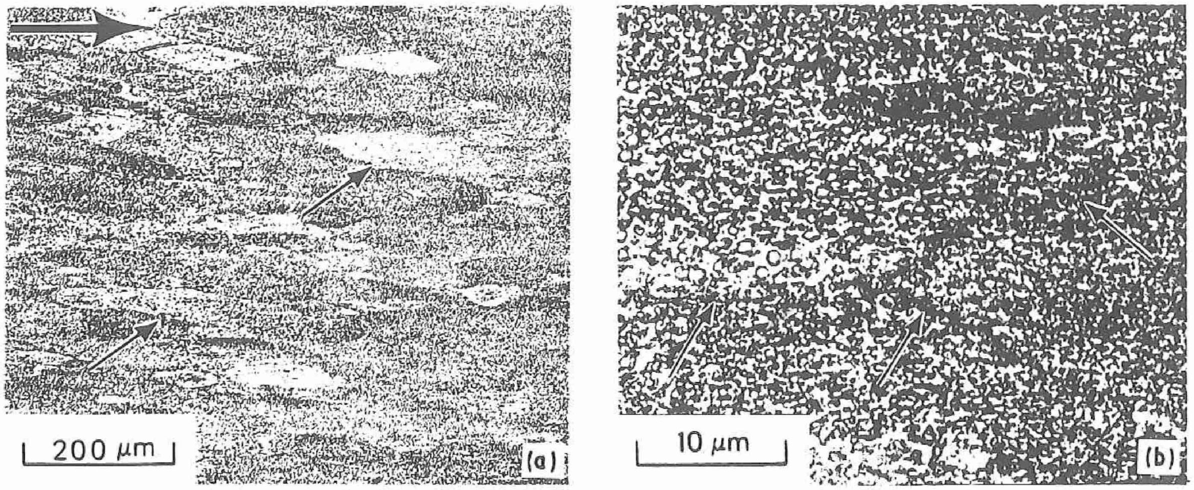

Figure 2 Light micrographs of Al-8.7Fe-2.8Mo-1V extrusion. Large arrow in (a) indicates extrusion direction, small arrows in (a) and (b) indicate powder particle boundaries.

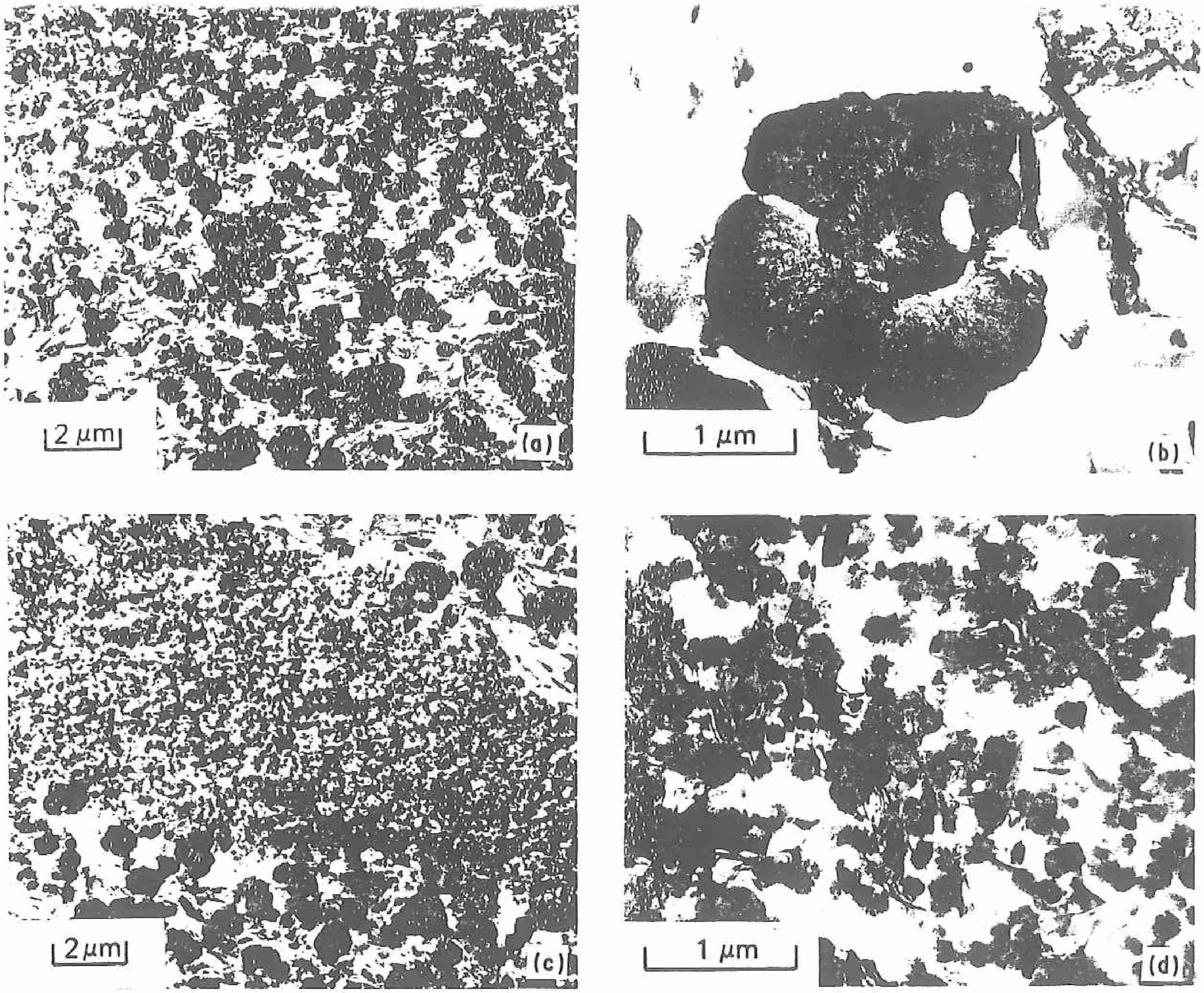

Figure 3 TEM bright-field micrographs of Al–8.7Fe–2.8Mo–1V extrusion: (a, b) predominant microstructure; (c, d) elongated region exhibiting fine dispersoid structure.

this atomization process. Powder particle diameters range from about 25 to 100 μm.

Subsequent to atomization, powders were screened, hot vacuum degassed and extruded to a 250 mm diameter cross-section. Despite atomization and consolidation under completely inert conditions, the final product exhibited a hydrogen content sufficiently high to promote unacceptible levels of porosity in gas tungsten-arc fusion weldments. Cylindrical specimens 22.2 mm diameter and 50.8 mm long were dry machined from the extrusion with the specimen longitudinal axis along the extrusion direction. Prior to welding, each specimen surface was mechanically ground and cleaned with acetone.

2.2. Inertia-friction welding

Inertia-friction welds were produced on an MTI Model 120 inertia-friction welding system. Principal welding parameters, including the moment of inertia, rotational speed and axial force were determined from previous work [8]. These parameters were further optimized in preliminary welding trials which evaluated weld quality strictly from visual analysis of the metal flash and axial displacement. Optimized inertia-friction

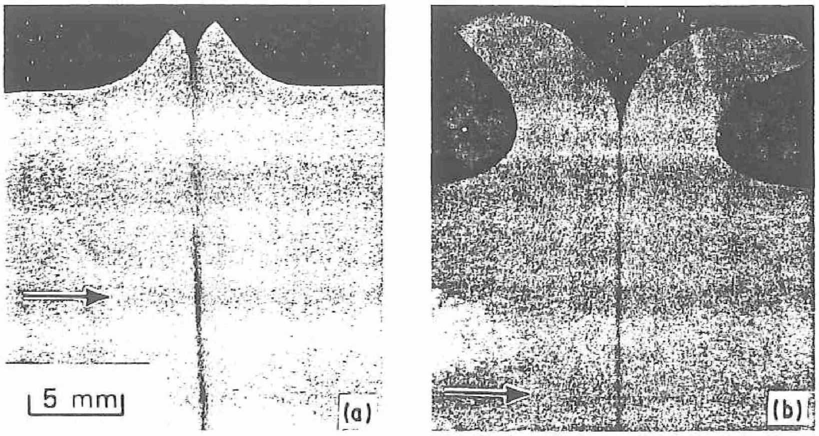

Figure 4 Light macrographs of inertia-friction welds produced in Al–8.7Fe–2.8Mo–1V with (a) low and (b) high axial force. Arrows indicate axial centreline.

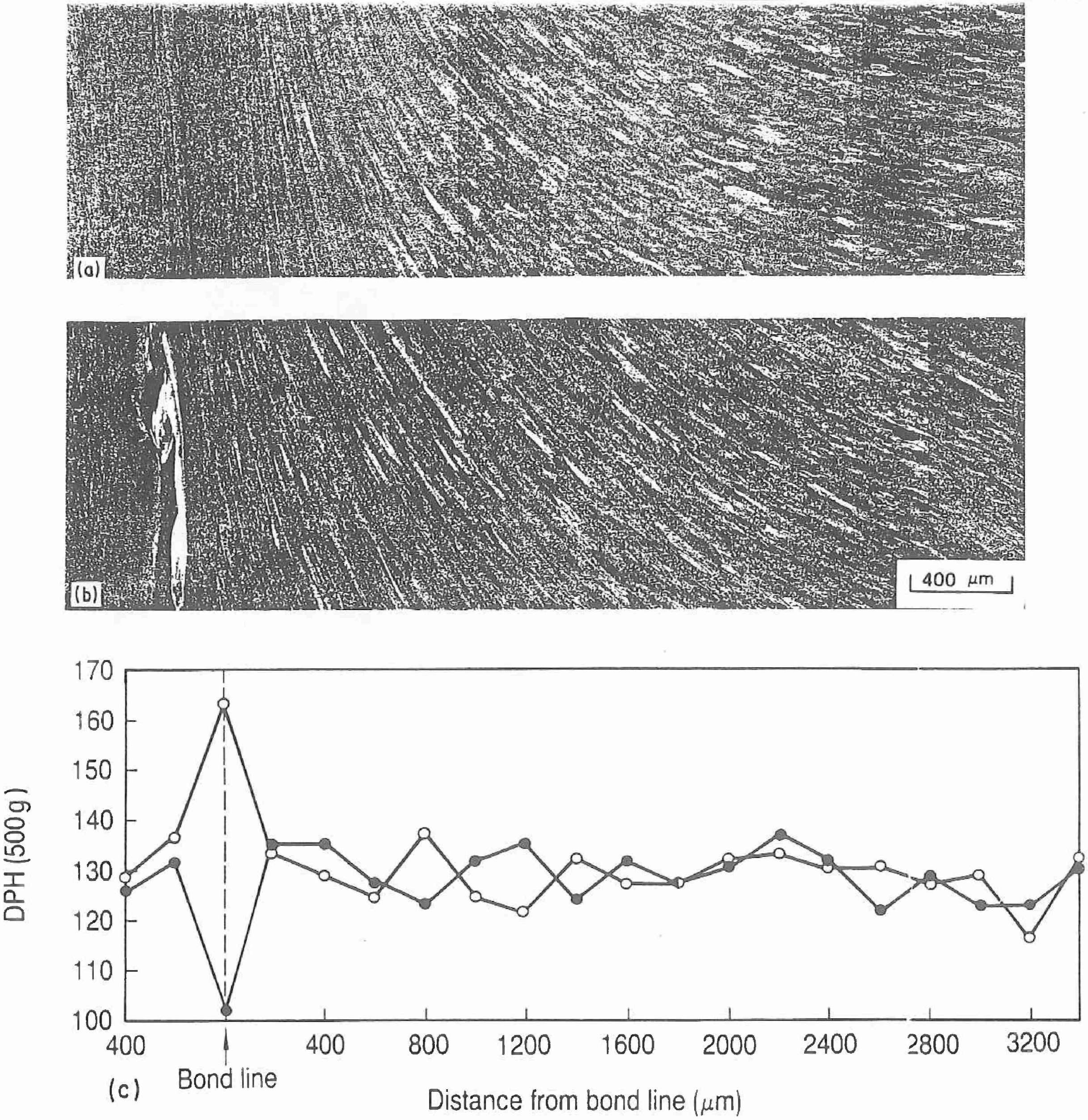

Figure 5 Light macrographs of the (a) centre and (b) outer periphery regions of an inertia-friction weld produced in Al-8.7Fe-2.8Mo-1V with low axial force and corresponding DPH hardness traverses (c). (○) Centre, (●) Outer periphery.

welding parameters were 0.29 $kg\,m^2$ moment of inertia, 471 $rad\,sec^{-1}$ rotational velocity, 126 kN axial force. As mentioned above, axial force had been shown to be very important in achieving an optimum weld zone microstructure and mechanical properties. Therefore, in addition to the "optimized" weldment produced at a "high" axial force, weldments were produced at a "low" axial force of 44.5 kN for comparative evaluation.

2.3. Weld characterization

The principal objective of the present work was to characterize in detail the nature of the weld interface microstructure using thin-foil electron microscopy techniques. Additional analyses performed to complement the electron microscopy analysis included conventional light microscopy, microhardness testing, bend testing and SEM fractographic analysis.

Representative "low"- and "high"-pressure inertia-friction welds were sectioned axially, mounted in epoxy and mechanically polished in a colloidal silica suspension. Following defect analysis of the as-polished specimen surface using light microscopy, microstructural characteristics were revealed by etching with Keller's reagent. Specimen "halves" were carefully sectioned longitudinally at the axial centreline into thin slices 0.3 mm thick using a diamond saw and mechanically thinned on SiC paper down to 0.125 mm. Discs of 3 mm diameter were punched from the foils in the unaffected base metal and from the weld interface regions and electrojet thinned in a solution of 25% nitric acid and methanol at −30° C. Thin foils were examined in a Jeol 200CX analytical electron microscope equipped with a Tracor-Northern TN2000 energy-dispersive X-ray analysis (EDS) system. Analysis included principally bright-field microscopy and semi-quantitative EDS analysis. Selected-area diffraction analysis of the metastable phases typically observed in these alloys is very complex and was not a subject of extensive investigation in the present work.

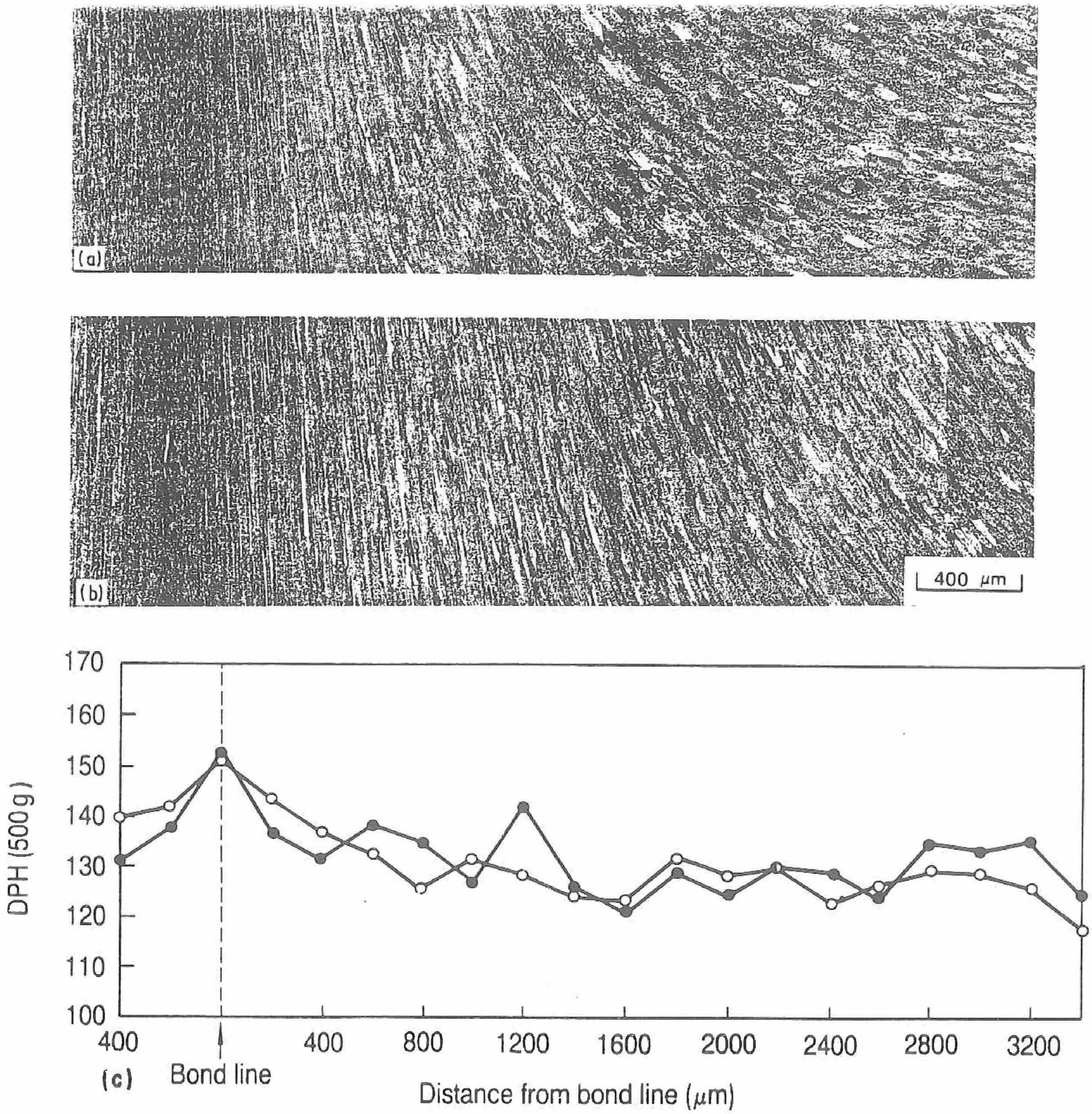

Figure 6 Light micrographs of the (a) centre and (b) outer periphery regions of an inertia-friction weld produced in Al–8.7Fe–2.8Mo–1V with high axial force and corresponding DPH hardness traverses (c). (○) Centre, (●) outer periphery.

Diamond pyramid hardness (DPH) testing was performed across the weld region at the axial centreline and the outer periphery using a load of 500 g and at selected weld interface locations using a load of 50 g. In addition to hardness analysis, three-point bend tests were conducted to identify the preferential failure location in the inertia-friction welded specimens. Bend specimens were produced by removing the weld flash and longitudinally sectioning the weldment into two pieces. Three-point bend testing was performed such that the flat surface (weld centre) was placed in tension. Fractographic examination of the bend specimen fracture surfaces was performed using an ETEC Autoscan scanning-electron microscope.

3. Results

3.1. Base metal microstructure

Although microstructure analysis of the as-solidified powder particles was not performed in the present investigation, previous studies of Al–Fe–Mo type powders produced by rotary atomization have shown that the rapid solidification rates generally prevent primary intermetallic formation and instead promote solidification to primary alpha aluminium with a fine intermetallic structure present at dendrite intersticies [10]. The coarseness of the dendritic structure is dependent on the cooling and solidification rates experienced by the individual powder particles, with increased cooling rates promoting finer dendrite and intermetallic structures and increased supersaturation of alloying elements in the alpha phase. During subsequent consolidation and thermo-mechanical processing, these interdendritic dispersoids coarsen and additional phases may form from the supersaturated alpha matrix, with the nature and extent of this phase coarsening and transformation dependent principally on the thermal cycle experienced during consolidation and thermomechanical processing.

Light micrographs of the Al–8.7Fe–2.8Mo–1V base alloy are shown in Fig. 2. Despite thermomechanical

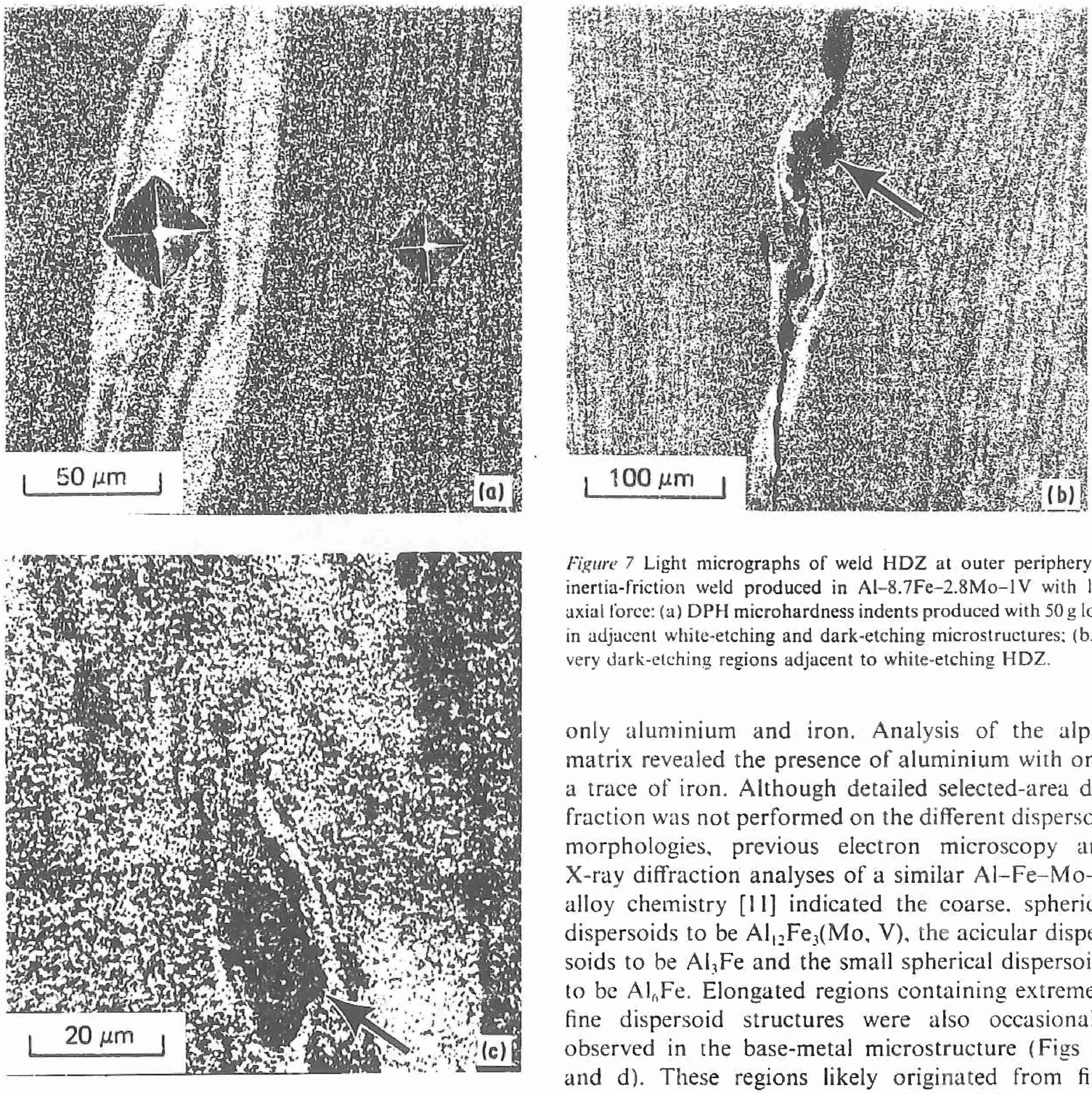

Figure 7 Light micrographs of weld HDZ at outer periphery in inertia-friction weld produced in Al–8.7Fe–2.8Mo–1V with low axial force: (a) DPH microhardness indents produced with 50 g load in adjacent white-etching and dark-etching microstructures; (b, c) very dark-etching regions adjacent to white-etching HDZ.

processing by hot pressing and extrusion, evidence of the original powder particles elongated in the extrusion direction can still be observed. Light microscopy at increased magnification (Fig. 2b) indicated that contrast differences between the particles result from variations in the coarseness of the dispersoid structure within the alpha matrix, with the dark-etching regions exhibiting a high density of fine dispersoids and the light-etching regions exhibiting fewer, coarser dispersoids.

Microstructural characteristics of the base metal were more clearly delineated by transmission-electron microscopy (TEM). As shown in Figs 3a and b, the microstructure consisted predominantly of relatively coarse, nearly spherical intermetallics ranging in diameter from about 500 to 2000 nm in a matrix of submicrometre alpha aluminium grains. Fine, acicular dispersoids ranging in length from approximately 200 to 1000 nm and fine, spherical dispersoids ranging in diameter from about 100 to 250 nm were also located throughout the alpha matrix. Semi-quantitative EDS analysis found the coarse, spherical dispersoids to contain iron, molybdenum and vanadium, while the acicular and small spherical dispersoids contained only aluminium and iron. Analysis of the alpha matrix revealed the presence of aluminium with only a trace of iron. Although detailed selected-area diffraction was not performed on the different dispersoid morphologies, previous electron microscopy and X-ray diffraction analyses of a similar Al–Fe–Mo–V alloy chemistry [11] indicated the coarse, spherical dispersoids to be $Al_{12}Fe_3(Mo, V)$, the acicular dispersoids to be Al_3Fe and the small spherical dispersoids to be Al_6Fe. Elongated regions containing extremely fine dispersoid structures were also occasionally observed in the base-metal microstructure (Figs 3c and d). These regions likely originated from fine powder particles which solidified to an extremely fine dendritic structure or completely to supersaturated alpha aluminium by a partitionless, planar mode of solidification.

3.2. Weldment characterization

3.2.1. Light microscopy analysis

Visual analysis of both the high and low axial force weldments found good symmetry and continuity of flash around the weld circumference. The appreciably greater flash observed in the high compared to the low axial force weld (Fig. 4) was consistent with the higher axial displacement measured for high compared to low axial force (21.9 compared to 3.81 mm, respectively).

Macroscopic characterization of axially sectioned weldments in the as-polished condition revealed occasional lack-of-bonding defects only at the outer periphery of the low axial force welds. No evidence of hydrogen-induced porosity or blistering, or oxide stringers was observed in either of the welds. Heavy etching of the weldments revealed macroscopic heat and deformation zones (HDZs) comprised of a featureless, grey-etching outer region and a dark-etching central region. The dark-etching centre of the HDZs

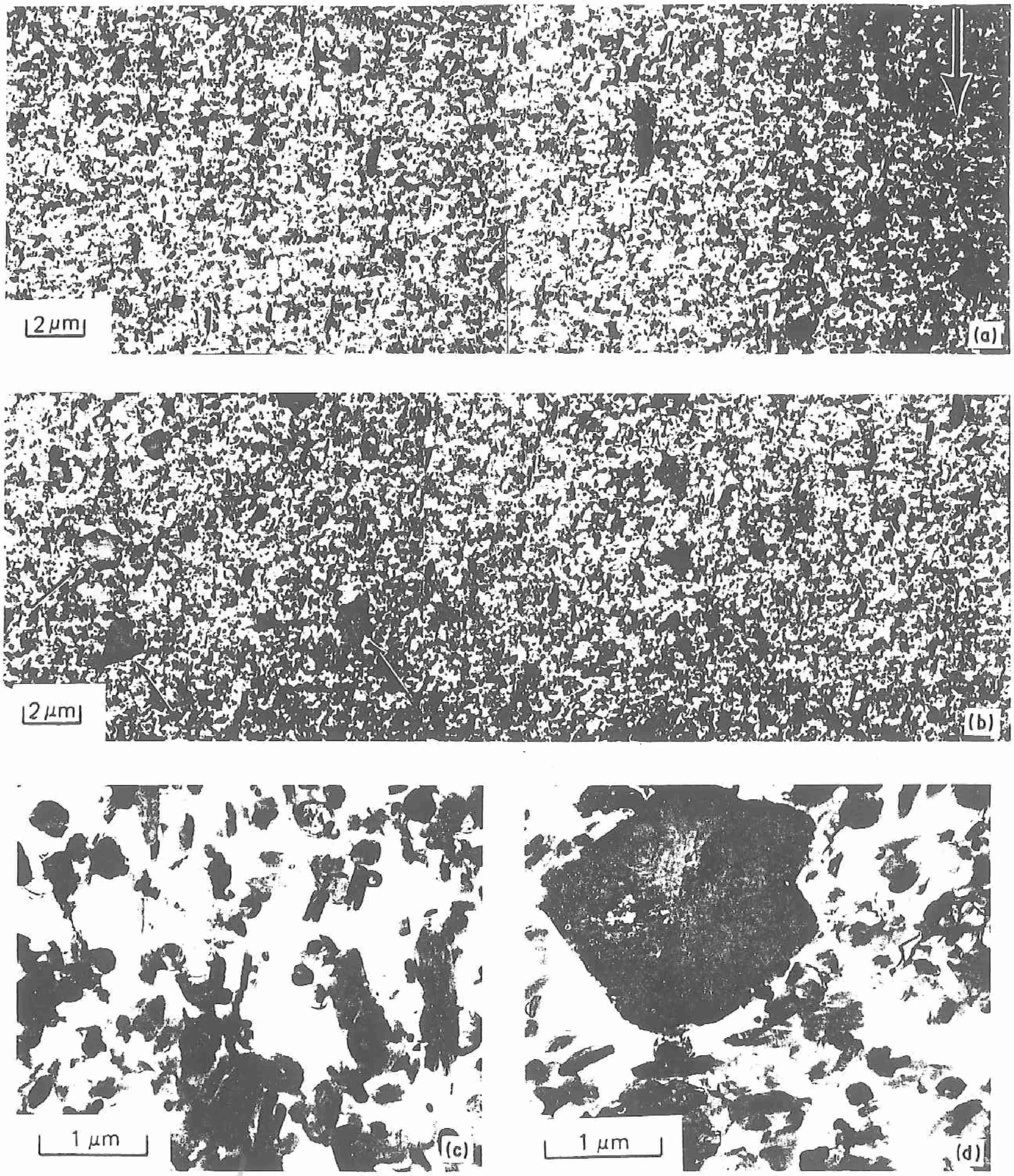

Figure 8 TEM bright-field micrographs of weld interface region at the centre of the inertia-friction weld produced in Al–8.7Fe–2.8Mo–1V with low axial force: (a, b) microstructure traverse across weld region (right side of (b) is continuation of left side of (a)), arrow in (a) indicates location and orientation of weld interface, arrows in (b) indicate angular-shaped coarse dispersoids; (c) interface at increased magnification; (d) angular-shaped dispersoid in (b) at increased magnification.

appeared relatively uniform across the weld and to be slightly wider in the low compared to the high axial force weld.

Light microscopy analysis at increased magnification more clearly revealed the nature of the HDZ regions in both weldment types. Microstructure traverses from the unaffected base metal to the weld interface at the centre and outer periphery of weldments produced at low and high axial force are shown in Figs 5 and 6, respectively. The circumferential, radially outward flow of metal, which is characteristic of inertia-friction welding, was apparent in the outer HDZ. As shown, the microstructure texture across this region continually changed in a uniform manner from parallel to perpendicular to the original base alloy extrusion direction. Nearer to the weld interface, the original base metal microstructure became increasingly "flattened," with the high temperatures and deformation levels directly at the weld interface completely disrupting the base metal microstructure texture and resulting in a uniform, dark-etching microstructure. In general, the width of the entire

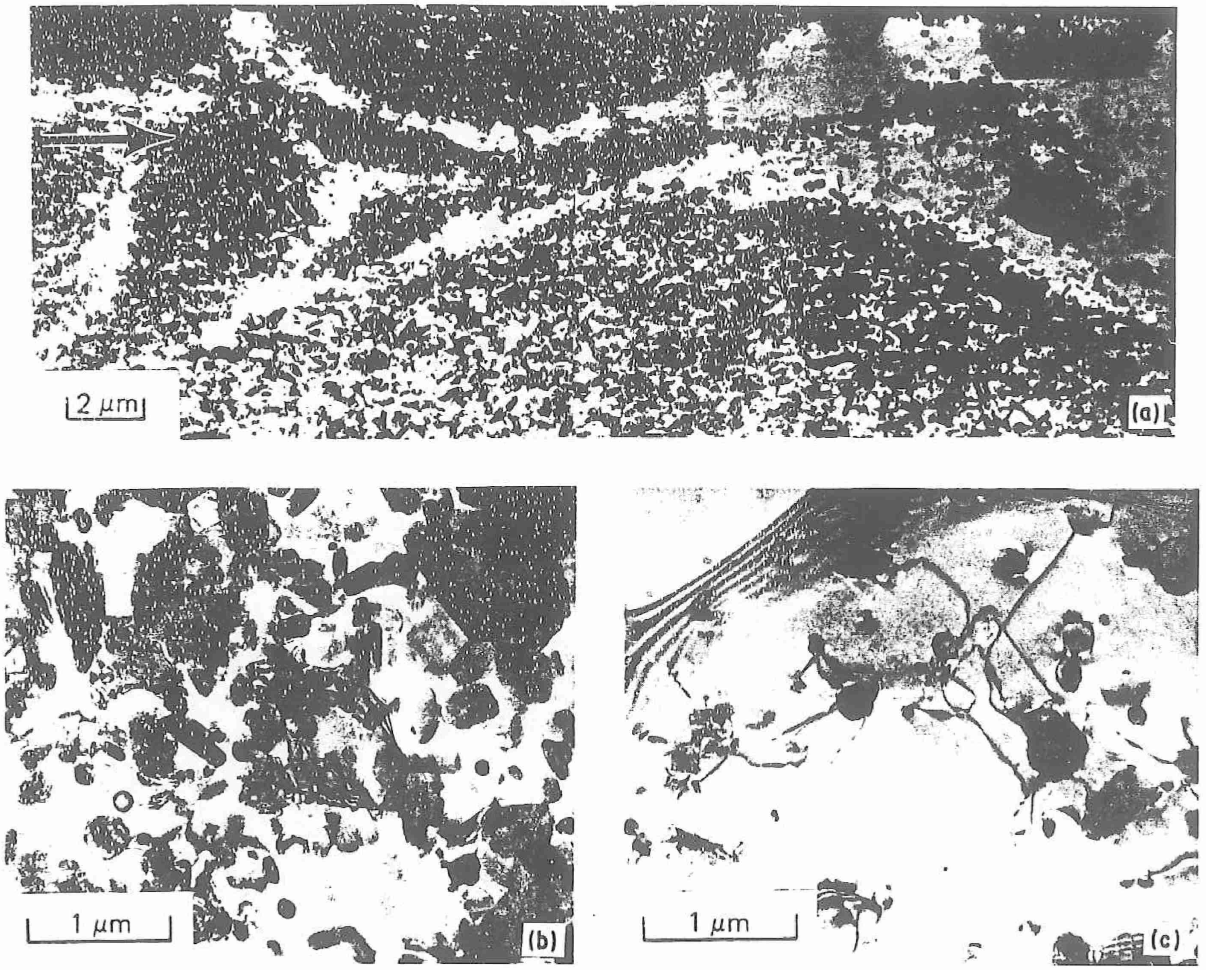

Figure 9 TEM bright-field micrographs of weld interface region at outer periphery of inertia-friction weld produced in Al–8.7Fe–2.8Mo–1V with low axial force: (a) microstructure along weld region, arrow indicates location and orientation of weld interface; (b) region of high dispersoid density at increased magnification; (c) region of low dispersoid density at increased magnification.

HDZ (dark-etching central region and grey-etching outer region in Figs 4a and b) was greater at the outer periphery compared to the weld centreline.

The weld outer periphery regions, particularly in the low axial force welds, commonly exhibited white-etching regions along the weld interface, as shown in Fig. 5b. The analysis of this region at increased magnification suggested a lower dispersoid density compared to the base metal (Fig. 7a). As shown in Figs 7b and c, regions which etched darker than the base metal typically bounded the white-etching regions. Light microscopy indicated a higher dispersoid density in these dark-etching regions as compared to the base metal.

3.3.2. *TEM analysis*

Transmission electron microscopy was effective in revealing microstructural details of the central HDZ which were unresolvable with light microscopy. Figs 8a and b show a TEM bright-field microscopy traverse at the axial centreline of a weld produced with low axial force from the outer edge of the central HDZ to the weld interface (indicated by the arrow in Fig. 8a). As shown in Figs 8a to c, the region was characterized by a relatively uniform, dense distribution of cigar-shaped dispersoids and lesser quantities of finer acicular and spherical dispersoids, with a near absence of the coarse, spherical dispersoids present throughout the unaffected base metal microstructure. The length, width and specific morphology of the cigar-shaped dispersoids varied locally throughout the microstructure, as shown in Fig. 8c. Interestingly, the cigar-shaped and acicular intermetallics appeared to be aligned nearly parallel to the weld interface (i.e. perpendicular to the applied axial force). EDS analysis showed the cigar-shaped particles and coarser spherical particles to contain aluminium, iron, molybdenum and vanadium in levels comparable to those in the coarse base-metal dispersoids, while the fine acicular particles contained only aluminium and iron. Darker contrast evident at the weld interface resulted from a slightly high density of dispersoids and increased density of dislocations in the alpha aluminium. In correlating the contrast of the light and TEM bright-field micrographs, it is apparent that the uniform, dark-appearing region at the weld interfaces resulted principally from the etching response of the extremely fine distribution of dispersoids present in this region. At distances further from the weld interface (left-hand side of Fig. 8b) the density of coarse intermetallics gradually increased while the proportion of finer acicular and cigar-shaped dispersoids decreased. In contrast to their approximately spherical morphology in the unaffected base metal (Fig. 3b), the coarse dispersoids in the HDZ appeared very angular and faceted (arrows in Figs 8b

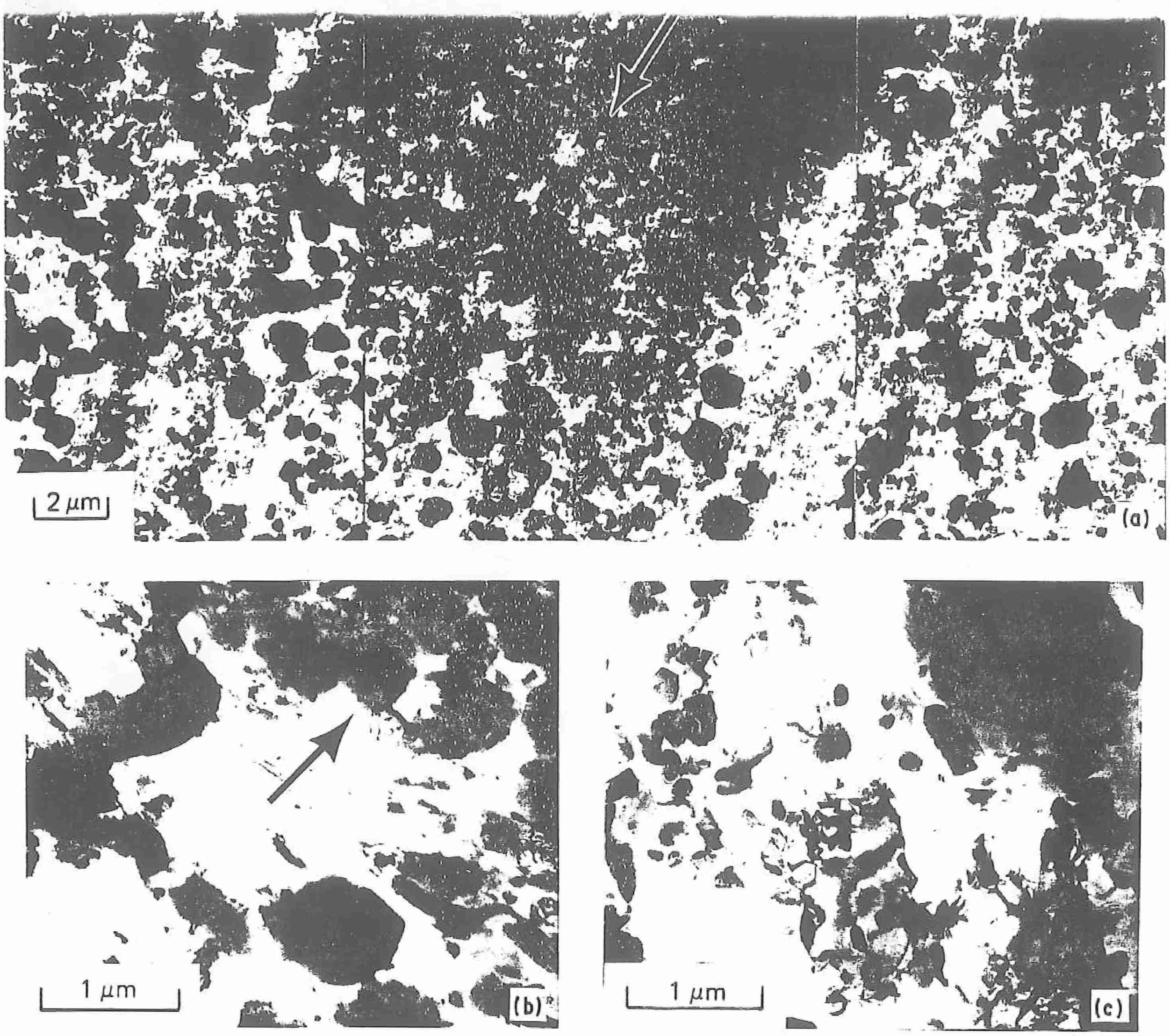

Figure 10 TEM bright-field micrographs of weld interface region at centre of inertia-friction weld produced in Al–8.7Fe–2.8Mo–1V with high axial force: (a) microstructure traverse across weld region, arrow indicates location and orientation of weld interface; (b) region of low dispersoid density at increased magnification; (c) region of high dispersoid density (arrow) at increased magnification.

and d), indicating their partial brittle fracture during welding.

Fig. 9 shows a TEM bright-field traverse along the weld interface at the outer periphery of a weld produced with low axial force. The dark-etching region observed in the light micrograph was comprised of a high density of fine, cigar-shaped and spherical dispersoids (Fig. 9b), with no evidence of the original coarse base-metal dispersoids. Examination of the elongated, white-appearing regions found a very low density of small, spherical dispersoids and occasional cigar-shaped dispersoids (Fig. 8c) in appreciably coarsened alpha grains ranging from 2 to 10 μm diameter. As in the central weld region, the alpha aluminium matrix was found to contain negligible alloying elements while the cigar-shaped and spherical dispersoids contained aluminium, iron, molybdenum and vanadium.

The TEM bright-field microscopy traverse across the weld interface at the centre of a weld produced with a high axial force revealed an appreciably different microstructure compared to that of the low-axial force weld (Fig. 10a). A "striated" microstructure comprised of alternating regions of coarse, spherical dispersoids in a matrix lean in the finer dispersoids (Fig. 10b) and dense mixtures of coarse and fine dispersoids (Fig. 10c) was observed. Further from the interface, the widths of these regions gradually increased as the structure transitioned to that of the unaffected base metal far from the interface.

Fig. 11a shows a TEM bright-field microscopy traverse across the weld zone at the outer periphery of the high axial force weld. A distinct transition was observed from the unaffected base metal microstructure to a region comprised of a high density of fine, spherical and cigar-shaped dispersoids (Fig. 11b). At the particular location shown in Fig. 11, the structure ultimately transitioned at the weld interface to a coarse, equiaxed alpha aluminium grain structure containing a low density of spherical dispersoids (Fig. 11c).

3.3. Mechanical property and fracture analysis

DPH hardness traverses across the high and low axial force inertia-friction welds corresponded well with the observed microstructural characteristics (Figs 5 and 6). In both weld types, significant increases in hardness were associated with the dark-etching, central HDZ regions. This peak hardness rapidly decreased to

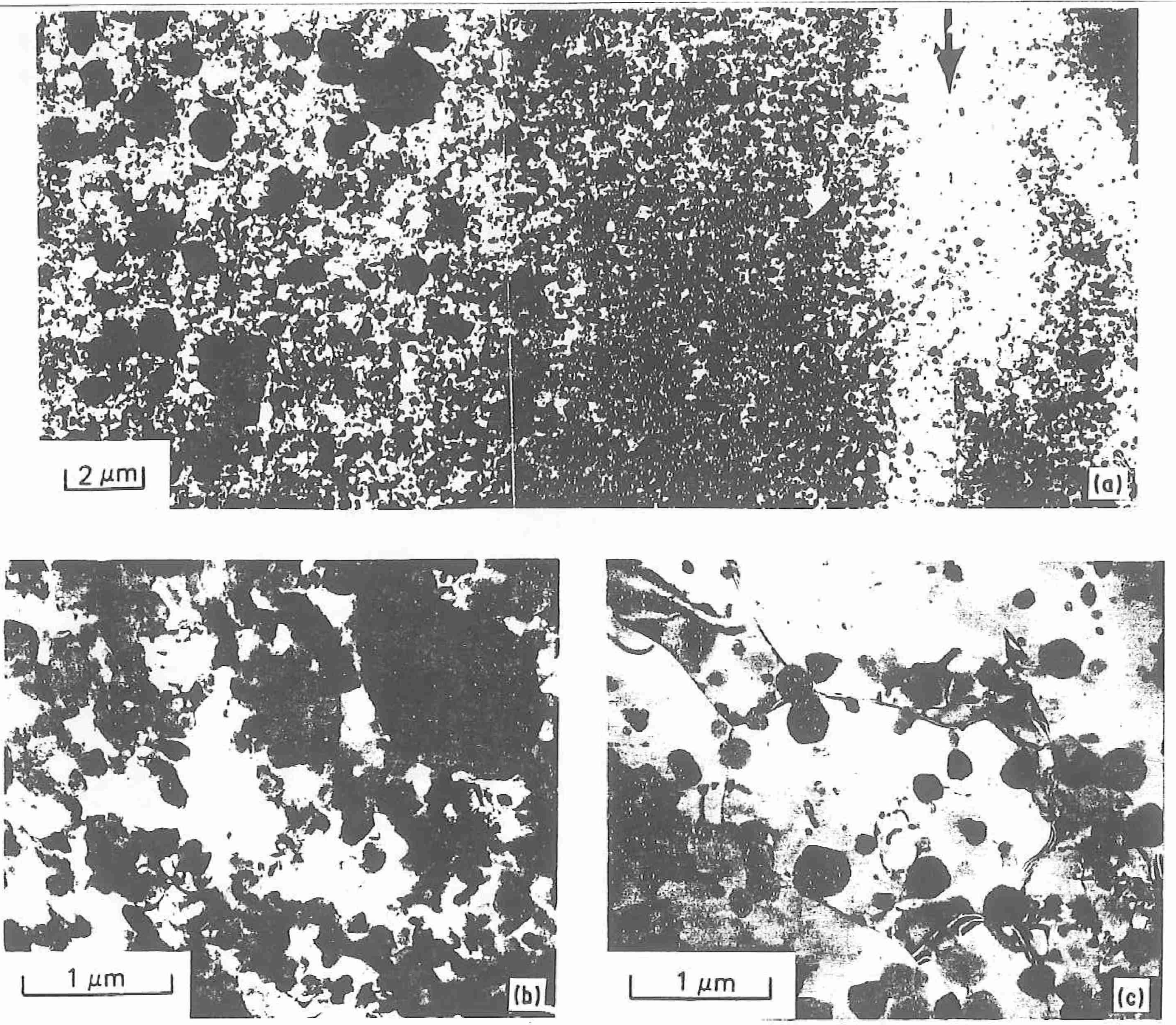

Figure 11 TEM bright-field micrographs of weld interface region at outer periphery of inertia-friction weld produced in Al–8.7Fe–2.8Mo–1V with high axial force: (a) microstructure traverse across weld region, arrow indicates location and orientation of weld interface, (b) region of high dispersoid density at increased magnification; (c) region of low dispersoid density at increased magnification.

base metal hardness levels in the outer HDZ region. Signficant decreases in hardness were observed in the white-etching, low-dispersoid density regions located principally at the outer periphery of low axial force welds. As shown in Fig. 7a, DPH microhardness testing using a low load of 50 g showed appreciable hardness differences between the low dispersoid density and high dispersoid density regions in this outer weld periphery.

Three-point bend tests performed on the high axial force welds failed in the unaffected base metal by a shear-type fracture following appreciable plastic deformation, which was consistent with the higher strength in the weld zone and an absence of fracture-initiating defects. Fracture in the low axial force welds occurred principally along the weld interface with negligible macroscopic deformation.

SEM fractographic analysis of the low axial force weld showed a distinct spiral appearance emanating from the centre of the bar (Fig. 12). As schematically illustrated in Fig. 13, this fracture pattern reflected the effects of the combined torsional and axial forging forces on metal flow experienced at the interface during inertia-friction welding. The fracture surface at the weld outer periphery appeared relatively flat and smooth even at relatively high magnification (Figs 12b and c), which was consistent with the low deformation fracture of this specimen. Near the centre of the bar the fracture path deviated into the far HDZ. Fracture in the far HDZ occurred essentially identical to that in the unaffected base metal by microvoid formation around fine dispersoids and ductile fractile of the soft alpha aluminium matrix (Figs 12d and e).

4. Discussion

Cylindrical specimens welded with the inertia-friction welding process experience complex combinations of axial and torsional forces and stresses across the weld interface [12]. As the schematic illustration in Fig. 13 shows, the plastic flow of metal heated to high temperatures by frictional heating occurs from the central region to the outer periphery in an outward spiralling pattern. Behind the weld interface, the metal flow is generally quite uniform. However, directly at the weld interface nonuniform mechanical mixing can occur in layers of highly plastic metal on each side of the weld

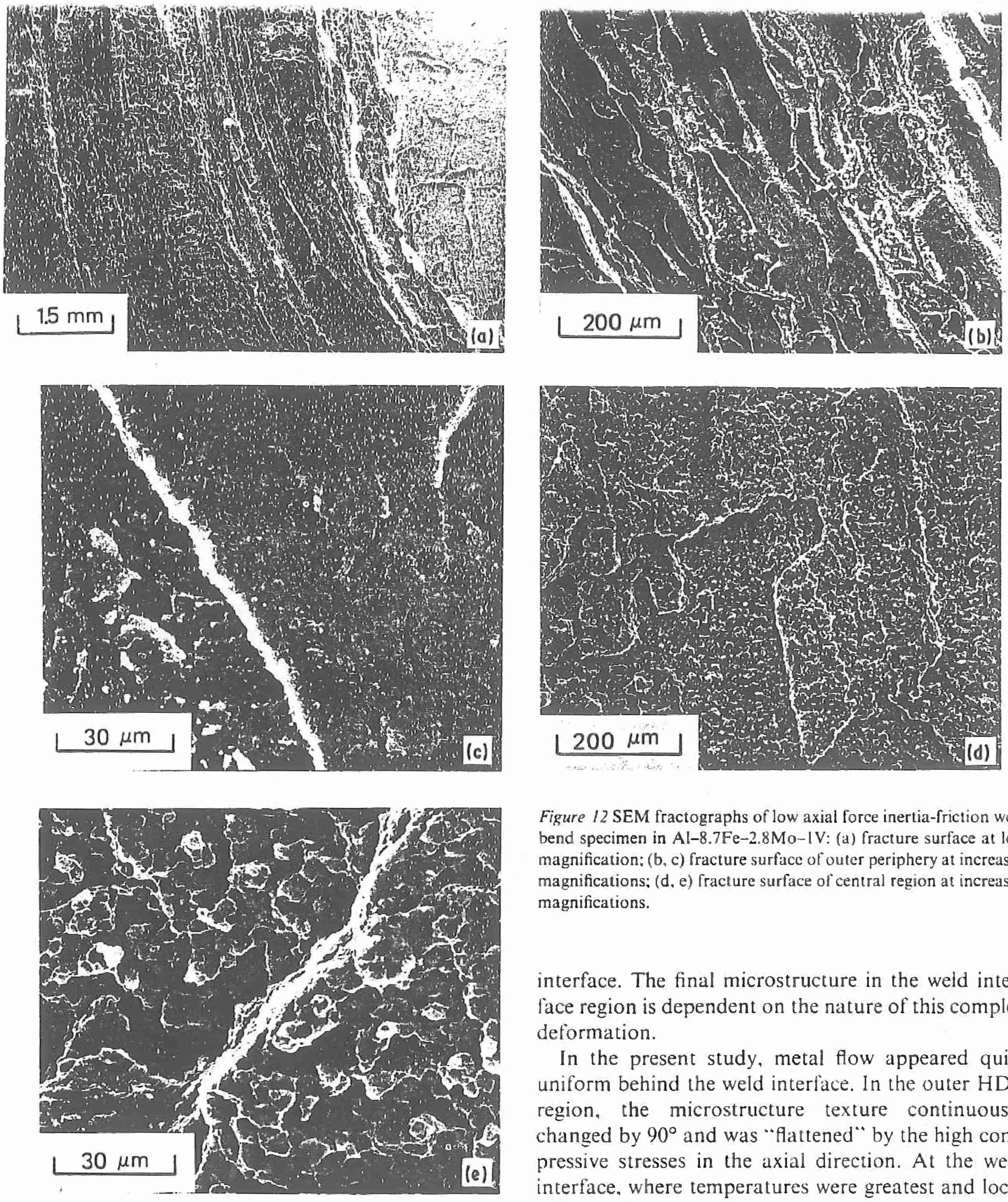

Figure 12 SEM fractographs of low axial force inertia-friction weld bend specimen in Al–8.7Fe–2.8Mo–1V: (a) fracture surface at low magnification; (b, c) fracture surface of outer periphery at increased magnifications; (d, e) fracture surface of central region at increased magnifications.

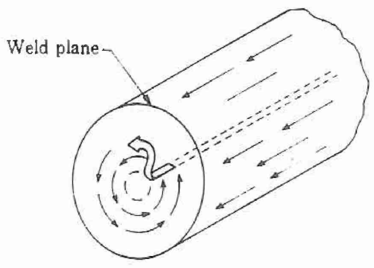

Figure 13 Schematic illustration of metal flow during inertia-friction welding [9].

interface. The final microstructure in the weld interface region is dependent on the nature of this complex deformation.

In the present study, metal flow appeared quite uniform behind the weld interface. In the outer HDZ region, the microstructure texture continuously changed by 90° and was "flattened" by the high compressive stresses in the axial direction. At the weld interface, where temperatures were greatest and local deformation and mechanical mixing most severe, deformation between coarse intermetallics in an extremely soft and plastic alpha aluminium matrix promoted their apparent fracture and dispersion, resulting in the formation of an appreciably finer distribution of cigar-shaped intermetallics. The occurrence of this phenomenon was suggested by the gradual disappearance of the coarse dispersoids in traversing from the unaffected base metal to the central HDZ and the angular appearance of partially fractured dispersoids. This refined dispersoid region was most extensive in the weld produced at low axial force due to the retention of this deformed metal at the weld interface. In the weld produced at high axial force, much of the refined structure was extruded out f the weld interface region as flash, thereby promotng final bonding between metal less affected by the elding process. Indeed, the appearance of the weld nterface microstructure (Fig. 10a) indicates final onding between severely deformed, but still coherent riginal powder particles, with the observed microtructure striations resulting from aforementioned ariations in the density, size and morphology of disersoids within different powder particles present in onsolidated base-metal microstructure.

Dispersoid-lean regions observed principally in the ow-axial force welds originated from localized nonniform deformation in the interface region. At these ocations, high compressive stresses appeared to 'extrude" the soft alpha aluminium and some of the iner dispersoids from the original base-metal microtructure. The occurrence of this nonuniform defornation also explains the origin of adjacent regions vhich exhibit a high density of dispersoids. The near bsence of these structures in welds produced with igh axial force was related to their extrusion from the veld interface during the final forging stage of the velding process. The large alpha grain size observed in hese regions was unexpected because hot working luring the welding process and associated dynamic ecrystallization would be expected to promote an xtremely fine grain size. The nature and density of the lispersoids in this microstructure were apparently nsufficient to pin grain boundaries and prevent grain rowth during weld cooling.

Based on a previous mechanical evaluation of nertia-friction welds in RS/PM Al–Fe–Ce alloys [8], it s expected that the higher hardness associated with the ispersoid-refined central HDZ region and an absence f softening in the outer HDZ would be associated ith a higher tensile strength in this region compared the base metal and a weld joint efficiency of 100%. lthough transverse-weld tensile properties were not etermined to confirm this supposition, the base metal acture of three-point bend tests in high axial force elds was consistent with this expected behaviour. he presence of low-strength, dispersoid-lean regions long the weld interface in low-axial force welds repreent a significant weld characteristic which may pronote tensile fracture along the weld interface at low rength and ductility. Clearly, from the standpoint of ptimizing the weldment structure and mechanical properties, weldments should be produced at sufficiently igh axial forces to minimize or eliminate the presence f the dispersoid-lean regions at the weld interface.

. Conclusions

everal important conclusions were obtained from the resent investigation.

1. The solid-state inertia-friction welding process as effective in producing high-integrity weldments ssentially free of defects.

2. The presence of a refined dispersoid structure in e central heat-and-deformation zone across the weld terface was attributed to the fracture and dispersion of relatively coarse dispersoids present in the original base metal microstructure. This refined dispersoid structure promoted a hardness appreciably greater than that of the unaffected base metal.

3. Nonuniform deformation in the outer weld periphery promoted the formation of dispersoid-rich and dispersoid-lean regions at the weld interface. The dispersoid-lean regions, which were particularly evident in the welds produced with low axial force, exhibited a low hardness and promoted preferential fracture during three-point bend testing along the weld interface. The use of a high axial force minimized microstructural inhomogenieties at the weld interface and promoted fracture during three-point bend testing in the unaffected base-metal region.

Acknowledgements

The authors thank Dr Walter Griffith, AFWAL Materials Laboratory, WPAFB, Ohio, for providing the Al–Fe–V–Mo alloy. They also thank Dr Y. W. Kim, Metcut-Materials Research Group, WPAFB, for helpful comments, Mr Hendrik O. Colijn, OSU Electron Optics Facility, for technical contributions and Dr S. Krishnaswamy for review of this manuscript. Finally, the authors acknowledge support of this work by the Army Research Office, under Contract no. DAAL03-88-0049.

References

1. S. L. LANGENBECK, W. M. GRIFFITH, G. J. HILDEMAN and J. W. SIMON, in "Rapidly-Solidified Powder Aluminum Alloys, ASTM STP 890", edited by E. A. Starke Jr and M. E. Fine (American Society for Testing Materials, Philiadelphia, Pennsylvania, 1986) p. 7.
2. W. A. BAESLACK III and S. KRISHNASWAMY, in "Advances in Welding Science and Technology", edited by S. A. David (ASM International, Metals Park, Ohio 1987) p. 357.
3. S. KRISHNASWAMY and W. A. BAESLACK III, *Mater. Sci. Engng.* **98** (1988) 137.
4. S. KRISHNASWAMY, PhD dissertation, The Ohio State University (1989).
5. W. A. BAESLACK III, K. H. HOU and J. H. DEVLETIAN, *J. Mater. Sci. Lett.* 7 (1988) 944.
6. *Idem, ibid.* 8 (1989) 1716.
7. V. ANANTHANARAYANAN, PhD dissertation, The Ohio State University (1988).
8. W. A. BAESLACK III and K. S. HAGEY, *Weld. J. Res. Suppl.* **67** (1988) 139s.
9. K. K. WANG, "Friction Welding-Welding Research Council Bulletin No. 204", (Welding Research Council, New York, 1975).
10. C. M. ADAM and R. G. BOURDEAU, in "Rapid Solidification Processing, Principles and Technologies II", edited by R. Mehrabian, B. H. Kear and M. Cohen (Claitors, Baton Rouge, 1980) p. 246.
11. S. L. LANGENBECK, R. A. RAINEN, *et al.* in "Elevated Temperature Aluminum Alloy Development", AF-WAL-TR-86-4027 (1986) pp. 6–68.
12. M. RAO and T. H. HAZLETT, *Weld. J. Res. Suppl.* **49** (1970) 181s.

Received 14 February
and accepted 24 August 1989

Appendix 1E

APPENDIX IE

H. H. Koo, K. Sampath and W. A. Baeslack III, "Characterization of Inertia-Friction Welds Between a Rapidly-Solidified Al-Fe-Mo-V Alloy and IM 2024-T351," Journal of Materials Science (in press).

CHARACTERIZATION OF INERTIA-FRICTION WELDS BETWEEN A RAPIDLY-SOLIDIFIED AL-FE-MO-V ALLOY AND IM 2024-T351

H. H. Koo, K. Sampath and W. A. Baeslack III

Department of Welding Engineering
The Ohio State University
Columbus, OH 43210, USA

ABSTRACT

The structures, mechanical properties and fracture behavior of inertia-friction welds produced between rapidly-solidified/ powder metallurgy (RS/PM) Al-9Fe-3Mo-1V (wt%) and ingot metallurgy (IM) 2024-T351 aluminum have been investigated. Visual examination showed the axial displacement experienced by the specimens during welding and the degree of metal expulsion from the weld interface (ie., "flash") to increase with an increase in axial force. The weld flash was observed to originate principally from the IM 2024-T351, which was consistent with the lower elevated-temperature strength of this precipitation-hardened alloy. Although the weld interface region remained nearly flat in welds produced using low axial force, this surface became increasingly curved (concave into the Al-9Fe-3Mo-1V alloy) with an increase in axial force. Microstructure analysis using both light and analytical-electron microscopy characterized the heat-and-deformation affected zones (HDZ's) in each of the base metals and the weld interface regions. The HDZ directly adjacent to the weld interface in the IM 2024-T351 exhibited fine, recrystallized alpha aluminum grains and an

absence of S′ precipitates present in the base metal microstructure. The HDZ directly adjacent to the weld interface in the Al-9Fe-3Mo-1V exhibited fine alpha grains and fine, spherical and acicular dispersoids which in part originated from the plastic deformation and fracture of coarse base metal dispersoid particles. The extent of this dispersoid-refined region was greatest at the center of the weld versus the outer periphery, and in the low versus the high axial force weld. At the weld interface in the vicinity of the axial centerline, the occurrence of highly localized mechanical mixing between the two alloys was determined using both light and electron microscopy and electron-microprobe analysis techniques.

Microhardness traverses showed relatively little variation in hardness across the weld interface and an absence of hardness degradation at any location relative to the unaffected base metals. Room-temperature transverse-weld tensile testing showed tensile strengths to range between 85 and 90% of the RS/PM base metal, with fracture occurring in the Al-9Fe-3Mo-1V HDZ remote from the weld interface. Three-point guided bend testing also revealed fracture to occur in the Al-9Fe-3Mo-1V HDZ. SEM fractographic analysis of the fracture surfaces found fracture in the Al-9Fe-3Mo-1V to involve microvoid formation at dispersoid/alpha aluminum interfaces and subsequent ductile rupture in the alpha aluminum matrix.

1. Introduction

Al-9Fe-3Mo-1V (wt%) belongs to a relatively new family of dispersion-strengthened aluminum alloys produced by rapid solidification and powder metallurgy (RS/PM) processing (Ref. 1). These alloys are based on hypereutectic Al-Fe base compositions with ternary and quaternary additions of Mo, Ce, V and/or Si. RS/PM processing of these novel chemistries generates a microstructure comprised of a uniform distribution of sub-micron sized dispersoid particles in a fine-grained (1 to 2 microns) alpha aluminum matrix. The ternary and quaternary alloy additions are characterized by low solid-solubility and solid-state diffusivity in alpha aluminum. In addition to forming complex, metastable dispersoids, these alloy additions also reduce the interfacial energy or lattice disregistry across the dispersoid particle/alpha aluminum matrix interface and thereby provide a minimal driving force for particle coarsening at elevated-temperatures. The microstructural features exhibited by these alloys provide high room-temperature strength and excellent elevated-temperature mechanical properties. As shown in Fig. 1, the Al-9Fe-3Mo-1V alloy exhibits elevated-temperature strength superior to that of IM-2024-T351 and from a specific strength standpoint compares favorably with Ti-6Al-4V between 150 and 300 °C (Refs. 2-4).

In recent years, several weldability investigations have developed effective joining approaches for RS/PM dispersion-stengthened aluminum alloys. One approach is based on the utilization of high energy density fusion welding methods such as pulsed Nd:YAG laser welding (Ref. 5) and electron beam welding (Ref. 6) to join alloys which contain a low residual hydrogen content (<1 mL/100 g of Al). The rapid cooling rates which characterize these processes have been shown to recreate a rapidly-solidified fusion zone and minimize structural coarsening in the adjacent heat-affected zone. Alternative joining approaches including capacitor-discharge welding (Ref. 7) and solid-state welding methods such as inertia-friction welding (Ref. 8) have also been demonstrated to effectively join RS/PM base materials which contain a high residual hydrogen content (>5 mL/100 g of Al). In contrast to fusion welding, solid-state welding methods avoid melting and re-solidification and thereby preclude the formation of weld defects such as porosity and solidification cracking. Further, these methods also enable optimization of specific process parameters to restrict the heat-and-deformation zone (HDZ) to a relatively narrow region.

A previous investigation evaluated structure/property/fracture relationships in inertia-friction welds produced between cylindrical sections of an RS/PM Al-Fe-Ce alloy with similar (Al-Fe-Ce) and dissimilar (IM-2024) alloy combinations (Ref. 8). That investigation determined that the utilization of a sufficiently high weld axial force produced joints with room-temperature weld mechanical properties comparable to those of the base material. However, the limited spatial resolution of light and scanning-electron microscopy (SEM) utilized in that study precluded detailed microstructural characterization of the weld region. A subsequent investigation used transmission-electron microscopy (TEM) to characterize the weld interface region of similar-alloy inertia-friction welds in an RS/PM Al-9Fe-3Mo-1V (wt%) alloy (Ref. 9). This analysis showed that during welding extensive plastic deformation occurs at the weld interface which fractures the coarse base metal dispersoid particles into fine-sized acicular and spherical particles, thereby improving the dispersoid density and correspondingly the weld zone hardness and strength. The present investigation was performed to complement this earlier study on Al-9Fe-3Mo-1V by characterizing in detail the microstructure across dissimilar alloy inertia-friction welds produced between this RS/PM alloy and the conventional, ingot metallurgy alloy 2024-T351.

2.0 Experimental Methods

2.1. Materials

The RS/PM Al-8.7Fe-2.8Mo-1V (actual chemistry, wt %) alloy originated as rapidly-solidified powder produced by Pratt and Whitney Aircraft's "rapid solidification rate" (RSR) process. In the RSR process, a rapidly-spinning disk produces centrifugal forces and disperses a thin stream of melt into fine-sized, spherically symmetric liquid droplets. The concurrent application of a helium gas shroud produces forced convective cooling conditions ranging from 10^4 to 10^6 °C/s and promotes rapid solidification of the individual liquid droplets. The helium gas also minimizes surface oxide and hydrate formation. Following atomization, the powder particles were hot vacuum degassed and extruded into a 250 mm diameter cylinder.

In the present investigation, the RS/PM Al-9Fe-3Mo-1V alloy was welded in the as-extruded condition while the IM-2024 was welded in the extruded and heat-treated condition (T351 temper). Inertia-friction welding was performed using cylindrical specimens (22.2 mm in diameter and 76.2 mm in length). The longitudinal specimen directions for the RS/PM Al-9Fe-3Mo-1V and IM-2024-T351 alloys were oriented transverse and parallel to the extrusion directions, respectively. The specimen faying surfaces were dry machined immediately prior to welding.

2.2. Inertia-Friction Welding

Inertia-friction welds were produced using an MTI Model 120 inertia-friction welding system. Welding parameters previously established for similar alloy welds in Al-9Fe-3Mo-1V alloy (Ref. 9) were utilized in preliminary trials. Specific welding parameters including the moment of inertia, rotational speed and axial force were optimized through visual examination of the extruded flash and measurement of the axial displacement. Based on the results of these preliminary tests, welds for detailed characterization were produced at low, medium and high levels of axial force (Table 1).

2.3. Weld Characterization

Representative weld coupons were sectioned axially, mounted in epoxy and mechanically polished down to 0.3 micron alumina followed by a final polish using an 0.06 micron colloidal silica suspension. Following defect analysis of the as-polished surface using light microscopy, the metallographic specimens were etched with Keller's reagent and examined using both light microscopy and scanning-electron microscopy (SEM).

The weld interface region of welds produced with low and high axial force were examined in detail using a JEOL-200CX transmission-electron microscope (TEM) operated at 200 kV and equipped with a Tractor-Northern TN-2000 energy-dispersive X-ray spectrometer (EDS). Thin foils for TEM analysis were produced from 0.3 mm thick slices carefully sectioned along the weld longitudinal axis using a diamond saw and thinned to a thickness of 0.1 mm by grinding with 600 grit SiC paper. Three millimeter diameter disks were subsequently punched from the unaffected base metal and weld interface regions at the center and outer periphery of each weld and twin-jet electropolished in a solution of one-part nitric acid in three-parts methanol at -30 °C. The thin foils were removed just prior to perforation and ion-beam milled to increase the size of the electron-transparent region. TEM examination involved imaging under bright-field (BF) and dark-field (DF) conditions and energy-dispersive X-ray (EDS) analysis at selected locations.

Quantitative compositional analysis across the weld interface was also obtained using a Camica SX50 electron probe micro-analysis (EPMA) system. Compositional analysis was performed utilizing a 1 micron diameter probe size in order to minimize the effect of reaction volume on the quantitative data.

Knoop micro-hardness (KHN) traverses were performed across the weld interface at both the weld axial center and outer periphery using a 200 g load, with the longitudinal axis of the indenter oriented parallel to the weld interface. Tensile tests were performed on cylindrical, transverse-weld-oriented specimens (6.35 mm gauge diameter and 25.4 mm gauge length) machined from the half-radius of the welded coupons and tested as per ASTM E-8-89a at an extension rate of 4.2 x 10^{-3} mm/s. Additionally, three-point guided-bend testing were performed to identify preferential failure locations. Testing was performed on longitudinal sections (weld flash removed) with the flat surface (weld center) placed in tension. Finally, SEM fractographic analysis was performed on the three-point bend test specimens.

3. Results

3.1. Microstructure of Al-9Fe-3Mo-1V and IM-2024-T351 Base Materials

Light microscopy analysis of the Al-9Fe-3Mo-1V base metal showed both dark and light-etching regions (Fig. 2a). Examination at higher magnification (Fig. 2b) revealed that the observed differences in contrast resulted from variations in the size and distribution of the dispersoid particles. Boundaries between the individual powder particles (arrows in Fig. 2b) were clearly delineated, suggesting limited particulate deformation during extrusion.

TEM examination revealed three different base metal dispersoid morphologies (Figs. 3a and b), ie., coarse, spherical dispersoids ranging from 500 to 1,000 nm in diameter, fine, acicular dispersoids ranging from 200 to 1000 nm in length and small, spherical dispersoids ranging from 100 to 250 nm in diameter. Previous electron microscopy and X-ray diffraction analysis of this Al-Fe-Mo-V alloy (Ref. 10) indicated the coarse spherical dispersoids to be enriched in Al, Mo and V and likely to be $Al_{12}Fe_3(Mo,V)$. The small spherical dispersoids, which were enriched in both Mo and V, were likely Al_6Fe type while the acicular particles were Al_3Fe type. EDS analysis performed on the dispersoids in this study corroborated results of this previous work. TEM examination at higher magnification of selected regions containing fine dispersoid particles (regions of dark contrast in Fig. 2a) showed a near absence of acicular particles (Figs. 3c and d). These regions likely originated from fine powder particles which underwent rapid solidification to extremely fine dendritic alpha aluminum.

Light microscopy of the IM 2024-T351 alloy showed elongated alpha aluminum grains decorated by dark-etching grain boundary dispersoids (Fig. 4a). In addition, several fine, dark-etching particles were observed within the alpha aluminum grains. Examination of the grain boundary particles at higher magnification (Fig. 4b) revealed agglomerations of different types of dispersoids. Consistent with the T351 temper, TEM bright-field imaging (Figs. 4c and d) showed subgrains within the elongated alpha aluminum grains and two types of intergranular particles. Based on the morphology of these particles and EDS analysis, the small lath-type precipitates and the large, columnar-shaped particles were identified as precursor S' particles (Al_2CuMg) and $Al_{20}Cu_2Mn_3$, respectively. Despite extreme care, the coarse, agglomerated dispersoids observed at the alpha aluminum grain boundaries (Fig. 4b) underwent preferential attack during electropolishing and consequently were not characterized using TEM/EDS in the present study.

3.2. Weld Macroscopic Examination

Visual examination of the welds showed an increase in the axial force to promote an increase in the axial displacement of the two workpieces (Table 1), and correspondingly an increase in the volume of flash extruded from the weld interface. This analysis also revealed the extrusion of flash to be minimal from the Al-9Fe-3Mo-1V but appreciable from the IM-2024-T351, an observation consistent with the relatively lower elevated-temperature strength of the precipitation-hardened IM alloy. Macroscopic examination of the weld axial cross-sections showed that increased weld axial force promoted a progressive transition in the shape of the weld interface (Figs. 5a-c). While the low axial force weld exhibited a nearly flat interface (Fig. 5a), the medium and high axial force welds exhibited increasingly curved interfaces concave into the Al-9Fe-3Mo-1V (Figs. 5b and 5c). Heavy etching of the welds revealed the presence of HDZ's on both sides of the weld interface, with the extent and width of this region greatest in the IM-2024-T351. The HDZ on either side of the weld interface exhibited a parallel shape at low axial force which transitioned into an increasingly hour-glass shape at higher axial force, particularly in the IM-2024-T351. As shown in Fig. 5c, the HDZ width was minimal at the axial centerline of the weld produced at the highest axial force.

3.3. Weld Microstructure Characterization

3.3.1. Light microscopy analysis

Light microscopy examination at increased magnification more clearly delineated microstructure transitions in each alloy from the unaffected base metal to the weld interface (Figs. 6 and 7). In the Al-9Fe-3Mo-1V, which did not exhibit a strong base metal texture, the microstructure gradually became "flattened" in a direction parallel to the weld interface. In the welds produced using low axial force (Figs. 6a and b), the width of this deformed region was greatest at the weld center versus the outer periphery. Near the weld interface, local deformation was sufficiently extensive that the heterogenous base metal microstructure appeared nearly homogenous, particularly at the center of the weld produced using a low axial force. The application of a higher axial force promoted an increase in the width of the structurally "flattened" region, but the presence of a narrower homogenized region, particularly at the axial centerline.

Microstructural variations in the IM 2024-T351 HDZ's were much more apparent. Remote from the weld interface, the base metal alpha grains gradually changed orientation and became parallel to the weld interface, with the region over which this transition occurred (ie., the width of the HDZ) being greater at the outer periphery versus the axial centerline. Nearer to the weld interface, extensive deformation promoted microstructural homogenization of the grain structure, as in the Al-9Fe-3Mo-1V. The widths of these homogenized HDZ regions appeared similar for all welds and weld locations. As shown in Fig. 7B, the outer periphery of the high-axial force weld also showed the presence of occasional cracks or voids oriented parallel to the interface.

Light microscopy at higher magnification of both the high and low axial force welds (Fig. 8) revealed that although appearing homogenous at lower magnification, the HDZ directly adjacent to the weld interface still retained structural variations residual from the original base metal (and RS powder) microstructures. Figure 8 also shows varying degrees of mechanical mixing at the interface between the dissimilar aluminum alloys. The central region of the weld produced at low axial force (Fig. 8a) showed the most significant extent of this mixing, with fine, narrow "fingers" of IM-2024-T351 extending into the Al-9Fe-3Mo-1V. The extent of this mixing (as delineated by light microscopy) was much less near the outer periphery of the weld produced using low axial force, and also less across the entire interface of the weld produced using high axial force. Figure 8 also shows stringers of intermetallic particles oriented along the deformation direction in the IM-2024-T351. These intermetallics likely originated as clusters of grain boundary dispersoids present along grain boundaries in the base metal (Fig. 4b) which were deformed and aligned during the severe plastic deformation of this weld region.

As indicated above, dark-etching discontinuities were occasionally observed in the IM 2024-T351 near the outer periphery of the weld produced using a high axial force (Fig. 7b). The occurrence of similar linear discontinuities in IM-2024-T351 had been previously reported in dissimilar inertia-friction welds with Al-8Fe-4Ce (Ref. 8). Light microscopy examination of the as-polished surface of axial cross-sections through the welds revealed that the linear discontinuities observed in IM-2024-T351 were pre-existing microcracks (Fig. 9a). Examination after etching with Keller's reagent showed the microcracks to be associated with grain boundary dispersoid (intermetallic) particles (Fig. 9b). They apparently originated from the limited ductility of the intermetallic particles in combination with the severe plastic deformation observed at these locations. An alternative mechanism for their origin may be highly localized eutectic melting along grain boundaries, although this could not be confirmed.

3.3.2. TEM analysis

Figure 10 shows a TEM bright-field traverse across the weld interface at the center of the low axial force weld. Traversing from the Al-9Fe-3Mo-1V side toward the weld interface (left to right in the top traverse in Fig. 10), adjacent regions showed dark and light contrast depending on the local dispersoid size and density. Regions containing a higher density of coarse dispersoids typically exhibited a darker contrast while regions containing finer dispersoids exhibited a lighter contrast. Examination of the region nearest to the weld interface showed an increase in the number of fine dispersoids and an absence of the coarse, spherical dispersoids. This observation was consistent with previous work (Ref. 9) on the similar alloy inertia-friction welding of Al-9Fe-3Mo-1V which showed an absence of the coarse dispersoids near the weld interface due to their fracture and dispersion. Bright and dark-field imaging of Al-9Fe-3Mo-1V directly adjacent to the weld interface showed an extremely fine-grained recrystallized alpha aluminum matrix. In the vicinity of the weld interface, alternating bands of Al-9Fe-3Mo-1V and IM 2024-T351 (small arrows) were observed, indicating highly localized mechanical mixing between the two base alloys. The Al-9Fe-3Mo-1V bands in this region were devoid of the coarse, spherical dispersoids, again indicating their fracture and dispersion. This structure gradually transitioned (extreme right of bottom traverse in Fig. 10) to an entirely IM-2024-T351 microstructure which exhibited fine, equiaxed alpha aluminum grains, indicating the occurrence of dynamic recrystallization during the welding cycle. In this region, the columnar $Al_{20}Cu_2Mn_3$ particles which were uniformly aligned in the unaffected base metal grains (Fig. 4c) became more randomly oriented, and the fine S′ was not in evidence due to its dissolution during the weld thermal excursion. Outside of the recrystallized zone (RXZ) in the IM-2024-T351, a gradual microstructural transition from the fine grain structure to an irregular, coarse grain structure (similar to that of the base metal shown in Fig. 4d) was observed.

In comparison with Fig. 10, the TEM bright-field traverse across the interface of the low axial force weld at the outer periphery (Fig. 11) showed two significant differences. Although a random distribution of fine and coarse dispersoids was evident near the weld interface in the Al-9Fe-3Mo-1V (large arrow in Fig. 11), the number of coarse dispersoids was greater and correspondingly the density of fine dispersoids was less as compared to the weld center, indicating a lesser extent of dispersoid breakup. A difference in the extent and nature of interface deformation at the outer periphery versus the weld center was further indicated by the minimal evidence of mechanical mixing between the IM 2024-T351 and the Al-9Fe-3Mo-1V, and the presence of a clearly defined weld interface (large arrow in Fig. 11).

Figure 12 shows a TEM bright-field traverse across the weld interface at the center of the high axial force weld. The Al-9Fe-3Mo-1V side of this interface showed a mixture of coarse and fine dispersoids, with an absence and possible breakup of the coarse dispersoids only directly adjacent to the interface (within 5 microns of the interface). The absence of a wider dispersoid-refined region adjacent to the weld interface, as observed in the weld produced using low axial force, was consistent with light micrographs showing a very narrow HDZ at the center of the high axial force weld. TEM examination with minimum beam tilt also revealed extremely fine, recrystallized alpha aluminum grains in both the Al-9Fe-3Mo-1V and the IM 2024-T351 (extreme right of Fig. 12) adjacent to the weld interface. Despite experiencing higher axial force, mechanical mixing between the IM-2024-T351 and Al-9Fe-3Mo-1V was minimal as compared to that observed at the center of the low axial force weld.

TEM examination of the weld interface region at the outer perphery of the high axial force weld was not possible due to the presence of interface discontinuities which precluded the preparation of high quality thin foils.

3.3.3 EPMA analysis across weld interfaces

Figures 13 and 14 show composition profiles obtained by EPMA across the weld interface near the weld center and outer periphery for low and high axial force welds, respectively. At the center of the weld produced using low axial force (Fig. 13a and c), localized mechanical mixing of the two alloys promoted variations in composition across the weld interface. A more definitive interface at the outer periphery of this weld showed a correspondingly more abrupt compositional change in Figs. 13b and d. Note that the size of the volume actually sampled during the analysis, and "averaging" effects of the alpha matrix and the intermetallic phases, made the investigation of compositional gradients in the alpha phase due to interdiffusion (eg., Cu into the Al-9Fe-3Mo-1V) difficult. Considering the extremely rapid thermal cycle experienced during welding, it is unlikely that such interdiffusion in the alpha matrix was significant.

At the center of the weld produced using a high axial force, mechanical mixing between the base alloys was evidenced both in the SEM micrograph of the weld interface by a gradual change in the dispersoid density (Fig. 14a), and by the compositional variations across the interface (Fig. 14c) This mixing occurred in a uniform and more gradual manner than observed at the center of the weld produced using low axial force. As in the weld produced at low axial force, the transition in the outer periphery was much more abrupt due to negligible mechanical mixing (Figs. 14b and d).

3.4. Weld mechanical properties

Hardness evaluation of the base metals showed an average hardness of KHN 160 (200 g load) for IM-2024-T351 and KHN 131 for Al-9Fe-3Mo-1V. Consistent with the microstructural analysis and differences in dispersoid sizes and density, the coarse-dispersoid regions in the Al-9Fe-3Mo-1V (Fig. 2b) exhibited a relatively lower hardness compared to the fine-dispersoid regions.

Figures 6c and 7c show microhardness traverses across the center and outer periphery of welds produced using both low and high axial force, respectively. In all traverses performed, the hardness in the IM-2024-T351 and across the weld zone exceeded the lowest hardness levels recorded in the unaffected Al-9Fe-3Mo-

1V (about 125 KHN), suggesting weld joint efficiencies of 100%. In the weld produced with low axial force, variations in hardness of the IM and RS/PM base metals due to microstructural variations decreased nearer to the weld interface due to microstructural homogenization. It is of interest to note that in the weld produced at low axial force the hardness across the IM-2024-T351 HDZ was generally greater at the outer periphery than at the axial center, while the reverse was observed for the weld produced using a high axial force. Considering similarities in the IM-2024-T351 HDZ microstructures for these welds, the reason for this difference was not clear.

Room-temperature tensile testing of transverse-weld oriented tensile specimens determined that failures occurred preferentially in the Al-9Fe-3Mo-1V (Table 1). Although the tensile test specimens showed marginal ductility (2-4 percent elongation), the tensile strength of the three types of welds varied from between 323 to 346 MPa, indicating joint efficiencies ranging from about 85 to over 90% relative to the lower room-temperature strength Al-9Fe-3Mo-1V base alloy (tensile strength of approximately 380 MPa).

Three-point guided bend testing of axial sections through the welds was performed to determine the fracture path through the entire weld (assuming axisymmetry) since the tensile specimens only characterized fracture at a location approximately midway between the axial centerline and the outer periphery. Analysis of failed bend specimens revealed preferential fracture initiation and propagation through the Al-9Fe-3Mo-1V HDZ, with negligible evidence of macroscopic plastic deformation. It is of interest to note that despite the presence of micro-cracks in the IM-2024-T351 at the outer periphery of the the high axial force weld, failure initiated in softer Al-9Fe-3Mo-1V.

3.5. Fracture Characteristics

As indicated above, metallographic analysis indicated fracture of the dissimilar welds to occur through the lower strength Al-9Fe-3Mo-1V alloy. Fractographic characteristics of bend specimens produced from welds generated using low and high axial forces generally appeared quite comparable. Figure 15 shows the characteristics of a typical fracture surface for a bend test specimen produced from a high axial force weld. At low magnification, the fracture surface exhibited a relatively flat topography and a unidirectional texture across the fracture face. This texture may be related to the extrusion direction of the base metal, which was perpendicular to the longitudinal specimen length and therefore parallel to the weld interface. This observation suggests a fracture path outside of the central HDZ region. If fracture had occurred near the center of the HDZ, a macroscopic fracture surface exhibiting an outward spiral typical of inertia-friction welds should have been observed. The analysis of this surface at increased magnification clearly showed fracture initiation by microvoid formation at dispersoid/alpha aluminum interfaces and final ductile rupture of alpha aluminum matrix (Figs. 15b and c).

4.0. Discussion

The inertia-friction welding process is very amenable to the joining of similar and dissimilar alloys which cannot be welded using fusion processes. During dissimilar alloy inertia-friction welding, one alloy generally maintains a higher yield strength throughout the entire range of temperatures experienced at or near the weld interface. In contrast, the present study involved a unique case in which a strength "reversal" occurred as the temperature increased from room temperature, where the IM-2024-T351 alloy was the strongest, to elevated temperatures where the RS/PM Al-9Fe-3Mo-1V alloy was the strongest (Fig. 1).

The cylindrical specimens joined using the inertia-friction welding process experienced complex combinations of axial and torsional forces and stresses across the weld interface. In conventional inertia-friction welds between the same material, the plastic flow of metal heated by frictional heating occurs from the axial centerline of the weld out toward the outer periphery in a spiral pattern. In the present work, such metal flow and deformation was observed to be relatively uniform in the HDZ remote from the weld interface, particularly within the microstructurally "flattened" regions observed in both alloys. In the vicinity of the interface, however, nonuniform deformation both within the HDZ of each respective alloy and highly localized mechanical mixing directly at the interface between the dissimilar alloys was very complex. In the present work, the nature and extent of this mechanical mixing was highly dependent on both the axial force and the location within the weld.

In the dissimilar Al-9Fe-3Mo-1V/IM 2024-T351 inertia-friction welds differences in the strength of the two alloys between room and elevated temperatures appeared to influence both the macroscopic and microscopic characteristics of the weld. In considering the origins of the observed macrostructures and microstructures, it is important to understand the influence the welding process on the local temperature and pressure distribution across the interface. During inertia-friction welding, a larger quantity of frictional heat is generated near the outer periphery than at the center (arising from differences in the relative velocity of the specimens at these two locations). Therefore, a higher peak temperature occurs at the outer periphery versus the specimen center. In contrast, normal compressive stresses at the outer periphery of the weld may be lower than at the axial centerline due to a "friction hill effect," as in plane strain forging. The combination of these velocity and pressure differences can actually promote peak temperatures at a location near but not directly at the outer periphery of the weld interface.

Macroscopically, the IM 2024-T351 "penetrated" into the Al-9Fe-3Mo-1V thereby promoting a concave interface particularly at the high axial force level, despite the appreciably greater expulsion of the IM 2024-T351 as flash. Considering the aformentioned differences in heating across the weld interface, it is suggested that the relatively low peak temperatures experienced just behind the weld interface at the axial centerline of the high axial force weld promoted minimal softening of the IM 2024-T351, and that the compressive strength of this region remained above that of the adjacent Al-9Fe-3Mo-1V into which it macroscopically penetrated. The presence of a steep temperature gradient and narrow high-temperature region at this location was consistent with the hourglass shape of the high axial force weld. Toward the outer periphery of the weld, higher temperatures generated at the interface promoted the strength reversal shown in Fig. 1 and rapid softening of the IM 2024-T351. The rapid softening of the IM 2024-T351 relative to the stronger Al-9Fe-3Mo-1V resulted in appreciable deformation and in a large quantity of flash being extruded from the IM 2024-T351, as observed in Fig. 5.

Variations in temperature and pressure across the weld interface also explain the origin of microstructural characteristics along the interface. Light and TEM microscopy analysis revealed significant mechanical of the two alloys at the interface near the axial centerline, particularly in the low axial force weld. Rao et al. (Ref. 11) reported that mechanical mixing during friction welding originates from the interlocking of initial asperity peaks at the specimen faying surfaces and subsequent formation of "wedges" and smearing of wedges. This action occurs on an extremely fine scale may account for some of the mixing observed with TEM. The more macroscopic mechanical mixing observed both with light microscopy and TEM at the center of the low axial force weld may further be related to differences in the tensile strengths of the alloys at high temperatures, and the influence of these strength differences on the nonuniform deformation experienced at this interface.

Considering the aforementioned difference in welding pressure across the interface, the decrease in mechanical mixing near the outer periphery was anticipated. However, the greater extent of mixing observed in the low versus the high axial force weld was not easily explained. This difference in mixing may be attributed to differences in the uniformity of deformation at this location and/or the duration of the welding cycle.

In general, the extent of coarse dispersoid fracture and dispersion in the Al-9Fe-3Mo-1V was appreciably less than that observed previously for similar alloy welds produced at comparable axial force levels (Ref. 9). In addition, the RS/PM alloy HDZ showed no evidence of dispersoid-free regions which formed near the outer periphery of similar alloy welds due to extremely nonuniform deformation at and near the weld interface. Both of these phenomena are related to the complex stresses experienced at the weld interface and the manner in which the material responds to these stresses via deformation. It is proposed that the appreciably softer IM 2024-T351 accomodated more deformation and thereby promoted less extensive, and perhaps more uniform deformation in the higher strength Al-9FE-3Mo-1V, thereby precluding the occurrence of these phenomena.

Although the parametric analysis performed in this study was very limited, weld tensile property analysis indicated very high weld joint efficiencies exceeding 90% for the optimum welding conditions. A rational for the inability to achieve 100% joint efficiencies despite an absence of hardness degradation across the weld zone was not apparent. The observation of fracture in the weld HDZ away from the weld interface indeed suggests that a highly localized softened region may have existed which was not revealed by hardness testing or microscopy. Acceptible hardness levels across the weld zone were promoted by an effective absence of visible dispersoid coarsening in the RS/PM alloy and the dynamic recrystallization of the alpha grains near the interface in both alloys. This recrystallization and the generation of an extremely fine alpha grain size was most important within the IM-2024-T351 HDZ in which the strengthening S′ precipitates had been resolutionized during the rapid weld heating and cooling cycle. Although not performed in this study, the low-temperature aging of the weld may further strengthen the IM 2024-T351 HDZ due to the reprecipitation of this phase.

5.0. Conclusions

1. High integrity weld joints were produced between RS/PM Al-9Fe-3Mo-1V and IM 2024-T351 using the solid-state inertia-friction welding process.
2. Differences in the strength of the Al-9Fe-3Mo-1V and IM-2024-T351 alloys at room versus elevated-temperatures promoted a curved weld interface concave into the Al-9Fe-3Mo-1V and the formation of weld flash principally from the

IM 2024-T351.

3. Weld axial force significantly influenced the appearance of the weld interface, characteristics of the weld HDZ, joint integrity and the occurrence of weld defects.

4. The weld interface was characterized by highly-localized mechanical mixing of the dissimilar aluminum alloys, with the extent of this mixing most significant near axial centerline of the weld produced using low axial force. The weld interface was bounded by heat-and-deformation-affected zones (HDZ's) comprised of extremely fine alpha aluminum grains (1-2 microns) and fine dispersoid particles.

5. Knoop hardness testing revealed an absence of hardness degradation across the weld interface. Transverse-weld riented tensile testing determined joint efficiencies of 85 to 90%, and fracture in the Al-9Fe-3Mo-1V HDZ. This location also served as the preferential fracture path for three-point guided bend test specimens.

Acknowledgements

The authors are indebted to Dr. Walter Griffith of the Wright Laboratories at WPAFB, OH for providing the Al-9Fe-3Mo-1V alloy. Appreciation is also expressed to Messrs. M. Shalosky, P. Griffin, E.Barnhouse, T. Smith, J. Davis and J. Banal for their assistance in inertia-friction welding and Mr. Hendrick Colijn and Mr. David Little of OSU for assistance in EDS and EPMA analysis respectively. The investigation was performed with financial support from the Army Research Office under contract No. DAAL03-88-K-0049.

References

1. W. E. QUIST and R. E. LEWIS, in "Rapidly Solidified Powder Aluminum Alloys, STP 890", edited by E. A. STARKE Jr. and M. E. FINE (American Society for Testing and Materials, Philadelphia, PA, 1986) p. 7.
2. C. M. ADAM and R. G. BOURDEAU in " Rapid Solidification Processing: Principles and Technologies", edited by R. MEHRABIAN, B. H. GEAR and M. COHEN (Claitors Publishing, Baton Rouge, LA, 1980) p. 246.
3. E. P. CONE and P. M. KOMATER in " Exploratory Development of Processing Elevated Temperature Powder Metallurgy Alloys", (AFWAL-FR-18804-7, 1988) p. 6.
4. Metals Handbook, 9th Ed. vol. 2, (American Society for Metals, Materials Park, OH, 1983) p. 75.
5. S. KRISHNASWAMY and W. A. BAESLACK III, in "Recent Trends in Welding Science and Technology," edited by S. A. David, J. M. Vitek, J. M. (ASM International, Materials Park, OH, 1990) p. 631.
6. W. A. BAESLACK III and S. KRISHNASWAMY in "Advances in Welding Science and Technology," edited by S. A. DAVID, (ASM International, Materials Park, OH, 1987) p. 357.
7. W. A. BAESLACK III, K. H. HOU and J. H. DEVELETIAN, J. Mater. Sci. Lett. 7 (1988) 944.
8. W. A. BAESLACK III and K. S. HAGEY, Weld. J. Res. Suppl. 67 (1988) 139s.

9. K. H. HOU and W. A. BAESLACK III, J. Mat. Sci. 25 (1990) 2642.

10. S. L. LANGENBECK and R. A. RAINEN in "Elevated Temperature Aluminum Alloy Development," (AFWAL-TR-86-4027, 1986) p. 6.

11. M. RAO and T. HAZLETT, Weld. J. Res. Suppl. 49 (1970) 181s.

Table 1. Inertia-Friction Welding Parameters(a) and Results of Weld-tensile and Three-point Guided Bend Tests

Inertia-Friction Welding			Tensile Test			Bend Test
Spec. Type	Axial force (KN)	Axial disp. (mm)	YS (MPa)	UTS (MPa)	El. (%)	Fracture Site(b) (mm from IF)
LAF-1	97.8	2.78	278.0	335.8	3.7	0.25
LAF-2	97.8	2.78				
MAF-1	126.6	6.35	266.7	323.5	4.2	0.2
MAF-2	126.6	5.56				
HAF-1	153.6	11.91	294.5	345.5	2.4	0.2
HAF-2	153.6	9.92				

a. Moment of Inertia = 0.16588 Kg-m^2
Angular Speed = 366.5 rad/s
Inertial Energy = 11.134 KJ

b. All bend and tensile test failures occurred in Al-9Fe-3Mo-1V. The numbers in the column denote distance from the fracture initiation site to the weld interface for guided bend test specimens.

LIST OF FIGURES

Figure 9	Light micrographs of weld defects in IM-2024-T351 at the outer periphery of high axial force weld: (a) unetched; (b) after etching with Keller's reagent. Large arrows indicate weld interface.
Figure 10	TEM bright-field traverse across weld interface region at the center of low axial force weld. Lower traverse is continuation of right side of top traverse. Left side of top traverse is Al-9Fe-3Mo-1V and right side of bottom traverse is IM-2024-T351. Large arrow indicates location of the interface between mechanically-mixed region and IM-2024-T351. Small arrows indicate regions of IM-2024-T351 in mechanically-mixed region.
Figure 11	TEM bright-field traverse across interface near the outer periphery of the low axial force weld. Large arrow indicates location of weld interface between Al-9Fe-3Mo-1V (left) and IM-2024-T351 (right).
Figure 12	TEM bright-field traverse across interface at the weld center of the high axial force weld. Large arrow indicates location of weld interface between Al-9Fe-3Mo-1V (left) and IM-2024-T351 (right).
Figure 13	EPMA traverses across low axial force weld produced between Al-9Fe-3Mo-1V (right) and IM-2024-T351 (left). Straight lines in (a) and (b) are Cu K-alpha trace scans while (c) and (d) are results of point analysis.
Figure 14	EPMA traverses across high axial force weld produced between Al-9Fe-3Mo-1V (right) and IM-2024-T351 (left). Straight lines in (a) and (b) are Cu K-alpha trace scans while (c) and (d) are results of point analysis.
Figure 15	SEM fractographs of high axial force weld bend test specimen: (a) general view at low magnification; (b) and (c) fracture surface near specimen center at increased magnification.

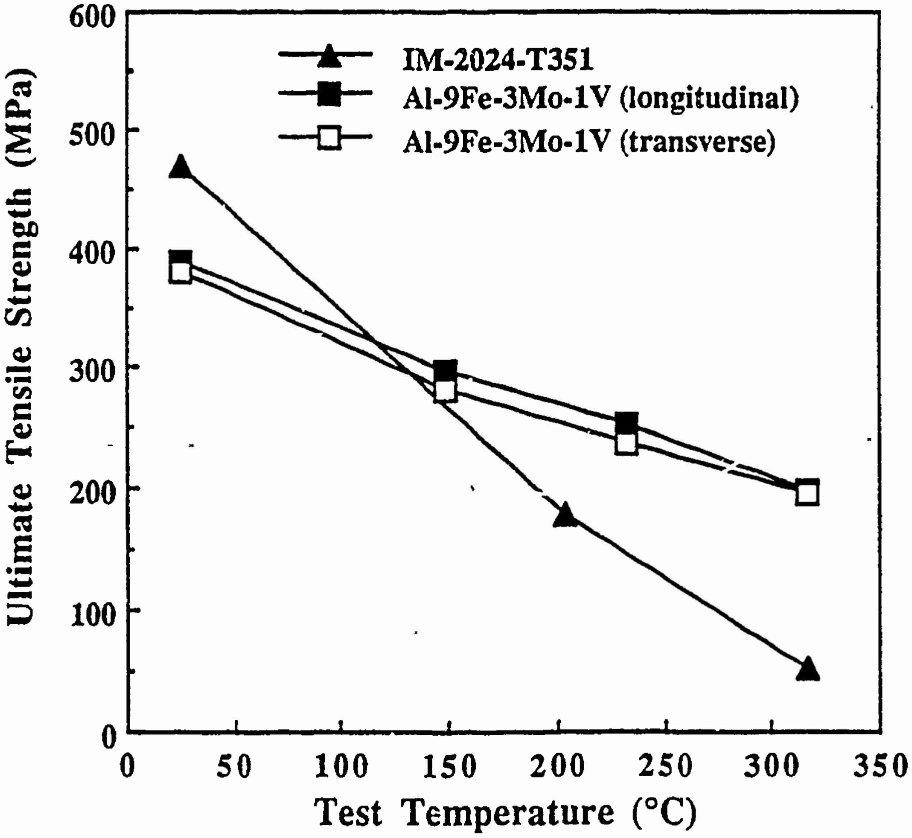

Figure 1 Tensile strength versus test temperature for RS/PM Al-9Fe-3Mo-1V and IM-2024-T351 (Refs. 3 and 4).

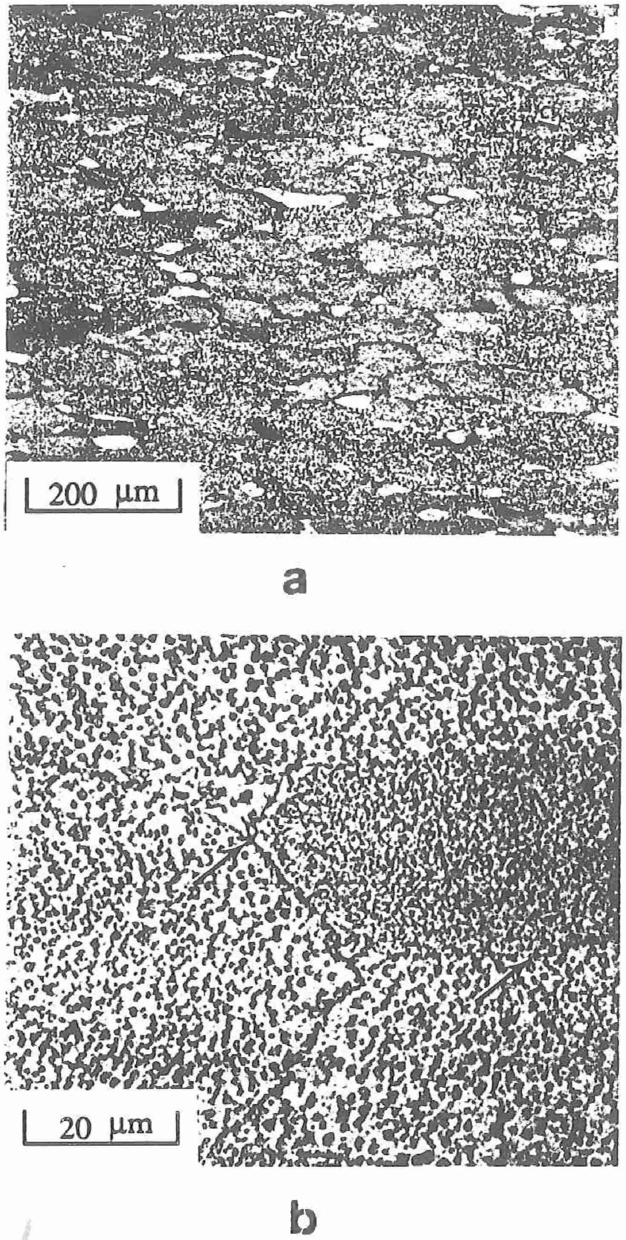

Figure 2 Light micrographs of Al-9Fe-3Mo-1V base metal. Arrows in (b) indicate boundary between powder particles.

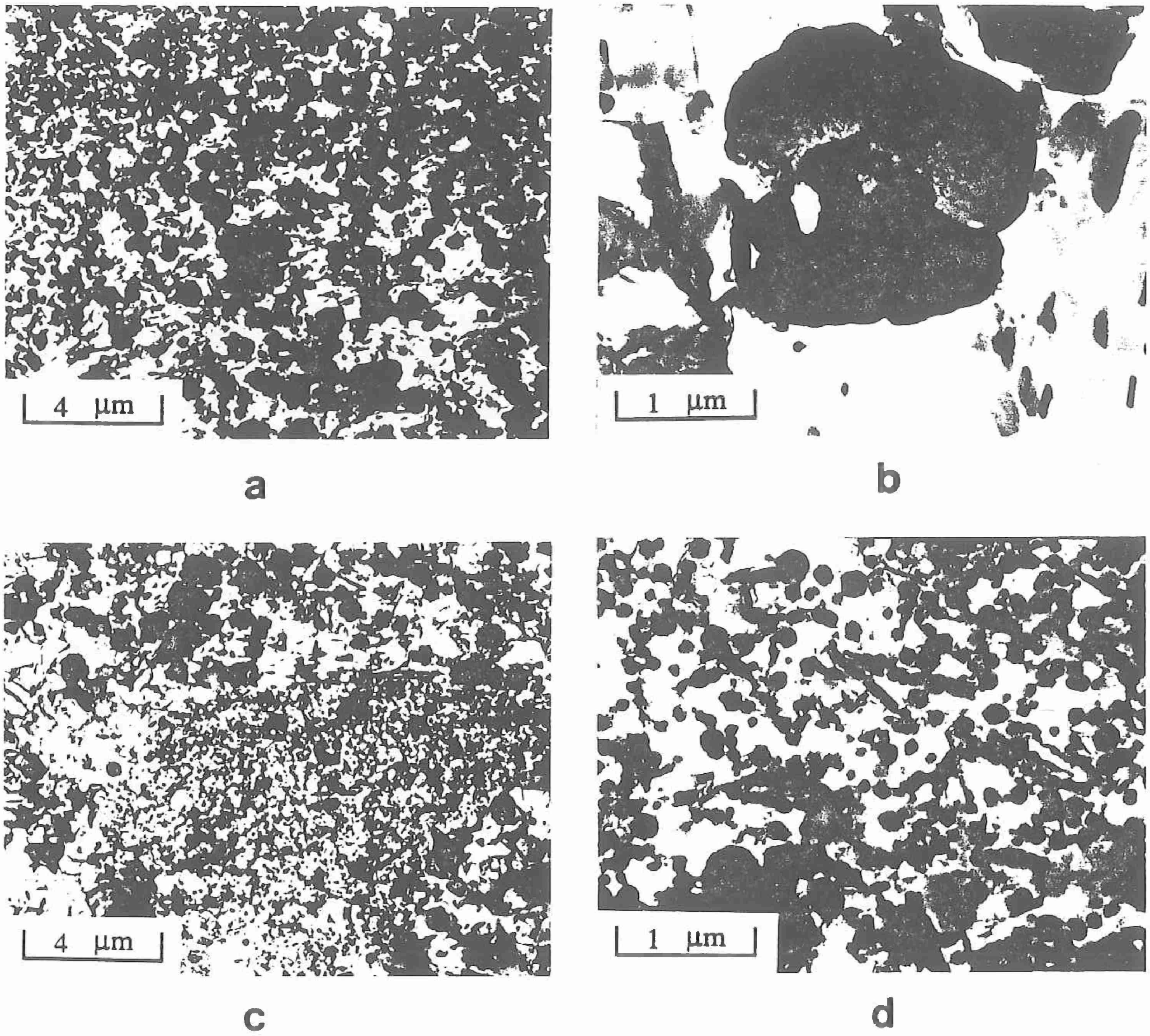

Figure 3 TEM bright-field micrographs of Al-9Fe-3Mo-1V base metal: (a, b) predominant microstructure; (c, d) regions containing fine dispersoids.

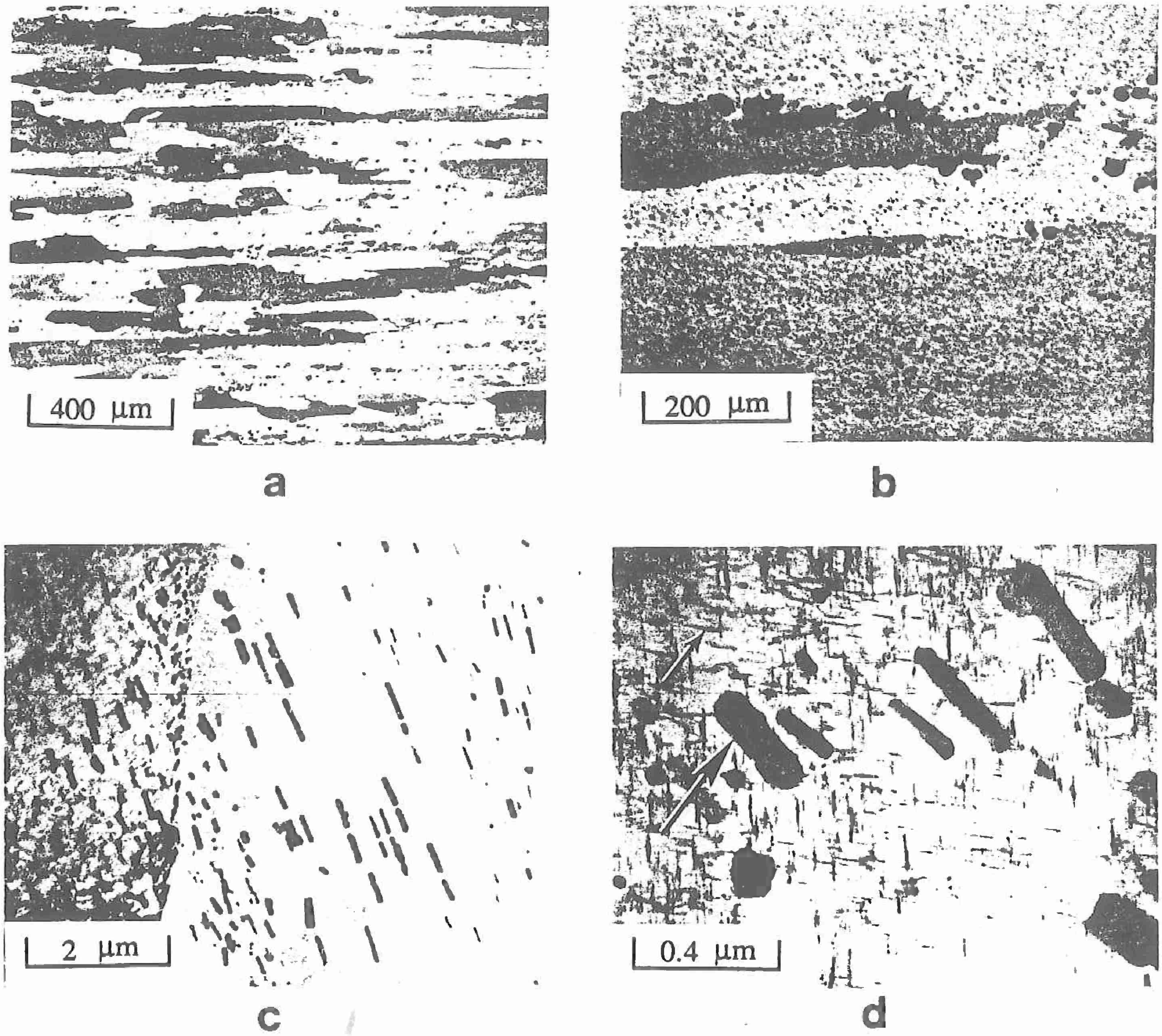

Figure 4 Light (a, b) and TEM bright-field (c, d) micrographs of IM-2024-T351 base metal: (a) elongated alpha grain structure; (b) higher magnification showing grain boundary particles; (c) subgrain boundary and columnar $Al_{20}Cu_2Mn_3$ particles; (d) fine S'precipitates (small arrow) and large columnar $Al_{20}Cu_2Mn_3$ particles (large arrow).

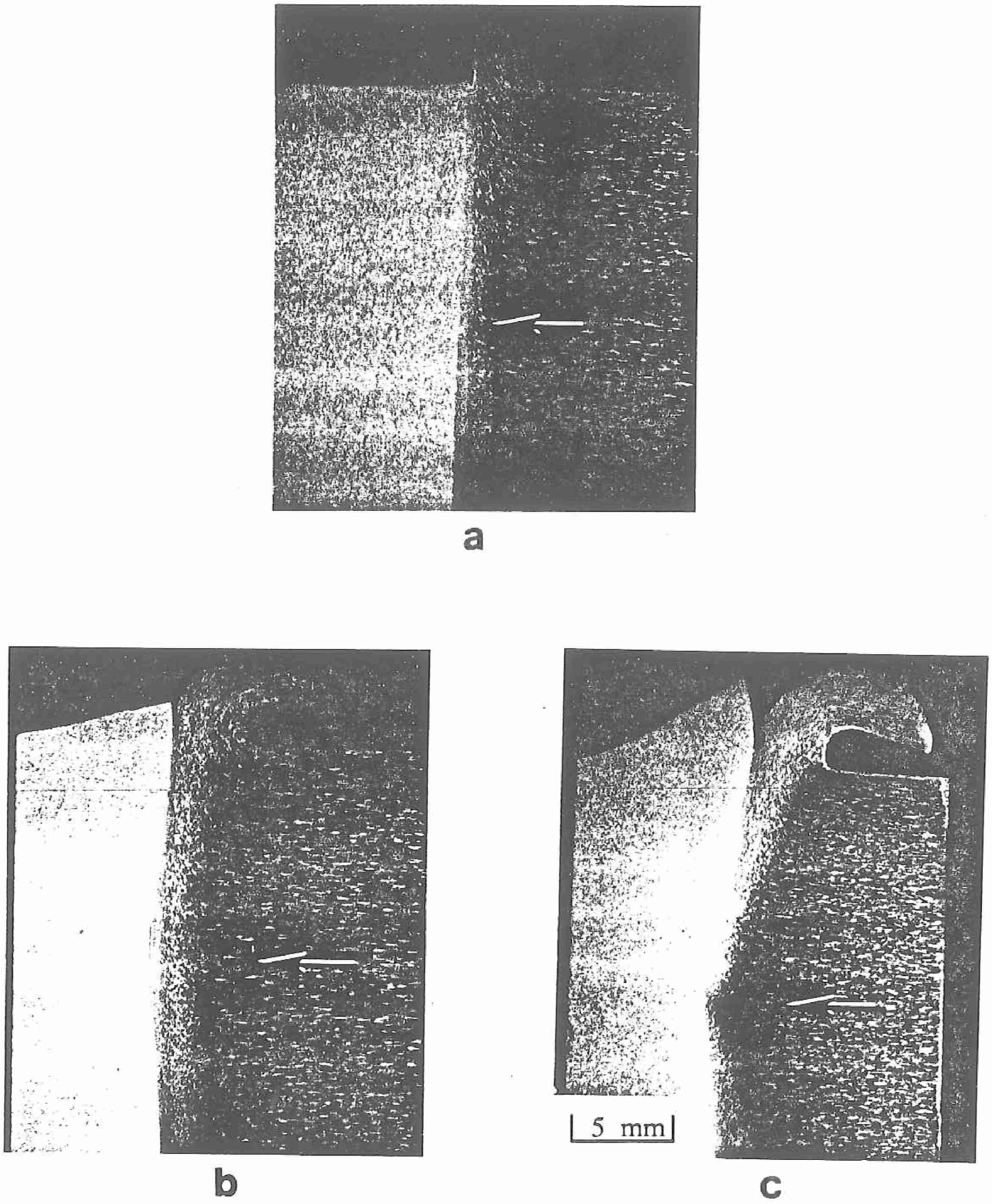

Figure 5 Light macrographs of inertia-friction welds between Al-9Fe-3Mo-1V (left side) and IM-2024-T351 (right side) produced at different axial force levels: (a) low axial force; (b) medium axial force; (c) high axial force. Arrows indicate the axial centerline.

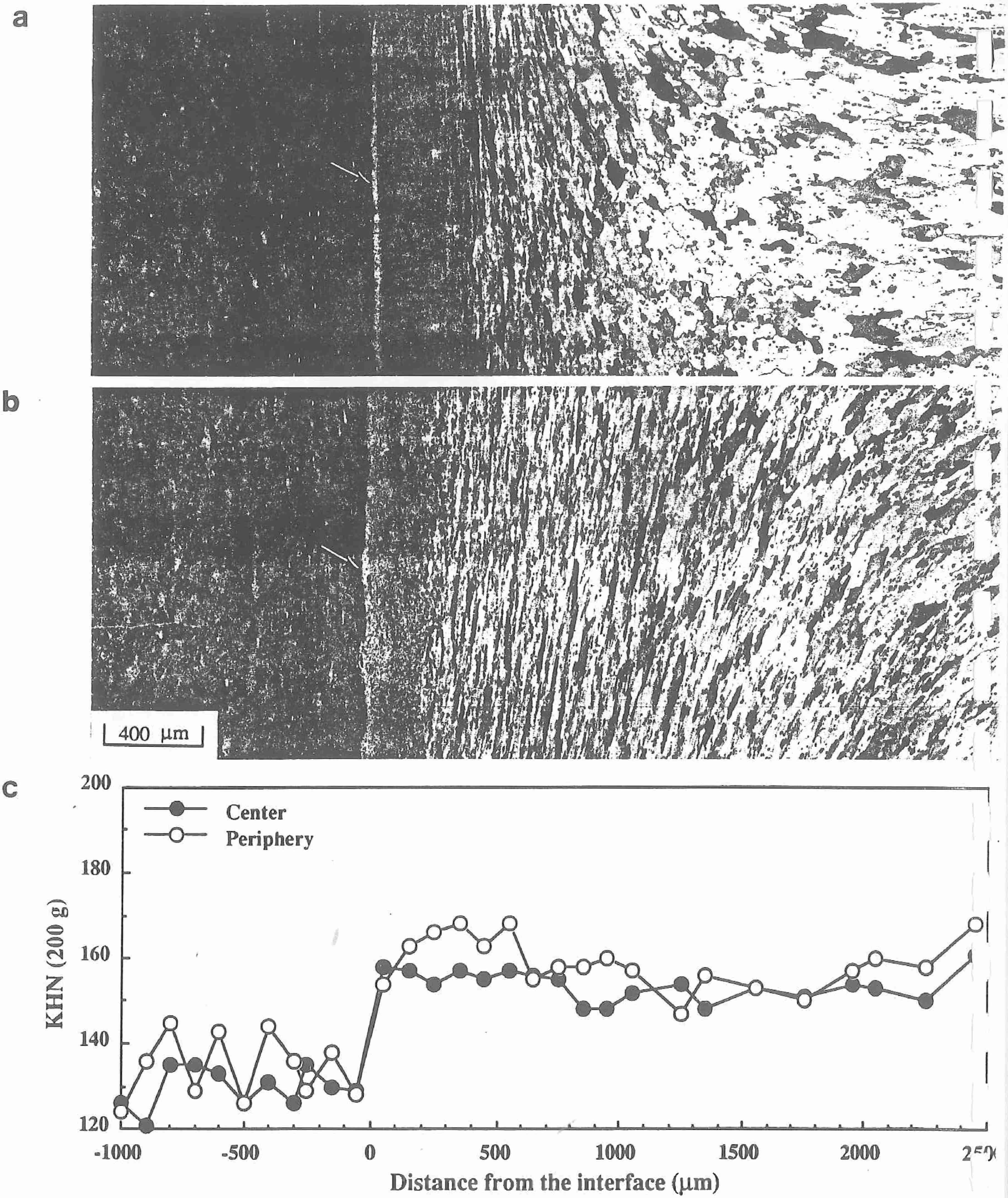

Figure 6 Light micrographs of the (a) center and (b) outer periphery regions of an inertia-friction weld produced between Al-9Fe-3Mo-1V (left side) and IM-2024-T351 (right side) at low axial force and (c) corresponding KHN hardness traverse. Arrows in (a) and (b) indicate weld interface.

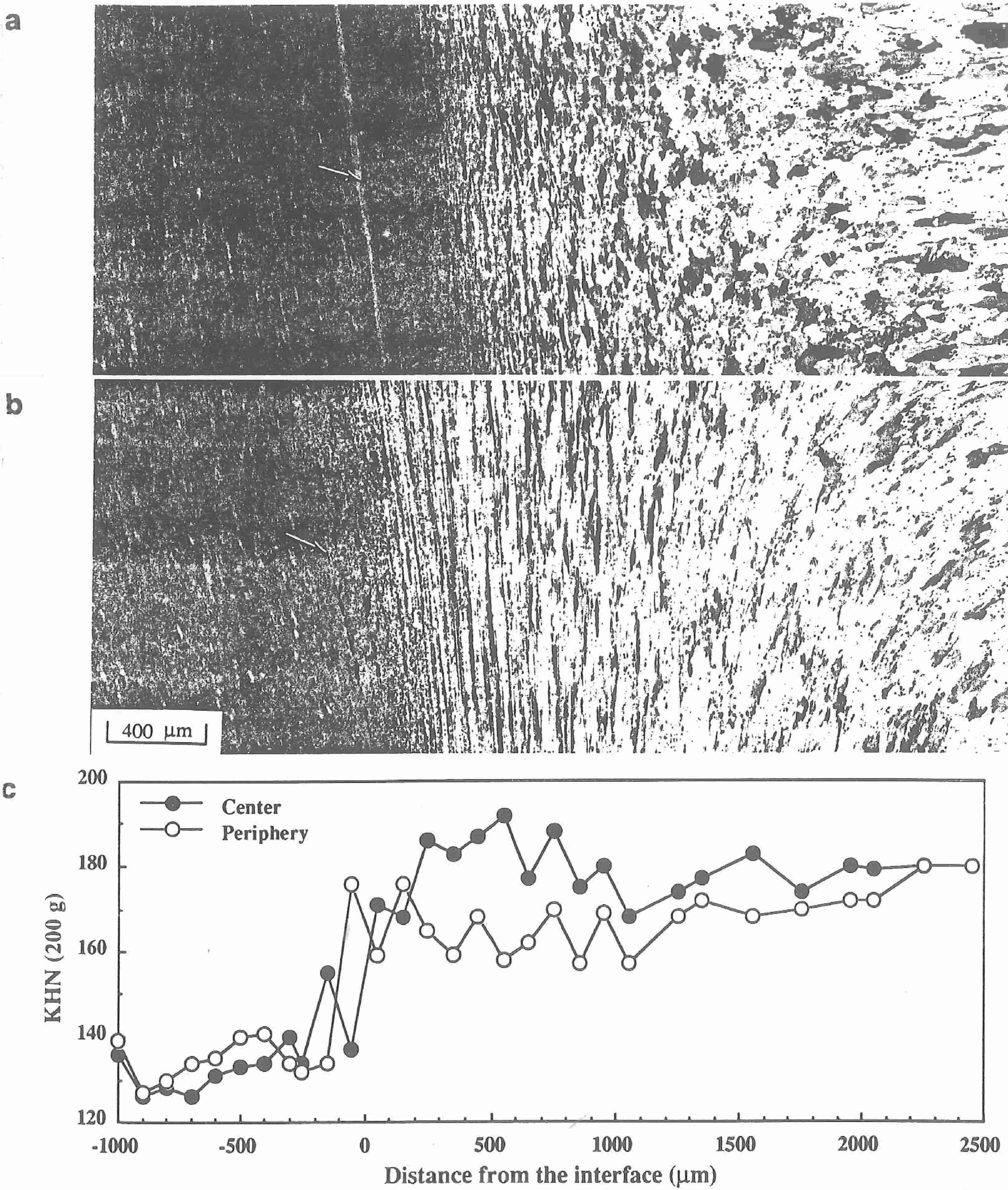

Figure 7 Light micrographs of the (a) center and (b) outer periphery regions of an inertia-friction weld produced between Al-9Fe-3Mo-1V (left side) and IM-2024-T351 (right side) at high axial force and (c) corresponding KHN hardness traverse. Arrows in (a) and (b) indicate weld interface.

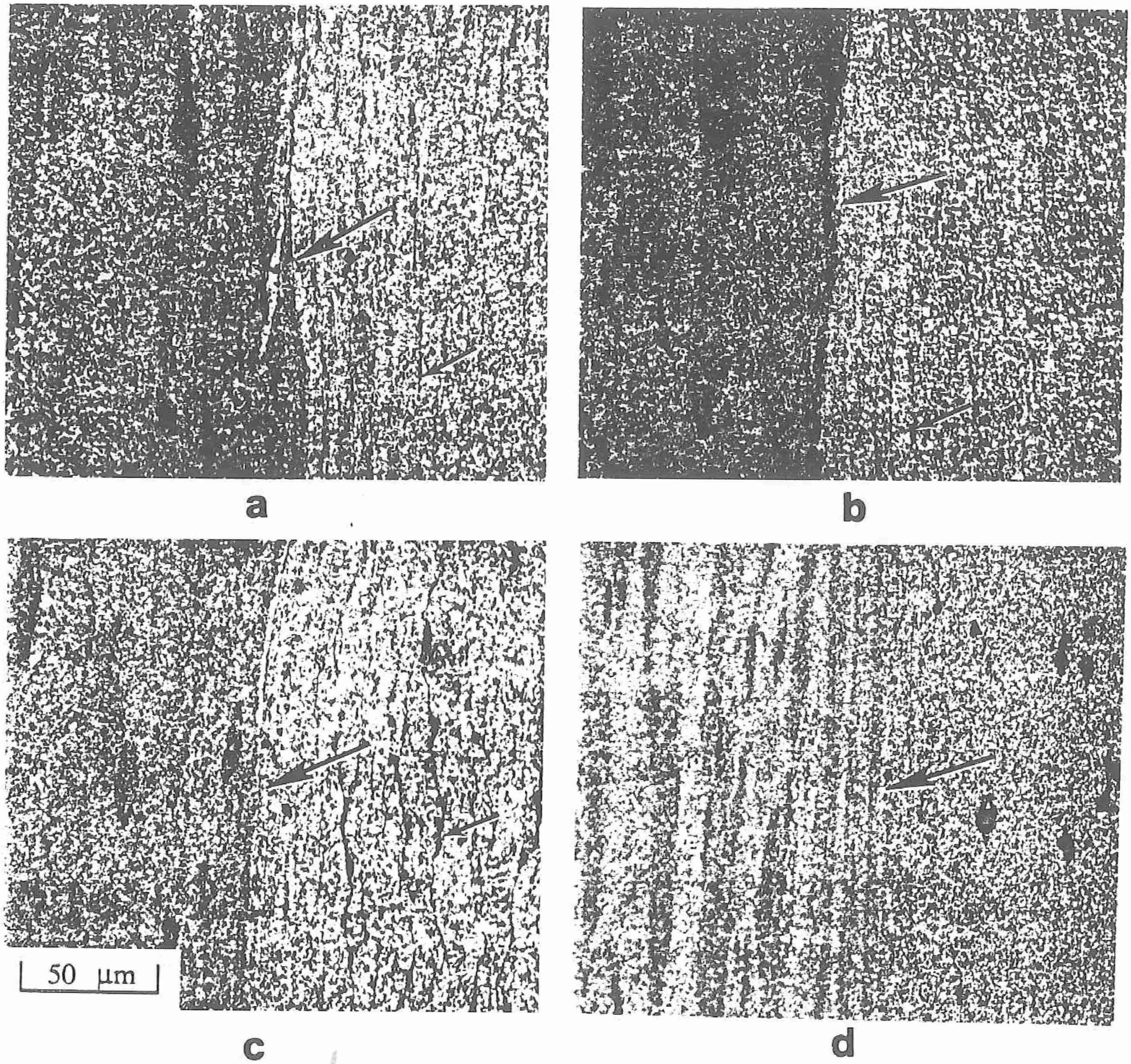

Figure 8 Light micrographs of the interface regions of inertia-friction welds produced between Al-9Fe-3Mo-1V (left side) and IM-2024-T351 (right side): (a) center of low axial force weld; (b) outer periphery of low axial force weld; (c) center of high axial force weld; (d) outer periphery of high axial force weld. Small arrows indicate intermetallic stringers aligned along the deformation direction in IM-2024. Large arrow indicates weld interface.

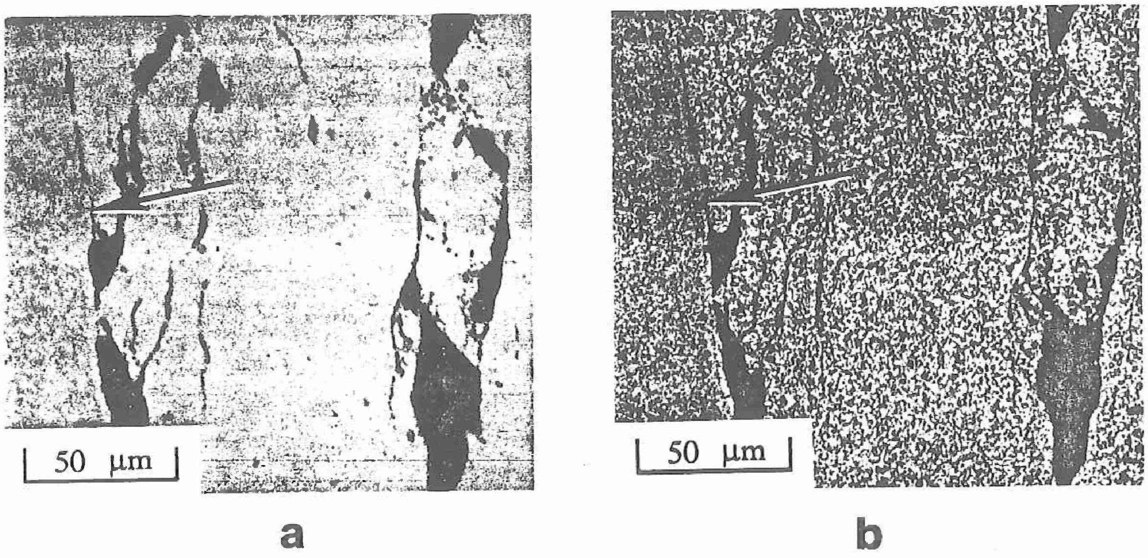

Figure 9 Light micrographs of weld defects in IM-2024-T351 at the outer periphery of high axial force weld: (a) unetched; (b) after etching with Keller's reagent. Large arrows indicate weld interface.

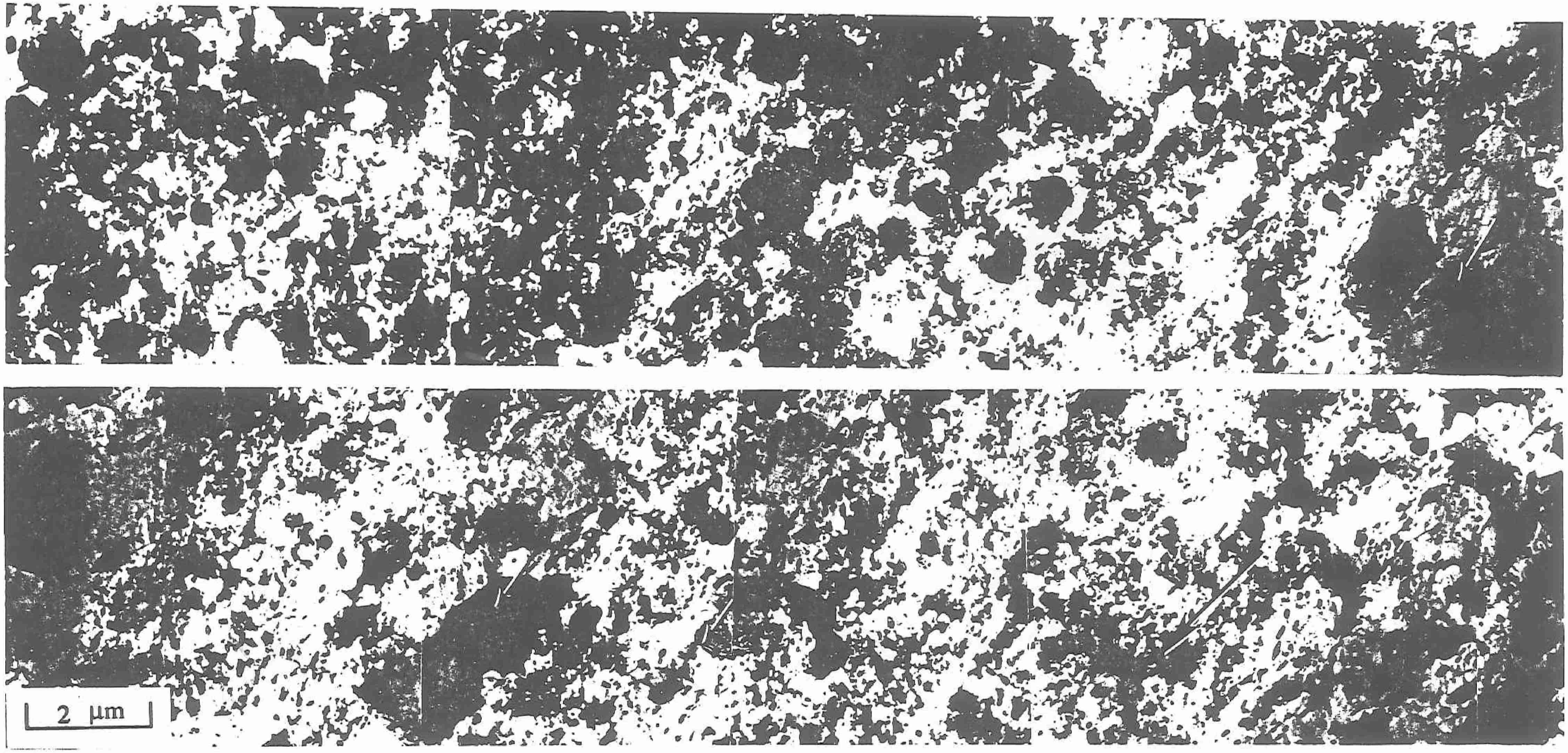

Figure 10 TEM bright-field traverse across weld interface region at the center of low axial force weld. Lower traverse is continuation of right side of top traverse. Left side of top traverse is Al-9Fe-3Mo-1V and right side of bottom traverse is IM-2024-T351. Large arrow indicates location of the interface between mechanically-mixed region and IM-2024-T351. Small arrows indicate regions of IM-2024-T351 in mechanically-mixed region.

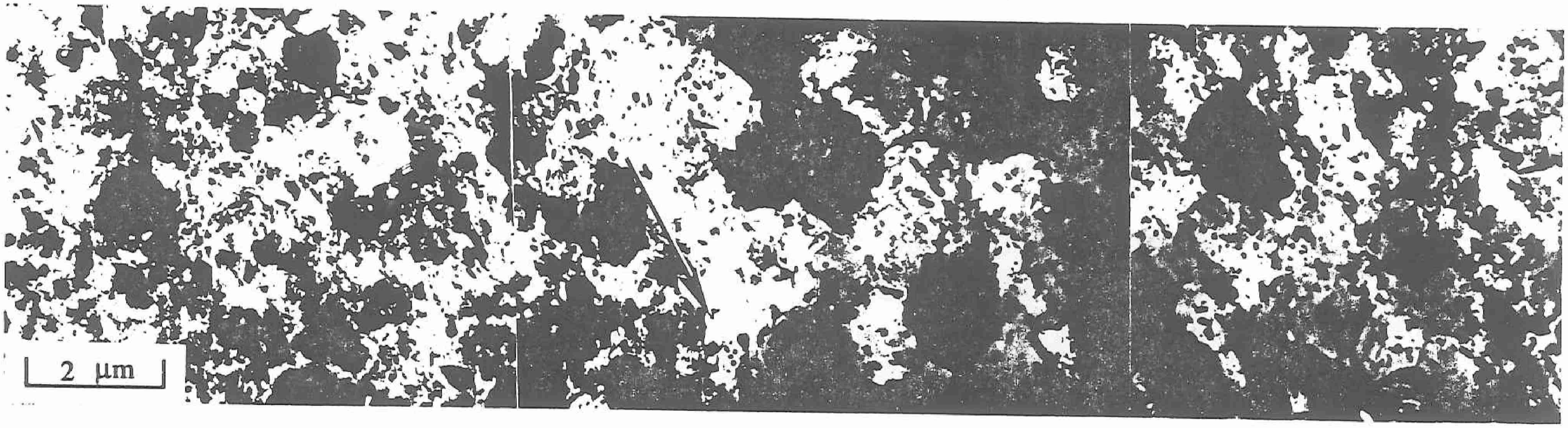

Figure 11 TEM bright-field traverse across interface near the outer periphery of the low axial force weld. Large arrow indicates location of weld interface between Al-9Fe-3Mo-1V (left) and IM-2024-T351 (right).

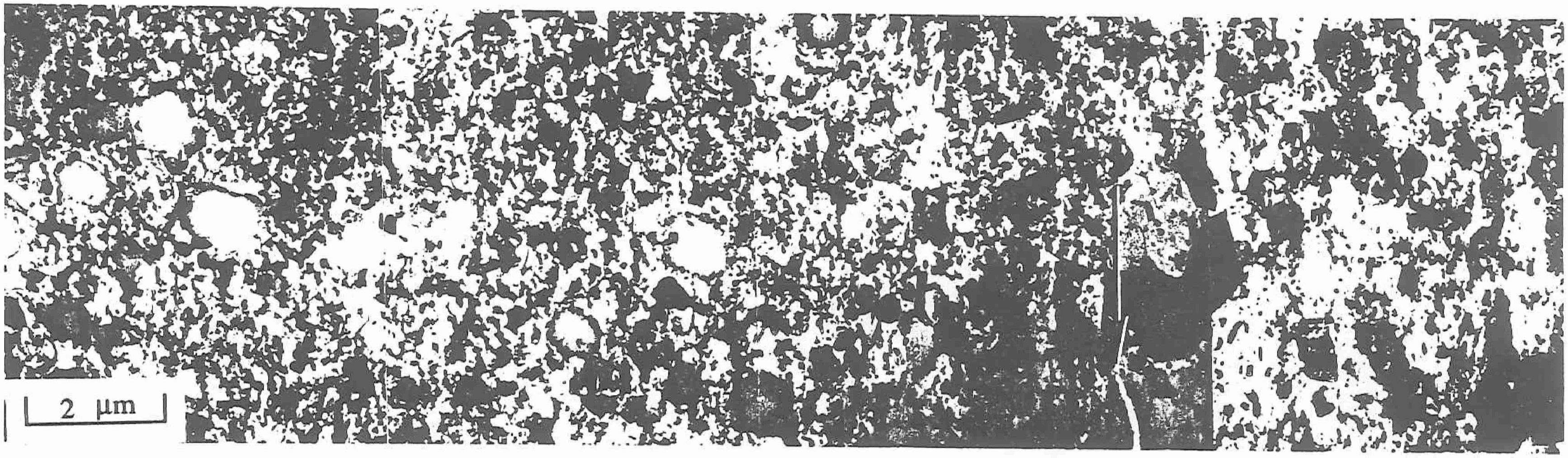

Figure 12 TEM bright-field traverse across interface at the weld center of the high axial force weld. Large arrow indicates location of weld interface between Al-9Fe-3Mo-1V (left) and IM-2024-T351 (right).

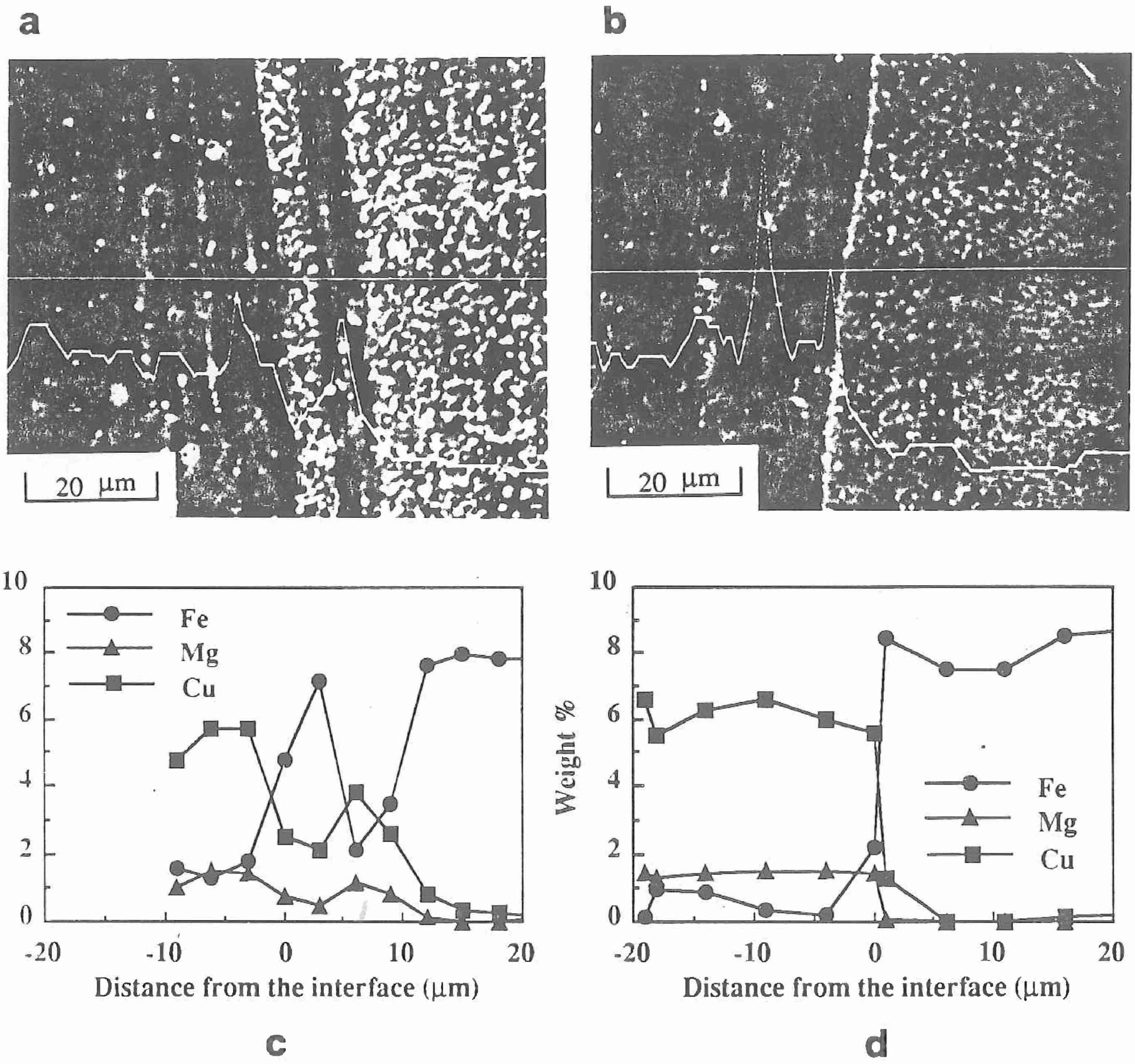

Figure 13 EPMA traverses across low axial force weld produced between Al-9Fe-3Mo-1V (right) and IM-2024-T351 (left). Straight lines in (a) and (b) are Cu K-alpha trace scans while (c) and (d) are results of point analysis.

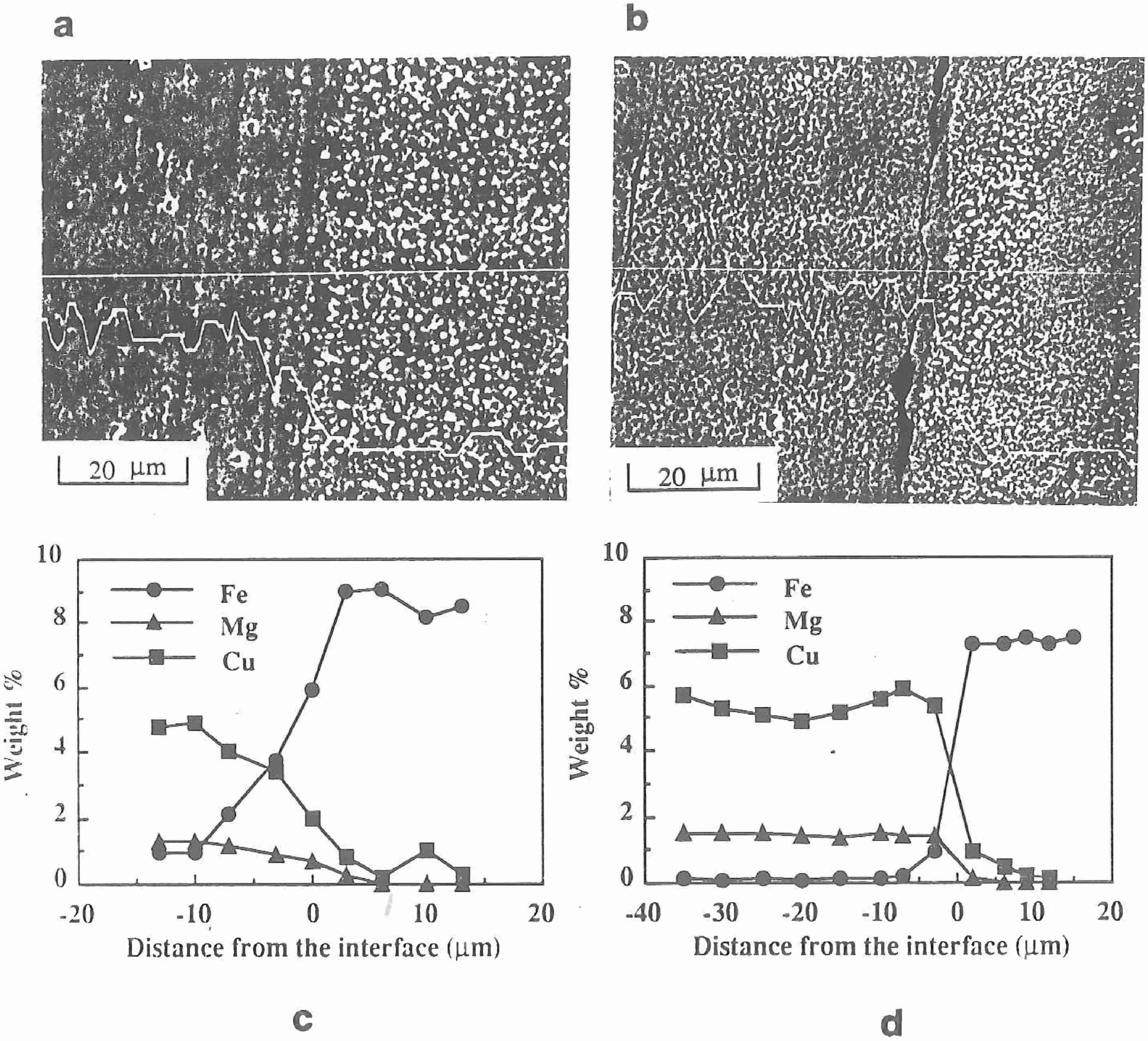

Figure 14 EPMA traverses across high axial force weld produced between Al-9Fe-3Mo-1V (right) and IM-2024-T351 (left). Straight lines in (a) and (b) are Cu K-alpha trace scans while (c) and (d) are results of point analysis.

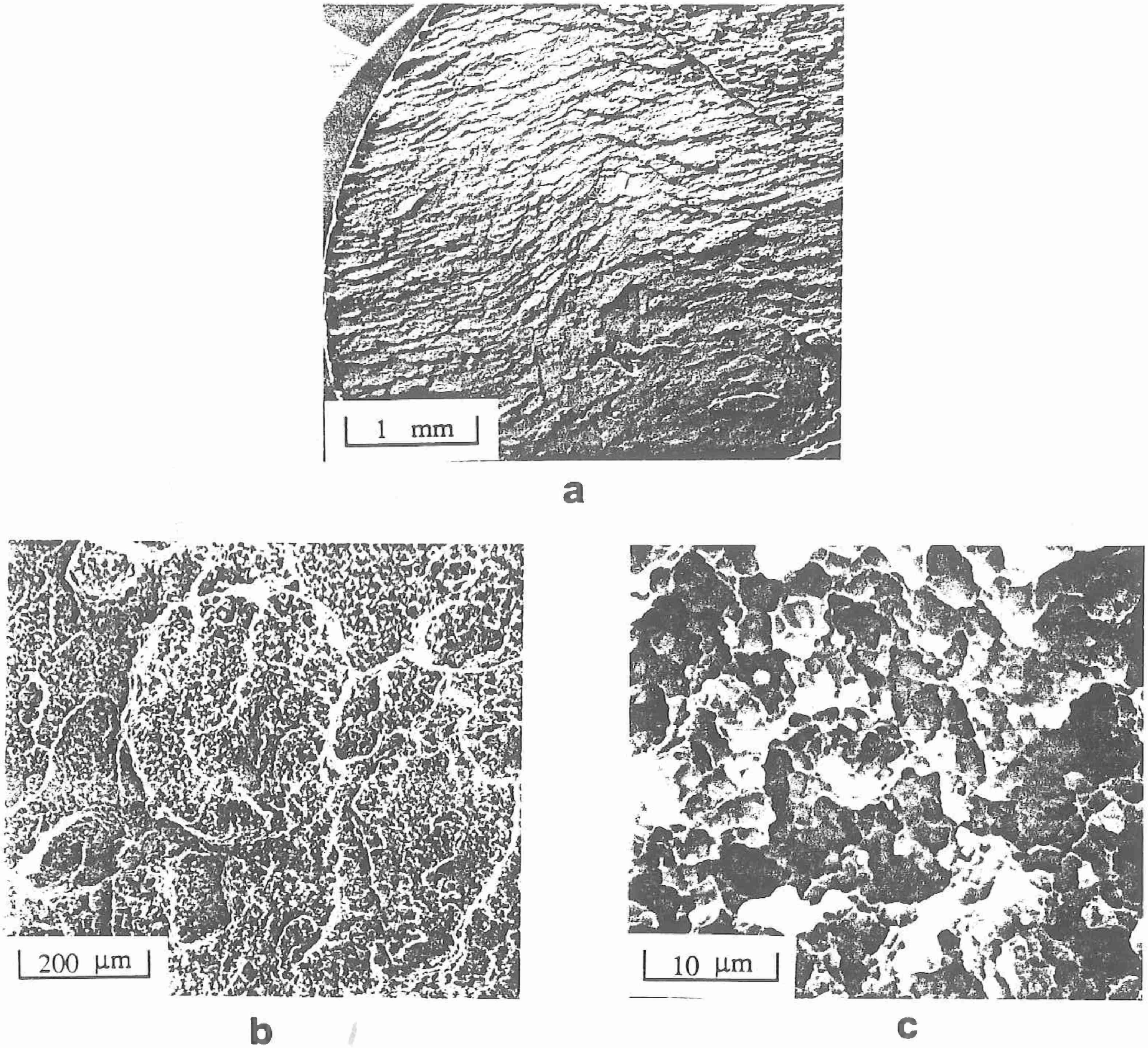

Figure 15 SEM fractographs of high axial force weld bend test specimen: (a) general view at low magnification; (b) and (c) fracture surface near specimen center at increased magnification.

Appendix 1F

APPENDIX IF

H. H. Koo, S. Krishnaswamy and W. A. Baeslack III, "Solid-Phase Welding of a Rapidly-Solidified Al-Fe-V-Si Alloy - FVS1212," Low Density, High Temperature Powder Metallurgy Alloys, W. E. Frazier, M. J. Koczak and P. W. Lee, Eds., TMS/AIME (1991) 183-196.

Presented at 1990 TMS Fall Meeting in Detroit, Michigan.

SOLID-PHASE WELDING OF A RAPIDLY-SOLIDIFIED DISPERSION-STRENGTHENED Al-Fe-V-Si ALLOY- FVS1212

H. H. Koo, S. Krishnaswamy and W. A. Baeslack III

Department of Welding Engineering
The Ohio State University
Columbus, OH 43210 USA

Abstract

The effect of weld axial force on the structure, mechanical properties and fracture behavior of inertia-friction welds produced in a rapid-solidification/powder metallurgy (RS/PM) Al-11.7 wt.% Fe-1.2 wt.% V-2.4 wt.% Si alloy (also designated as FVS1212) was investigated. Light and analytical-electron microscopy revealed that extensive high-temperature deformation at the center of the weld heat-and-deformation zone (HDZ) effectively homogenized the macroscopically inhomogeneous base metal microstructure, but did not promote significant dispersoid coarsening or dispersoid fracture. In welds produced using a low axial force (56.1 kN), nonuniform deformation at the weld outer periphery resulted in the formation of dispersoid-lean, coarse-grained regions with a hardness appreciably lower than that of the base metal. The application of a sufficiently high axial force (83.7 kN) eliminated the presence of this undesirable region and prevented hardness degradation across the weld zone. Results of transverse-weld oriented tensile testing were generally consistent with hardness data and showed joint efficiencies of up to 85% for welds produced with high axial force.

Low Density, High Temperature Powder Metallurgy Alloys
Edited by William E. Frazier, Michael J. Koczak and Peter W. Lee
The Minerals, Metals & Materials Society, 1991

Introduction

Dispersion strengthened Al-Fe-V-Si alloys belong to a new family of high performance structural materials produced by rapid-solidification/powder metallurgy (RS/PM) processing specifically for use in elevated-temperature applications [1-4]. These alloys are based on hyper-eutectic Al-Fe compositions (8.5 - 12 wt% Fe) with ternary and quaternary additions of vanadium and silicon. RS/PM processing of these novel chemistries produces a unique, "engineered" microstructure consisting of nearly-spherical, sub-micron $Al_{13}(Fe,V)_3Si$ (body-centered cubic) dispersoids in an extremely fine-grained alpha aluminum matrix. The low interfacial energy between the dispersoid particles and the matrix, and the low solid-state diffusivity of transition elements in alpha aluminum provide minimal driving force for particle coarsening, thereby promoting excellent particle stability and superior mechanical properties at temperatures up to 400°C. Indeed, on a specific strength basis (depending on the volume fraction of the dispersoid particles), the Al-Fe-V-Si alloys exhibit strengths comparable to Ti-6Al-4V. Further, the spherical morphology of the $Al_{13}(Fe,V)_3Si$ dispersoids, and absence of acicular Al_3Fe (monoclinic) dispersoids, promote excellent ductility, fracture toughness and fatigue properties comparable to those of conventional high-strength aluminum alloys. Among the Al-Fe-V-Si alloys currently under development and evaluation, FVS0812 (nominal chemistry: Al-8.5 wt.% Fe-1.3 wt.% V - 1.7 wt.% Si) and FVS1212 (nominal chemistry: Al-11.7 wt%. Fe-1.2 wt.% V-2.4 wt.% Si) alloys are considered potential materials to replace conventional elevated-temperature aluminum alloys (eg., 2XXX series alloys) and titanium alloys.

The effective utilization of Al-Fe-V-Si alloys in structural applications will require their joining. However, the unique, "engineered" microstructures exhibited by these RS/PM alloys restrict the application of many conventional fusion welding processes and methodologies. Rather, joint efficiency considerations require the application of welding processes and procedures which can "recreate" and/or "retain" in the weld zone the "engineered" microstructures, thereby producing weld properties comparable to the base alloy. Recent studies have shown that the solid-state inertia-friction welding process offers a strong potential for the effective joining of dispersion-strengthened aluminum alloys [5,6], including Al-Fe-V-Si alloys [7,8]. This process combines frictional heat generated at the faying surfaces with a high axial force to produce localized plastic deformation and to form a metallic bond between nascent surfaces. The absence of melting at the faying surfaces during this process eliminates the occurrence of solidification-related discontinuities, such as porosity or cracking. In addition, the expulsion of surface contaminants and severely heat-and-deformation-affected metal present at the weld interface during the forging stage of the process can promote final coalescence between nearly unaffected base metals. A recent inertia-friction welding study on the Al-Fe-V-Si alloy FVS0812 showed that high joint efficiencies of up to 95% can be achieved through proper process parameter control [7]. A subsequent investigation involving the microstructural characterization of inertia-friction weld in FVS0812 alloy showed the weld axial force to appreciably affect the weld zone microstructure [8]. The present investigation was performed to evaluate the effect of weld axial force on the microstructural characteristics of inertia-friction welds in the Al-Fe-V-Si alloy FVS1212 and to correlate weld microstructure with hardness, tensile properties and fracture behavior.

Experimental

The FVS1212 alloy utilized in this investigation originated as rapidly-solidified ribbons produced by Allied-Signal Inc.'s planar-flow casting (PFC) process. Following rapid solidification, the ribbons were comminuted into fine particles, vacuum degassed, hot-pressed into billets and finally extruded into 32 mm diameter rod. Prior to inertia-friction welding, the rods were sectioned into 50 mm lengths and machined down to a diameter of 22 mm. Weld faying surfaces were dry machined immediately prior to welding.

Inertia-friction welds were produced using an MTI Model 120 inertia-friction welding system. Based on previous inertia-friction welding studies of dispersion-strengthened aluminum alloys [5,6,8] and preliminary testing, welding parameters were selected which provided two levels of axial displacement and extruded flash. These two weld types were produced using the same moment-of-inertia (0.17 Kg-m^2), rotational velocity (523.6 rad./s) and inertial energy (22.7 kJ), but two different axial force levels of 56.1 kN (designated as "low axial force") and 83.7 kN (designated as "high axial force").

Following welding, the weld axial displacement and flash uniformity were evaluated by visual analysis. Representative welds were sectioned axially, mounted in epoxy, mechanically ground down to 600 grit SiC paper, rough polished with 3 μm diamond compound and final polished using a colloidal silica suspension. Following defect analysis of the as-polished specimen surfaces using light microscopy, microstructural characteristics were revealed by etching with Keller's reagent for light microscopy analysis.

Alternate specimen halves were carefully sectioned longitudinally at the axial centerline into thin slices 0.3 mm thick using a diamond saw and mechanically thinned on SiC paper down to 0.125 mm. Disks 3 mm in diameter were punched from the foils in the unaffected base metal and from representative regions in the weld HDZ and electrojet thinned in a solution of 1 part nitric acid in 3 parts methanol at -30°C. Thin foils were examined in a JEOL 200CX analytical-electron microscope equipped with a Tracor-Northern TN-2000 energy-dispersive X-ray analysis (EDS) system.

Knoop microhardness testing (150 gram load) was performed across the weld region at the axial centerline and the outer periphery for correlation with microstructural characteristics. Transverse-weld oriented tensile specimens (gage section: 25 mm length x 4.5 mm width x 1.5 mm thickness) were sectioned from each weld type and tested as per ASTM E8-87 at an extension rate of 0.25 mm/min. Following testing, fractured specimens were characterized using light microscopy.

Results and Discussion

Base Metal Microstructure

Light Microscopy Analysis

Figures 1a and b show light micrographs of the base metal microstructure oriented parallel to the extrusion direction. Even at relatively low magnification, evidence of boundaries between the original PFC ribbon particles can be observed. Contrast differences at low magnification (Fig. 1a) appeared to depend on local variations in the dispersoid size and population density, with the light-appearing regions exhibiting a higher population density of finer-sized dispersoids than the dark-appearing regions. Variations in the dispersoid size and population density were more clearly apparent at higher magnification (Fig. 1b).

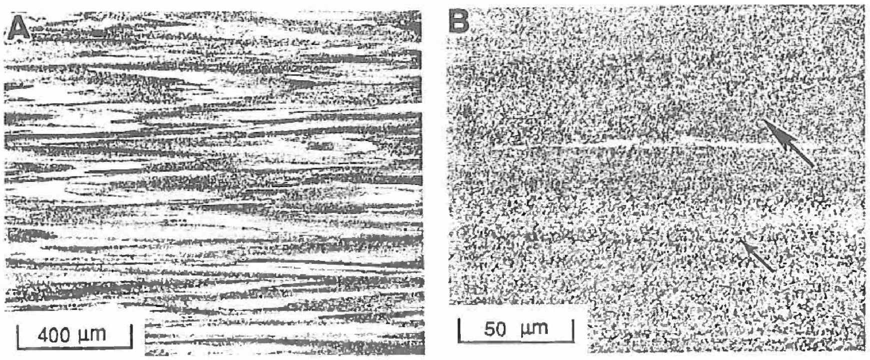

Fig. 1. Light micrographs of as-extruded FVS1212 base metal.

Regions which exhibited a light contrast at lower magnification actually showed a uniform dark contrast at higher magnification (large arrow in Fig. 1b), while the dark-appearing regions at low magnification exhibited a coarser-appearing dispersoid structure in which alpha regions between dispersoids could be readily observed (small arrow in Fig. 1b). Regions containing both coarse and fine dispersoids were commonly observed within a single ribbon particle. These microstructural variations within a single particle originated from differences in the cooling rate of the original ribbon, with the side contacting the quenching wheel experiencing appreciably higher cooling rates than the opposite free surface side. Higher cooling rates correspondingly promoted a finer as-solidified microstructure and ultimately a finer as-processed dispersoid structure. As shown in Fig. 1b, occasional narrow white bands were observed along particle boundaries.

TEM Analysis

Microstructural characteristics of the base metal were more clearly delineated using TEM. Low magnification TEM bright-field micrographs revealed boundaries between ribbon particles and showed perceptible differences in the size, population density and distributions of dispersoids throughout the microstructure. Examination at increased magnification of regions containing relatively uniform, fine-sized dispersoids in Figs. 2a and 2b, and at other locations in the base metal, showed the dispersoids to exhibit a nearly spherical morphology with diameters ranging from about 75 to 150 nm. Dispersoids were located both within the alpha-aluminum matrix and at the boundaries of nearly equiaxed alpha aluminum grains. In certain locations (Figs. 2c and d), a bi-modal distribution of dispersoids consisting of fine dispersoids ranging from 75 to 100 nm in diameter and coarser dispersoids up to 400 nm in diameter was observed. Alpha grain sizes in these regions ranged from about 0.5 to 1 μm in diameter. TEM analysis of regions which exhibited at lower magnification coarse dispersoids and a high proportion of alpha phase (region indicated by small arrow in Fig. 1b) showed clusters of fine dispersoids (50 to 100 nm in diameter) decorating alpha grain boundaries (Figs. 2e and f). Generally, these regions exhibited a lower population of dispersoids as compared to the regions of uniform fine dispersoid distribution (eg., Figs. 2a and b) and a somewhat coarser alpha grain size, up to about 1.5 μm in diameter. Since the as-solidified ribbon particulate was not characterized in this investigation, it was not possible to precisely determine the origin of this inhomogeneous cluster-type dispersoid

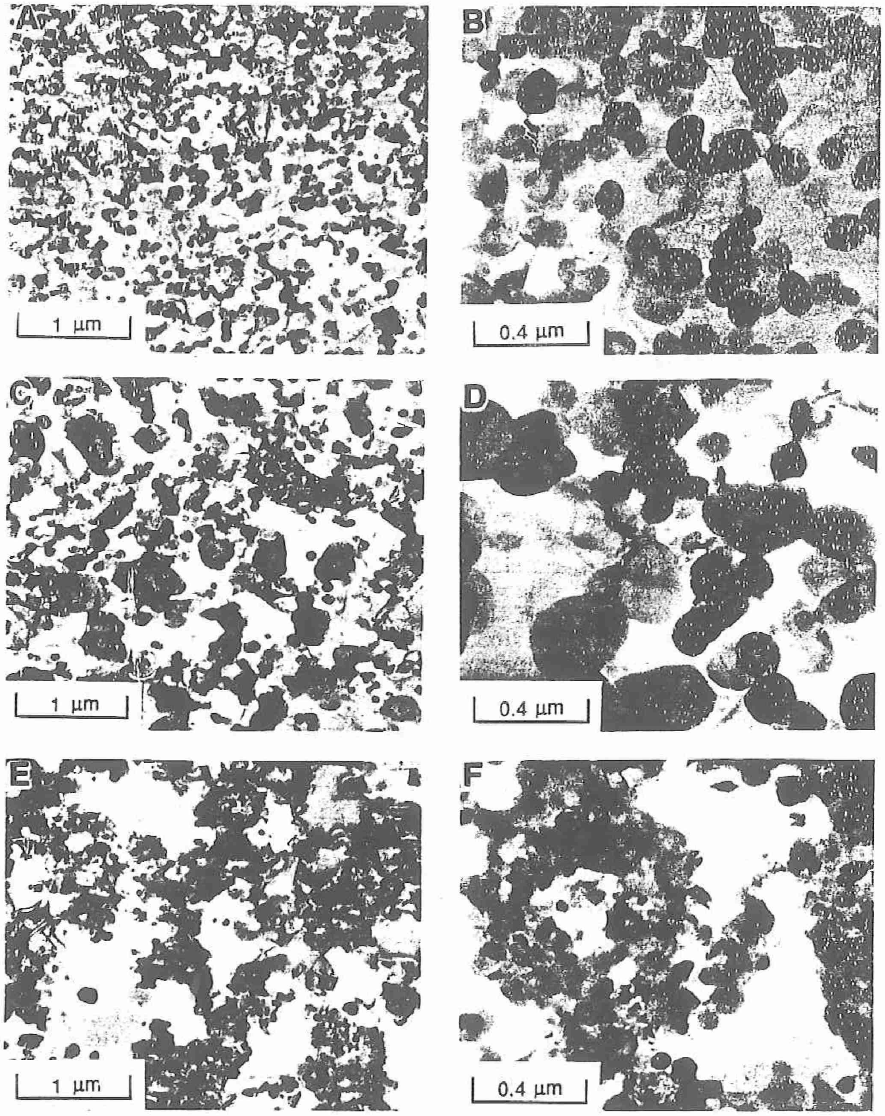

Fig. 2. TEM bright-field micrographs of FVS1212 extruded base metal: (a,b) uniform distribution of fine dispersoids; (c,d) mixture of fine and coarse dispersoids; (e,f) clusters of fine dispersoids along alpha boundaries.

distribution. However, it is suggested that the formation of these structures may be associated with slowly cooled regions of the PFC ribbon particles, possibly originating as interdendritic regions between coarse columnar or equiaxed dendrites located near the free surface. As shown in Fig. 1b, occasional dispersoid-free bands were also observed in the base metal microstructure. These structures may have originated from the rapidly cooled (dispersoid-free) regions of the PFC ribbon particles located near the quenching wheel side, or possibly from non-homogeneous deformation during extrusion. In the present study, the various dispersoid particles were not characterized using selected-area diffraction or EDS analysis. However, previous characterization studies on these alloys [1-4] and such characterization by the authors on inertia-friction welds in FVS0812 alloy [8] indicated the presence of only $Al_{13}(Fe,V)_3Si$ type dispersoids. No evidence of acicular dispersoids, as previously observed in studies of a rapidly-solidified Al-Fe-Mo-V alloy [6], was observed. This result was consistent with the previously observed influence of V in stabilizing the cubic $Al_{13}(Fe,V)_3Si$ over the hexagonal Al_8Fe_2Si or monoclinic Al_3Fe phases [3].

Weld Zone Characterization

Light Microscopy Analysis

Visual examination of the low and high axial force inertia-friction welds found the presence of smooth, symmetrically uniform flash around the entire weld circumference. A greater extent of extruded flash in the weld produced at higher axial force was consistent with the appreciably greater axial displacement experienced by this weld (8.51 mm versus 3.12 mm).

Macroscopic examination of the axially-sectioned weld specimens in the as-polished condition found no evidence of lack-of-bonding defects. Etching of the specimens revealed approximately hourglass-shaped heat-and-deformation zones in both weld types (Figs. 3a and b), with the width of the HDZ (at a constant distance from the axial centerline) generally narrower for the weld produced at high axial force. This observation was consistent with the greater extent of flash produced in the high axial force weld.

Light microscopy analysis at increased magnification more clearly revealed the characteristics of the weld HDZ, and differences in this region between the axial center and outer periphery. Figures 4a and b show microstructure traverses from the unaffected base metal to the center of the weld HDZ at the axial center and outer periphery of a weld produced using low axial force. The base metal microstructure showed a continual reorientation from parallel to perpendicular to the original base alloy extrusion direction. This change in orientation resulted from the complex combination of axial and torsional stresses experienced in the weld zone during inertia-friction welding. During welding, the plastic flow of metal heated to high temperatures by frictional heating occurred from the center region to the outer periphery in an outward spiraling pattern. Nearer to the center of the weld HDZ, the reoriented base metal microstructure became increasingly "flattened" due to high axial compressive stresses. In this region, microstructural variations which existed in the base metal due to differences in dispersoid size, population density and distribution became less apparent. Indeed, at the center of the HDZ the structure appeared completely homogenized.

At the outer periphery of the low axial force weld (Fig. 4b), narrow, white-appearing bands and adjacent dark-appearing regions were observed oriented parallel to the weld interface. Although not shown, the examination of these regions at increased magnification indicated a very low dispersoid

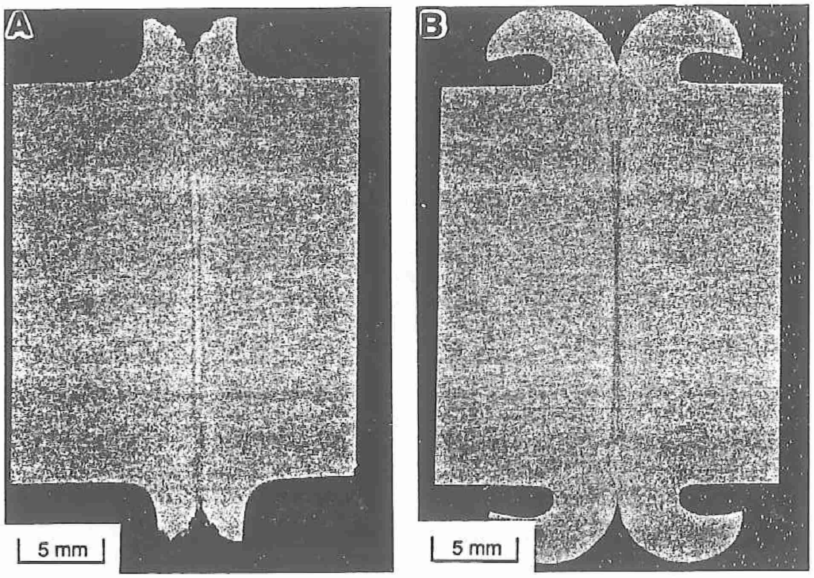

Fig. 3. Light macrographs of inertia-friction welds produced in FVS1212: (a) low axial force; (b) high axial force.

density in the light-appearing regions and a higher dispersoid density in the adjacent dark-appearing regions versus the surrounding near-HDZ.

Figures 5a and b show microstructure traverses across the weld produced using high axial force. At the weld centerline, where the HDZ width was relatively narrow, the textured base metal structure became increasingly "flattened", but did not achieve complete homogeneity as in the low axial force weld. Near the weld outer periphery, an appreciably wider HDZ was observed which exhibited regions comparable to those observed at the center of the low axial force weld. No evidence of light or dark-appearing regions was observed in the weld produced with high axial force. The absence of these structures in welds produced with high axial force was attributed to their extrusion from the weld interface during the final forging stage of the welding process.

TEM Analysis

TEM analysis of the HDZ center in the inertia-friction weld produced with low axial force revealed a uniform distribution of dispersoids ranging in size from about 75 to 500 nm. Consistent with light microscopy results, this homogenization appeared to result from the extensive mechanical mixing of base metal regions which originally contained varying distributions of relatively finer or coarser dispersoids (as shown in Figs. 2a and 2c). No evidence of the dispersoid clusters shown in Figs. 2e and 2f was observed in this region, indicating their complete breakup and mechanical mixing. Although a quantitative analysis of dispersoid size distributions was not performed, the dispersoid size distribution in this region generally appeared comparable to that observed in the unaffected base metal, with only a

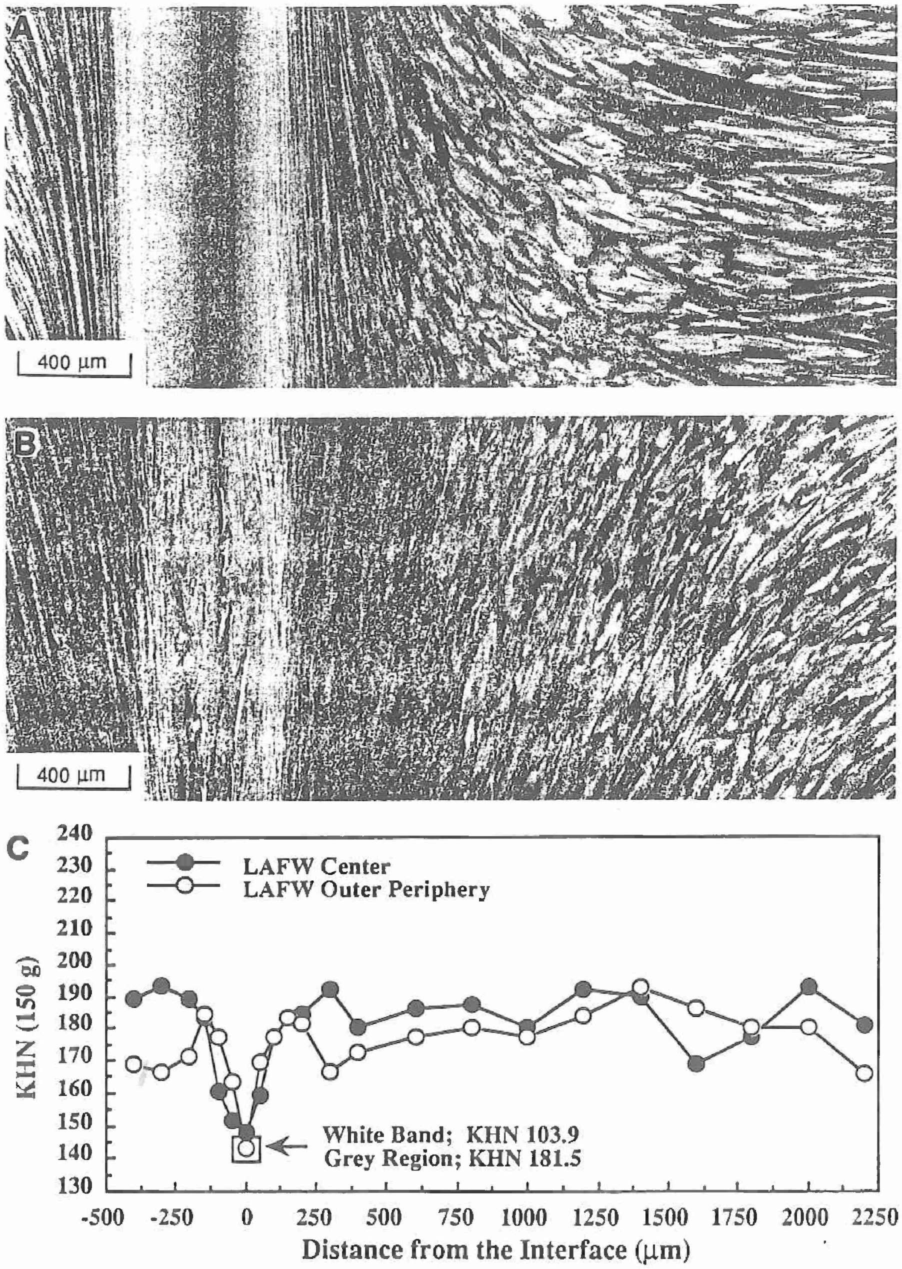

Fig. 4. Light micrographs of the (a) center and (b) outer periphery regions and (c) corresponding KHN hardness traverses for an inertia-friction weld produced in FVS1212 using low axial force.

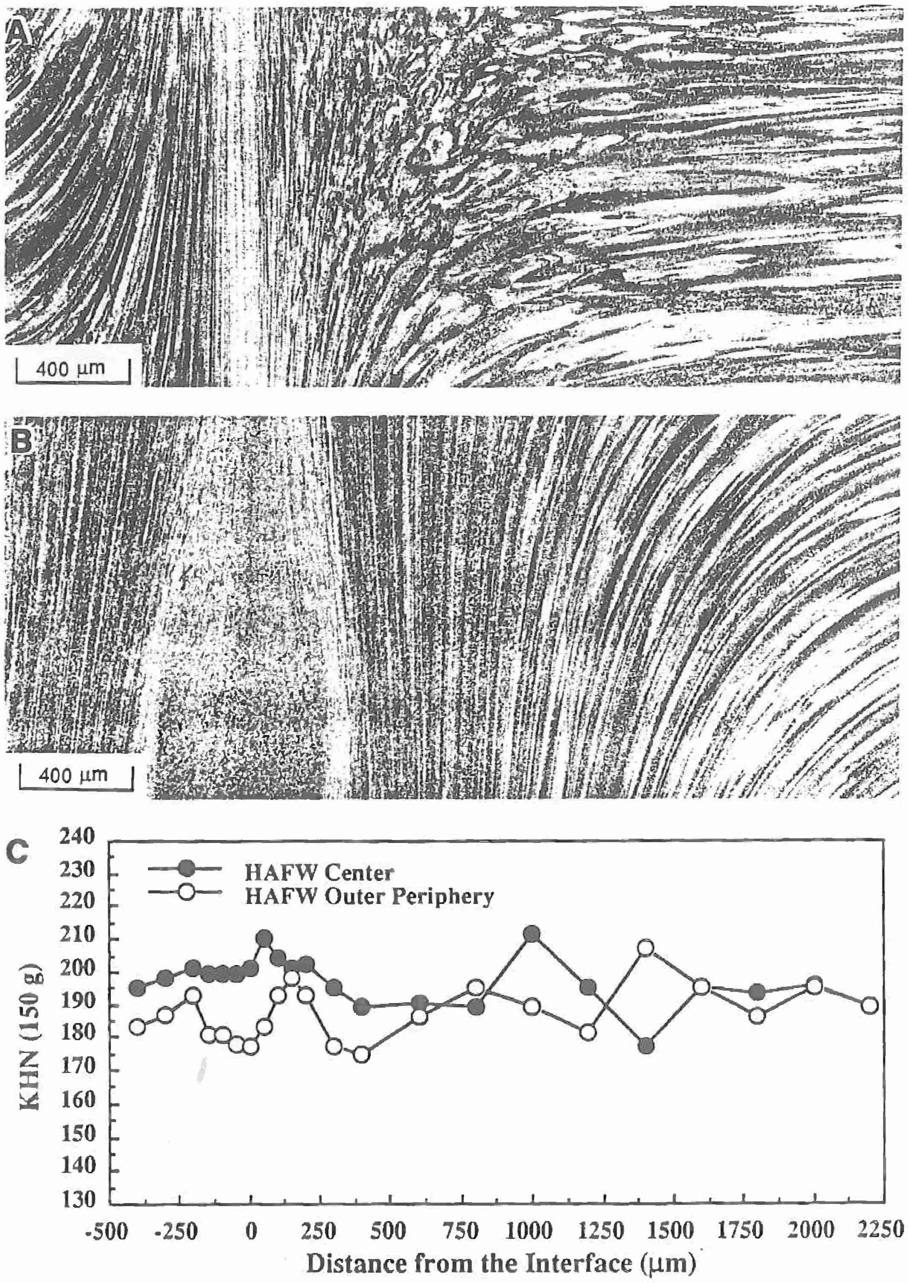

Fig. 5. Light micrographs of the (a) center and (b) outer periphery regions and (c) corresponding KHN hardness traverses for an inertia-friction weld produced in FVS1212 using high axial force weld.

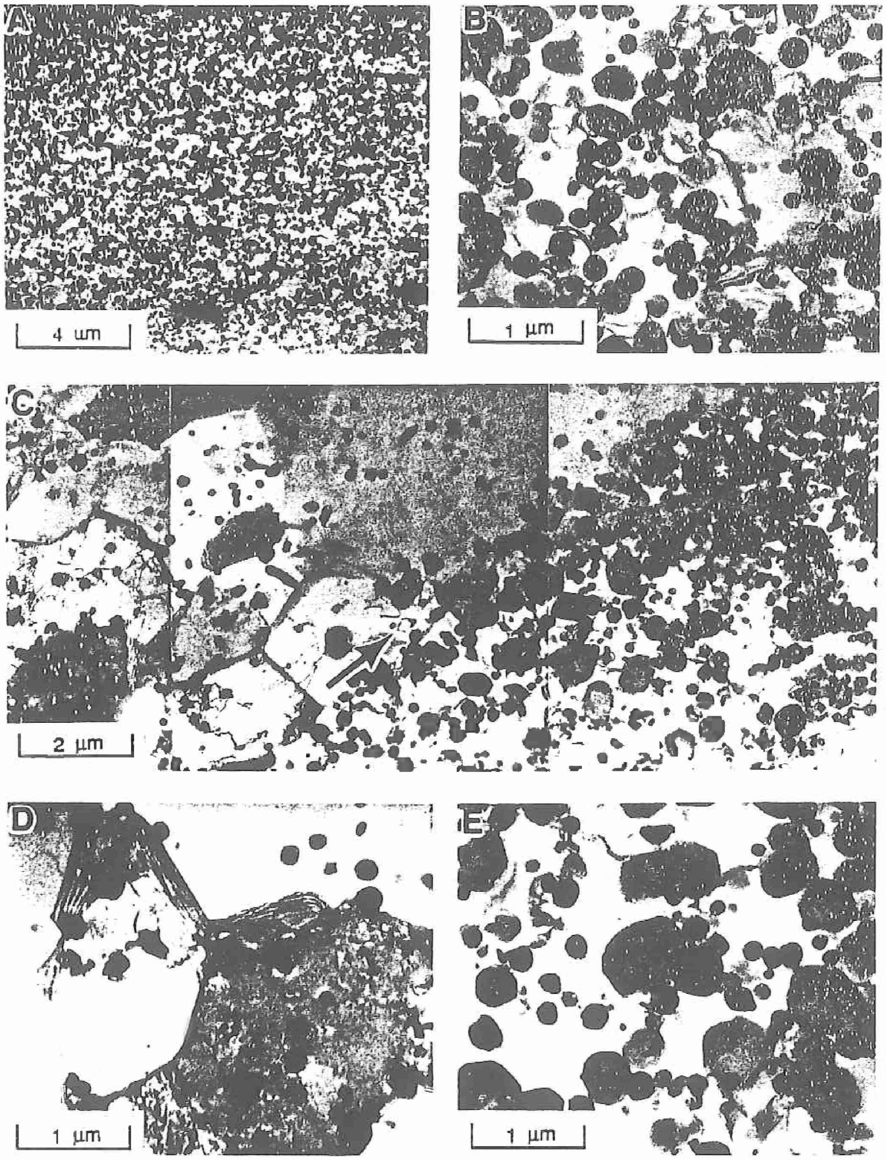

Fig. 6. TEM bright-field micrographs of inertia-friction weld produced in FVS1212 using low axial force: (a,b) center of HDZ at axial centerline; (c-e) center of HDZ at outer periphery. Arrow in (c) is parallel to weld interface.

marginal increase in the range of dispersoid coarseness. This minimal coarsening was attributed to the extremely rapid weld thermal cycle associated with the inertia-friction welding process. In contrast to previous studies of inertia-friction weld microstructures in Al-Fe-Mo-V alloys [6], which showed the cleavage-type fracture of relatively coarse dispersoids (up to two microns in diameter) in the HDZ, no evidence of dispersoid fracture was observed. This absence of fracture was likely attributed in part to the appreciably smaller dispersoid size and also to differences in the structure and fracture strength of the dispersoids.

Analysis of the near-HDZ region at the axial center of the weld produced using low axial force showed that alternating regions exhibiting light and dark-appearing contrast in the lower magnification TEM micrograph originated from variations in the dispersoid population density. Regions of dark contrast exhibited a higher dispersoid population density, while regions of light contrast exhibited a lower dispersoid population density. These differences in contrast and dispersoid structure were associated with variations in the original base metal microstructure which in this region of the HDZ had been "flattened" but not completely homogenized.

The morphology and size of the alpha aluminum grains in the central and near-HDZ regions were similar to those exhibited by the base metal, being nearly equiaxed and ranging in diameter from about 0.25 to 1.0 μm. Considering the extensive elevated-temperature deformation and mechanical mixing experienced in this region, it is suggested that these grains resulted from dynamic recrystallization. Coincidentally, the morphology and size of these grains compared closely with those of the unaffected base metal.

TEM bright-field micrographs in Figures 6c-e show the dispersoid-lean regions at the outer periphery of welds produced using low axial force (white-appearing regions in Figure 4b). In addition to a low dispersoid population density, these regions showed a slightly elongated alpha aluminum grain morphology and a coarser alpha grain size of up to several microns in diameter. One possible explanation for the formation of these regions is localized melting at the weld interface, which is likely to occur at the outer periphery due to the higher rotational velocities and peak temperatures. However, analysis of the regions indicate no evidence of a resolidified microstructure. Alternatively, these regions could result from localized, nonuniform deformation in the HDZ. At these locations, high compressive stresses may locally extrude soft alpha aluminum containing a low dispersoid population from the original base metal microstructure. The occurrence of such nonuniform deformation may also explain the presence of adjacent dark-etching regions which contained a high population density of dispersoids (Fig. 6e). The large alpha aluminum grain size observed in these regions resulted from dynamic recrystallization and grain growth during weld cooling, and the absence of dispersoids which limited such growth in other locations. The near-HDZ at the weld outer periphery appeared comparable to that at the axial centerline.

TEM bright-field micrographs in Figures 7a and b show the center of the HDZ at the axial centerline of the weld produced using high axial force. Although light microscopy analysis (Fig. 5a) indicated incomplete homogenization of the base metal texture in this region, considerable homogenization was, in fact, indicated by the presence of a wide range of dispersoid sizes within a highly localized region. The adjacent near-HDZ showed regions of alternating dark and light-appearing contrast as in the weld produced using low axial force. Consistent with light microscopy observations, TEM observations of the weld zone at the outer periphery of the high axial force weld compared closely with the center of the weld produced at low axial force.

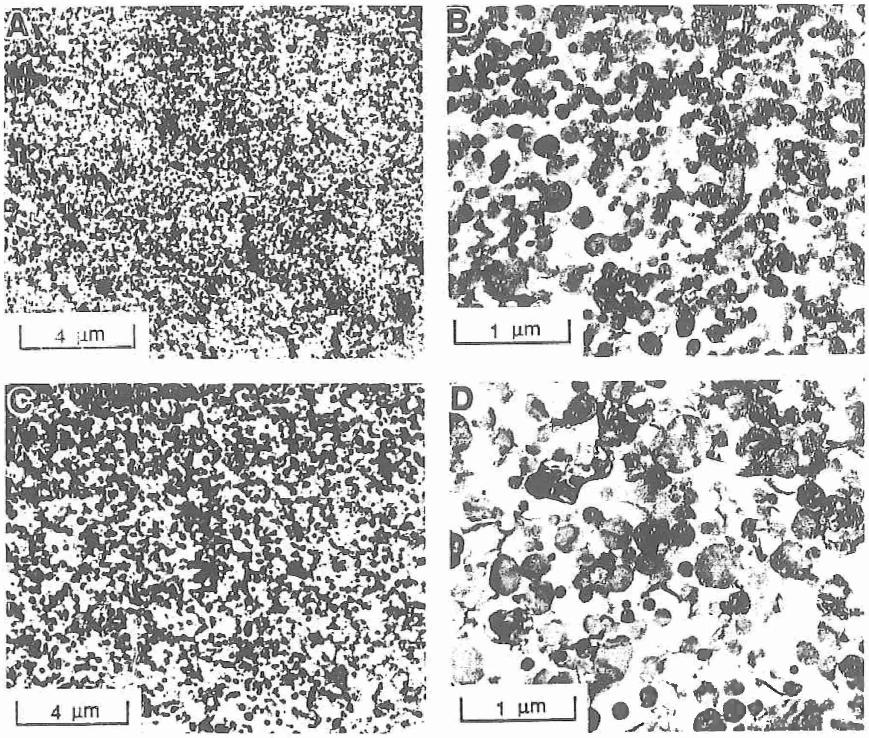

Fig. 7. TEM bright-field micrographs of inertia-friction weld produced in FVS1212 using high axial force: (a,b) center of HDZ at axial centerline; (c,d) center of HDZ at outer periphery.

Hardness and Tensile Testing

Knoop microhardness traverses across the low and high axial force inertia-friction welds generally corresponded with the aforementioned microstructural characteristics. Local variations in the base metal dispersoid structures resulted in a range of hardnesses from about 170 to 210 KHN. As shown in Fig. 4c, hardness values across the weld zone at the axial centerline for the weld produced with low axial force became increasingly consistent within this range in the far HDZ, but decreased down to 150 KHN at the center of the HDZ. This decrease in hardness was attributed to the marginal increase in dispersoid coarseness and possibly the alpha grain size. The hardness traverse at the outer periphery of this weld appeared similar, except at the dispersoid-lean white-appearing regions which exhibited a very low hardness down to about 104 KHN. As shown in Figure 5c, the KHN hardness across the HDZ of the high-axial force weld became more consistent and actually increased to a maximum of 210 KHN at the center, with no evidence of a hardness loss. This high hardness was attributed to the essential absence of a dispersoid or grain coarsening in this structure, the breakup and redistribution of dispersoid clusters and possibly from residual cold work in the structure, although a higher dislocation structure was not evident from TEM. The homogenized but slightly coarsened dispersoid structure at the outer periphery of the high axial force weld exhibited a consistent hardness of about 175 KHN, which represented the lower end of the base metal hardness range.

Tensile test results showed the weld produced at low axial force to exhibit a tensile strength of 462 MPa (67 ksi) and a joint efficiency of 81%. Consistent with the hardness test results, the weld produced with a higher axial force exhibited a higher tensile strength of 489 MPa (71 ksi) and a joint efficiency of 85%. Fracture of both weld types initiated within the HDZ and propagated both across the HDZ and unaffected base metal. It should be noted that the purpose of the present study was not to optimize tensile properties, and it is anticipated that through such a parametric study weld properties could be further improved to achieve nearly 100% joint efficiency.

Summary

Results of the present study have shown that high-integrity, defect-free joints can be generated in FVS1212 using the inertia-friction process. Extensive, high-temperature deformation during welding promoted a continuous reorientation of the base metal grains and a progressive structural transition from the unaffected base metal to the weld center. At the center of the HDZ, this deformation effectively homogenized the macrosopically inhomogeneous dispersoid structure which existed in the as-extruded base metal. Despite reaching near-solidus temperatures and experiencing high stresses, evidence of dispersoid coarsening in the HDZ was negligible. In addition, fracture of the dispersoids in this region was not observed. Nonuniform deformation at center of the HDZ in the outer periphery of the weld produced with low axial force promoted the formation of a dispersoid-lean, coarse alpha grained structure. However, the application of a high axial force eliminated the presence of these soft, undesirable regions, presumably due to their extrusion from the weld zone as flash. Transverse-weld oriented tensile testing showed the tensile strength to be highest for the weld produced with high axial force, providing a joint efficiency of 85%.

Acknowledgements

The authors express appreciation to Drs. S. K. Das and Paul Gilman of Allied-Signal, Inc. for providing the alloy evaluated in this study. The authors are grateful to Dr. Andrew Crowson and the Army Research Office for providing financial support for this work under contract #DAAL03-88-K-0049.

References

1. High Temperature Aluminum Alloy - FVS1212 Data Sheet, Allied-Signal Inc.
2. S. K. Das and L. A. Davis, "High performance aerospace alloys via RS processing," Materials Science and Engineering, 98 (1988) 1-12 .
3. D. J. Skinner, "The physical metallurgy of dispersion strengthened Al-Fe-V-Si alloys," Dispersion Strengthened Aluminum Alloys, ed. Y. W. Kim and W. M. Griffith (Warrendale, PA:TMS/AIME, 1988), 181-197.

4. R. L. Bye, N. J. Kim, D. J. Skinner, D. Raybould, A. M. Brown, "RS/PM aluminum alloys prepared from melt-spun ribbons," Processing of Structural Metals by Rapid Solidification, ed. F.H. Froes and S. J. Savage (Metals Park, OH:ASM International, TMS/AIME, 1988) 283-289.
5. W. A. Baeslack III and K. S. Hagey, "Inertia-friction welding of a rapidly-solidified, powder metallurgy aluminum alloy," Welding Journal, Research Supplement, 67 (1988) 139s-149s .
6. K. H. Hou and W. A. Baeslack III, "Electron microscopy of inertia-friction weldments in a rapidly solidified Al-Fe-Mo-V alloy," Journal of Materials Science and Engineering, 25 (1990) 2642-2653 .
7. P. S. Gilman, M. S. Zedalis, J. M. Peltier and S. K. Das, "The joining of rapidly solidified aluminum-iron-vanadium-silicon alloys for aerospace applications," Advances in Powder Metallurgy - 1989, Vol. 3, ed. T. G. Gasbarre and W. F. Jandeska, Jr., (Princeton, NJ:Metal Powder Industries Federation, American Powder Metallurgy Institute, 1989) 237-250.
8. H. H. Koo, S. Krishnaswamy and W. A. Baeslack III, "Characterization of inertia-friction welds in a high-temperature RS/PM Al-8.5Fe-1.3V-1.7Si alloy (AA-8009)," submitted for publication in Materials Characterization.

Appendix 1G

APPENDIX IG

H. H. Koo, S. Krishnaswamy and W. A. Baeslack III, "Characterization of Inertia-Friction Welds in a High-Temperature RS/PM Al-8.5Fe-1.3V-1.7Si Alloy (AA-8009)," Materials Characterization, 26 (1991) 123-136.

Characterization of Inertia-friction Welds in a High-temperature RS/PM Al-8.5Fe-1.3V-1.7Si Alloy (AA-8009)

H. H. Koo, S. Krishnaswamy, and W. A. Baeslack III

Department of Welding Engineering, The Ohio State University, Columbus, OH 43210

The microstructures of inertia-friction welds produced in a rapid-solidification/powder metallurgy (RS/PM) Al-8.5 wt.% Fe-1.3 wt.% V-1.7 wt.% Si alloy (also designated as FVS0812 or AA-8009) were investigated using black-and-white and color light microscopy, and transmission electron microscopy. These analyses revealed that extensive high-temperature plastic deformation at the center of the weld heat-and-deformation zone effectively homogenized the macroscopically inhomogenous base metal microstructure but did not promote significant dispersoid coarsening or dispersoid fracture. In welds produced using a low axial force, nonuniform deformation at the weld outer periphery resulted in the formation of dispersoid-lean, coarse-grained regions with a hardness appreciably lower than that of the base metal. The application of a sufficiently high axial force eliminated the presence of this undesirable region and prevented hardness degradation across the weld zone.

INTRODUCTION

Dispersion strengthened Al-Fe-V-Si alloys produced by rapid-solidification/powder metallurgy (RS/PM) represent an important new class of structural materials for high-performance, elevated-temperature applications [1–4]. These alloys are based on hypereutectic Al-Fe compositions (8.5–12 wt.% Fe) with ternary and quaternary additions of vanadium and silicon. Through RS/PM processing, a unique, "engineered" microstructure is obtained that consists of nearly spherical, submicron $Al_{13}(Fe,V)_3Si$ (body-centered cubic) dispersoids in an extremely fine-grained alpha aluminum matrix. The low interfacial energy between the dispersoid particles and the matrix, and the low solid-state diffusivity of transition elements in alpha aluminum minimize the driving force for particle coarsening, thereby promoting excellent particle stability at temperatures up to 400°C. Indeed, on a specific strength basis, the alloys compete with Ti-6Al-4V. The spherical morphology of the $Al_{13}(Fe,V)_3Si$ dispersoids, and absence of acicular Al_3Fe (monoclinic) dispersoids, further promote excellent ductility, fracture toughness, and fatigue properties comparable to those of conventional high-strength aluminum alloys.

The effective utilization of Al-Fe-V-Si alloys in structural applications as potential replacements for conventional elevated-temperature aluminum alloys (e.g., 2XXX series alloys) and titanium alloys will require their joining. However, the unique microstructures exhibited by these RS/PM alloys preclude the application of many conventional fusion welding processes and methodologies. Instead, joining processes and procedures will be required that can "recreate" and/or "retain" in the weld

© Elsevier Science Publishing Co., Inc., 1991
655 Avenue of the Americas, New York, NY 10010

zone the "engineered" microstructures upon which alloy properties are dependent. Recent studies have shown that the solid-state inertia-friction welding process offers a strong potential for the effective joining of dispersion-strengthened aluminum alloys [5, 6], including Al-Fe-V-Si alloys [7]. This process combines frictional heat generated at the faying surfaces with a high axial force to produce a metallic bond. The absence of melting at the interface during this process eliminates solidification-related discontinuities, such as porosity or cracking. In addition, the expulsion of surface contaminants and severely heat-and-deformation-affected metal present at the weld interface during the forging stage of the process can promote final coalescence between nearly unaffected base metals. Recently, an inertia-friction welding study on AA-8009 showed that high joint efficiencies of up to 96% can be achieved through proper process parameter control [7]. That investigation did not, however, investigate process parameter effects on the weld zone microstructure.

In view of the emerging trends in the utilization of dispersion-strengthened RS/PM aluminum alloys for structural applications, this investigation was performed to evaluate in detail the microstructural characteristics of inertia-friction welds in the Al-Fe-V-Si alloy AA-8009 (formerly FVS0812). In this work, both conventional black-and-white and color contrast light microscopy techniques were utilized to study microstructural transitions across the weld zone from the unaffected base metal to the weld center. In addition, the spatially fine dispersoid and alpha aluminum grain structures within each weld zone were investigated using transmission electron microscopy (TEM) techniques.

EXPERIMENTAL

The Al-8.5 wt.% Fe-1.3 wt.% V-1.7 wt.% Si alloy (nominal composition) utilized in this investigation originated as rapidly solidified ribbons produced by Allied Signal Inc.'s (Morristown, NJ) planar-flow casting process. Following rapid solidification, the ribbons were pulverized into fine particles, vacuum degassed, hot-pressed into billets, and finally extruded into 32-mm diameter rods. Prior to inertia-friction welding, the rods were sectioned into 50-mm lengths and machined down to a diameter of 22 mm. Weld faying surfaces were dry machined immediately prior to welding.

Inertia-friction welds were produced using an MTI (Mishawaka, IN) Model 120 inertia-friction welding system. Based on previous inertia-friction welding studies of dispersion-strengthened aluminum alloys [5, 6] and preliminary testing, welding parameters were selected that provided two levels of axial displacement and extruded flash. These two weld types were produced using the same moment-of-inertia (0.17 Kg·m^2), rotational velocity (523.6 rad/s) and inertia energy (22.7 kJ), but two different axial force levels of 56.1 kN (designated as "low-axial force") and 83.7 kN (designated as "high axial force").

Following welding, the weld axial displacement and flash uniformity were evaluated by visual analysis. Representative welds were sectioned axially, mounted in epoxy, mechanically ground down to 600-grit SiC paper, rough polished with 3-µm diamond compound, and final polished using a colloidal silica suspension. Following defect analysis of the as-polished specimen surfaces using light microscopy, microstructural characteristics were revealed by etching with Keller's reagent. In addition to conventional black-and-white light microscopy, color light microscopy was performed through the use of differential-interference contrast imaging in order to delineate more clearly microstructural characteristics of the base metal and weld zone.

Alternate specimen halves were carefully sectioned longitudinally at the axial centerline into thin slices 0.3 mm thick with a diamond saw and mechanically thinned on SiC paper down to 0.125 mm. Disks 3 mm in diameter were punched from the foils in the unaffected base metal and from representative regions in the weld HDZ and electrojet thinned in a solution of 25% nitric acid and 75% methanol at −30°C. Thin foils were examined in a JEOL (Peabody, MA) 200CX analytical-electron microscope equipped with a Tracor-Northern (Middleton, WI) TN-2000 energy-disperive x-ray analysis (EDX) system.

Knoop microhardness testing (150 g load) was performed across the weld region at the axial centerline and the outer periphery for correlation with microstructural characteristics.

RESULTS AND DISCUSSION

BASE METAL MICROSTRUCTURE

Light Microscope Analysis

The microstructure of the rapidly solidified ribbon was not characterized in this study. However, previous studies [3, 4] have shown that the extremely rapid cooling rates (10^5–10^7 °C/s) experienced during planar-flow casting promote an extremely fine, microcellular alpha aluminum structure supersaturated in Fe, Si, and V, with extremely fine dispersoids present at cell boundaries. During subsequent consolidation and thermomechanical processing, these intercellular dispersoids coarsen and additional dispersoids form from the supersaturated alpha matrix.

Figure 1(a,b) shows black-and-white and color contrast micrographs, respectively, of the base metal microstructure oriented parallel to the extrusion direction. Evidence of boundaries between individual ribbon particles can be observed in the color micrograph. Contrast differences in the black-and-white micrograph [Fig. 1(a)] resulted from local variations in the dispersoid size and population density, with the light-etching regions containing a higher population density of finer-sized dispersoids than the dark-appearing regions. Macroscopic variations in the dispersoid size and population density were more clearly revealed using color contrast [Fig. 1(b)]. Regions that showed a blue contrast appeared to exhibit the coarsest dispersoids and at least dense dispersoid populations and correspondingly the largest regions of dispersoid-free alpha aluminum. Conversely, regions that showed a light gold contrast exhibited the finest dispersoids and most dense dispersoid populations. Regions of dark gold or brown contrast contained dispersoids intermediate in size and population densities between these extremes. As shown, regions containing both coarse and fine dispersoids (i.e., blue and light gold contrast) were commonly observed within a single ribbon particle. These microstructural variations within a single particle originated from differences in the cooling rate of the original ribbon, with the side contacting the quenching wheel experiencing appreciably higher cooling rates than the opposite free surface side. Higher cooling rates correspondingly promoted a finer as-solidified microstructure and ultimately a finer as-processed dispersoid structure. Although not apparent in Fig. 1, occasional narrow white bands were observed at particle boundaries.

TEM ANALYSIS

Characteristics of the base metal microstructure were more clearly delineated using TEM. The low-magnification TEM bright-field micrographs in Fig. 2(a,b) show the boundary between ribbon particles and reveal differences in the dispersoid sizes and population densities on either side of this boundary. Examination of relatively uniform dispersoid structures at increased magnification in Fig. 2(b,c), and at other locations in the base metal, showed the dispersoids to exhibit a nearly spherical morphology with diameters ranging from about 50 to 250 nm. Dispersoids were located both within the alpha-aluminum matrix and at the boundaries of nearly equiaxed alpha aluminum grains.

In this unaffected base metal, the alpha grain sizes ranged from about 0.5 to 1 μm

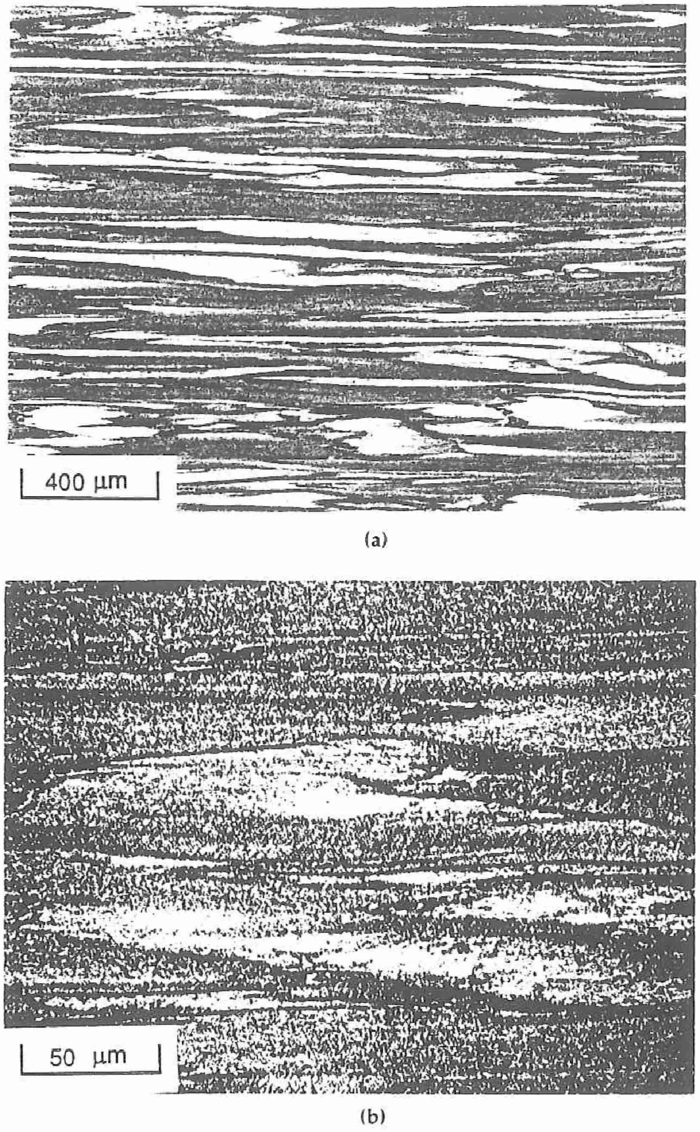

FIG. 1. Light micrographs of as-extruded AA-8009 base metal: (a) black-and-white contrast, (b) color contrast.

in diameter. Occasional regions exhibited what appeared at lower magnification to be coarser dispersoids and a high proportion of alpha phase, as in the lower-left-hand portion of Fig. 2(b). Analysis of these regions at increased magnification in Fig. 2(e) showed the presence of coarse dispersoids and clusters of finer dispersoids along alpha grain boundaries. Generally, these regions exhibited a lower population of dispersoids as compared to the regions of uniform dispersoid distribution [e.g., Fig. 2(c,d)] and a somewhat coarser alpha grain size, up to about 1.5 μm in diameter. Considering the heterogenous dispersoid structure in this region, which corresponded to the regions of blue contrast in Fig. 1(b), it is suggested that it likely experienced slower cooling rates than the adjacent regions that contained fine, uniform dispersoid distributions. However, since the analysis of powder particles was not performed, this correlation could not be precisely confirmed.

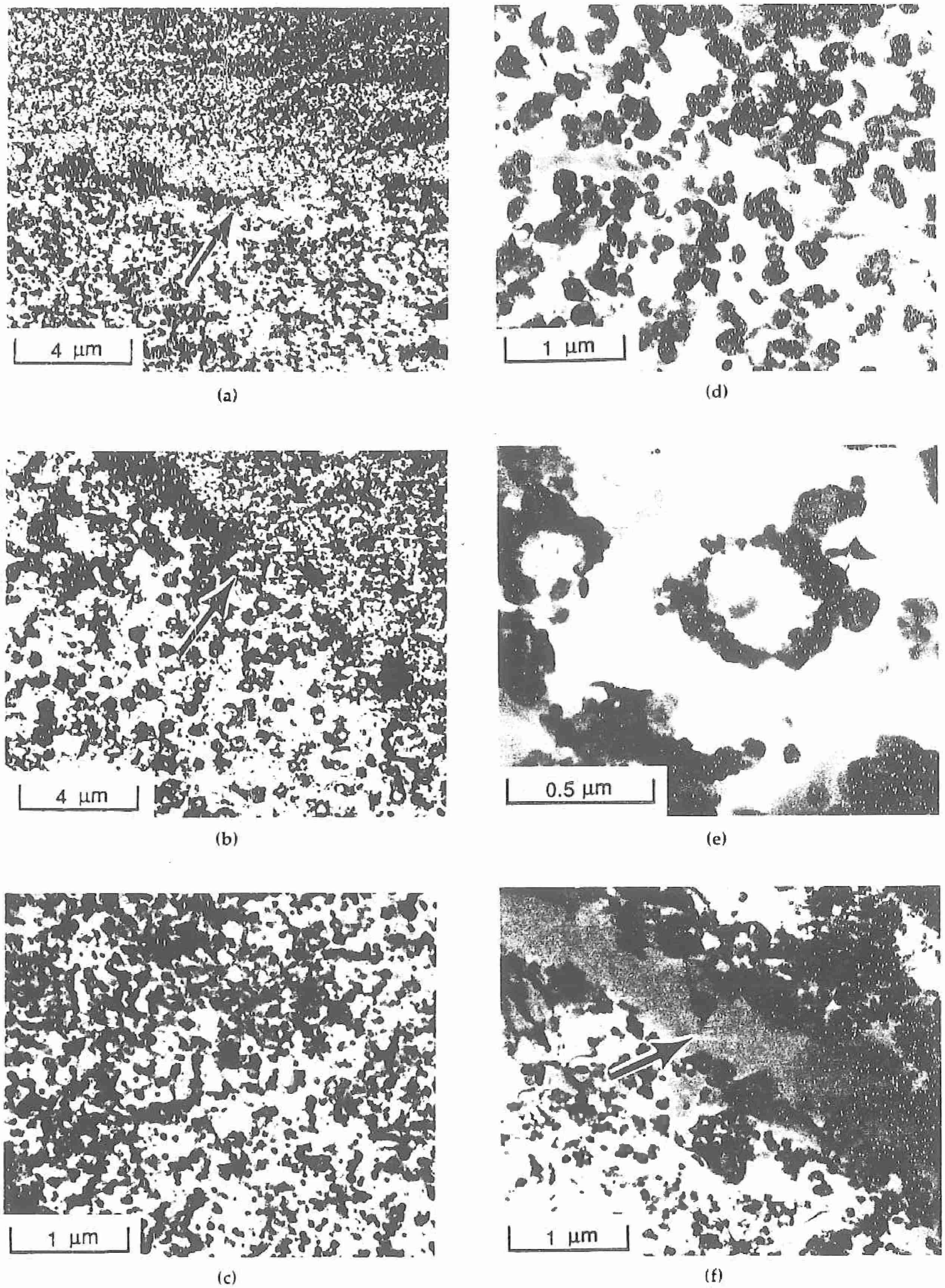

(a) (d)

(b) (e)

(c) (f)

FIG. 2. TEM bright-field micrographs of AA-8009 extruded base metal: (a,b) low magnification micrographs showing variations in dispersoid size, population density and distribution, and boundaries between ribbon particulates (arrows); (c,d) uniform dispersoid structures in (a); (e) dispersoids at alpha grain boundaries in lower portion of (b); (f) dispersoid-free band (arrow).

Limited selected-area diffraction of the dispersoids and EDX analysis of numerous dispersoids consistently indicated an approximately $Al_{13}(Fe,V)_3Si$ dispersoid type. As shown in Fig. 2(f), occasional dispersoid-free bands were also observed in the base metal microstructure. These regions may have originated from the presence of dispersoid-free ribbon particles, or possibly from nonhomogenous deformation during extrusion. No evidence of acicular dispersoids, as previously observed in studies of a rapidly solidified Al-Fe-Mo-V alloy [6], was observed. This result was consistent with the previously observed influence of V in stabilizing the cubic $Al_{13}(Fe,V)_3Si$ over the hexagonal Al_8Fe_2Si or monoclinic Al_3Fe phases [3].

WELD ZONE CHARACTERIZATION

Light Microscope Analysis

Visual examination of the low and high axial force inertia-friction welds found the presence of smooth, symmetrically uniform flash around the entire weld circumference. A greater extent of extruded flash in the weld produced at higher axial force was consistent with the appreciably greater axial displacement experienced by this weld (10.2 mm vs. 2.7 mm).

Macroscopic examination of the axially sectioned weld specimen in the as-polished condition found no evidence of lack-of-bonding defects. Etching of the specimens revealed approximately hourglass-shaped, heat-and-deformation zones in both weld types [Fig. 3(a,b)]. Interestingly, the widths of the heat-and-deformation zones (HDZs) did not vary appreciably (at a constant distance from the axial centerline) despite significant differences in the axial displacement and the quantity of extruded flash.

Light microscope analysis at increased magnification more clearly revealed the characteristics of the weld HDZ, and differences in this region between the axial center and outer periphery. Figure 4(a,b) shows microstructure traverses from the

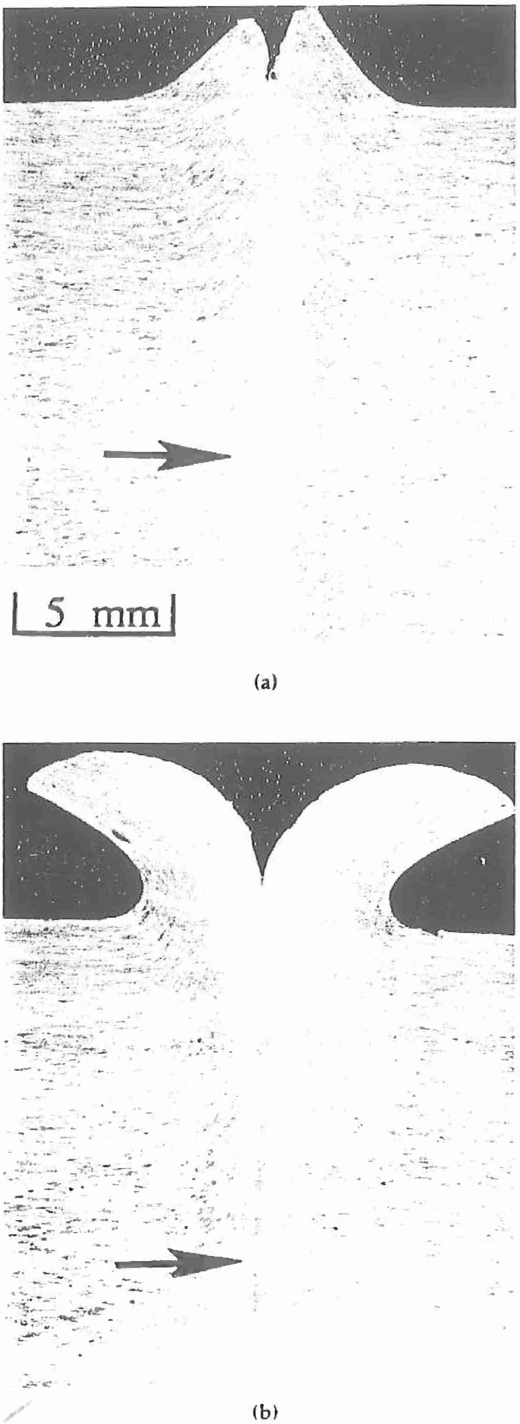

(a)

(b)

FIG. 3. Light macrographs of inertia-friction welds produced in AA-8009: (a) low axial force, (b) high axial force. Arrows indicate axial centerline.

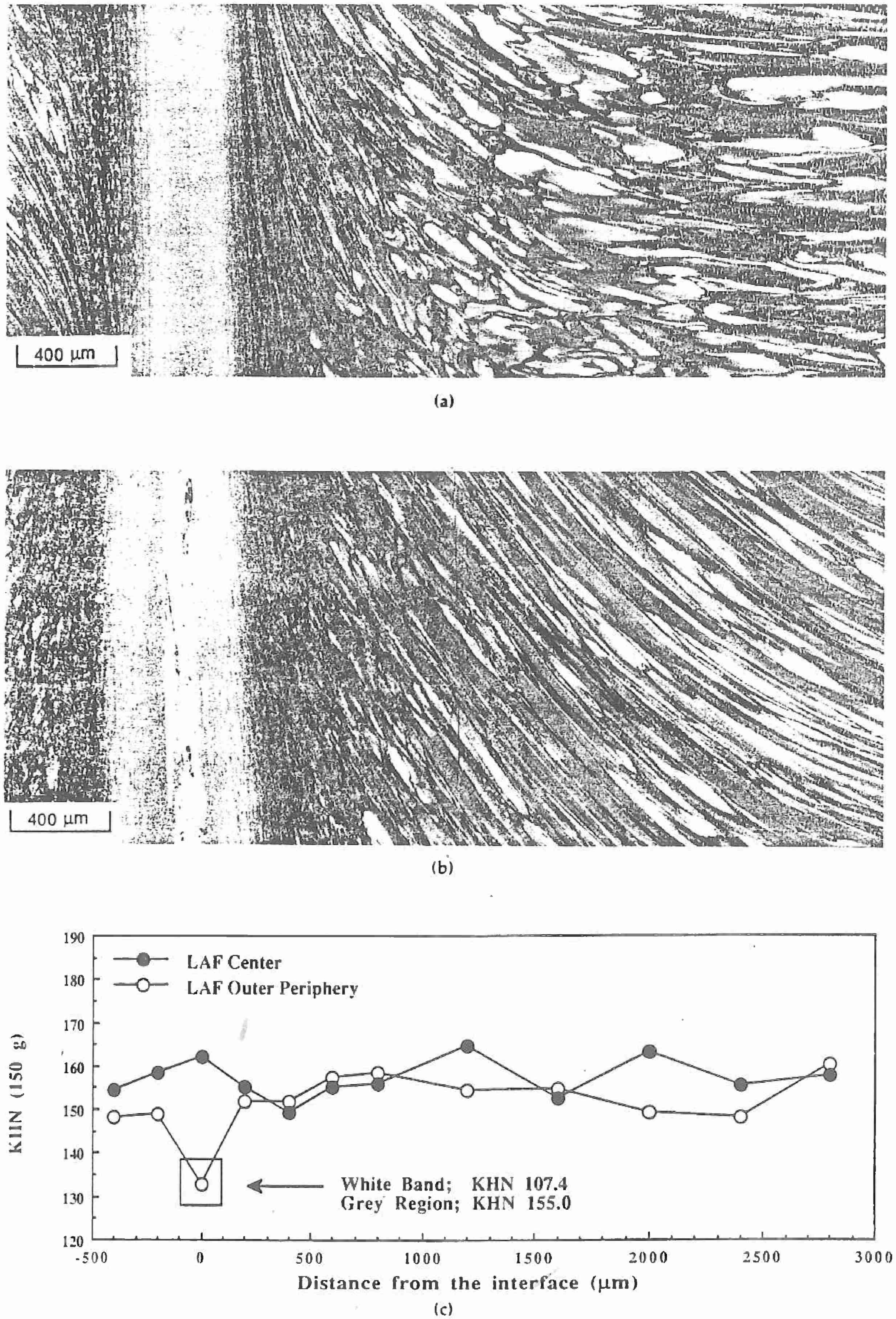

FIG. 4. Light micrographs of the (a) center and (b) outer periphery regions and corresponding KHN hardness traverses (c) for an inertia-friction weld produced in AA-8009 using low axial force.

unaffected base metal to the center of the weld HDZ at the axial center and outer periphery of a weld produced using low axial force. The orientation of the base metal microstructure continually changed from parallel to perpendicular to the original base alloy extrusion direction. This change in orientation resulted from the complex combination of axial and torsional stresses experienced in the weld zone during inertia-friction welding. During welding, the plastic flow of metal heated to high temperatures by frictional heating occurred from the center region to the outer periphery in an outward spiraling pattern. Nearer to the center of the weld HDZ, the reoriented base metal microstructure became increasingly "flattened" because of high axial compressive stresses. In this region, microstructural variations that existed in the base metal because of differences in dispersoid size, population density, and distribution became less apparent. Indeed, at the center of the HDZ, the structure appeared completely homogenized.

The nature of this base metal microstructure "deformation" and "homogenization" is more clearly delineated by the color contrast micrographs shown in Fig. 5. As shown, the originally blue, brown, and light gold regions were still clearly discernable in the low-deformation outer HDZ [Fig. 5(a)] but became "flattened" and increasingly homogenized nearer to the center of the HDZ, exhibiting a nearly uniform gold contrast in the near HDZ and a homogenous light blue contrast at the center of the HDZ [Fig. 5(b)].

At the outer periphery of the low axial force weld [Fig. 4(b)], narrow, white-appearing bands and adjacent dark-appearing regions were observed oriented parallel to the weld interface. Although not shown, the examination of these regions at increased magnification indicated a very low dispersoid population density in the light-appearing regions and a higher population dispersoid density in the adjacent dark-appearing regions versus the surrounding near HDZ.

Figure 6(a,b) shows microstructure traverses across a weld produced using high axial force. At the weld centerline, where the HDZ width was relatively narrow, the textured base metal structure became increasingly "flattened" but did not achieve complete homogeniety as in the low axial force weld. Near the weld outer periphery, an appreciably wider HDZ was observed that exhibited regions comparable to those observed at the center of the low axial force weld. No evidence of light- or dark-appearing regions was observed in the weld produced with high axial force. The absence of these structures in welds produced with high axial force was attributed to their extrusion from the weld interface during the final forging stage of the welding process.

TEM Analysis

TEM analysis of the HDZ center in the inertia-friction weld produced with low-axial force revealed a uniform distribution of dispersoids ranging in size from about 50 to 300 nm. Consistent with light microscope results, this homogenization appeared to result from the extensive mechanical mixing of base metal regions that originally contained varying distributions of relatively finer or coarser dispersoids [as shown in Fig. 2(a,b)]. Despite the elevated temperatures experienced in this region during the weld thermal cycle (albiet for very short times), negligible evidence of dispersoid coarsening was observed. In contrast to previous studies of inertia-friction weld microstructures in Al-Fe-Mo-V alloys [6], which showed the cleavage-type fracture of relatively coarse dispersoids (up to 2 μm in diameter) in the HDZ, no evidence of dispersoid fracture was observed in AA-8009. This absence of fracture was likely attributed in part to the appreciably smaller dispersoid size and also to differences in the structure and fracture strength of the dispersoids.

Figure 7(c,d) shows the near-HDZ region at the axial center of the weld pro-

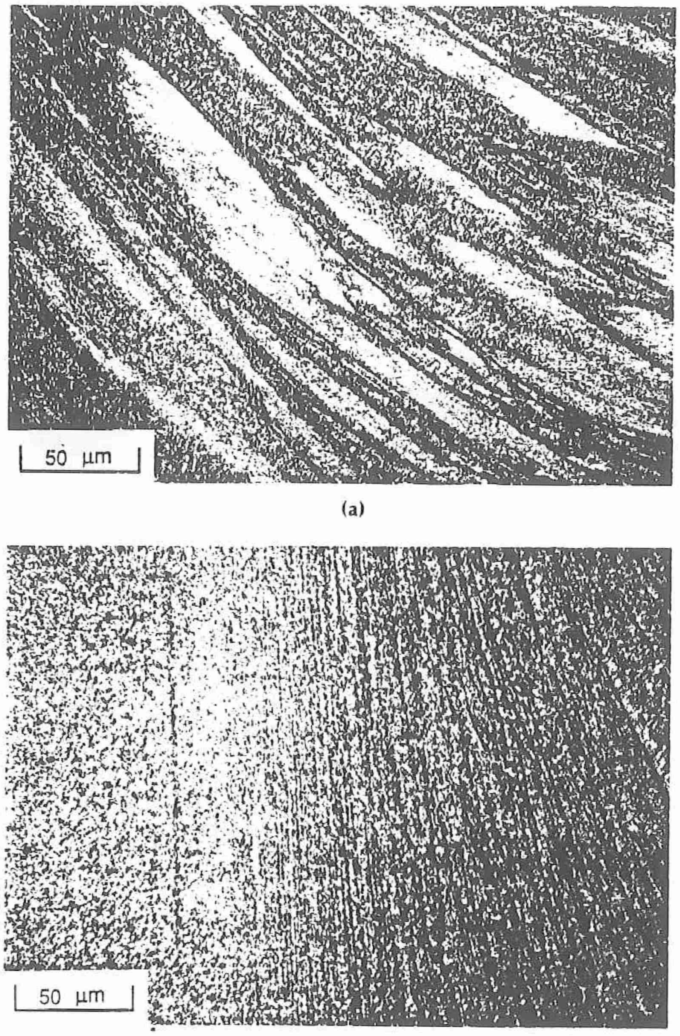

(a)

(b)

Fig. 5. Light micrographs (color contrast) of inertia-friction weld produced in AA-8009 using low axial force: (a) outer HDZ, (b) center of HDZ.

duced using low axial force. In Figs. 4 and 5, this region appeared as the severely "flattened" microstructure adjacent to the homogenous structure at the center of the HDZ. Alternating regions exhibiting light- and dark-appearing contrast in the lower magnification TEM micrograph [Fig. 7(a)] originated from variations in the dispersoid population density. Regions of dark contrast exhibited a higher dispersoid population density [right-hand side of Fig. 7(d)], while regions of light contrast [left-hand side of Fig. 7(d)] exhibited a lower dispersoid population density. These differences in contrast and dispersoid structure were likely associated with variations in the original base metal microstructure that in this region of the HDZ had not been completely homogenized. Alternatively, they may have been promoted by non-uniform deformation of the metal at the weld interface during welding.

The morphology and size of the alpha aluminum grains in the central and near-HDZ regions were similar to those exhibited by the base metal, being nearly equiaxed and ranging in diameter from about 0.25 to 1.0 µm. Considering the extensive elevated-temperature deformation and mechanical mixing experienced in this

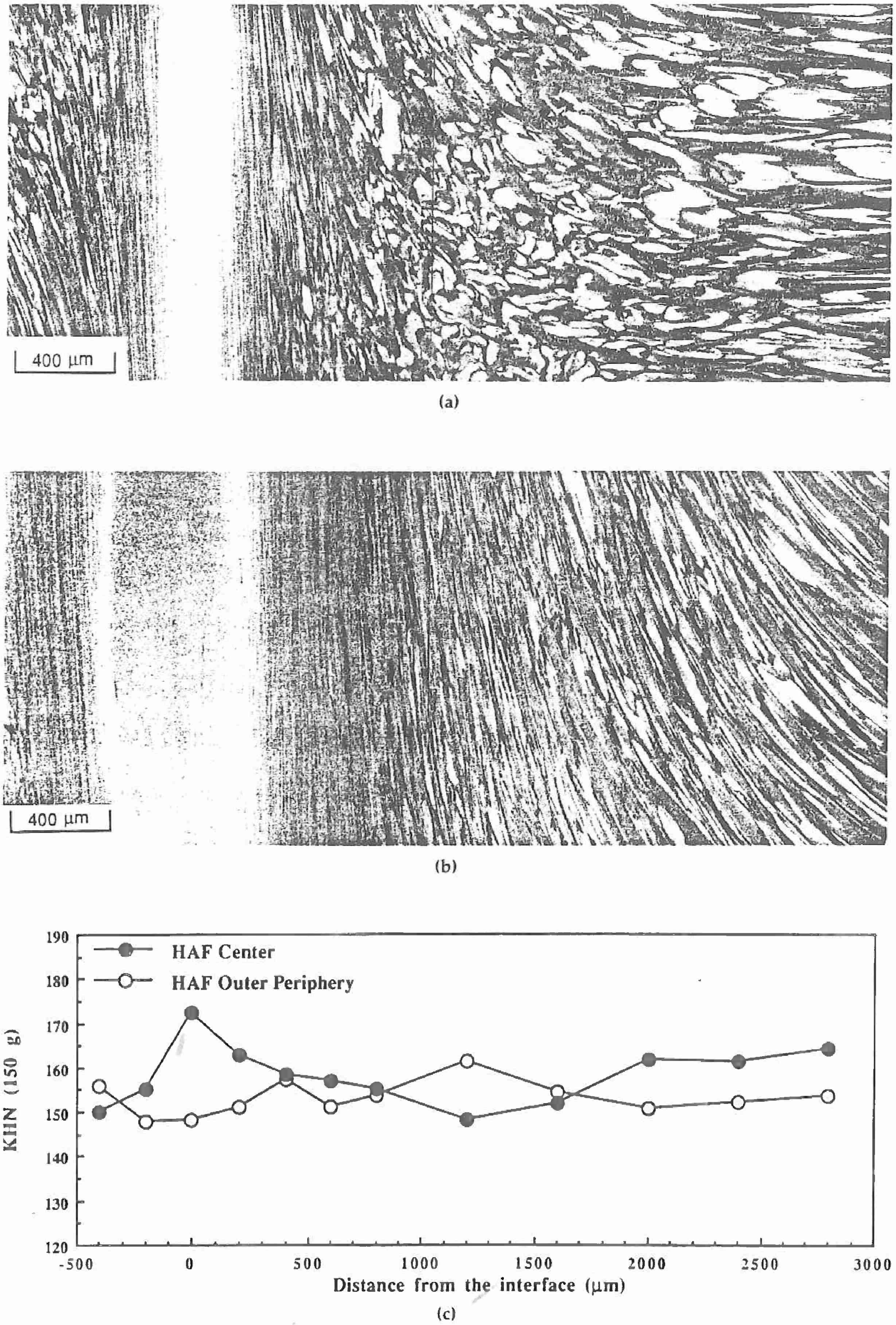

FIG. 6. Light micrographs of the (a) center and (b) outer-periphery regions and corresponding KHN hardness traverses (c) for an inertia-friction weld produced in AA-8009 using high axial force.

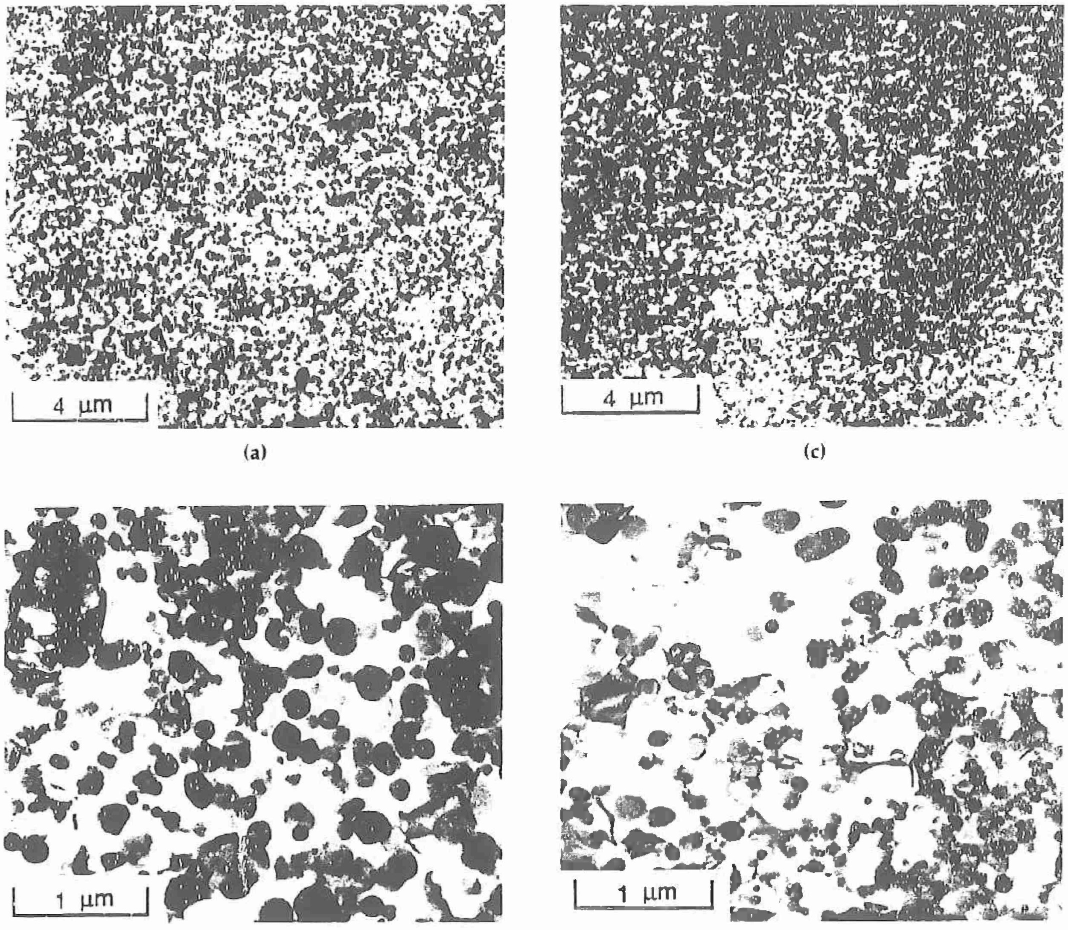

(a) (c)

(b) (d)

FIG. 7. TEM bright-field micrographs at axial centerline of inertia-friction weld produced in AA-8009 using low axial force: (a,b) center of HDZ, (c,d) near HDZ.

region, it is suggested that these grains must be the result of dynamic recrystallization. Coincidentally, however, the morphology and size of these grains compared closely with those of the unaffected base metal.

TEM bright-field micrographs in Figure 8(a–c) show the dispersoid-lean regions at the outer periphery of welds produced using low axial force [white-appearing regions in Fig. 4(b)]. In addition to a low dispersoid population density, these regions showed a slightly elongated alpha aluminum grain morphology and a coarser alpha grain size of up to several microns in diameter. One possible explanation for the formation of these regions is localized melting at the weld interface, which would occur most likely at the outer periphery because of the higher rotational velocities and peak temperatures. However, analysis of the regions indicate no evidence of a resolidified microstructure. Alternatively, these regions more likely resulted from localized, nonuniform deformation in the HDZ. At these locations, high compressive stresses may locally extrude soft alpha aluminum containing a low-dispersoid population from the original base metal microstructure. The occurrence of such nonuniform deformation may also explain the presence of adjacent dark-etching regions that contained a high-population density of dispersoids [Fig. 8(c)]. The large alpha

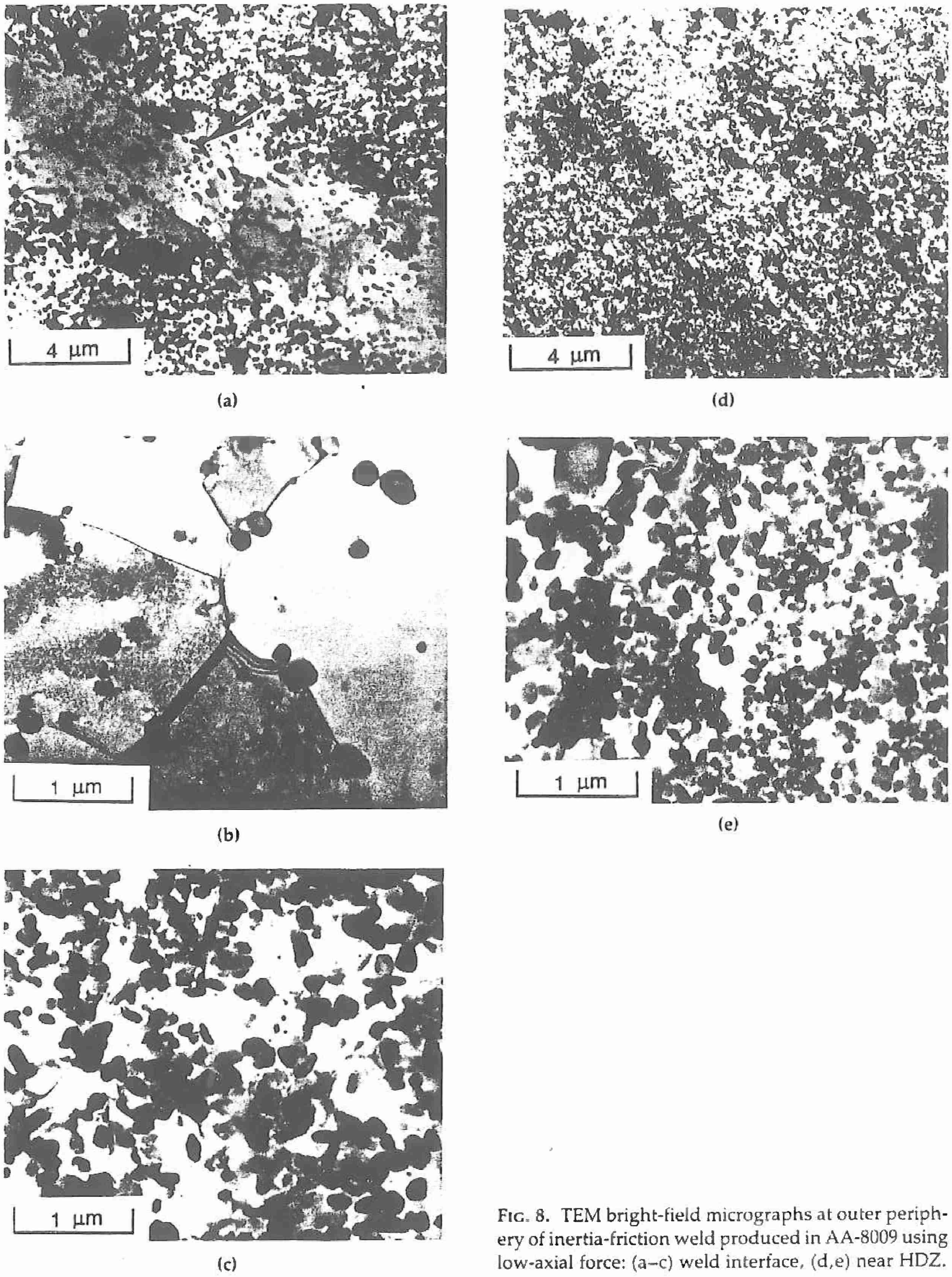

FIG. 8. TEM bright-field micrographs at outer periphery of inertia-friction weld produced in AA-8009 using low-axial force: (a–c) weld interface, (d,e) near HDZ.

aluminum grain size observed in these regions resulted from dynamic recrystallization and grain growth during weld cooling, and the absence of dispersoids that limited such growth in other locations. The near HDZ at the weld outer periphery shown in Fig. 8(d,e) appeared comparable to that at the axial centerline. The striated structure appeared related primarily to the original base metal structure. Intimate mix-

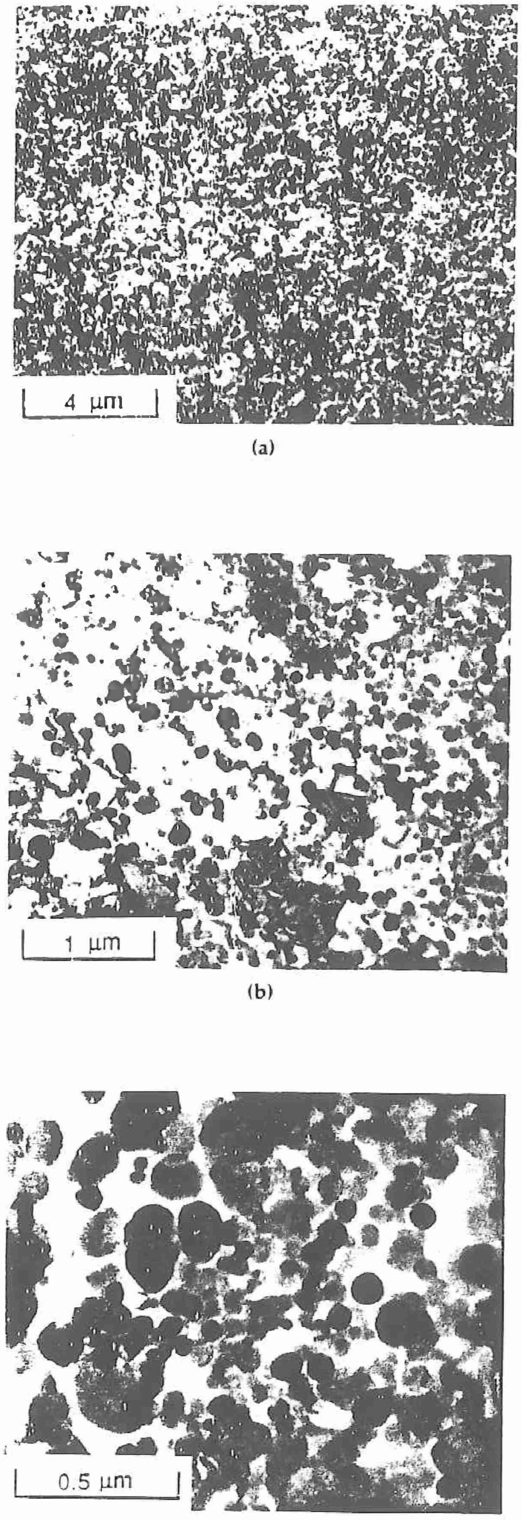

FIG. 9. TEM bright-field micrographs at center of HDZ along axial centerline of inertia-friction weld produced in AA-8009 using high-axial force.

tures of a wide range of dispersoid sizes in Fig. 8(e), however, did suggest some degree of mechanical mixing in this region. The exact origin of what appear to be "clusters" of dispersoids on the left-hand side of Fig. 8(e) was unclear.

TEM bright-field micrographs in Fig. 9(a–c) show the center of the HDZ at the axial centerline of the weld produced using high axial force. Although light microscope analysis [Fig. 6(a)] indicated incomplete homogenization of the base metal texture in this region considerable homogenization was, in fact, indicated by the presence of a wide range of dispersoid sizes within a highly localized region, as shown in Fig. 9(c). The adjacent near HDZ showed regions of alternating dark- and light-appearing contrast as in the weld produced using low axial force. Consistent with light microscope observations, TEM analysis observations of the weld zone at the outer periphery of the high-axial force weld compared closely with the center of the weld produced at low axial force.

HARDNESS TESTING

Knoop microhardness traverses across the low and high axial force inertia-friction welds corresponded well with the aforementioned microstructural characteristics. Local variations in the base metal dispersoid structures resulted in a range of hardnesses from about 150 to 165 KHN. As shown in Fig. 4(c), hardness values across the weld zone at the axial centerline for the weld produced using low axial force were within this range of values measured for the unaffected base metal. These observations were consistent with the negligible evidence of dispersoid and alpha grain coarsening in these HDZ regions. As expected, the white-appearing, low-dispersoid density regions located at the outer periphery of the welds produced using a low axial force exhibited a hardness (107 KHN) appreciably below that of the base metal and surrounding HDZ.

As shown in Fig. 6(c), the KHN hardness increased substantially at the center of the weld produced using a high axial force. Although the dispersoid structure in this region was nearly homogenized, the size and density appeared generally comparable to other weld regions. Therefore, the increase in hardness was most likely attributed to the formation of a finer alpha grain structure or the presence of residual cold working in this region of the weld. At the outer periphery of this weld, the hardness was comparable to that of the base metal. As in the low axial force weld, however, hardness measurements in this microstructurally "homogenized" HDZ region were more uniform than in the base metal, where variations were promoted by local differences in the dispersoid size and population density.

SUMMARY

Results of the present study have demonstrated that high-integrity, defect-free joints can be produced in AA-8009 using the inertia-friction process. Extensive, high-temperature deformation during welding promoted a continuous and relatively uniform microstructural transition from the unaffected base metal to the weld center. At the center of the HDZ, this deformation effectively homogenized the macroscopically inhomogenous dispersoid structure that existed in the as-extruded base metal. Evidence of dispersoid coarsening in this region was negligible, apparently because of the rapid inertia-friction welding thermal cycle.

Nonuniform deformation at center of the HDZ in the outer periphery of the weld produced with low-axial force promoted the formation of dispersoid-lean, coarse alpha-grained structure. However, the application of a high axial force eliminated the presence of these soft, undesirable regions, presumably because of their expulsion from the weld zone as flash.

The authors express appreciation to Drs. S. K. Das and Paul Gilman of Allied-Signal, Inc., for providing the alloy evaluated in this study. Thanks are also extended to Mr. Peter Kerr of the Materials Department at The Welding Institute for his assistance with color metallography. Finally, the authors gratefully acknowledge Dr. Andrew Crowson and the Army Research Office for their support of this work under contract #DAAL03-88-K-0049.

References

1. *High Temperature Aluminum Alloy-8009 (FVS0812) Data Sheet,* Allied-Signal Inc., Morristown, NJ.
2. S. K. Das and L. A. Davis, High performance aerospace alloys via RS processing, *Mater. Sci. Eng.* 98:1–12 (1988).
3. D. J. Skinner, The physical metallurgy of dispersion strengthened Al-Fe-V-Si alloys, in *Dispersion Strengthened Aluminum Alloys* (Y. W. Kim and W. M. Griffith, eds.), TMS/AIME, Warrendale, PA (1988), pp. 181–197.
4. R. L. Bye, N. J. Kim, D. J. Skinner, D. Raybould, and A. M. Brown, RS/PM aluminum alloys prepared from melt-spun ribbons, in *Processing of Structural Metals by Rapid Solidification* (F. H. Froes and S. J. Savage, eds.), ASM International, Metals Park, OH (1988), pp. 283–289.
5. W. A. Baeslack III and K. S. Hagey, Inertia-friction welding of a rapidly-solidified, powder metallurgy aluminum alloy, *Weld. J.* 67(Res. Suppl.):139s–149s (1988).
6. K. H. Hou and W. A. Baeslack III, Electron microscopy of inertia-friction weldments in a rapidly solidified Al–Fe–Mo–V alloy, *J. Mater. Sci.* 25:2642–2653 (1990).
7. P. S. Gilman, M. S. Zedalis, J. M. Peltier, and S. K. Das, The joining of rapidly solidified aluminum-iron-vanadium-silicon alloys for aerospace applications, in *Advances in Powder Metallurgy—1989* (T. G. Gasbarre and W. F. Jandeska, Jr., eds.), Metal Powder Industries Federation, American Powder Metallurgy Institute, Princeton, NJ (1989), Vol. 3, pp. 237–250.

Received October 1990; accepted December 1990.

Appendix 1H

APPENDIX IH

H. H. Koo and W. A. Baeslack III, "Structure, Properties and Fracture of a Linear-Friction Weld in Rapidly-Solidified Al-Fe-V-Si," Materials Characterization, (in press).

Short Communication

STRUCTURE, PROPERTIES AND FRACTURE OF A LINEAR-FRICTION WELD IN RAPIDLY-SOLIDIFIED AL-FE-V-SI ALLOY 8009

H. H. Koo and W. A. Baeslack III

Department of Welding Engineering
The Ohio State University
Columbus, Ohio 43210

INTRODUCTION

Al-Fe-V-Si alloys produced by rapid solidification (RS) casting technology represent an important class of emerging materials for elevated-temperature aerospace applications. These alloys, which are basically hypereutectic Al-Fe compositions (8-12 wt% Fe) with ternary and quaternary additions of vanadium and silicon, exhibit a microstructure comprised of nearly-spherical, submicron $Al_{13}(Fe,V)_3Si$ dispersoids distributed uniformly in a matrix of fine-grained alpha aluminum. The slow coarsening rate of these dispersoids promotes microstructural stability and excellent tensile strength at temperatures up to 375°C. Furthermore, the absence of acicular Al_3Fe dispersoids provides superior ductility, toughness and fatigue properties comparable to those of conventional ingot metallurgy aerospace aluminum alloys.

Aluminum alloy 8009 (formerly designated FVS0812) is a commercially-available Al-Fe-V-Si alloy designed to provide an optimum combination of elevated-temperature strength and fracture toughness [1]. The incorporation of this alloy into structural aerospace applications will commonly require joining. Recently, the authors have demonstrated the effectiveness of inertia-friction welding in producing high-integrity, solid-state welds in 8009 [2]. Under optimum conditions, the expulsion of heat-and-deformation-affected, highly-plasticized metal at the weld interface during the final stage of welding can promote final coalescence between microstructures which retain the fine base metal dispersoid and alpha grain sizes. Although effective, the conventional inertia-friction welding process is limited to the joining of workpieces which exhibit a near-circular cross-section.

Linear-friction welding is a process which involves frictional heating of the workpiece faying surfaces by translational (ie., linear) motion (Fig. 1). Consequently, this process effectively extends the utility of friction welding to include the joining of non-circular workpieces. Recently, The Welding Institute in Cambridge, England developed a linear-friction welding machine capable of producing joints between engineering-sized components. The purpose of the present work was to generate and characterize linear-friction welded 8009 and to compare these characteristics with those determined previously for conventional inertia-friction welds in this alloy [2].

EXPERIMENTAL PROCEDURE

The Al-8.5 wt% Fe - 1.3 wt% V - 1.7 wt% Si alloy (nominal composition) evaluated in this study originated as 32 mm diameter extruded rod. For linear-friction welding, the rod was sectioned into 50 mm lengths and turned down to a diameter of 25 mm. Weld faying surfaces were dry machined immediately prior to welding.

Welds between the cylindrical specimens were produced on a full-scale linear-friction welding machine located at The Welding Institute. Welding parameters included a 2.5 mm linear displacement amplitude, a frequency of 50 Hz, a preset burnoff distance of 4 mm, and friction and forge forces of 30 and 50 kN, respectively. Note that from a welding process application standpoint, the object of this study was only to demonstrate the feasibility of linear-friction welding 8009 and not to fully optimize welding parameters and conditions.

Subsequent to welding, the axial displacement was measured and the flash uniformity was visually evaluated. The weld was sectioned axially, mounted in epoxy, mechanically ground to 600 grit SiC paper, rough polished with 3 micron diamond compound and final polished using a colloidal silica suspension. Microstructural characteristics were revealed by etching with Keller's reagent.

Thin slices 0.3 mm in thickness were sectioned longitudinally at the axial centerline using a diamond saw and mechanically thinned on SiC paper down to 0.125 mm. Disks 3 mm in diameter were punched from foils in the unaffected base metal and from representative regions in the weld HDZ and electrojet thinned in a solution of 25% nitric acid and 75% methanol at -30°C. Thin foils were examined in a JEOL 200CX analytical-electron microscope.

Following microstructure analysis, Knoop microhardness traverses (150 gm load) were performed at the weld axial centerline and the outer periphery. In addition, tensile test specimens (gage section: 25 mm length x 4.5 mm width x 1.5 mm thickness) were extracted from the center and outer periphery of the weld and tested as per ASTM E8-87 at an extension rate of 0.25 mm/min. Following mechanical testing, fracture surfaces were characterized using scanning-electron microscopy.

RESULTS AND DISCUSSION

Figure 2a shows a light micrograph of the as-extruded 8009 base metal microstructure. Regions of varying contrast oriented parallel to the extrusion direction result from local variations in the dispersoid size and population density, with light-etching regions exhibiting a higher population density of finer dispersoids than the dark-appearing regions. TEM analysis of the base metal microstructure, which has been described in detail previously [2], revealed a range of dispersoid sizes. The micrograph shown in Fig. 2b shows a typical region containing dispersoids approximately 100 to 250 nm in diameter and an alpha grain size of about 0.5 microns in diameter. The $Al_{13}(Fe,V)_3Si$ dispersoids were nearly spherical in shape and were located both along alpha grain boundaries and within the fine alpha grains.

The linear-friction welded coupon shown in Fig. 3 shows asymmetric flash formation, with a higher volume of flash produced in the direction of translation (arrow). The total upset produced during welding was 5.8 mm, which included the preset 4 mm burnoff displacement and the additional upset experienced during application of the forge force. These levels of flash formation and axial displacement were intermediate between those of conventional inertia-friction welds produced previously in 8009 using low and high axial force levels [2].

Figure 4 shows a light macrograph of the axially-sectioned linear-friction weld. A distinctly hourglass-shaped heat-and-deformation zone can be observed to range in width from several millimeters at the outer periphery to less than 0.5 mm at the axial centerline. The "curling-back" of flash produced during linear-friction welding was much more pronounced than in high-axial force inertia-friction welds which exhibited an even greater volume of flash [2]. This difference in flash geometry may be associated with more continuous upset and flash formation during linear-friction welding versus inertia-friction welding, for which upset and flash formation occur principally during the final stage of the weld sequence.

Figures 5a and 5b show microstructure traverses from the unaffected base metal (in 5a) and the outer-HDZ (in 5b) to the center of the weld HDZ at the axial centerline and outer periphery of the linear-friction weld, respectively. As indicated in the macrograph shown in Fig. 4, the width of the outer-HDZ was extremely narrow at the axial centerline. Directly at the centerline, the macrostructure was deformed in a manner which made light or dark contrast regions appear nearly equiaxed, while directly adjacent to this axial centerline these regions rapidly changed their orientation from parallel to perpendicular to the original extrusion direction. At the outer periphery, the continuous change in the base metal orientation in the outer-HDZ occurred over a much wider region. The original base metal microstructure also became increasingly "flattened" due to the high compressive stresses and plastic deformation experienced in this region.

Within the light-contrast inner-HDZ regions, contrast variations associated with differences in dispersoid size and population density in the base metal were essentially absent, suggesting complete microstructure homogenization. Directly at the center of the inner-HDZ, a band of dark contrast was observed at both the axial centerline and outer periphery, suggesting dispersoid coarsening.

TEM bright-field analysis of the HDZ center at the axial centerline was consistent with light microscopy analysis in indicating homogenization of the base metal dispersoid microstructure due to intense mechanical mixing. As shown in Fig. 6a, in addition to homogenization of the base metal microstructure, TEM analysis revealed both dispersoid coarsening and morphological elongation, with a major axis length of up to 500-750 nm. Interestingly, the longitudinal axis of the elongated dispersoids frequently paralleled the weld interface. A relatively high proportion of finer, nearly-spherical dispersoids were also observed in this region. Although the inner-HDZ experienced extensive mechanical deformation, the alpha grain size remained about the same as in the unaffected base metal and the intragranular dislocation density was low, suggesting that recrystallization had occurred but that grain growth was prevented by dispersoid pinning effects. From a comparative standpoint, previously studied inertia-friction welds showed no evidence of dispersoid grain coarsening within the HDZ [2]. This suggested that the thermal cycle experienced was more rapid in the inertia-friction versus the linear-friction welds.

At the outer edge of the inner-HDZ (region of white contrast in Fig. 5), dispersoid homogenization was also observed, but coarsening was appreciably less than within the center of the inner-HDZ. As shown, evidence of dispersoid elongation was also observed (Fig. 6b). Although the regions of dispersoid coarsening were wider, TEM analysis of inner-HDZ at the weld outer periphery appeared comparable to that observed at the axial centerline.

TEM analysis of the outer-HDZ at the axial centerline and outer periphery showed variations in dispersoid size and population density comparable to that of the unaffected base metal, with essentially no noticible change in dispersoid or alpha grain size.

Knoop microhardness traverses taken across the axial centerline at the outer periphery of the linear-friction weld corresponded very closely with the microstructure analysis, indicating relatively little change in the outer-HDZ from the average base metal hardness of approximately KHN 150-155. Within the light-contrast inner-HDZ region, the hardness actually increased slightly up to KHN 155-160. As described above, TEM examination of this region showed partial homogenization of the base metal dispersoid structure, but no evidence of a change in the dispersoid size or population density. Alternate explanations for this slight hardness increase may be incomplete recrystallization or the generation of a finer alpha grain size via dynamic recrystallization. This explanation, however, appeared to be precluded by TEM analysis, which showed an alpha grain size comparable to that of the base metal and a relatively low dislocation density within the grains. Within an extremely narrow region directly at the center of the inner-HDZ (dark-appearing line at center of inner-HDZ in Figs. 5a and b), where dispersoid-coarsening was observed with TEM, the hardness decreased to about KHN 135-140.

Table 1 compares room-temperature tensile properties of the linear-friction weld with those of inertia-friction welds produced previously at low and high axial force. Relatively high joint efficiencies were observed both at the axial centerline (86%) and outer periphery (84%) of the linear-friction weld. Despite exhibiting a decrease in hardness at the center of the HDZ, the tensile strength of the linear-friction weld was only slightly below that of the high-axial force inertia-friction weld which showed no decrease in hardness across the HDZ [2]. This negligible difference in weld strength may be attributed to the extremely narrow width of the dispersoid-coarsened region (approximately 25 microns in width) and constraint effects of the surrounding high strength material.

Analysis of the fractured tensile specimens showed failure in the linear-friction weld to occur exclusively across the inner-HDZ, which was consistent with that observed in inertia-friction welds.

Figure 7 shows SEM fractographs of the linear-friction weld tensile specimen fracture surface. The surface exhibited a fibrous appearance comprised of planer regions of ductile fracture bounded by tear ridges. Macroscopic characteristics of the linear-friction and inertia-friction weld fracture surfaces differed principally in the orientation of the tear ridges, which were relatively parallel in the linear-friction welds, but which exhibited a curvilinear (outward spiraling) pattern in the inertia-friction welds. This difference in macroscopic fracture pattern was clearly associated with differences in the nature of metal flow associated with linear versus rotational interface motions. At increased magnification, the tear ridges appeared more irregular. Analysis of the relatively flat regions between the tear ridges at increased magnification revealed ductile fracture which was associated with microvoid formation within the soft alpha aluminum, presumably at interfaces with the hard dispersoid particles. On a microscopic scale, fracture of the two weld types appeared identical.

In summary, the present investigation determined that defect-free, solid-phase joints can be effectively produced in 8009 using the linear-friction welding process. A relatively slower weld thermal cycle than experienced in previously generated inertia-friction welds, and a lesser extent of expulsion from the weld interface region, promoted the presence of a coarser dispersoid structure at the center of the weld HDZ and correspondingly softening of this region. Despite this softening, transverse-weld tensile strengths were quite high (84-86%) and comparable to those of inertia-friction welds.

Acknowledgements

The authors are indebted to Dr. S. K. Das of Allied-Signal, Inc. for supplying the material evaluated in this study. Appreciation is also extended to Messrs. David Nicholas and Edward Watts of The Welding Institute, Cambridge, for their performance of the linear-friction welding experiments. Finally, the authors gratefully acknowledge Dr. Andrew Crowson and the Army Research Office for their support of this work under contract #DAAL03-88-K-0049.

References

1. High Temperature Aluminum Alloy - 8009 (FVS0812) Data Sheet, Allied-Signal Inc., Morristown, New Jersey.
2. H. H. Koo, S. Krishnaswamy and W. A. Baeslack III, Characterization of inertia-friction welds in a high-temperature RS/PM Al-8.5Fe-1.7Si-1.3V Alloy (AA-8009), Materials Characterization (in press).

List of Figures

Table 1
Room-Temperature Tensile Properties of Linear- and Inertia-Friction Welds in AA8009

Process/ Axial Force	Specimen Location	YS (MPa)	TS (MPa)	EL (%)	Joint Efficiency (%)	Fracture Location
IFW/L[a]	Outer Periphery	345	400	1.6	85	IHDZ
	Center	360	409	2.8	87	IHDZ
IFW/H[a]	Outer Periphery	356	415	2.3	89	IHDZ
	Center	356	410	2.6	87	IHDZ
LFW	Outer Periphery	350	396	1.9	84	IHDZ
	Center	347	404	2.6	86	IHDZ
Base Metal[b]		434	469	16.5		

[a] IF welding parameters are given in Ref. 2.

[b] Ref. 1

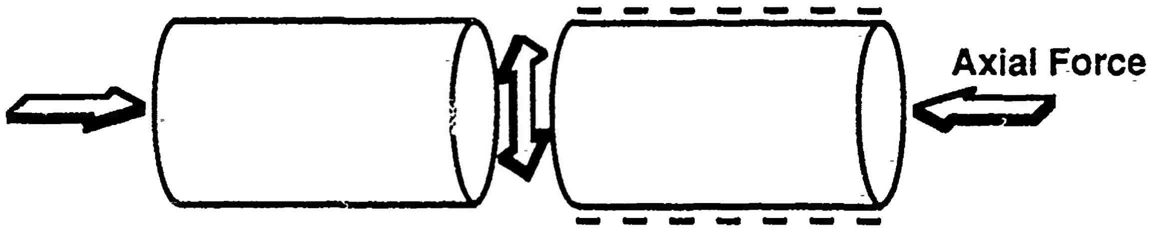

Fig. 1. Schematic representation of linear-friction welding process.

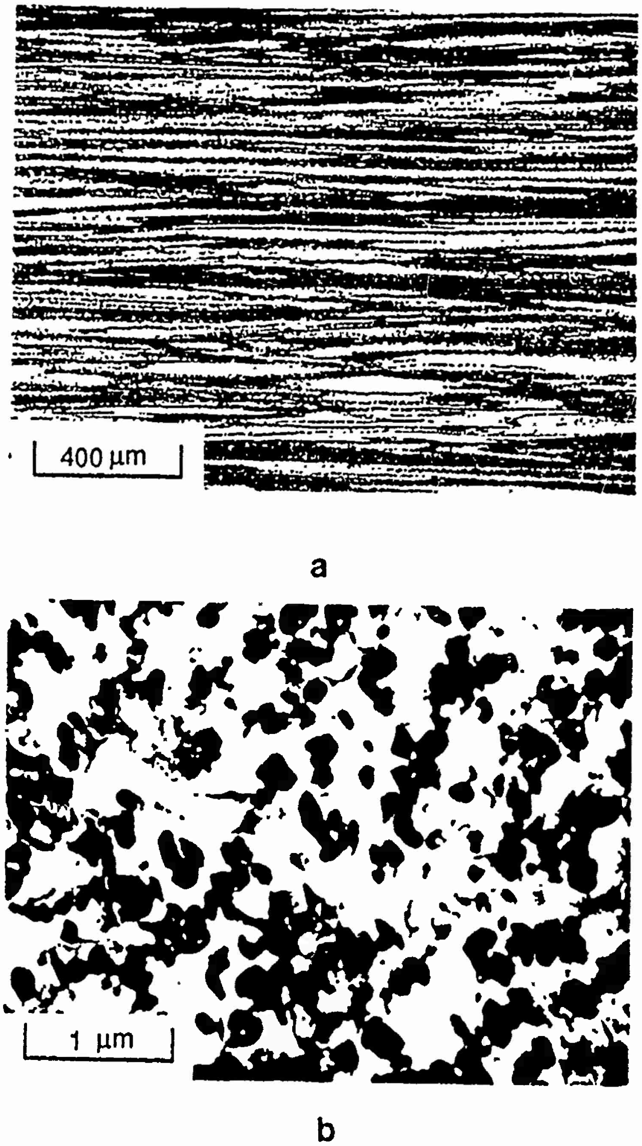

Fig. 2. Light (a) and TEM bright-field (b) micrographs of as-extruded 8009.

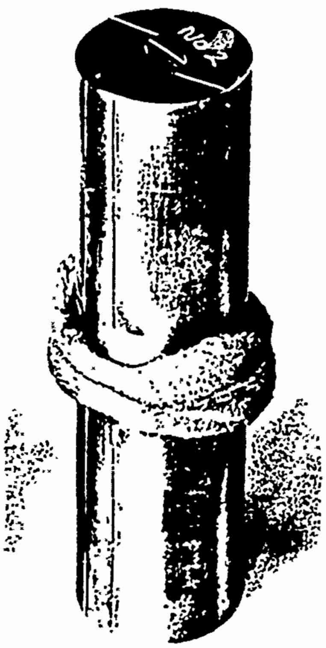

Fig. 3. Linear-friction welded specimen produced in 8009. Arrow on top of specimen indicates direction of linear displacement during welding.

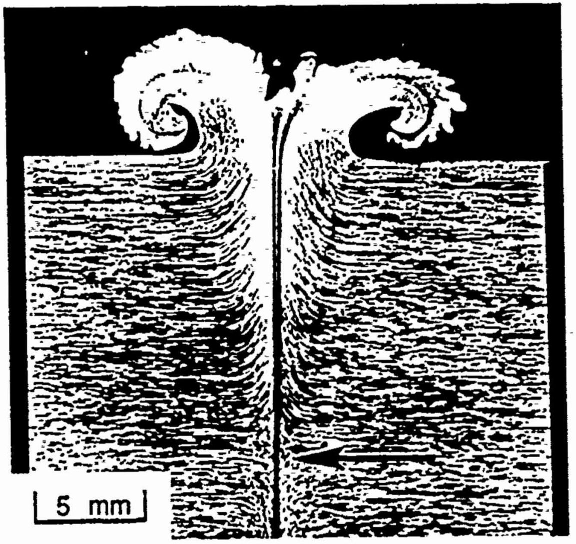

Fig. 4. Light macrograph of linear-friction weld produced in 8009. Arrow indicates axial centerline.

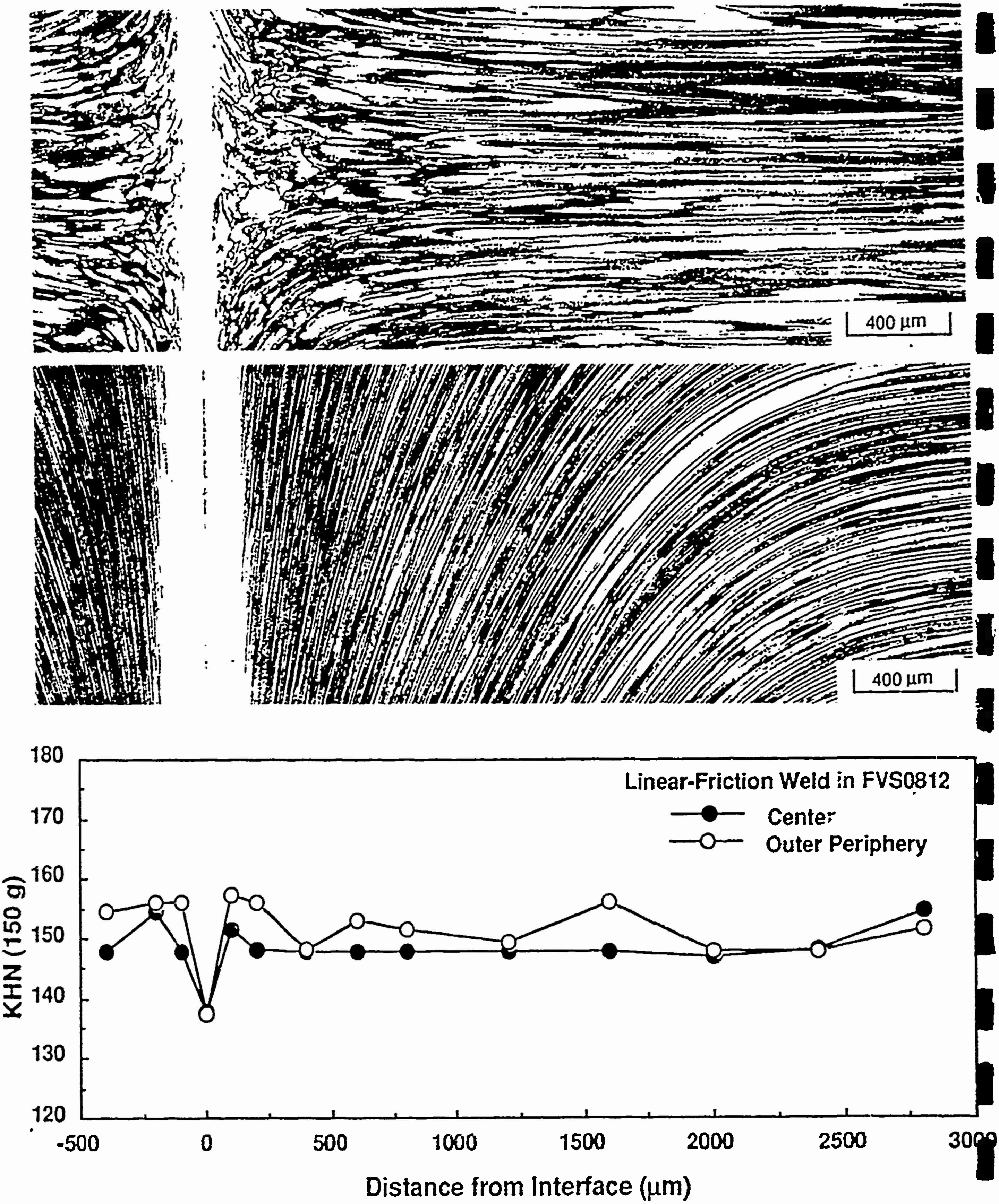

Fig. 5. Light micrographs of (a) center and (b) outer periphery region and corrresponding KHN hardness traverses (c) for a linear-friction weld produced in 8009.

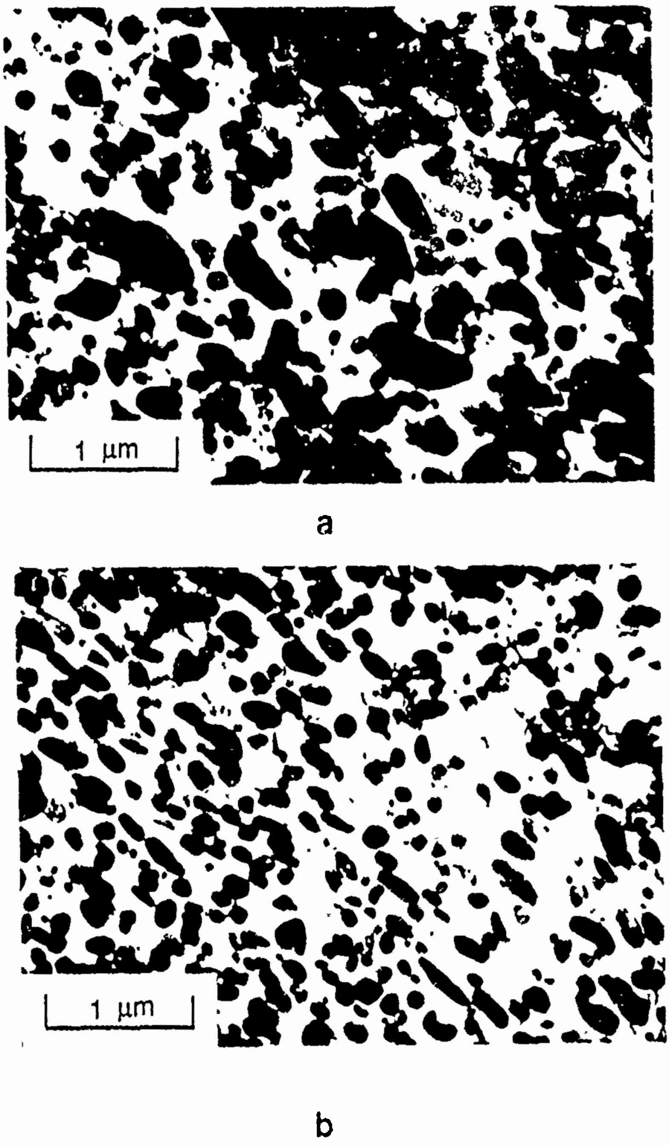

Fig. 6. TEM bright-field micrographs at axial centerline of linear-friction weld produced in 8009: (a) center of inner-HDZ; (b) outer edge or inner-HDZ.

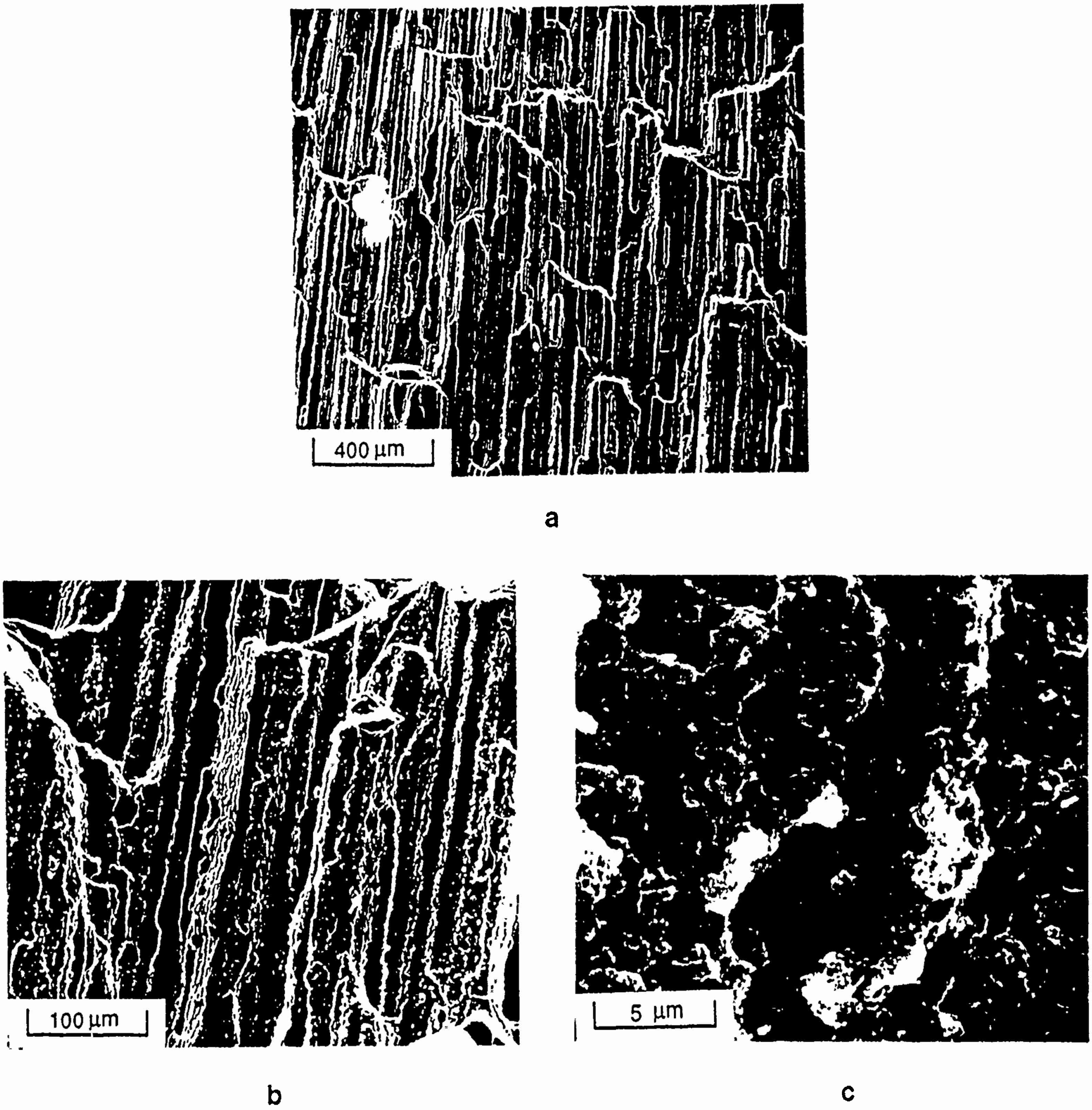

Fig. 7. SEM fractographs of tensile test specimen extracted from center of linear-friction weld produced in 8009.

Appendix 1I

APPENDIX II

H. H. Koo and W. A. Baeslack III, "Friction Welding of a Rapidly-Solidified Al-Fe-V-Si Alloy," Welding Journal, Research Supplement, (in review).

Presented at 1991 AWS Annual Meeting in Detroit, Michigan.

Friction Welding of a Rapidly-Solidified Al-Fe-V-Si Alloy

Metallurgical characteristics of inertia- and linear-friction welds
in an advanced, elevated-temperature aluminum alloy
have been comparatively evaluated

H. H. Koo and W. A. Baeslack III

Department of Welding Engineering
The Ohio State University
Columbus, Ohio 43210

ABSTRACT. Inertia- and linear-friction welds produced in a rapidly-solidified/powder metallurgy Al-Fe-V-Si alloy have been investigated from a metallurgical perspective. Similar-alloy welds in Al-11.7 wt% Fe-1.2 wt% V-2.4 wt% Si (hereafter designated as FVS1212) and dissimilar-alloy welds between FVS1212 and ingot metallurgy 2024-T351 were generated and characterized using light and analytical-electron microscopy, mechanical testing and fractographic analysis.

The application of a relatively high axial force during inertia-friction welding was found to be critical in promoting sufficient expulsion of severely heat-and-deformation-affected metal out of the weld interface region, thereby maintaining a fine dispersoid and alpha grain size in the weld zone and achieving a high joint efficiency (85%). Although linear-friction welds in FVS1212 exhibited a greater extent of dispersoid coarsening in the weld zone due to a comparatively

slower thermal cycle and lower degree of expulsion, only a slight decrease in joint efficiency (down to 80%) was measured versus the optimum inertia-friction welds. Consistent with hardness and tensile test data, fractographic analysis of tensile and three-point bend specimen surfaces using scanning-electron microscopy revealed fracture to occur at the center of the heat-and-deformation-affected zones in all similar-alloy welds.

Light and analytical-electron microscopy analysis of the dissimilar-alloy friction welds showed microstructural changes to occur predominantly in the 2024-T351. These changes included severe deformation and reorientation of the base metal alpha grains, reversion and/or solutionizing of the strengthening precipitates, and the promotion of dynamic recrystallization directly adjacent to the weld interface. Mechanical mixing between the alloys was limited to an extremely narrow region across the weld interface, and was less extensive in the linear-friction versus the inertia-friction welds. Results of the hardness traverses correlated closely with microstructural features, showing a hardness decrease in the 2024-T351 heat-and-deformation-affected zone but no change in the FVS1212. Transverse-weld tensile test results showed high joint efficiencies of 95 and 86% (based on the 2024-T351 base metal strength) for the high axial force inertia-friction and linear-

friction welds, respectively. Scanning-electron microscopy/energy-dispersive X-ray fractographic analysis of both tensile and three-point bend specimens showed fracture to occur along the weld interface, or within the 2024-T351 of FVS1212 directly adjacent to this interface. The proportion of fracture directly along the interface was most extensive near the outer periphery versus the center of both the inertia-friction and linear-friction welds.

The present study has demonstrated feasibility of both the inertia- and linear-friction welding processes for the effective solid-state joining of FVS1212, and has determined process effects on the joint structure and mechanical properties. It is anticipated that further process parameter optimization, particularly for the linear-friction welding process, would result in further improvements in joint properties.

KEY WORDS
Dispersion-Hardened Alloy
RS/PM Alloy
Al-Fe-V-Si
2024-T351
Inertia-Friction Welding
Linear-Friction Welding
Similar-Alloy Welds
Dissimilar-Alloy Welds

W. A. Baeslack III is a Professor and H. H. Koo is a Research Associate, Department of Welding Engineering, The Ohio State University, Columbus, Ohio 43210.

Introduction

Recent advances in rapid solidification and powder metallurgy (RS/PM) technology have led to the development of a new generation of high-strength aluminum alloys for elevated-temperature applications up to 425°C (Refs. 1-4). These alloys are based on hypereutectic Al-Fe base compositions (8.5 - 12 wt% Fe) with lesser ternary and quaternary additions of vanadium and silicon. Through RS/PM processing, a unique, "engineered" microstructure is obtained which consists of a high volume percentage of nearly spherical, sub-micron $Al_{13}(Fe,V)_3Si$ dispersoids (body-centered cubic) in an extremely fine-grained alpha aluminum matrix (Ref. 2). The low interfacial energy between the dispersoid particles and the matrix and the low solid-state diffusivity and solid-state solubility of the transition metal alloying elements in alpha aluminum minimize the driving force for particle coarsening, thereby promoting their stability at temperature up to 425°C. These microstructural features provide high room-temperature strength and excellent elevated-temperature mechanical properties in contrast to conventional precipitation-hardened aluminum alloys which rapidly lose their strength above 150°C due to overaging of the strengthening precipitates. As shown in Fig. 1, the Al-Fe-V-Si alloys exhibit specific strengths comparable to Ti-6 wt.% Al-4 wt. % V up to 425°C (Ref. 2). The spherical morphology of $Al_{13}(Fe,V)_3Si$ and absence of acicular Al_3Fe (monoclinic) dispersoids further promote excellent ductility, fracture toughness and fatigue properties comparable to those conventional high-strength aluminum alloys. Consequently, the RS/PM Al-Fe-V-Si alloys are currently being considered as a strong candidate material to replace titanium alloys and conventional high-strength aluminum alloys in many structural aerospace applications.

The effective utilization of these new RS/PM Al-Fe-V-Si alloys in structural applications will in many instances be contingent on their joining both to themselves and to dissimilar aluminum and possibly titanium alloys. The unique microstructural characteristics exhibited by RS/PM aluminum alloys preclude the application of many conventional fusion welding processes and methodologies. Major problems in the fusion welding of these RS/PM aluminum alloys include difficulties in assuring retention of the RS base metal microstructure and the formation of porosity due to a high residual hydrogen content originating from the aluminum powder or particulates. Preliminary gas tungsten-arc welding experiments on early-generation Al-Fe-V-Si alloy by the authors resulted in unacceptable porosity levels and the formation of coarse acicular intermetallics.

In recent years, several fusion welding approaches have successfully joined RS/PM Al-Fe-X alloys. Pulsed Nd:YAG laser (Ref. 5) and electron beam welding (Ref. 6) were effectively used for the fusion welding of an RS/PM Al-Fe-Mo alloy characterized by a low hydrogen content. The extremely rapid thermal cycle associated with these processes and low base metal hydrogen content resulted in the formation of fine weld fusion zone (FZ) and heat-affected zone (HAZ) microstructures free of hydrogen-induced porosity. Capacitor-discharge welding was used for the fusion welding of an RS/PM Al-Fe-Ce alloy which contained a moderate hydrogen content (Refs. 7 and 8). The simultaneous application of pressure during weld generation and a rapid thermal cycle resulted in a fine, high-strength solidification microstructure free of porosity.

Solid-state joining processes offer an alternate approach to the joining of RS/PM aluminum alloys which are not amenable to joining by fusion welding processes. Diffusion welding and transient-liquid phase welding using a silver interlayer have been reported to provide joint effiencies of up to 70% in Al-Fe-Ce alloys (Ref. 9). Inertia-friction (IF) welding was also utilized to join Al-Fe-Ce (Ref. 10) and Al-Fe-Mo-V (Ref. 11) alloys which contained high hydrogen contents. Results showed that the rapid thermal cycle associated with the inertia-friction welding process, and the expulsion of severely heat-and-deformation-affected metal out of the weld interfaces can promote high-integrity weld zone microstructures and correspondingly high joint efficiencies. Further studies have demonstrated the feasibility of inertia-friction welding these RS/PM aluminum alloys to conventional high-strength aluminum alloys (Refs. 10 and 12).

The recently-developed linear-friction welding process significantly extends the utility of friction welding to the joining of non-axisymmetric parts (Ref. 13). As schematically illustrated in Fig. 2, frictional heating during linear-friction welding is provided by the linear translation of two workpiece interfaces versus the rotational translation during conventional friction welding. Although the feasibility of utilizing linear-friction welding for the joining of engineering-sized components has recently been demonstrated for several alloys (Ref. 13), relatively little work has been published regarding the metallurgical characterization of linear-friction welds and their comparison with conventional friction welds.

The present study was performed to investigate and comparatively evaluate the metallurgical characteristics of inertia-friction and linear-friction welds in an advanced elevated-temperature Al-Fe-V-Si alloy, FVS1212, and dissimilar-alloy welds between this alloy and the conventional high-strength aluminum alloy 2024-T351. Specific objectives for the present work were as follows.

1. Determine the feasibility of producing high integrity inertia- and linear-friction welds in FVS1212 and in dissimilar-alloy combination with 2024-T351.

2. Investigate effects of the welding process and process parameters on the weld integrity, macro- and microstructural characteristics.

3. Establish metallurgical relationships between the weld zone microstructure, mechanical properties and fracture characteristics.

Experimental Methods

Materials

The commercially-available FVS1212 alloy utilized in this study was produced by Allied-Signal's planar-flow casting (PFC) process. Following rapid solidification, the ribbons were comminuted into fine particles, vacuum degassed, hot pressed into billets and finally extruded into 32 mm diameter rod. A 25 mm diameter extrusion of 2024 in a T351 temper condition was utilized in dissimilar-alloy welding studies. Prior to inertia-friction welding, the rods were sectioned into 50 mm lengths and machined down to a diameter of 22 mm. For linear-friction welds, rods 25 mm in diameter were used. Weld faying surfaces were dry machined immediately prior to welding.

Friction Welding

Inertia-friction welds were produced using an MTI Model 120 inertia-friction welding system. Based on previous inertia-friction welding studies of dispersion-strengthened aluminum alloys (Refs. 10 and 11), welds parameters were selected which provided two levels of axial displacement for similar welds in FVS1212 and dissimilar welds between FVS1212 and 2024-T351. In addition, similar and dissimilar linear friction welds were produced using a linear-friction welding machine located at The Welding Institute in Cambridge, England. Welding parameters utilized for each process are shown in Table 1. It is important to note that welds were produced to demonstrate feasibility of the processes, and not necessarily to fully optimize the weld structure and mechanical properties.

Weld Characterization

After welding, the weld axial displacement and flash uniformity were visually evaluated. Representative welds were sectioned axially, mounted in epoxy, mechanically ground down to 600 grit SiC paper, rough polished with 3 micron diamond compound and 0.3 micron alumina and final polished using a colloidal silica suspension. Following defect analysis of the as-polished specimen surfaces using light microscopy, microstructural features were revealed by etching with Keller's reagent.

Alternate specimen halves were carefully sectioned longitudinally at the axial centerline into thin slices 0.3 mm in thickness and mechanically thinned down to 0.125 mm. Disks three mm in diameter were punched from the foils in the unaffected base metal and from representative regions in the weld HDZ's and electrojet polished in one part nitric acid and three parts methanol at -30 °C. Thin foils were examined in a JEOL 200CX analytical-electron microscope equipped with Tracor-Northern TN-2000 energy-dispersive X-ray analysis (EDS) system.

Knoop microhardness testing (150 gram load) was performed across the weld region at the axial centerline and the outer periphery for correlation with microstructural characteristics. Transverse-weld oriented tensile test specimens (gage section: 25 mm length x 4.5 mm width x 1.5 mm thickness) were sectioned from the center and outer periphery of each weld type and tested as per ASTM E8-87 at an extension rate of 0.25 mm/min. Also, three-point guided bend testing was performed on axial half-sections to reveal the fracture characteristics. Following mechanical testing, fracture surfaces were characterized using light and scanning-electron microscopy.

Results and Discussion

Base Metal Characterization

The microstructure of the FVS1212 base metal oriented parallel to the extrusion direction is shown in black and white contrast in Figs. 3a and 3b, and in color contrast in Figs. 3c and 3d. Fig. 3a shows the overall microstructure at low magnification, with boundaries between the planar-flow cast and comminuted particles clearly observable. Regions of dark contrast in Fig. 3a which contained coarser dispersoids and conversely exhibited light contrast in Fig. 3b at increased magnification. The white alpha aluminum matrix between the dispersoids was readily observable at high magnification. Regions of light contrast in Fig. 3a which contained extremely fine dispersoids actually appeared dark grey at higher magnification in Fig. 3b. Occasionally, narrow white bands devoid of dispersoids were observed.

Color contrast light micrographs of the base metal microstructure more clearly revealed microstructural details (Figs. 3c and 3d). Regions of fine dispersoids exhibited a yellow contrast (large arrow in Fig. 3d), while regions of coarser dispersoids exhibited a blue contrast (small arrow in Fig. 3d). Regions containing mixtures of both coarse and fine dispersoids exhibited a dark brown contrast within a single ribbon particle. The microstructural variations within a single particle (as revealed by different colors) originated from differences in the cooling rate of the original ribbon, with the side contacting the quenching wheel experiencing appreciably higher cooling rates than the opposite free surface side. Higher cooling rates correspondingly promoted a finer as-solidified microstructure and ultimately a finer as-processed dispersoid/grain structure.

TEM observation more clearly revealed microstructural characteristics of the FVS1212 base metal, as shown in Fig. 4. Consistent with light microscopy observations, low magnification TEM bright-field micrographs revealed distinct boundaries between the original ribbon particles and exhibited noticeable differences in the size and distribution of the dispersoids throughout the microstructure. TEM examination at an increased magnification showed three different regions in regard to the dispersoid size and distribution: those containing; 1) fine dispersoids; 2) a mixture of fine and coarse dispersoids and 3) clusters of fine dispersoids. Fig. 4a shows a region containing relatively uniform, fine-sized dispersoids. The fine dispersoids exhibited a nearly spherical morphology with diameters ranging from about 75 to 100 nm. Another representative region showed a bi-modal distribution of dispersoids consisting of fine dispersoids ranging from 50 to 100 nm in diameter and coarser dispersoids up to 400 nm in diameter (Fig. 4b). Alpha aluminum grains in these regions were equiaxed and ranged in diameter from 0.5 to 1 micron. TEM analysis of the regions which exhibited coarse dispersoids and a high proportion of alpha phase at low magnification (region indicated by small arrow in Fig. 3b) showed clusters of fine dispersoids (50 to 100 nm in diameter) located at alpha grain boundaries (Figs. 4c and 4d). The population density of dispersoids in this region was generally lower than the regions of uniform, fine dispersoid distribution (Figs. 4a) and the alpha grain size was also coarser, up to about 1.5 micron in diameter. It is suggested that the formation of these structures may be associated with slowly cooled regions on the free surface side of the PFC ribbons. Occasionally, dispersoid-free bands shown in Fig. 2b were observed, which may have originated from non-homogenous deformation during extrusion. From the previous studies on these alloys (Refs. 3 and 4) and characterization by the authors of inertia-friction welds in a similar-alloy FVS0812 (Ref. 14) indicated the various dispersoids to be $Al_{13}(Fe,V)_3Si$ type. Acicular dispersoids observed in previous studies of a rapidly-solidified Al-Fe-Mo-V alloy (Ref. 11) were not observed. This result confirms the previously observed influence of vanadium in stabilizing the cubic

$Al_{13}(Fe,V)_3Si$ over the hexagonal Al_8Fe_2Si or monoclinic Al_3Fe phases (Ref. 3).

Figs. 5a and 5b show light micrographs of the 2024-T351 base metal oriented parallel to the extrusion direction. The microstructure exhibited a light and dark contrast depending on the orientation of alpha grains or subgrains (Fig 5a). Observation at a higher magnification showed agglomerations of various dispersoids and precipitates at grain boundaries and fine particles within the grains (Fig. 5b). TEM bright-field imaging revealed columnar intermetallic particles and fine intragranular second phase particles (Figs. 5c and 5d). Based on the morphology of these particles (Ref. 14) and EDS analysis, the small, lath-type precipitates were identified as precursor S'(Al_2CuMg) particles and the large columnar particles were $Al_{20}Cu_2Mn_3$ dispersoids. Despite extreme care, the large-sized grain boundary dispersoid particles underwent preferential attack during twin-jet electropolishing and could not be effectively characterized.

Weld Zone Characterization

Macroscopic Analysis

The as-welded inertia-friction (IF) and linear-friction (LF) welds are shown in Fig. 6. Visual examination of the similar-alloy IF welds found the presence of smooth, symmetrically uniform flash around the entire weld circumference, with the flash and axial displacement increasing with an increase in axial force. Consistent with appreciably lower high-temperature strength of 2024-T351 relative to FVS1212, dissimilar-alloy IF welds exhibited preferential flash formation in 2024-T351 versus the FVS1212.

In contrast to the IF welds, similar-alloy LF welds exhibited flash formation principally in the direction of linear displacement. Dissimilar-alloy LF welds exhibited flash only in 2024-T351 with preferential flash formation similar to that observed in the IF welds, and was circumferentially more uniform than the similar-alloy LF welds. Axial displacement data for different alloy/parameter combinations are given in Table 1.

Examination of the as-polished surfaces of each specimen revealed no evidence of defects except at the very outer periphery of the interface region of the dissimilar-alloy LF weld. Macrographs of the axially-sectioned weld specimens for different alloy/parameter combinations are shown in Figs. 7 and 8. The similar-alloy IF welds revealed that the entire weld heat-and-deformation zone (HDZ) typically exhibited an hour-glass shape, with the HDZ width narrower for the high axial force (Figs. 7a and 7b). The center of the HDZ's (referred to hereafter as the inner-HDZ) exhibited featureless regions of light and/or dark contrast. In the low axial force IF weld, a light-contrast center was surrounded by a region exhibiting a dark contrast, while in the high axial force IF weld only a region of dark contrast was apparent. The width of the inner-HDZ remained relatively constant across the low-axial force IF weld, and gradually decreased in width toward the axial centerline in the high-axial force IF weld. Macrostructural features of the similar-alloy LF welds showed similar features to those of the IF welds (Fig. 7c). Interestingly, the inner-HDZ was comprised of adjacent regions of light contrast (left side) and dark contrast (right side), which gradually decreased in total width from the outer periphery to the axial centerline.

The dissimilar-alloy IF welds exhibited an hour-glass shaped HDZ only in the 2024-T351 (Figs. 8a and 8b). The effect of the axial force was similar to the similar alloy IF welds. Macrostructural feature of the dissimilar-alloy LF welds showed similar features to those of the dissimilar-alloy IF welds (Fig. 8c). The width of the outer-HDZ in the dissimilar alloy LF weld was slightly wider than that of the dissimilar-alloy IF welds.

Microstructure Characterization

Figures 9 - 11 and 13 -14 show microstructure and corresponding hardness traverses from the unaffected base metal to the center of the weld HDZ at the axial center and outer periphery for each alloy/process combination.

Similar Alloy Welds

For the similar-alloy IF (Figs. 9 and 10) and LF (Fig. 11) welds, the base metal microstructure showed a continuous reorientation from parallel to perpendicular to the original base metal extrusion direction. Nearer to the center of the weld HDZ, the reoriented microstructure became increasingly "flattened" due to high axial compressive stresses. Comparing Figs. 9, 10 and 11, the width of the inner-HDZ was greater for the IF welds produced at both the high and low axial force as compared to the LF weld.

In the inner-HDZ of the low axial force weld, microstructural variations which existed in the base metal became featureless due to severe mechanical mixing. As shown, the inner-HDZ was comprised of a grey cnetral region and a white outer region (Note that the contrast of these regions are actually reverse of those observed at low magnification). The color light micrograph in Fig. 12 efffectively revealed the microstructural changes near the weld interface region. In the IF welds, the base metal microstructure became increasingly homogeneous and yellow in color at the boundary region between the inner-HDZ and outer-HDZ, showing, an absence of blue-appearing coarse dispersoid regions (Fig. 12a). The center region of the homogeneous inner-HDZ which showed grey contrast in black-and-white micrographs appeared bluish-yellow or brown implying some coarsening of the dispersoid size and grain size. The inner-HDZ at the outer periphery region of the low axial force IF weld exhibited a grey contrast central region and neighboring light contrast region similar to the axial center. However, narrow, white-appearing bands and adjacent dark-appearing regions in the inner-HDZ at the interface (Fig. 9b). Examination at an increased magnification indicated a very low dispersoid density in the light-appearing regions and a higher dispersoid density in the adjacent dark-appearing regions versus the surrounding inner-HDZ.

Figures 10a and 10b show microstructure traverses across the high axial force IF weld in FVS1212. In the inner-HDZ, the region of grey contrast was barely observable. The higher compressive stress expelled the homogenized and coarsened microstructure to the outer periphery, leaving only the fine textured structure as observed in the white-contrast region in the low axial force weld. The outer periphery region of the weld exhibited an appreciably wider HDZ which appeared comparable to the center of the low axial force weld. Dispersoid-lean bands were not observed in the high axial force weld. The absence of these structures in high axial force welds was attributed to the increased expulsion of the softened metal from the weld interface with the increase in weld axial force.

Figures 11a and 11b show microstructure traverses across the LF weld in FVS1212. Compared with the IF welds, the inner-HDZ was macroscopically homogeneous but comprised of several narrow, grey-and white-contrast layers. The transition from the inner-HDZ to the outer-HDZ was more abrupt than in IF welds. The outer periphery region exhibited an asymmetric inner-HDZ, with one side showing white contrast and the other side showing grey contrast. The color light micrograph of the LF weld (Fig. 12b) exhibited more details of inner-HDZ showing light-yellow color at the boundary region with the inner-HDZ and streaks of brown or bluish-yellow at the center of the inner-HDZ, indicating dispersoid coarsening in this region.

Dissimilar Alloy Welds

For the dissimilar-alloy IF welds (Fig. 13) and LF weld (Fig. 14), microstructural changes and reorientation of the base metal structure were observed only in the 2024-T351 due to the lower strength of the 2024-T351 relative to FVS1212 at elevated temperatures. Outer HDZ's at the axial centerline elongated alpha grains in the base metal to tradually change to near-equiaxed grains, and then to a severly laminated structure and finally to a featureless (dark contrast) microstructure within the inner-HDZ. At the outer periphery of each weld, elongated alpha grains gradually reorient and flattten, with a similar dark contrast structure at the inner-HDZ. The width of the inner-HDZ was wider in the IF welds than in the LF weld. Higher axial force resulted in narrower inner-HDZ's in the IF welds. Contrary to the similar alloy welds, the width of the inner-HDZ at the outer periphery was narrower than at the center for both the IF and LF welds. A small lack of bonding was observed at the outer periphery contacting the free surface in the LF weld at corners.

TEM Analysis

Similar Alloy Welds

TEM bright-field observation of the inner-HDZ at the axial centerline in the similar-alloy IF weld produced with low axial force (Figs. 15a and 15b) showed a uniform distribution of dispersoids ranging in size from about 75 to 500 nm. This homogenization of the base metal microstructure appeared to originate from extensive mechanical mixing. The clusters of fine dispersoids shown in Figs. 4e and 4f were not observed in this region, indicating their complete break-up and dispersion. The dispersoid sizes and size distribution in this region were generally comparable to that observed in the unaffected base metal, showing only a marginal increase in the range of dispersoid sizes. While the previous TEM analysis of inertia-friction welds in Al-Fe-Mo-V alloys (Ref. 10) showed the cleavage-type fracture of relatively coarse dispersoids (up to two microns in diameter) in the inner-HDZ, no evidence of dispersoid fracture was observed in this study. This absence of the dispersoid fracture was attributed to the appreciably smaller original dispersoid size and also to differences in the structure and fracture strength of the dispersoids.

The inner-HDZ of the low axial force weld adjascent to the homogenized center region, exhibiting alternating regions of light- and dark-appearing contrast at lower magnification. These observations were attributed to variations in the dispersoid population density and distribution; dark contrast for regions of a higher dispersoid population density and light contrast for regions of a lower population density. Regions containing clusters of fine dispersoids were also observed in light contrast. These differences in dispersoid size and distribution were associated with variations in the original base metal microstructure of which had been "flattened" but not completely homogenized in this region. The alpha aluminum grains in inner-HDZ regions showed a similar morphology and size to those observed in the base metal, being nearly equiaxed and ranging in diameter from about 0.25 to 1.0 microns. Considering the equiaxed nature and the size of the grains even with directional deformation in these regions, it is suggested that the grains were dynamically-recrystallized on weld cooling and that the growth was limited by the high volume fraction of dispersoids.

TEM bright-field micrographs in Figs. 15c-e show the region containing dispersoid-lean bands at the outer periphery of the IF welds produced using low axial force (white-appearing bands in Fig. 9b). In addition to a low dispersoid population density, this region contained coarser alpha grains up to several microns in diameter with a slightly elongated morphology. The low dispersoid density in this region apparently did not restrict the alpha grain growth. The occurrence of this microstructure may be explained by localized melting of the alpha phase at the weld interface, which is likely to occur at the outer periphery due to the higher rotational velocities and peak temperatures. However, analysis of the regions indicated no evidence of a resolidified microstructure. Alternatively, the microstructure could result from localized, nonuniform deformation in the HDZ. High tensile compressive stresses in combination with simultaneous shear stresses in this region may locally extrude soft alpha aluminum from the original base metal microstructure, resulting in dispersoid-lean regions. The presence of adjacent dark-contrast regions, which contained a high population density of dispersoids (Fig. 9b), may be explained by such nonuniform deformation. The coarsening of dispersoids in the dark-contrast regions was noticeable, with the diameter of dispersoids ranging from 75 to 800 nm.

TEM bright-field micrographs in Figs. 16a and 16b show the inner-HDZ at the axial centerline of the IF weld produced using high axial force. Considerable homogenization was indicated by the uniform distribution of a wide range of dispersoid sizes. The adjacent inner-HDZ exhibited regions of alternating dark and light-appearing contrast as in the weld produced using low axial force. Consistent with light microscopy observations, TEM observations of the weld zone at the outer periphery of the high axial force weld compared closely with the center of the weld produced at the low axial force (Figs. 16c and 16d)..

Compared to the similar-alloy IF welds, TEM bright-field analysis of the homogeneous interface region at the center of the LF weld (Figs. 17a and 17b) indicated a marked increase in dispersoid size, showing dispersoids ranging from 120 to 1,600 nm in length. While the finer dispersoids remained spherical, the coarser dispersoids experienced coarsening and elongation along the interface direction with an aspect ratio of approximately two. Despite this noticeable dispersoid coarsening, the alpha grain size in this region appeared equivalent to the base metal. Clusters of dispersoids observed in the base metal were not observed in this region, indicating their total break-up. Alternating layers observed in light microscopy (Fig. 12b) in the homogeneous inner-HDZ turned out to be slight variation of dispersoid distribution. An inhomogeneous region outside of the central homogeneous region, where light-yellow contrast was observed in Fig. 12b, showed alternating deformed layers of fine dispersoids and deformed coarse dispersoids (Fig. 17c). Even though it was located at the boundary region, coarsening and deformation was noticeable, showing dispersoids ranging from 120 to 1350 nm in diameter. The interface region at the outer periphery showed a very similar microstructure but with slightly less-deformed, lower aspect ratio dispersoids (Figs. 17d). The asymmetric nature of the interface in the region observed on the light microscopy was not discernable via TEM observation. The marked coarsening of dispersoids in the interface region originated from the slower thermal cycle experienced during the process and to a lesser extent of metal expulsion compared to the high-axial force IF weld. A higher axial force may be required to reduce the weld time and remove the dispersoid-coarsened region while achieving the same upset in the LF welds.

Dissimilar Alloy Welds

TEM bright-field micrographs of the dissimilar-alloy IF weld produced using high axial force are shown in Fig. 19. Figure 19a shows the general feature of the interface region at the axial center line. Mechanical mixing between the two alloys is evident showing penetrated layers of FVS1212 into the 2024-T351. Smearing of microstructure between the two alloys in the layers was minimal. Even with the deformation and mechanical mixing of FVS1212 near the interface, deformation or growth of the dispersoids was not noticeable (Fig. 19b). Recrystallized 2024 grains were nearly equiaxed and the alignment of intermetallic particles was not severe (Fig. 19c). The presence of fine, S' precipitates was not observed indicating that this region was totally solutionized during the welding process. The grain size of the recrystallized 2024-T351 ranged from 500 to 1000 nm. In the outer-HDZ of 2024-T351, the microstructure gradually changed from fully recrystallized structure to cold-worked cell structure with entangled dislocations and gradually changed to that of base metal nearing the unaffected base metal. An overaged structure was not observed in this region, rather an absence of precipitates indicated solutionizing or reversion. TEM observation of the outer periphery region of the same weld showed almost the same features. TEM observation of the low axial force IF weld showed features slightly different from those of the high axial force IF weld, showing abrupt transition across the interface with less mechanical mixing and slightly larger recrystallized grain sizes (500 to 1500 nm).

TEM bright-field micrographs of the dissimilar-alloy LF welds are shown in Figs. 20a - 20d. As shown in Figs. 20a and 20b, mechanical mixing between the two alloys appeared more smooth transitional structure showing smearing of FVS1212 into 2024-T351 across the interface, which was attributed to the longer contacting time at the peak temperature without large shear deformation as in the LF weld. The dispersoids in FVS1212 showed no evidence of coarsening or deformation (Fig 14b). Recrystallized 2024-T351 near the interface showed a wide range of alpha grain size distributions with the grain boundary intermetallics aligned semicontinuously along the interface direction (Fig. 14c and 14d), which was observed in Fig. 14b. The grain size of recrystallized grains ranged from 500 to 1500 nm. Microstructural features in the outer-HDZ were similar to those of IF welds.

Hardness Testing

Similar Alloy Welds

Knoop microhardness traverses for the similar-alloy welds are shown in Figs. 9, 10, and 11. Hardness values across the weld interface at the axial centerline for the low axial force IF weld (Fig. 9c) exhibited equivalent hardness as that of base metal (KHN 183.5 in average, ranging from 170 to 210) outside of the inner HDZ but decreased down to 150 KHN at the center of the inner HDZ. This decrease in hardness was attributed to the marginal increase in dispersoid coarseness and possibly the alpha grain size. The hardness traverse at the outer periphery of this weld exhibited a similar trend, except at the dispersoid-lean white-appearing regions which exhibited a very low hardness down to about 104 KHN. Hardness measurement at the grey region neighboring the dispersoid-lean region exhibited KHN 180, which was higher than the values at other regions of the inner HDZ. Even with coarsening of the dispersoids in the region, increase in local dispersoid population density apparently compensated the coarsening effect.

Fig. 10c shows the KHN hardness traverse across the interface of the similar-alloy high-axial force IF weld. Hardness values were more consistent with that of base metal without any loss and even increased to a maximum of 210 KHN in the inner-HDZ. This increased hardness was attributed to the essential absence of dispersoid or grain coarsening in this region, and the breakup and redistribution of dispersoid clusters. The increase in hardness at the boundary of the inner- and outer-HDZ was possibly attributed from residual cold work in the structure. Hardness traverse of the outer periphery of the high axial force weld exhibited a consistent hardness of about 175 KHN, which represented the lower end of the base metal hardness range. This slight loss of hardness was attributed to the homogenized but slightly coarsened dispersoid structure in the region.

Knoop microhardness traverses across the interface of the similar alloy FVS1212 LF weld are shown in Fig. 11c. A noticeable hardness drop was observed within 200 m of the interface at the axial center and within 500 m of the outer periphery. The hardness drop at the interface region is explained by the presence of coarsened dispersoids in the region, as observed in Fig. 18b.

Dissimilar Alloy Welds

Figs. 13 and 14 compare the hardness traverses in the dissimilar alloy high axial force IF weld and the LF weld. For the both welds, the hardness in the FVS1212 remained constant across the region in accordance with TEM observations, which showed no structural changes. Both welds showed extensive hardness variations in the inner- and outer-HDZ's in the 2024-T351. For the high axial force IF weld, hardness showed the lowest value (145 KHN vs. 177 in the base metal) at the recrystallized inner-HDZ, which gradually increased nearer to the base metal. At the boundary between the outer HDZ and BM, the hardness value reached a maximum (KHN 210). It is suggested that the hardness drop in this region is related to recrystallization and solutionizing or reversion of the S′ precipitates. Even with the large deformation in this region, work-hardening was apparently relieved by the recrystallization and recovery processes. The peak hardness values at the HDZ/BM boundary are suggested to be due the combined effect of aging and work-hardening. The low axial force dissimilar alloy IF weld showed similar trends with slightly lower hardness values and wider regions of low hardness.

For the dissimilar LF weld, the HDZ region also showed decreased hardness values with a minimum value of KHN 130 (Fig. 14c). Hardness variations for all the welds were well in accordance with macroscopic observations of HDZ's in Figs. 7 and 8.

Tensile Testing

Tensile testing results are shown in Table 2. The similar alloy low axial force IF weld in FVS1212 exhibited a tensile strength of 463 MPa (67.1 ksi) and a joint efficiency of 66%. The lower joint efficiency of the low axial force IF weld in FVS1212 resulted from the presence of dispersoid-lean bands in the interface region at the outer periphery. Consistent with the hardness test results, the similar alloy higher axial force IF weld exhibited a higher tensile strength of 489 MPa (71 ksi) and a joint efficiency of 85%. Tensile fracture of both weld types occurred within the inner HDZ. The similar alloy LF weld of FVS1212 exhibited a joint efficiency of 78 %, which was attributed to the greater coarsening of the dispersoids at the interface. Confirming the above, tensile fracture of the LF weld also occurred at the interface.

Dissimilar-alloy welds exhibited fracture at the inner HDZ in 2024-T351 and also exhibited a slightly lower strength than the 2024-T351 base metal. Some portion of the fracture occurred at the interface at the outer periphery region. Dissimilar-alloy IF welds produced with high axial force weld showed the highest joint efficiency of 95 %, which was consistent with the hardness test results. The low axial force IF weld showed a similar fracture location. Even with same minimum hardness values at the inner HDZ as those of high axial force IF weld, a wider softened region in the low axial force weld showed a joint efficiency of 80 %. Dissimilar-alloy LF weld showed a joint efficiency of 85 % for the same reason, with fracture occurring in 2024-T351 at the interface.

Fracture Analysis

SEM fractographs of bend and tensile test specimens are shown in Figs. 22 and 23 for similar-alloy welds in FVS1212 and in Fig. 24 for dissimilar-alloy welds between FVS1212 and 2024-T351.

Similar-alloy welds

SEM observation of the fracture surfaces of the bend test specimens are shown in Fig. 21. Fracture surfaces of the similar-alloy low axial force welds exhibited basically two different regions depending on the fracture locations; a smooth surface with fine shear tracks (Figs. 21a and 21b) and a rough surface with coarse shear tracks (Figs. 21c and 21d). Comparing with the light microscopy results, the smooth surface region corresponded to the homogenized inner-HDZ region, where the mechanical texture and powder particle boundaries were totally disappeared and homogenized. Fine shear tracks are remnant of plastic deformation of powder particles and alignment of dispersoids in the rotation direction. The rough surface with coarse shear tracks corresponds to the region which experienced subsurface shear deformation but did not experience complete homogenization and break-up of particulate boundaries. Occasional steps in the tracks correspond to the severely elongated particle boundaries. Observation of the fracture surface at higher magnification showed typical dimple patterns with microvoid formation at the dispersoids and final rupture of alpha aluminum matrix. Similar-alloy high axial force IF welds exhibited similar features as those of low axial force weld with a greater proportion of coarse shear tracks, as shown in Figs. 21c and 21d, which is due to the severe deformation and narrow recrystallized region as observed in the light microscopy.

The fracture surface of the LF weld exhibited a slightly different flow pattern at a low magnification (Fig. 21e). While the fracture surface of IF weld exhibited a spiral pattern, with narrow tracks, the fracture surface of LFW exhibited major flow principally in the linear displacement direction, with wide tracks. The wide track was attributed to the lower shear deformation in LFW process, with particulates being deformed principally by the normal compressive stress. Observation at a higher magnification exhibited similar features as those of IF welds (Fig. 21f).

SEM observation of the fracture surfaces of tensile test specimens exhibited similar features as those of bend test specimens as shown in Fig. 22. Compared with IF welds (Figs. 22a and b), LF welds occasionally exhibited region free of shear tracks as shown in Figs. 22c and d as well as regions containing shear tracks. Occasional absence of shear tracks is basically due to the lack of subsurface-shear deformation.

Dissimilar-alloy welds

SEM fractographs of the bend test specimens of dissimilar-alloy welds are shown in Fig. 23. The IF weld produced with low axial force exhibited fracture at the interface with the transfer of FVS1212 metal across and with a major portion of fracture surface in inner-HDZ of 2024-T351 (Fig. 23a). At increased magnification, fine, elongated features were observed on the 2024-T351 side, which was caused by deformation of previous base metal grains and alignment of grain boundary intermetallics as stringers (Figs. 23b). The center region of the bend test specimen exhibited fracture on the FVS1212 side, which was attributed to the mechanical mixing at the region between the two alloys. The fracture surface of IF weld produced with high axial force exhibited similar features as those of the low axial force IF weld with slightly wider steps caused by higher compressive deformation of the 2024-T351 base metal. Fracture surfaces of the bend specimens of LF weld exhibited similar features as those of the IF welds (Figs. 23c and 23d) but the shear track was more irregular and random due to the lesser shear deformation in linear-friction welding compared with inertia-friction welding.

EDAX analysis of the fracture surfaces in Fig. 23b revealed that the light appearing regions are FVS1212 carrying higher percentage of Mg and Cu originated from the 2024-T351 (3.67 wt. % Mg and 2.79 wt. % Cu). The transfer of alloying elements was due to the combined effect of mechanical mixing and diffusion across the interface. The dark regions in Fig. 23b showed the same composition of the base metal with small increase in Fe content. It was concluded the dark region is 2024-T351 with slight transfer of dispersoids by mechanical mixing across the interface and diffusional transfer was minimal due to the lower diffusivity and solubility of Fe, V and Si in FVS1212.

The fracture surface of the tensile test specimens of the low axial force IF welds exhibited similar features with major portion of the fracture surface located in the 2024-T351 (Fig. 24a and b). EDAX analysis of the fracture surfaces showed similar results as in the bend test fracture surfaces, showing light region as FVS1212 with Mg and Cu and dark regions as 2024-T351. Some portion of the fracture surface was carrying trace of FVS1212 type dispersoids on 2024-T351 fracture surface, implying that fracture occurred at the interface across thin layers of mechanical mixing (Fig. 24b) and some portion of the fracture propagated through the FVS1212. The fracture surface of the high axial force IF welds exhibited similar features as those of the low axial force weld with slightly wider steps caused by higher compressive deformation of the 2024-T351 base metal (Figs. 24c and d) and higher portion of FVS1212. The higher portion of FVS1212 resulted from severe mechanical mixing with higher axial force. Tensile fracture surface of the LF weld showed similar features as those of the IF welds except deformation pattern of the fracture surface, where a random wave pattern was observed (Fig. 24e). A larger portion of FVS1212 was observed on the fracture surface as shown in Fig. 24f, which was caused by smooth smearing of FVS1212 into 2024-T351 as shown in Fig. 20a and b. Summarizing the above for dissimilar-alloy welds, all the fracture surfaces of the bend tests located in the inner-HDZ of 2024-351 interfaces. Tensile tests resulted in major portion of fracture in the inner-HDZ of 2024-T351 interface occasionally FVS1212 across the interface, of which proportion depends on welding processes and parameters. For the IF welds, increase in axial pressure increased mechanical mixing across the interface and the tensile fracture surface of the high axial force IF weld showed more proportion of FVS1212 than the low axial force IF weld. For the LF weld, the smooth smearing of FVS1212 into 2024-T351, showed more proportion of FVS1212 than the high axial force IF weld.

Process, Structure, Properties and Fracture Relationships

Similar-Alloy Welds

Inertia-Friction welds showed that high joint efficiency welds in RS/PM FVS1212 is feasible without coarsening of dispersoids and microstructure due to its rapid thermal cycle and expulsion of softened metals in the interface region. Weld axial force played an important role in the formation HDZ microstructure showing the low axial force IF welds resulted in dispersoid-lean band at the interface due to the inhomogeneous deformation resulted from simultaneous compressive and shear stresses at high temperature, while the high axial force IF welds showed a free of defects and coarsening of the microstructure.

Initial try of linear-friction welds of FVS1212 resulted in a moderate coarsening of dispersoids in the interface region. It is concluded for the given weld parameters, thermal cycle is relatively slow compared to the IF welds in this study. However, homogenous interface microstructure independent from radial location in the LF weld gives a good advantage to produce a homogenous weld compared to the inertia-friction welding in addition to its capability to join the non-symmetric components. Future optimization study with a higher axial force and resulting short welding time will reduce the coarsening effect by shortening the thermal cycle and increasing the expulsion of softened metals from the interface region.

Results of hardness testing and tensile testing well agreed with microstructural observation. Most important factor to affect the mechanical properties of the welds is the coarsening of dispersoids and grain structure in the weld region, showing the highest strength and hardness for the high axial force IF welds where the microstructural coarsening was minimum. In addition, distribution of dispersoids affects the mechanical properties. Tensile and bend test fracture occurred at the interface region for all the similar-alloy welds and the features of both fracture surfaces were same for each alloy/process combination. Fracture characteristics were also closely related with the microstructural differences of each weld. The wide homogeneous inner-HDZ of low axial force IF welds resulted in a relatively smooth fracture surface with a fine shear tracks while the narrow striated microstructure in the high axial force IF welds resulted in a rough fracture surface with coarse shear tracks. Directional flow in the LF welds to the linear displacement direction resulted in directional fracture surface patterns. The narrow inner-HDZ of the LF weld showed similar features as those of the high axial force IF weld other than fracture patterns.

Dissimilar-Alloy Welds

For the dissimilar-alloy welds most of the structural changes were observed in 2024-T351. Coarsening and other structural changes were negligible in FVS1212 for both the IF and LF welds, which was attributed to the fact that most of the applied energy was consumed in the flash formation in the softer

2024-T351. Mechanical mixing in the low axial force IF weld was minimal while the high axial force weld showed penetrated layers of FVS1212 in the 2024-T351. For the LF weld penetrated layers were not observed but smooth smearing of FVS1212 into 2024-T351 was noticed.

Results of hardness testing and tensile testing well agreed with microstructural observation. Even with the lowest hardness values in the inner-HDZ of the LF weld among the three types of welds, tensile strength of the LF weld exceeded that of the low axial force IF weld, which was attributed to the smooth smearing across the interface compared to the lack of mechanical mixing in the low axial force IF weld. Both the tensile and bend tests resulted in fracture initiation at the interface region of 2024-T351. Depending on the mechanical mixing and smearing the proportion of FVS1212 on the fracture surface changed showing higher proportion of FVS1212 for the high axial force IF weld and the LF weld. As in the similar-alloy welds, the fracture surfaces of the dissimilar welds also showed the flow patterns at the interface region, where IF welds showed a spiral shear patterns while LF weld showed a irregular wavy pattern.

Conclusions

1) Both the inertia- and linear-friction welds has been demonstrated to be promising processes for the joining of RS/PM Al-Fe-V-Si alloys.

2) For both the similar-alloy and the dissimilar-alloy welds, the high axial force inertia-friction welding showed the best results considering the microstructural and mechanical properties and fracture characteristics showing joint efficiencies of 84 and 95 % respectively.

3) For the similar-alloy welds, the mechanical properties and fracture characteristics was affected by the coarsening of dispersoids and microstructure in the weld region. In addition, the mechanical properties and fracture characteristics were also affected by the mechanical mixing at the interface for the dissimilar-alloy welds.

4) The linear-friction welds of FVS1212 resulted in a moderate coarsening of dispersoids in the interface region due to the slow thermal cycle for the given parameters but showed homogeneous microstructure independent from radial location. Future optimization study with a higher axial force would produce a homogeneous weld microstructure with minimal coarsening.

Acknowledgements

The authors are indebted to Drs. S. K. Das and Paul Gilman of Allied-Signal, Inc. for providing the alloy evaluated in this study, Mr. I. Varol for color metallography and Dr. K. Sampath for the helpful comments. Appreciation is also expressed to Messrs. David Nicholas and Edward Watts of The Welding Institute, Cambridge, for performing linear-friction welding trials. Finally, the authors are grateful to Dr. Andrew Crowson and the Army Research Office for providing financial support for this work under contract #DAAL03-88-K-0049.

References

1. High Temperature Aluminum Alloy - FVS1212 and FVS0812 Data Sheet, Allied-Signal Inc.
2. Das, S. K. and Davis, L. A. 1988, High performance aerospace alloys via RS processing. Materials Science and Engineering 98: 1-12
3. Skinner, D. J. 1988, The physical metallurgy of dispersion strengthened Al-Fe-V-Si alloys. Dispersion Strengthened Aluminum Alloys, eds. Kim, Y. W. and Griffith, W. M.: 181-197. Warrendale, PA: TMS/AIME
4. Bye, R. L., Kim, N. J., Skinner, D. J., Raybould, D., Brown, A. M. 1988, RS/PM aluminum alloys prepared from melt-spun ribbons. Processing of Structural Metals by Rapid Solidification, eds. Froes, F.H., and Savage, S. J.: 283-

289. Metals Park, OH: ASM International

5. Krishnaswamy, S., and Baeslack, W. A. 1989, Structure, properties and fracture of pulsed Nd:YAG laser weld in Al-8Fe- 2Mo Recent Trends in Welding Science and Technology TWR '89: 631. Metals Park, OH: ASM International

6. Baeslack, W. A., and Krishnaswamy, S. 1986, Electron beam weldability of a rapidly solidified aluminum alloy Advances in Welding Science and Technology, ed. David, S.: 357. Metals Park: ASM International

7. Baeslack, W. A., Hou, K. H. and Devletian, J., 1988. Rapid solidification joining of a powder metallurgy Al-Fe-Ce alloy J. Mat. Sci. 7: 947

8. Baeslack, W. A. and Hou K. H. 1989. Electron microscopy of rapidly solidified weldments in a powder metallurgy Al-Fe-Ce alloy J. Mat. Sci. Lett. 8: 2642 - 2653

9. Ananthananayaranan, V., 1988. Diffusion Welding of an RS/PM Aluminum Alloy, Ph.D. Dissertation, The Ohio State University, Columbus, Ohio.

10. Baeslack, W. A. and Hagey, K. S. 1988, Inertia friction welding of rapidly solidified powder metallurgy aluminum Weld. J. 67: 139s

11. Hou, K. H. and Baeslack, W. A. 1990, Electron microscopy of inertia-friction weldments in a rapidly solidified Al-Fe-Mo-

V alloy *J. Mat. Sci.* 25: 2642 - 2653

12. Koo, H. H., Krishnaswamy, S. and Baeslack III, W. A. 1991, Structure, properties and fracture relationships in inertia-friction weldments between a rapidly-solidified Al-Fe-Mo-V and IM 2024-T351 *J. Mat. Sci.* (in review)

13. Nicholas E. D. 1987, *Friction Welding Non-Circular Sections with Linear Motion - A Preliminary Study*, Cambridge, England: The Welding Institute

14. ASM. 1984, *Aluminum: Properties and Physical Metallurgy*: 78 Materials Park, OH: ASM

15. ASM International. 1990, *Metals Handbook vol. 2*, 10th ed.: 71 and 628, Metals Park OH:ASM International

Table 1. Welding parameters[a] for the alloy/process combinations.

Alloy/Process Combination		Axial Load (KN)	Pressure (MPa)	Relative Motion (m/s)	Upset (mm)
1212/1212	IFW/L	55.8	144	5.8	8.9
	IFW/H	83.7	216	5.8	4.5
1212/1212	LFW	30/50	216/360	0.1	6.5
1212/2024	IFW/L	83.7	216	4.1	2.4
	IFW/H	139.5	360	4.1	7.1
1212/2024	LFW	30/50	216/310	0.1	5.2

a. Inertia-Friction Welding:
Moment of Inertia; 0.17 Kg-m^2
Inertial-Energy; 22.7 KJ
Linear-Friction Welding:
Friction Force; 30KN
Forge Force; 50KN
Frequency; 50 Hz at Amplitude of 2 mm

Table 2. Tensile Test Results for the alloy/process combinations

Alloy/Process Combination	Specimen Location	YS (MPa)	TS (MP)	el. (%)	J.E. (%)	Fracture Location
1212/1212 IFW/L	periphery	376	376	0.5	66	IHDZ[a]
	center	414	463	1.1	81	IHDZ
1212/1212 IFW/H	periphery	415	487	2.1	85	IHDZ
	center	418	482	1.6	84	IHDZ
1212/1212 LFW	periphery	420	446	1.0	78	IHDZ
	center	409	474	2.1	83	IHDZ
1212/2024 IFW/L	periphery	299	385	6.0	82	2024 IHDZ
	center	319	376	1.7	80	2024 IHDZ
1212/2024 IFW/H	periphery	343	445	4.2	95	2024 IHDZ
	center	328	443	4.5	95	2024 IHDZ
1212/2024 LFW	periphery	305	393	2.3	85	2024 IHDZ
	center		314	409	2.6	87 2024 IHDZ
1212 BM extruded bar[b]		522	572	23.0		
2024-T351 extruded bar[c]		324	469	20.0		

a. IHDZ denotes inner heat- and deformation-affected zone
b. Ref. 1
c. Ref. 16

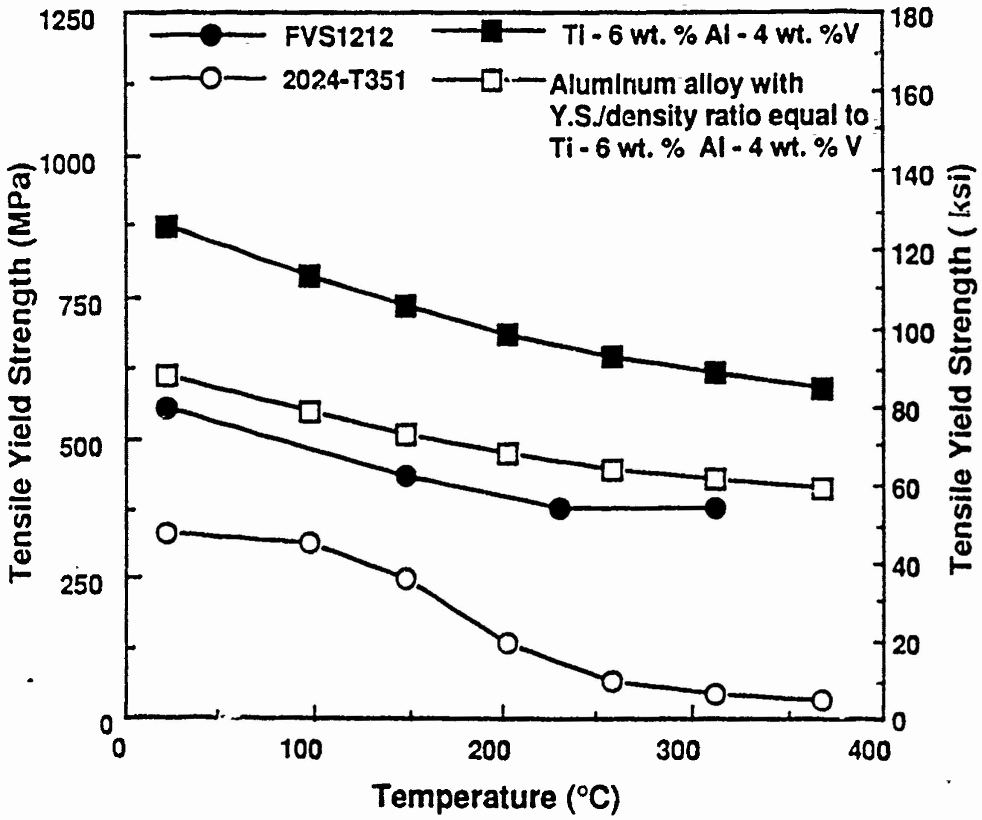

Fig. 1. A comparison of tensile yield strength versus test temperature for FVS1212, 2024-T351 and Ti-6wt.% Al-4 wt.% V (Refs. 1 and 15).

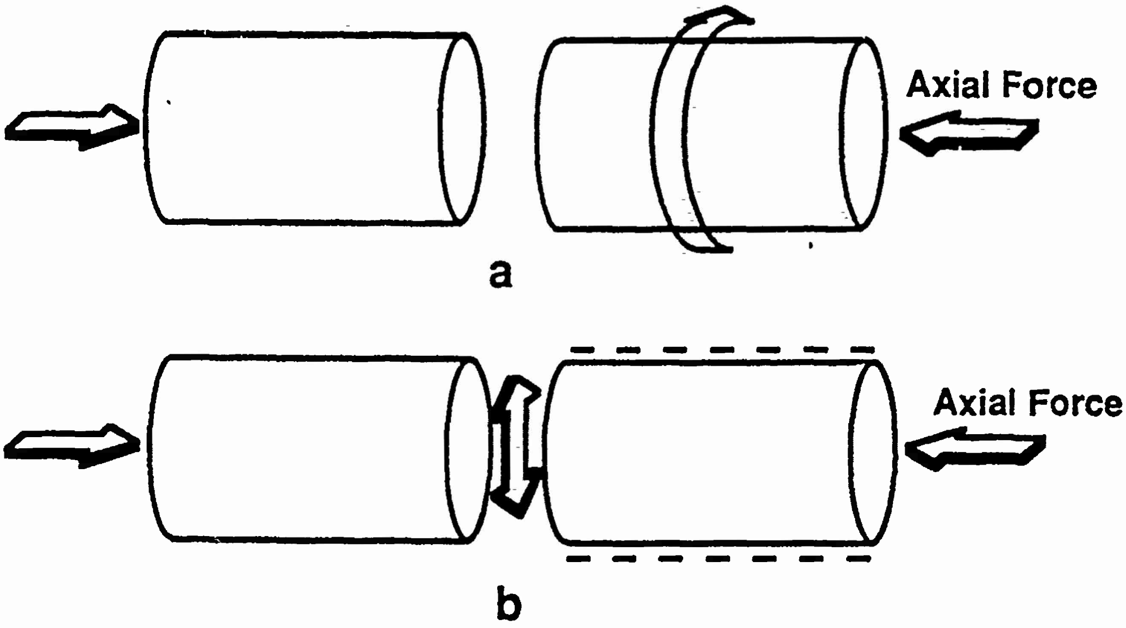

Fig. 2. Schematic representations of (a) inertia-friction welding process and (b) linear-friction welding process.

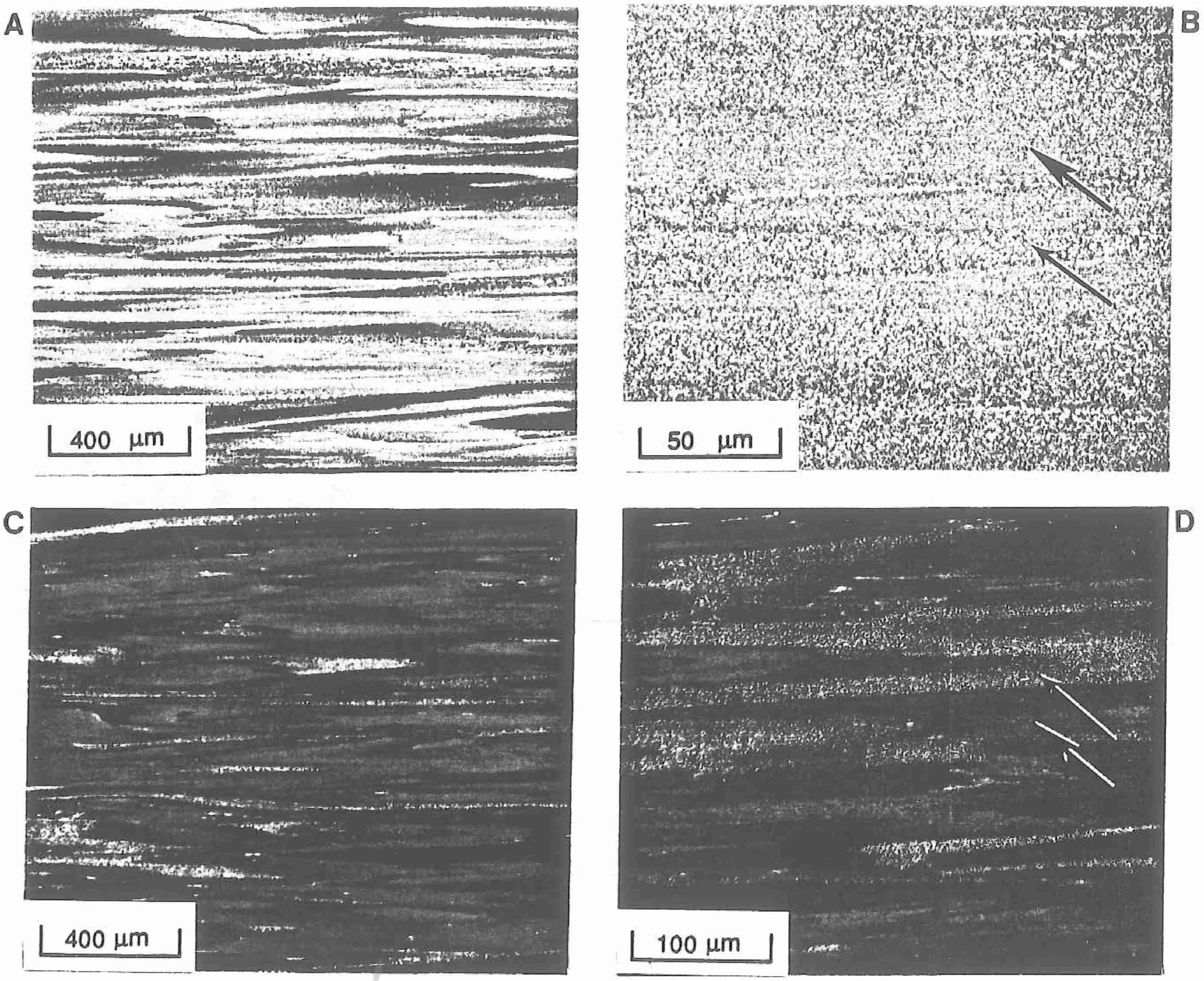

Fig. 3. Black-and-white (a,b) and color (c,d) light micrographs of as-extruded FVS1212 base metal. Large and small arrows in (b) and (d) indicate regions of fine and coarse dispersoids, respectively.

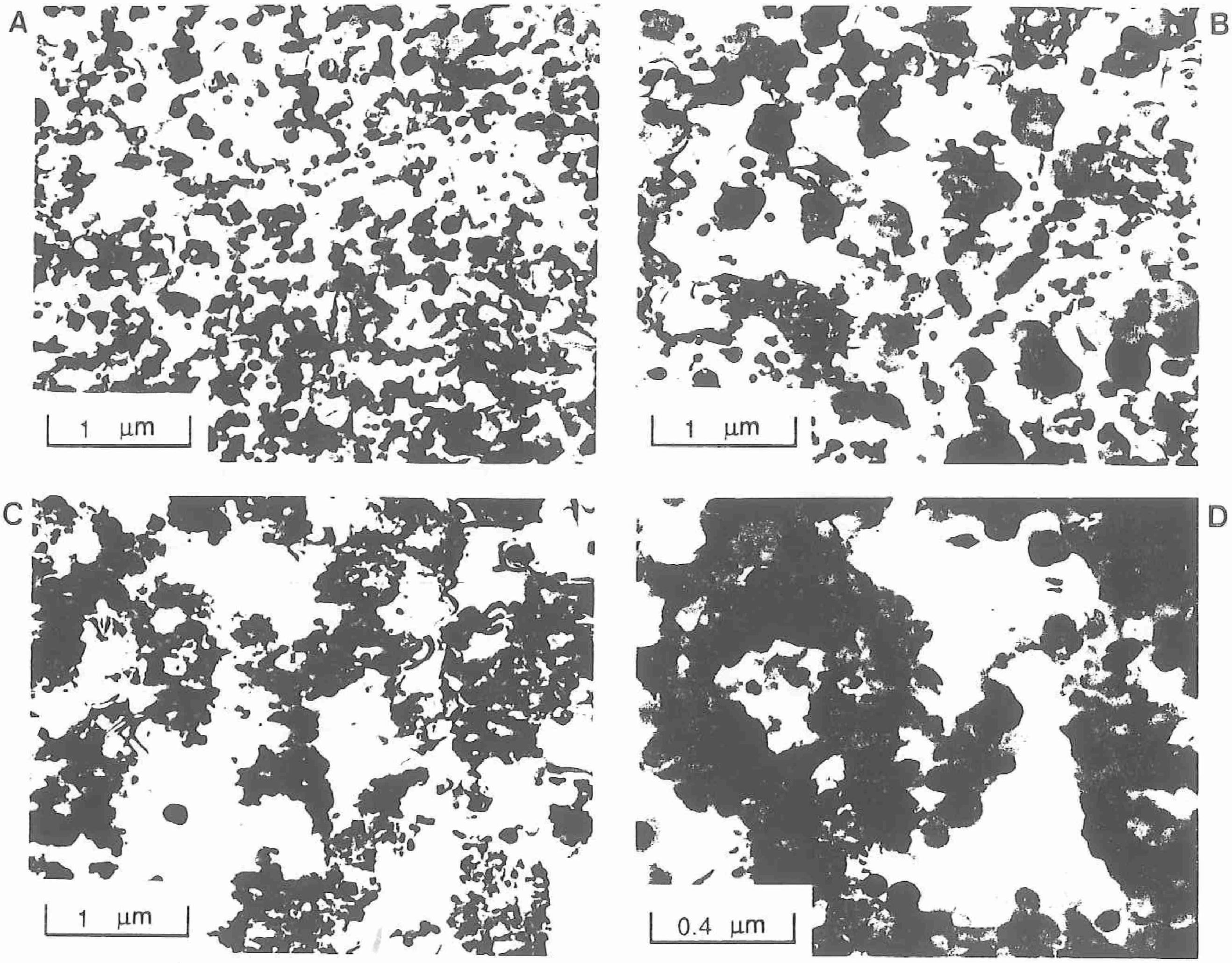

Fig. 4. TEM bright-field micrographs of FVS1212 extruded base metal: (a) uniform distribution of fine dispersoids; (b) mixture of fine and coarse dispersoids; (c, d) clusters of fine dispersoids along alpha grain boundaries.

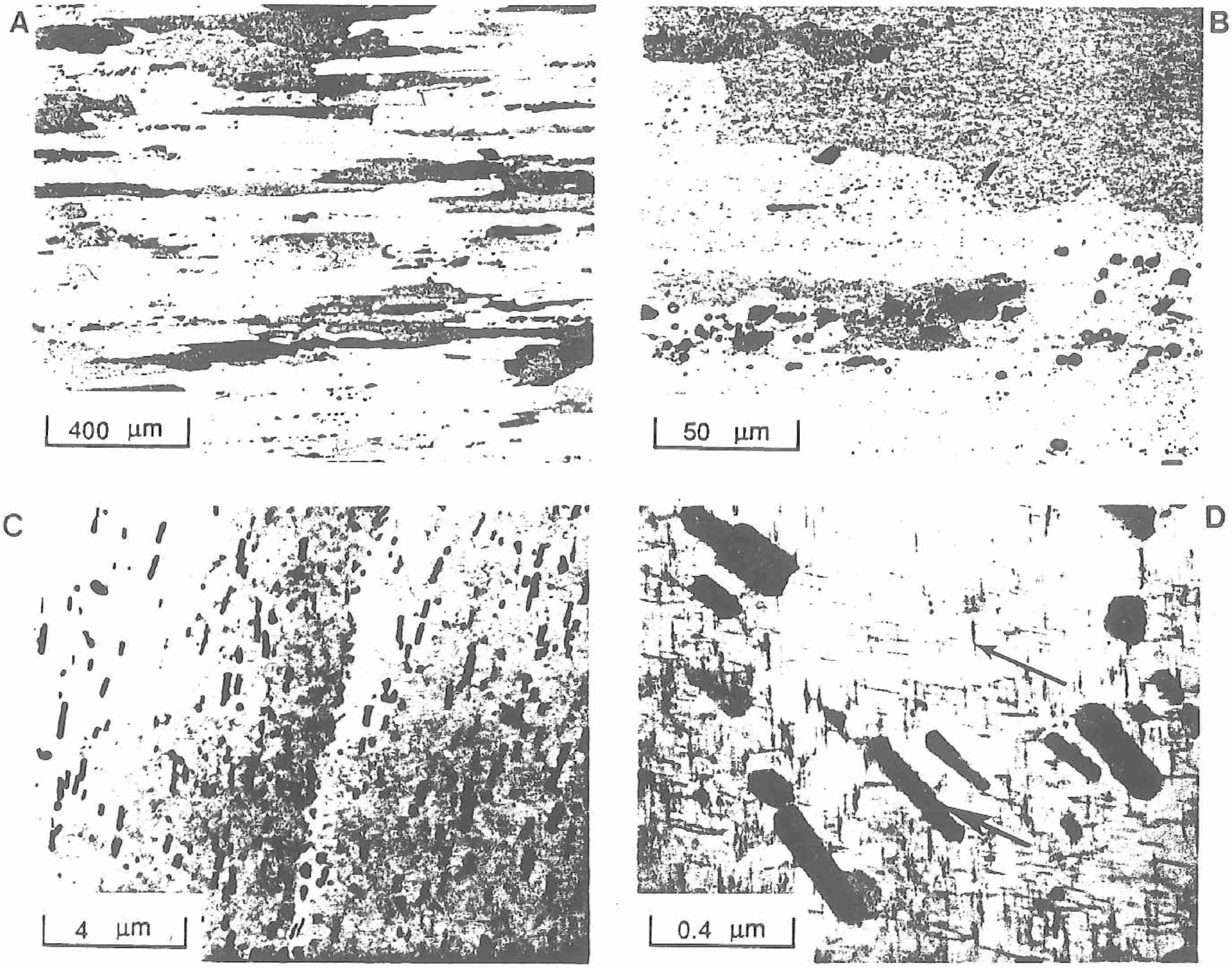

Fig. 5. Light (a, b) and TEM bright-field (c, d) micrographs of 2024-T351 base metal. Large and small arrows in (d) indicate $Al_{20}Cu_2Mn_3$ dispersoids and S′ (Al_2CuMg) precipitates, respectively.

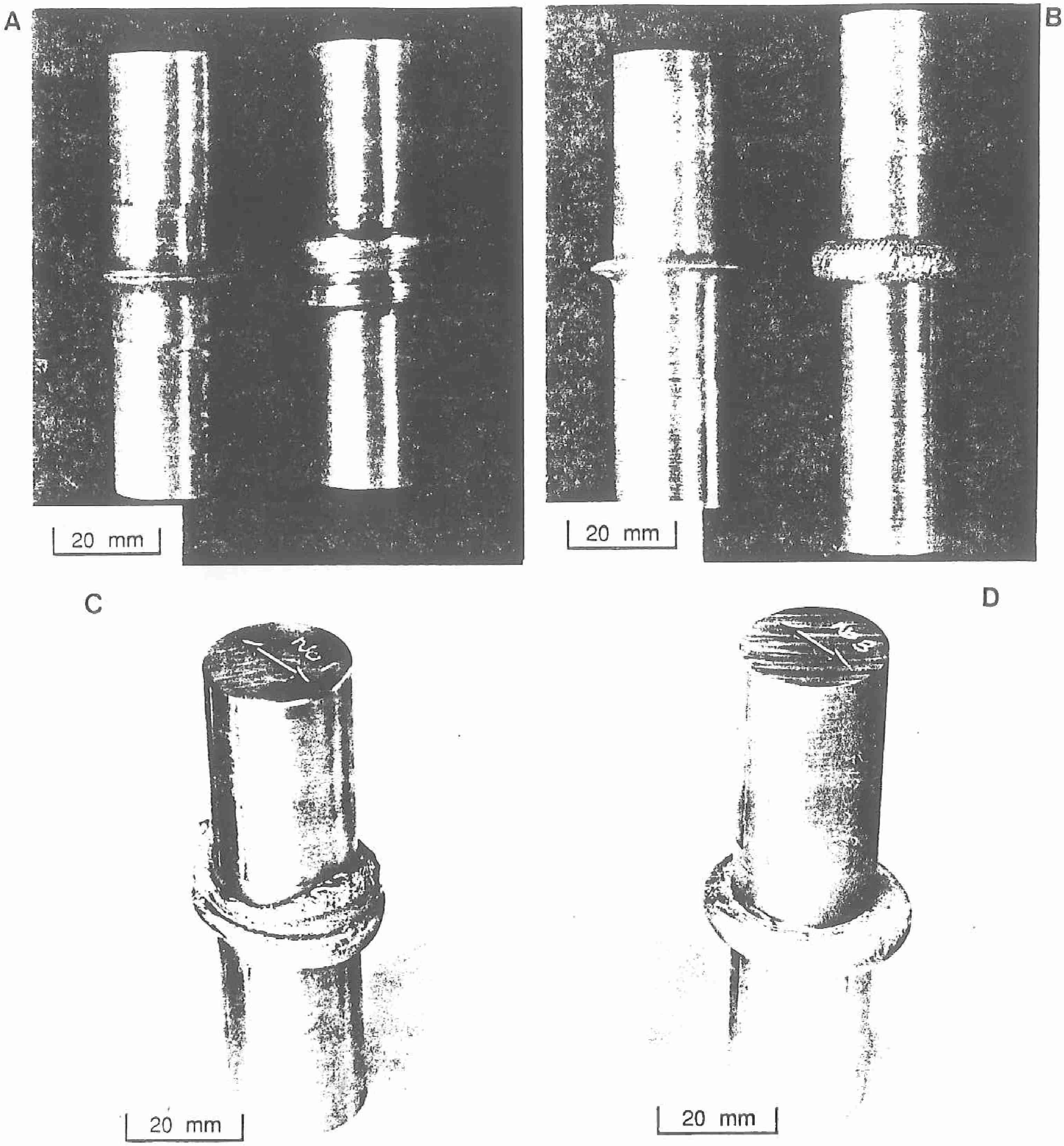

Fig. 6. As-welded friction welds: (a) similar-alloy IF welds in FVS1212 produced at low (left) and high (right) axial force; (b) dissimilar-alloy IF welds between FVS1212 and 2024-T351 produced at low (left) and high (right) axial force; (c) similar-alloy LF weld in FVS1212; (d) dissimilar-alloy LF weld between FVS1212 and 2024-T351. Arrows on top of linear-friction weld specimens indicate direction of linear displacement. In (b) and (d), FVS1212 is top half and 2024-T351 is bottom half.

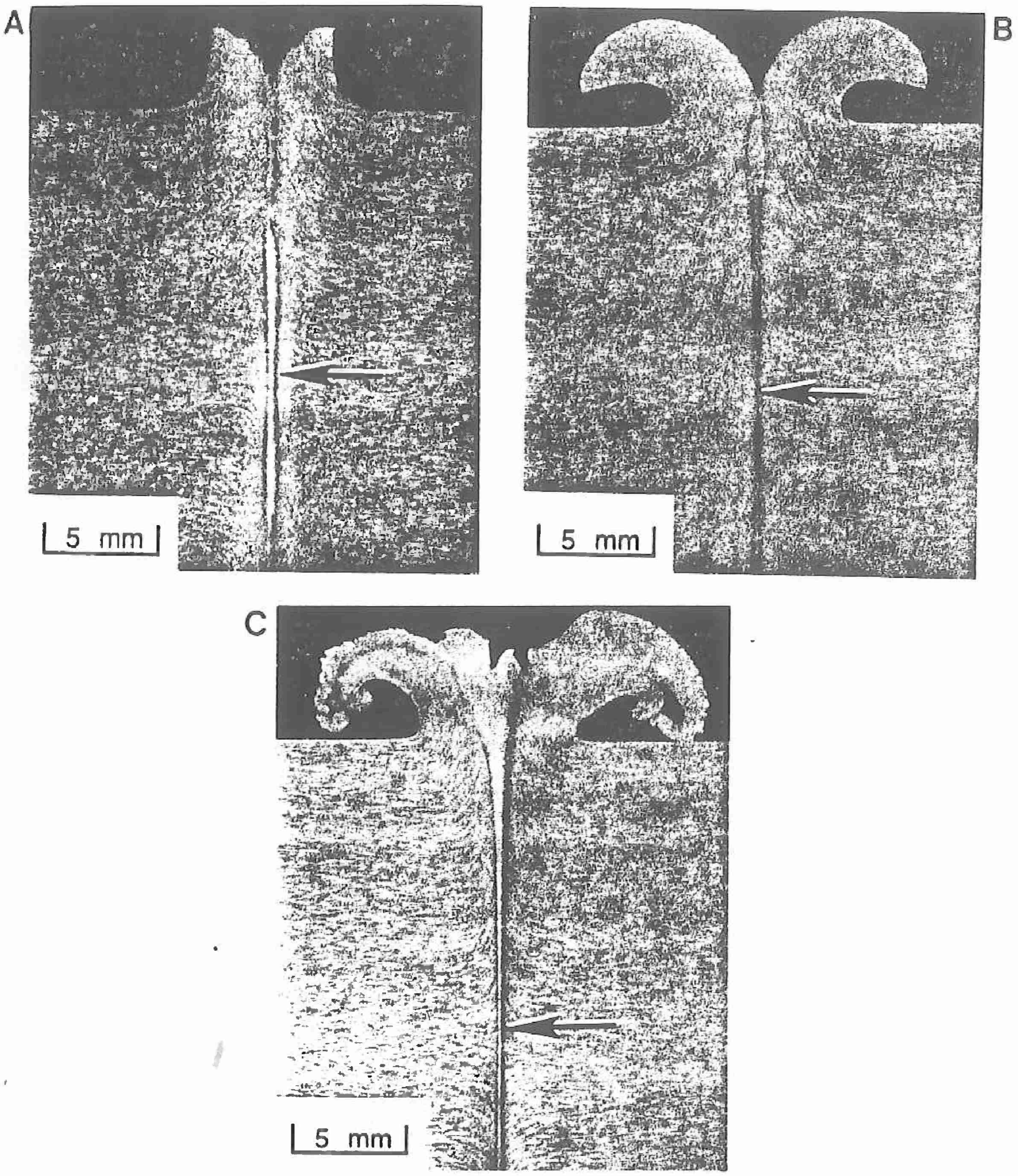

Fig. 7. Macrographs of the similar alloy welds in FVS1212: (a) inertia-friction weld produced with low axial force; (b) inertia-friction weld produced with high axial force; (c) linear-friction weld. Arrows indicate axial centerline.

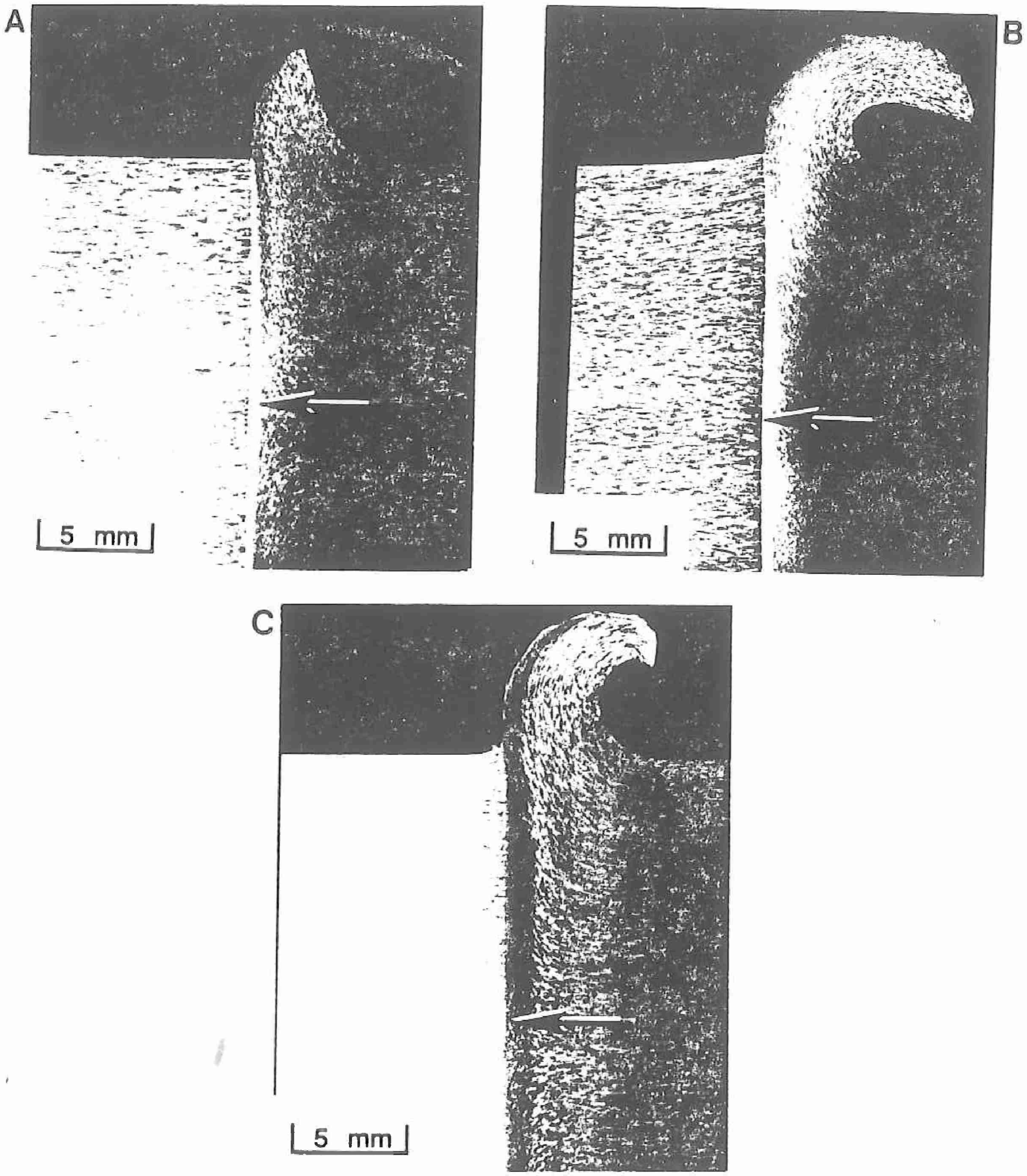

Fig. 8. Macrographs of the dissimilar alloy welds between FVS1212 and 2024-T351: (a) inertia-friction weld produced with low axial force; (b) inertia-friction weld produced with high axial force; (c) linear-friction weld. Arrows indicate axial centerline.

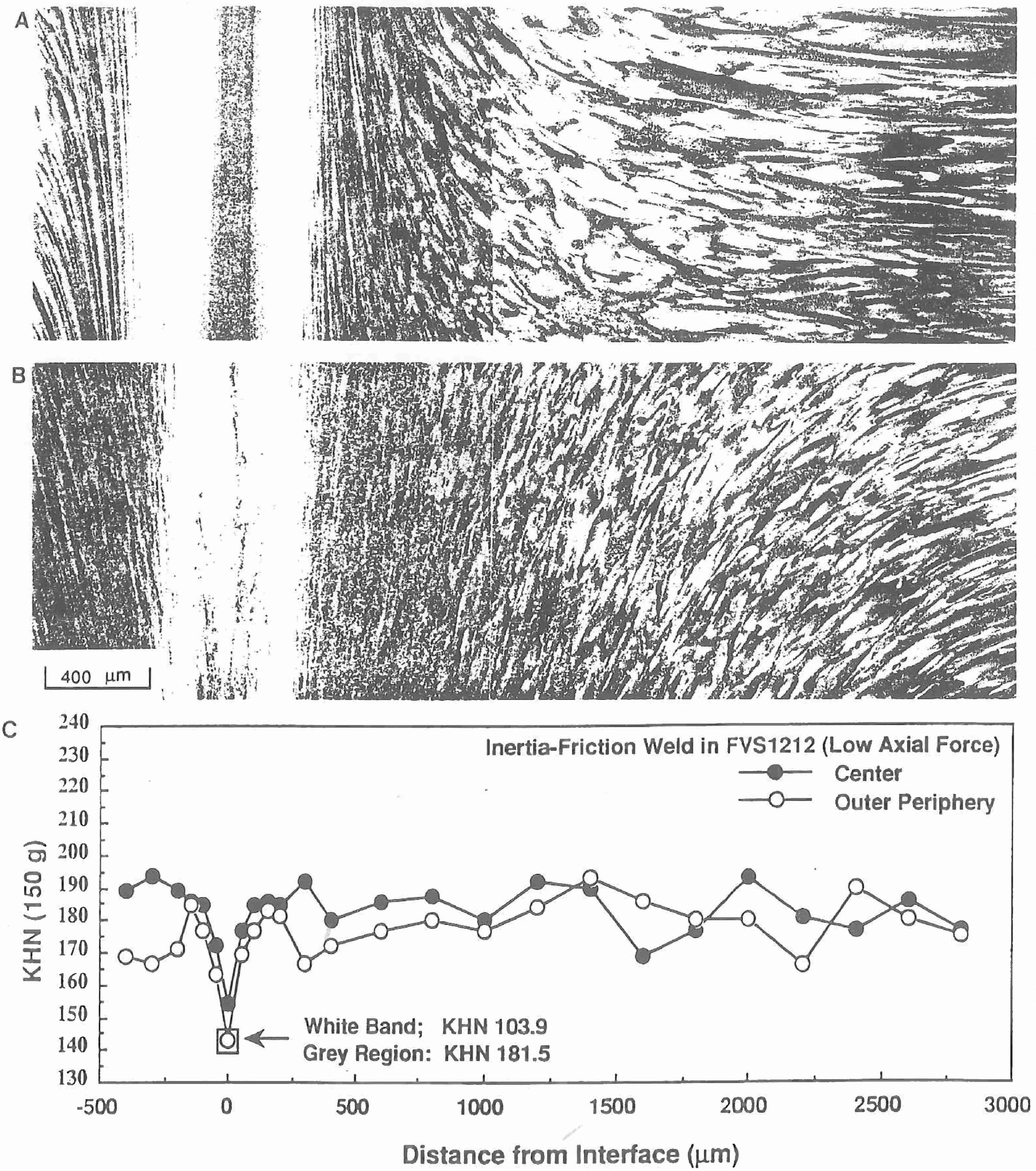

Fig. 9. Light micrographs of the (a) center and (b) outer periphery and corresponding KHN hardness traverses (c) for an inertia-friction weld produced in FVS1212 using low axial force.

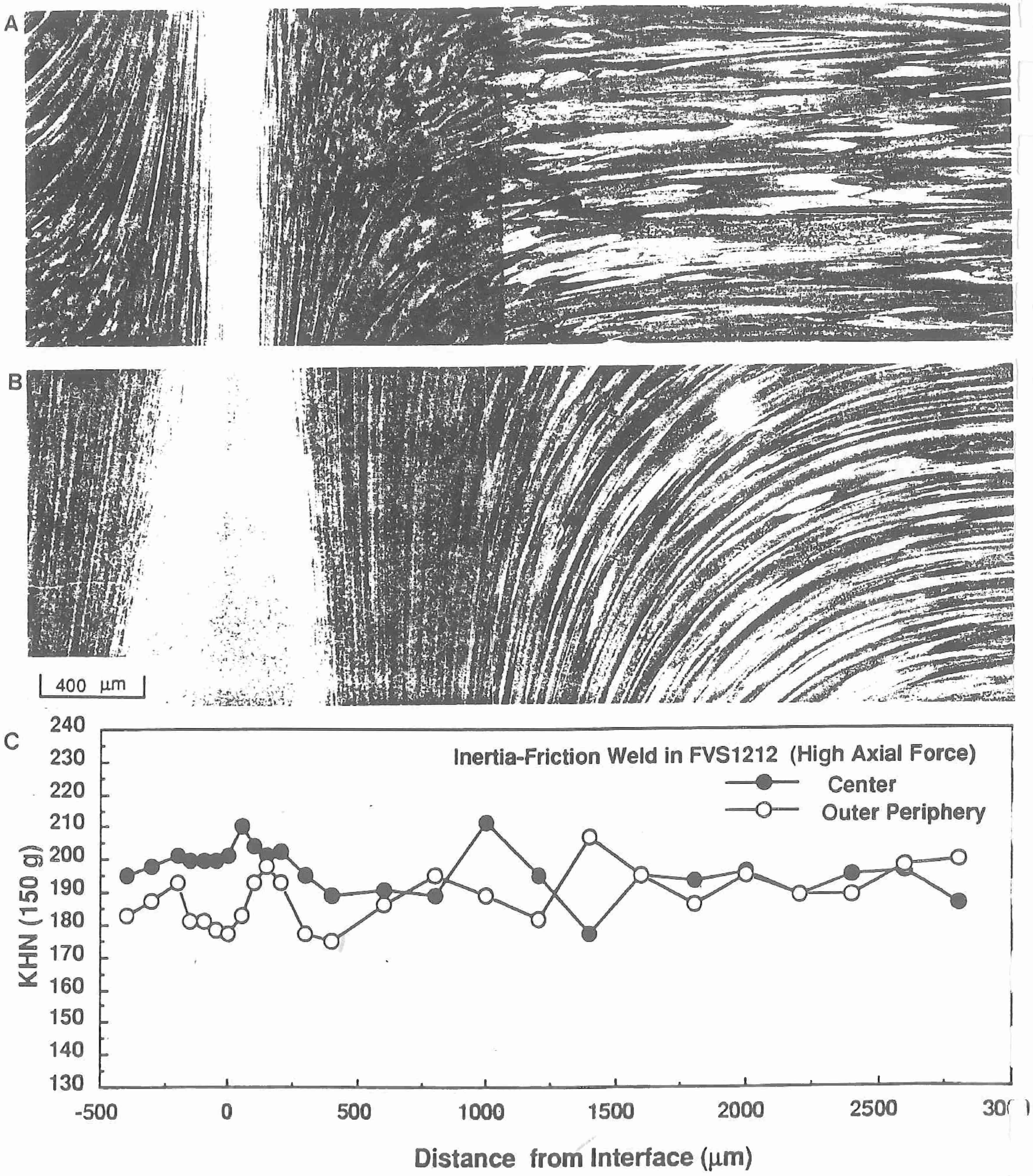

Fig.10. Light micrographs of the (a) center and (b) outer periphery regions and corresponding KHN hardness traverses (c) for an inertia-friction weld produced in FVS1212 using high axial force.

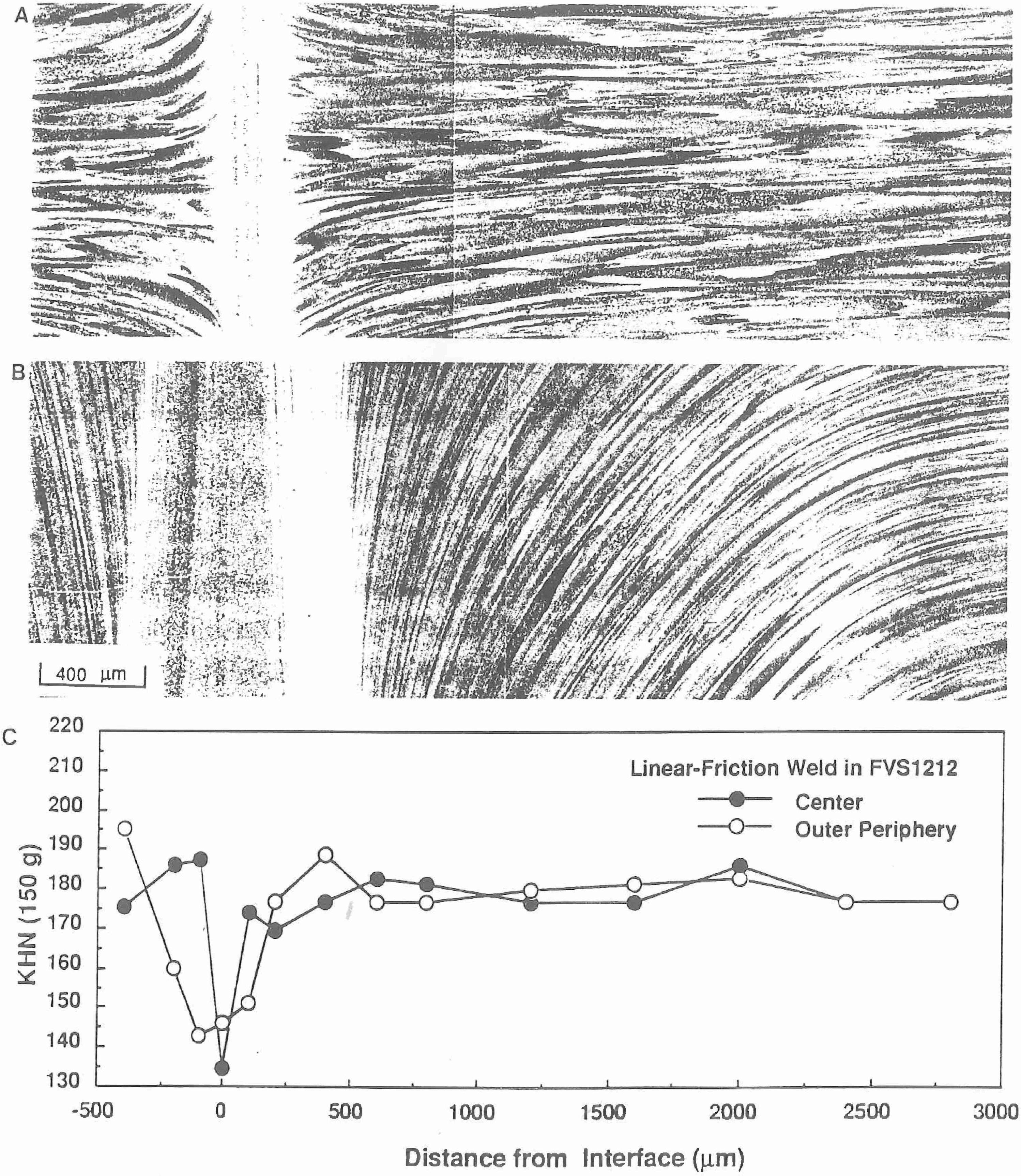

Fig.11. Light micrographs of the (a) center and (b) outer periphery and corresponding KHN hardness traverses (c) for a linear-friction weld produced in FVS1212.

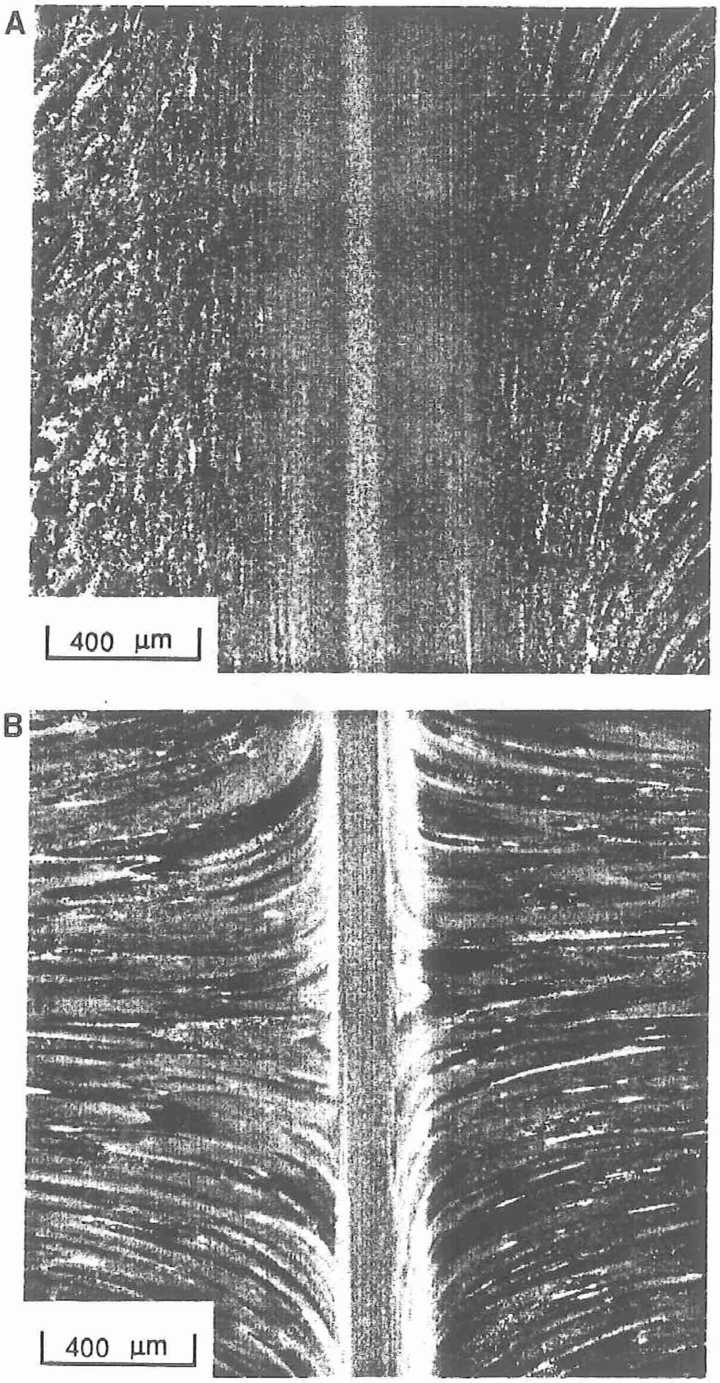

Fig.12. Color light micrographs of the interface regions at the axial centerlines of friction welds in FVS1212: (a) inertia-friction weld produced using low axial force; (b) linear-friction weld.

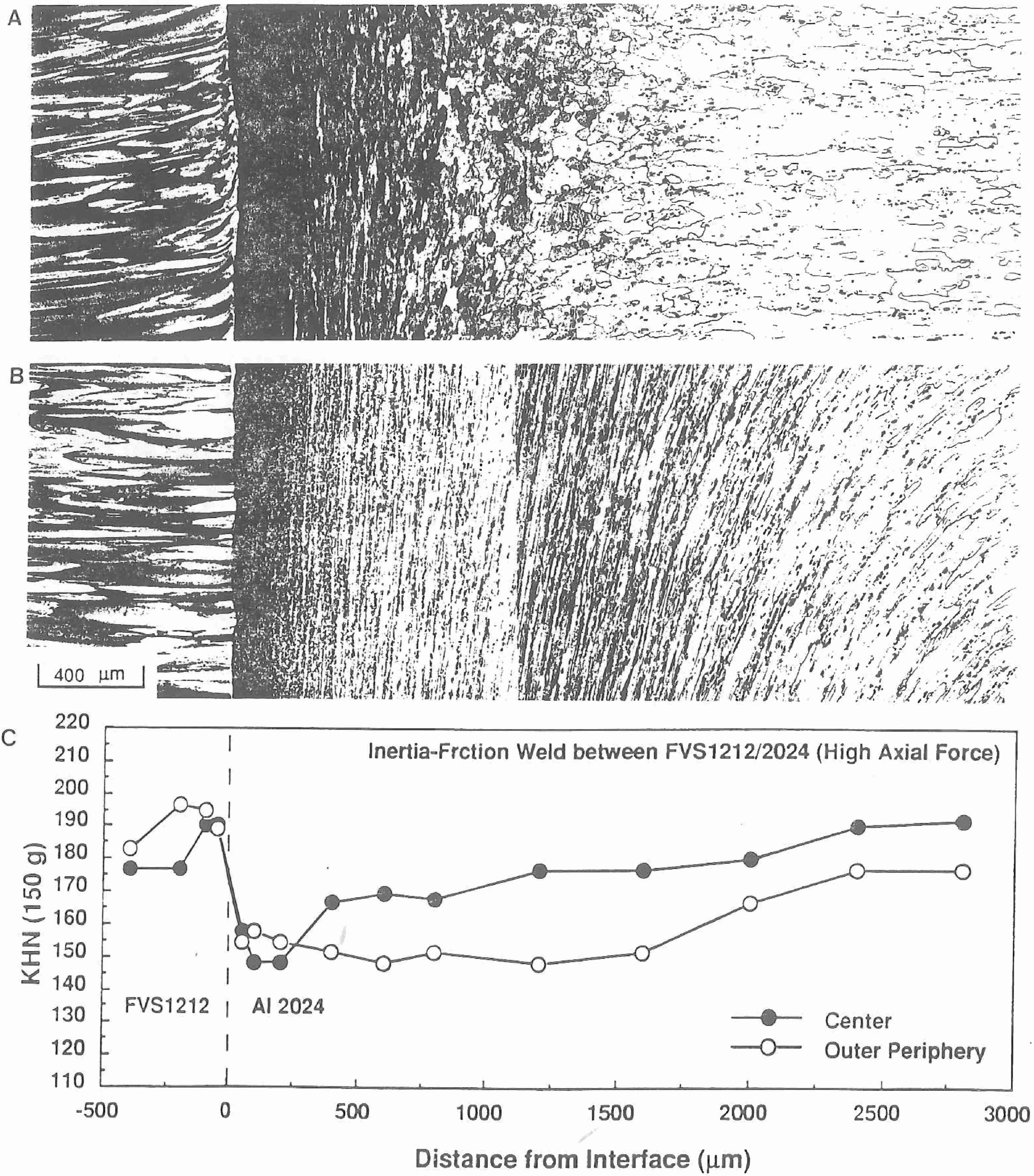

Fig.13. Light micrographs of the (a) center and (b) outer periphery and corresponding KHN hardness traverses (c) for an inertia-friction weld between FVS1212 and 2024-T351 produced using high axial force.

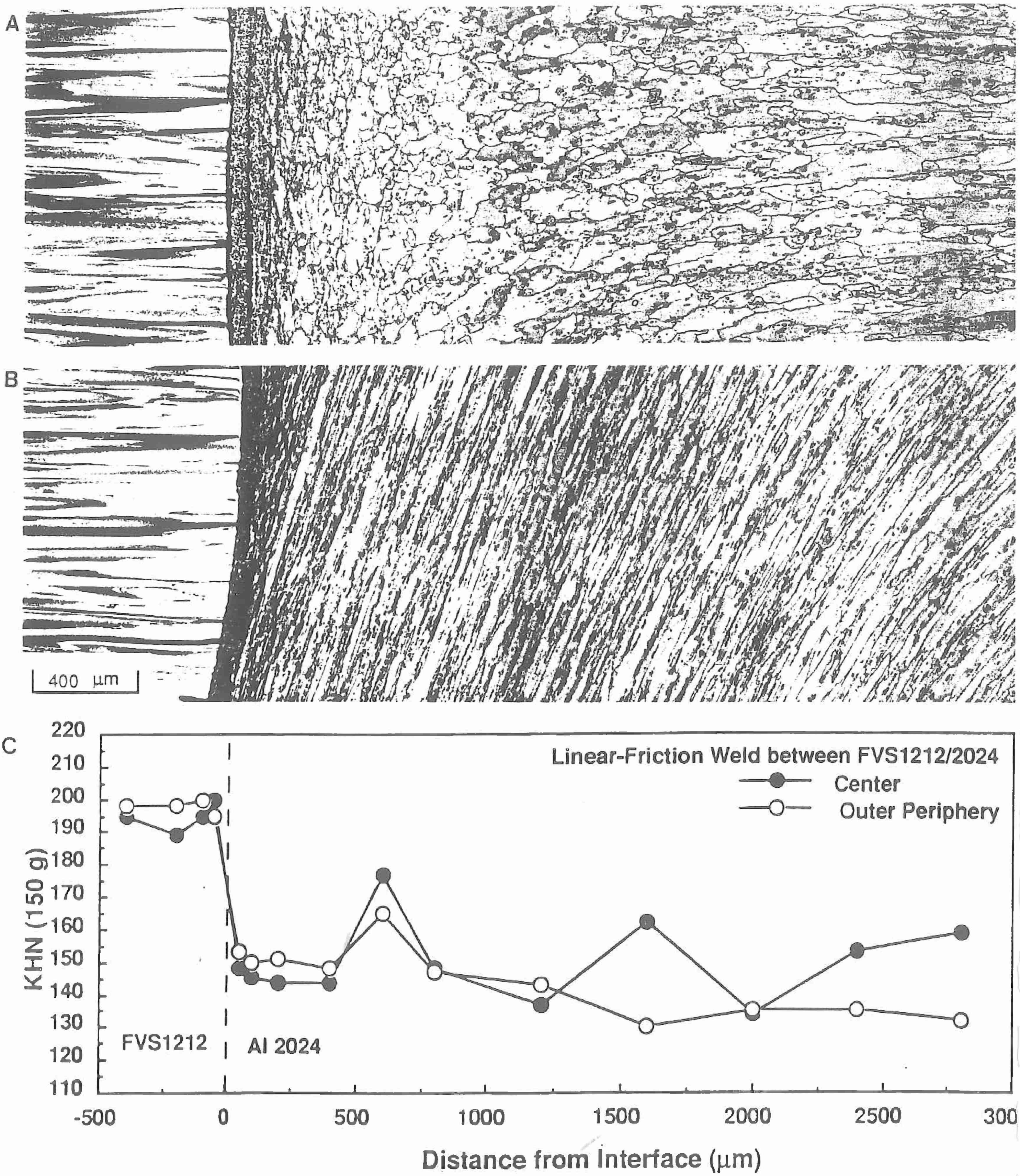

Fig.14. Light micrographs of the (a) center and (b) outer periphery regions and corresponding KHN hardness traverses (c) for a linear-friction weld between FVS1212 and 2024-T351.

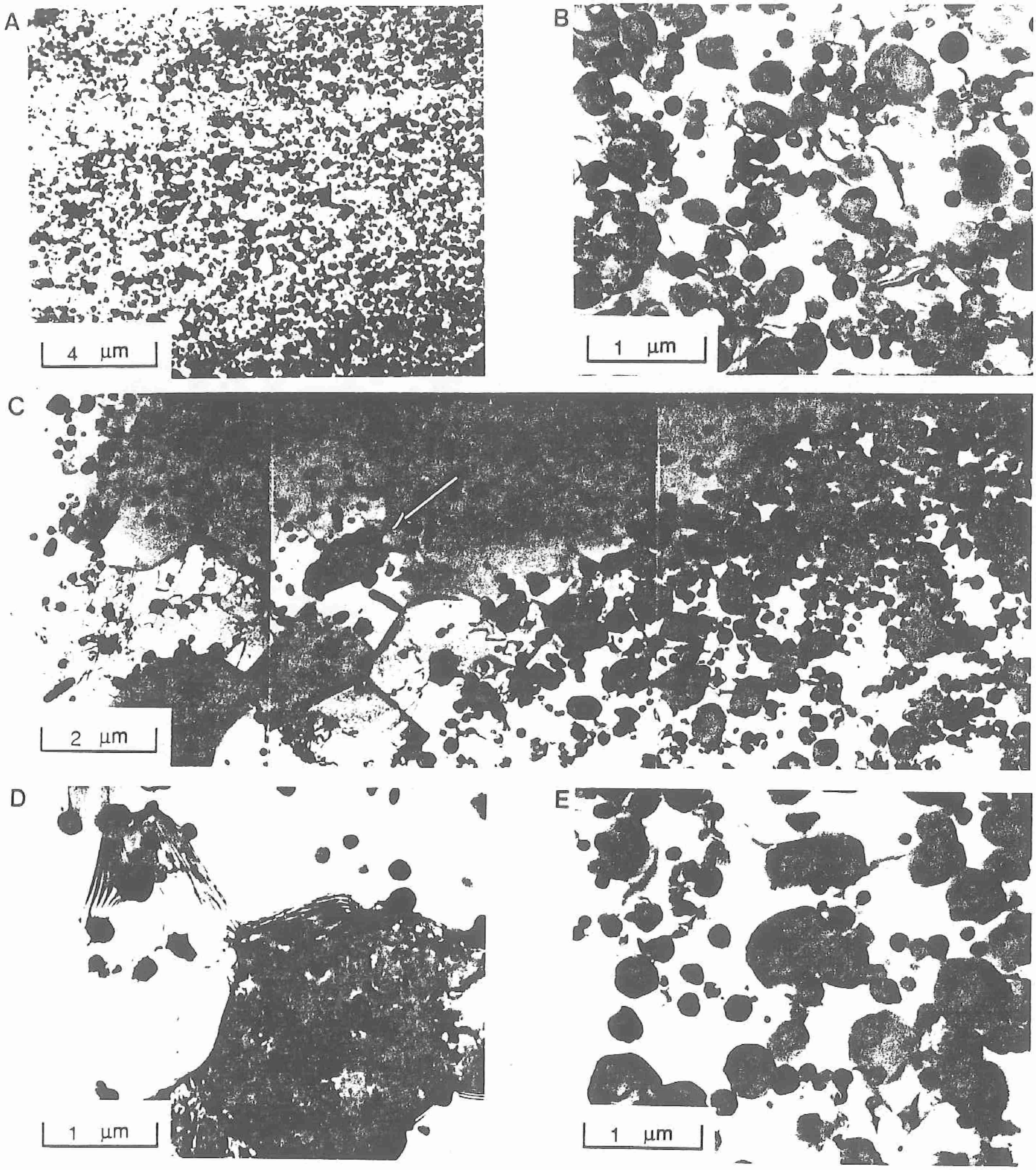

Fig.15. TEM bright-field micrographs of inertia-friction welds produced in FVS1212 using low axial force: (a,b) center of HDZ at axial centerline; (c-e) center of HDZ at outer periphery. Arrow in (c) is parallel to weld interface.

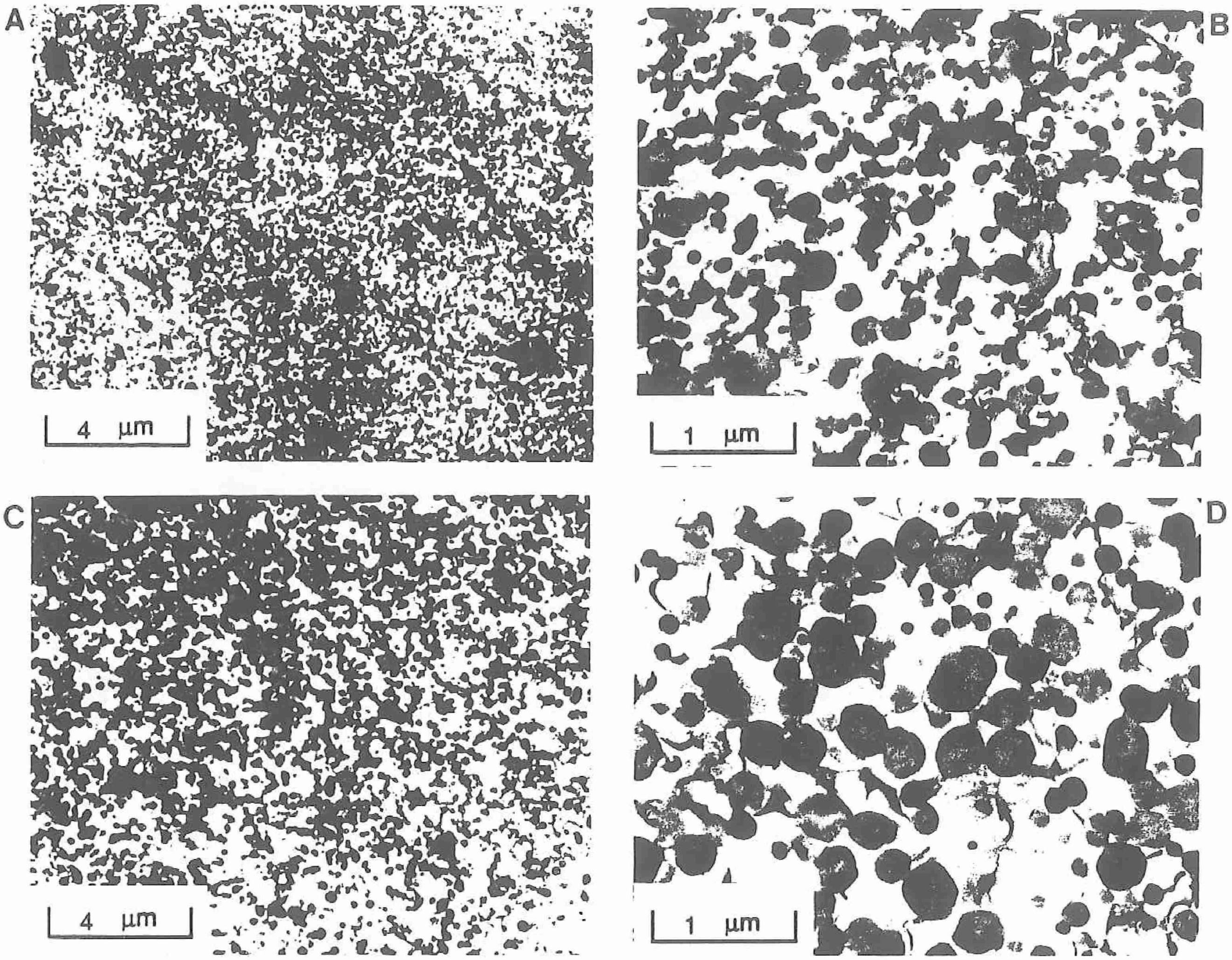

Fig.16. TEM bright-field micrographs of inertia-friction welds produced in FVS1212 using high axial force: (a,b) center of HDZ at axial centerline; (c,d) center of HDZ at outer periphery.

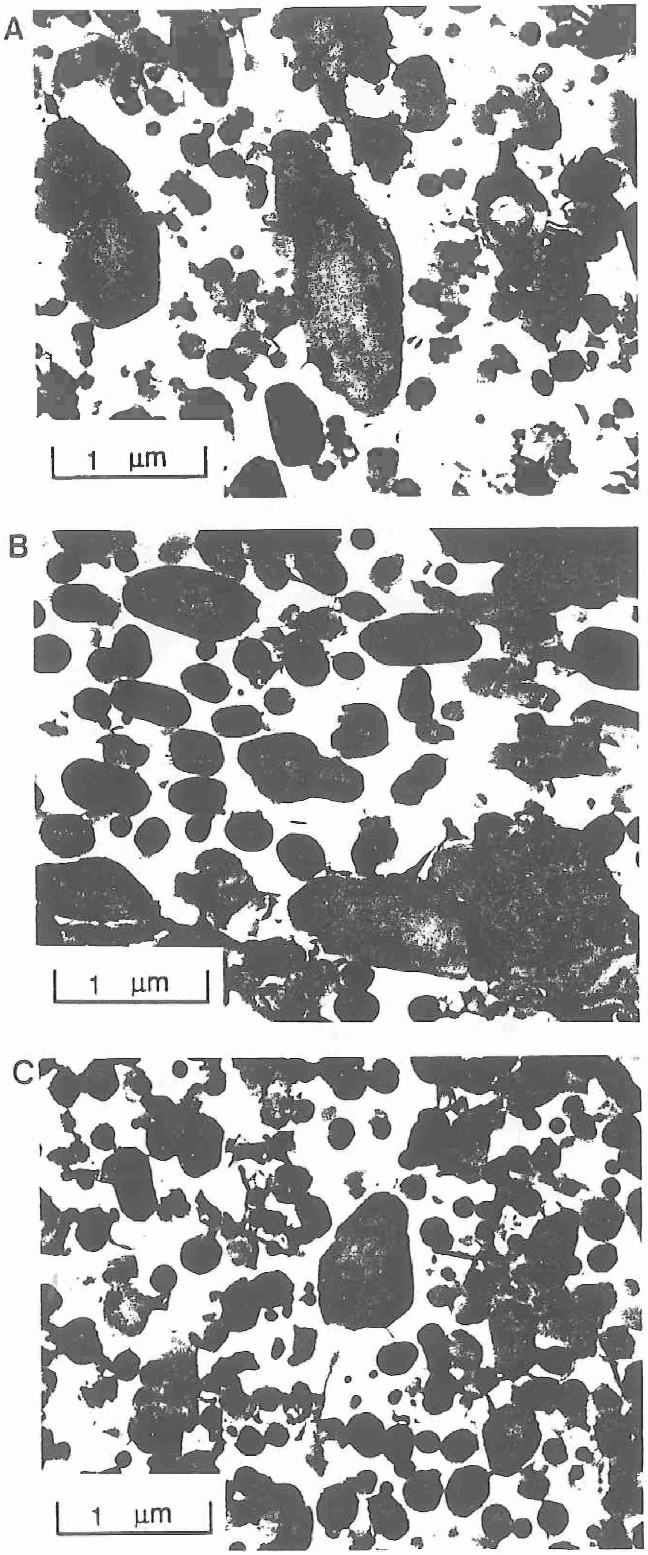

Fig.17. TEM bright-field micrographs of linear-friction welds produced in FVS1212: (a) center of HDZ at axial centerline; (b) adjacent layered region; (c) center of HDZ at outer periphery.

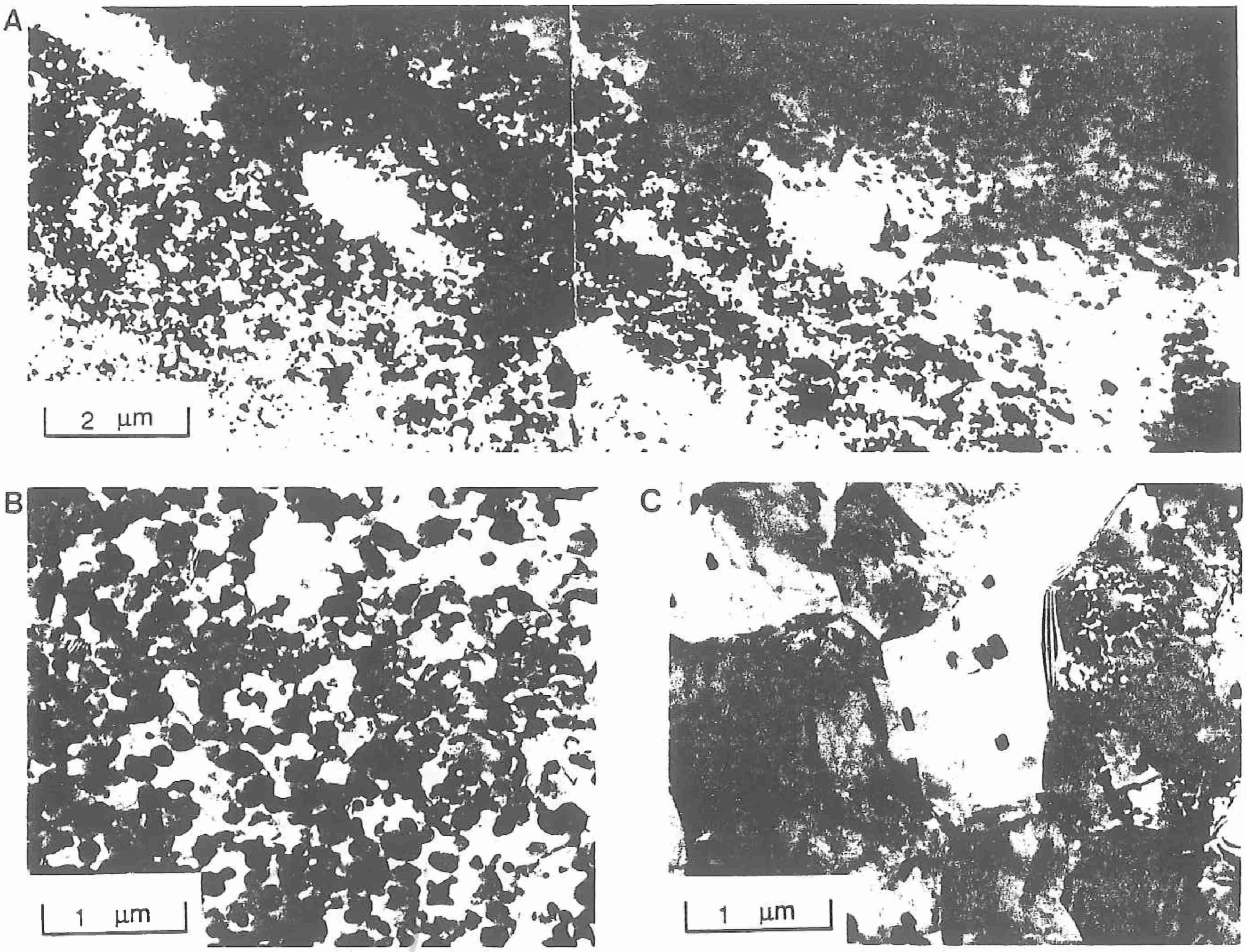

Fig.18. TEM bright-field micrographs of inertia-friction welds produced between FVS1212 and 2024-T351 using high axial force: (a) overall view of the interface; (b) FVS1212 near the interface; (c) 2024-T351 near the interface.

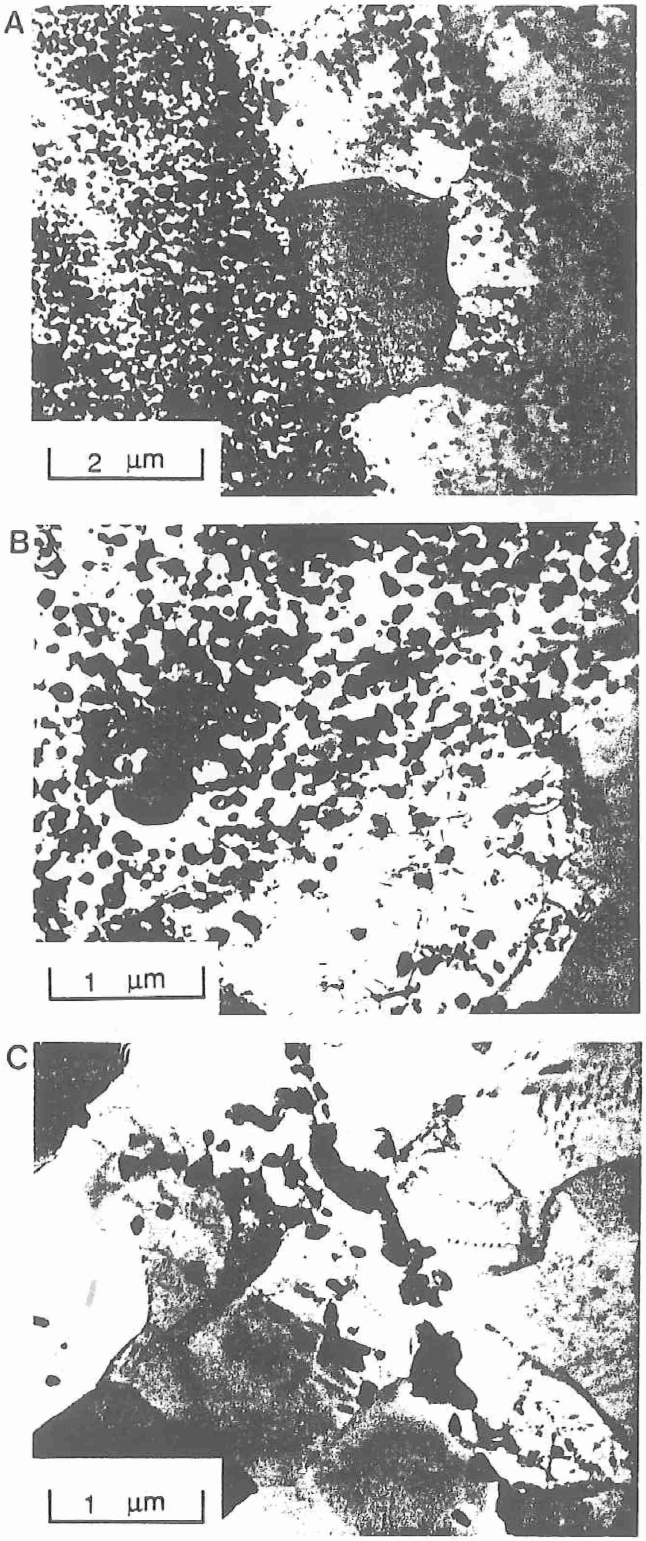

Fig.19. TEM bright-field micrographs of a linear-friction welds produced between FVS1212 and 2024-T351: (a, b) overall view of the interface; (c) 2024-T351 near the interface.

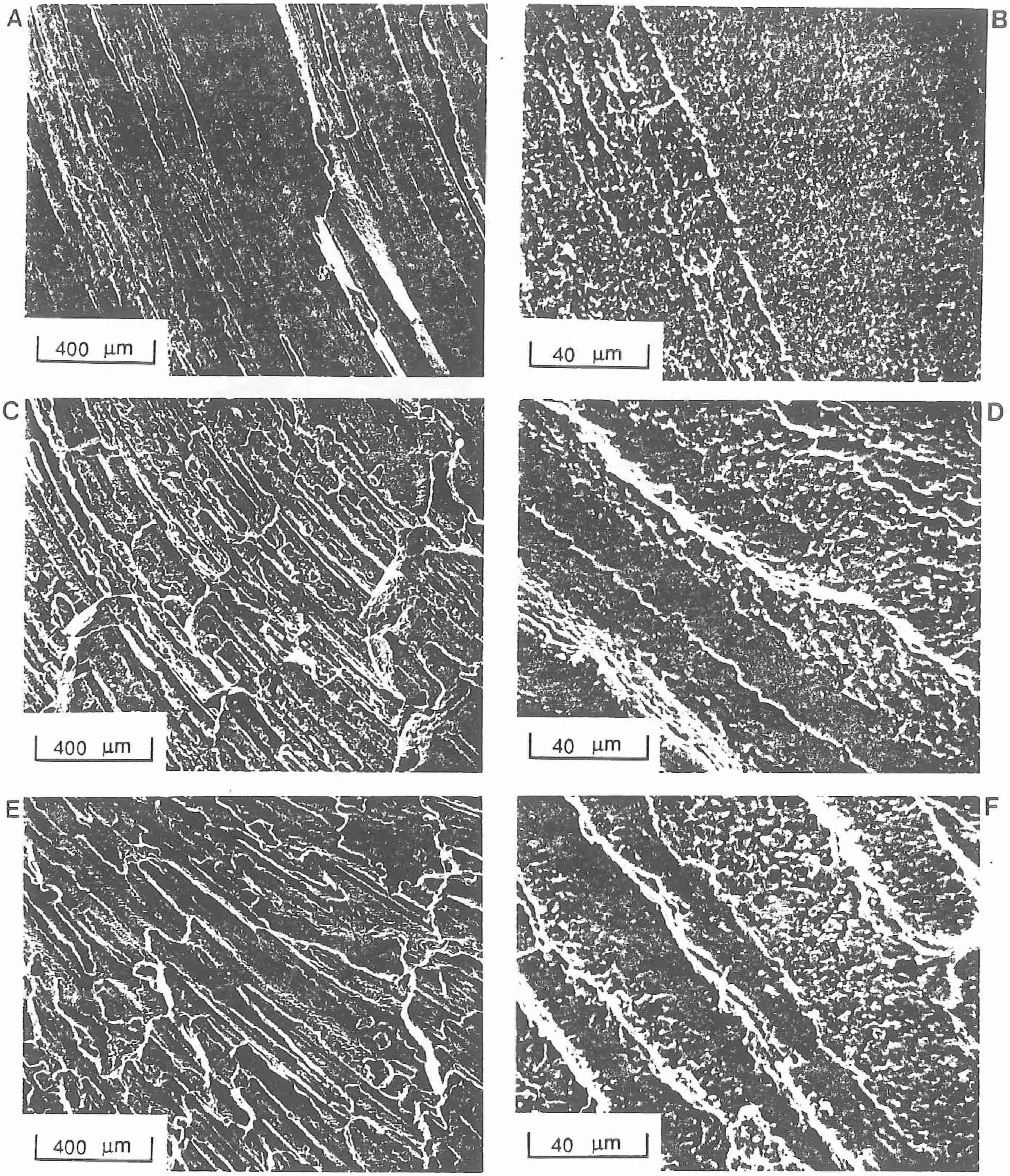

Fig.20. SEM fractographs of bend test specimens extracted from similar-alloy welds in FVS1212: (a,b) IFW produced with low axial force; (c,d) IFW produced with high axial force; (e,f) LFW.

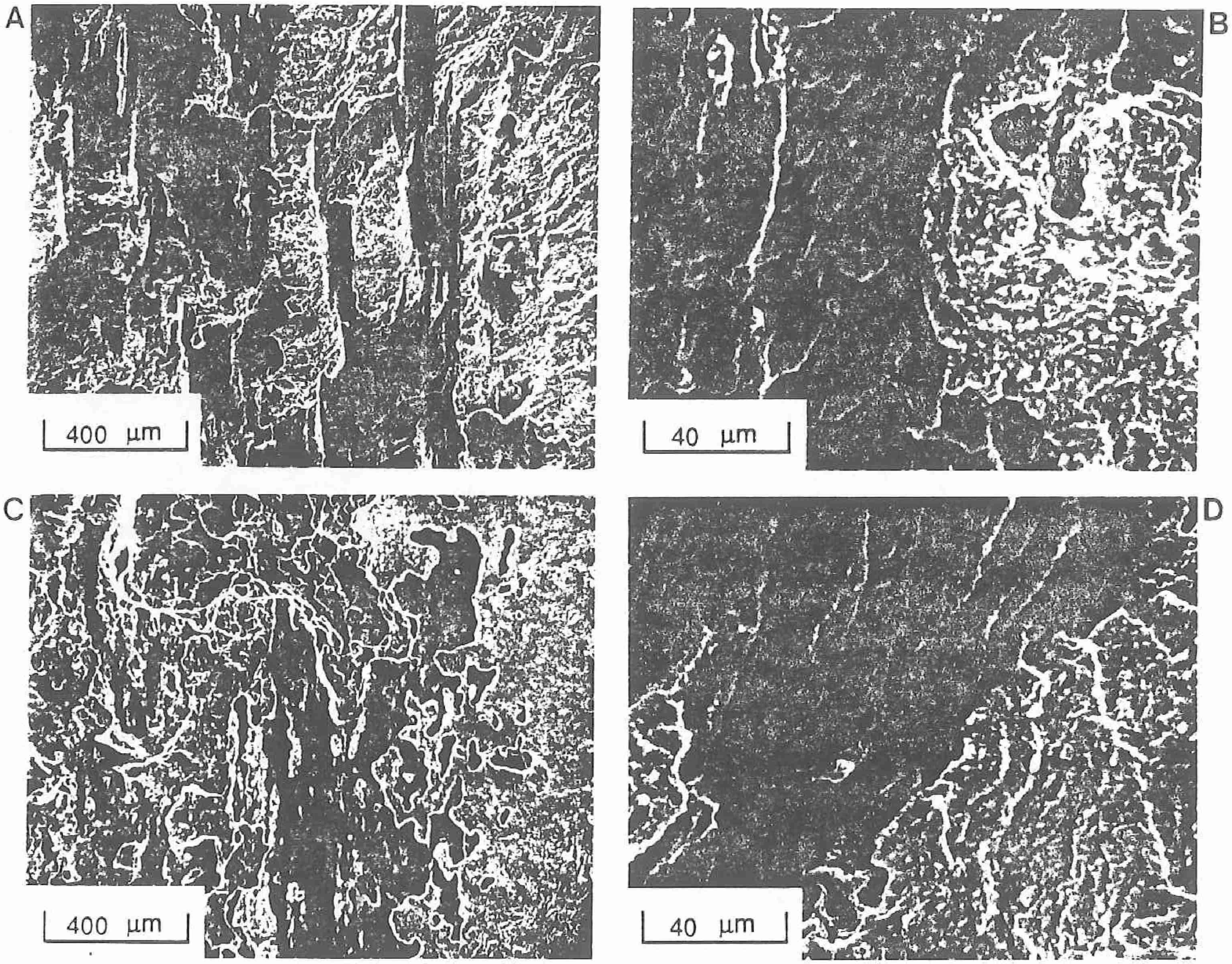

Fig.21. SEM fractographs of bend test specimens extracted from dissimilar-alloy welds between FVS1212 and 2024-T351: (a,b) outer periphery of IFW produced with low axial force; (c,d) outer periphery of LFW.

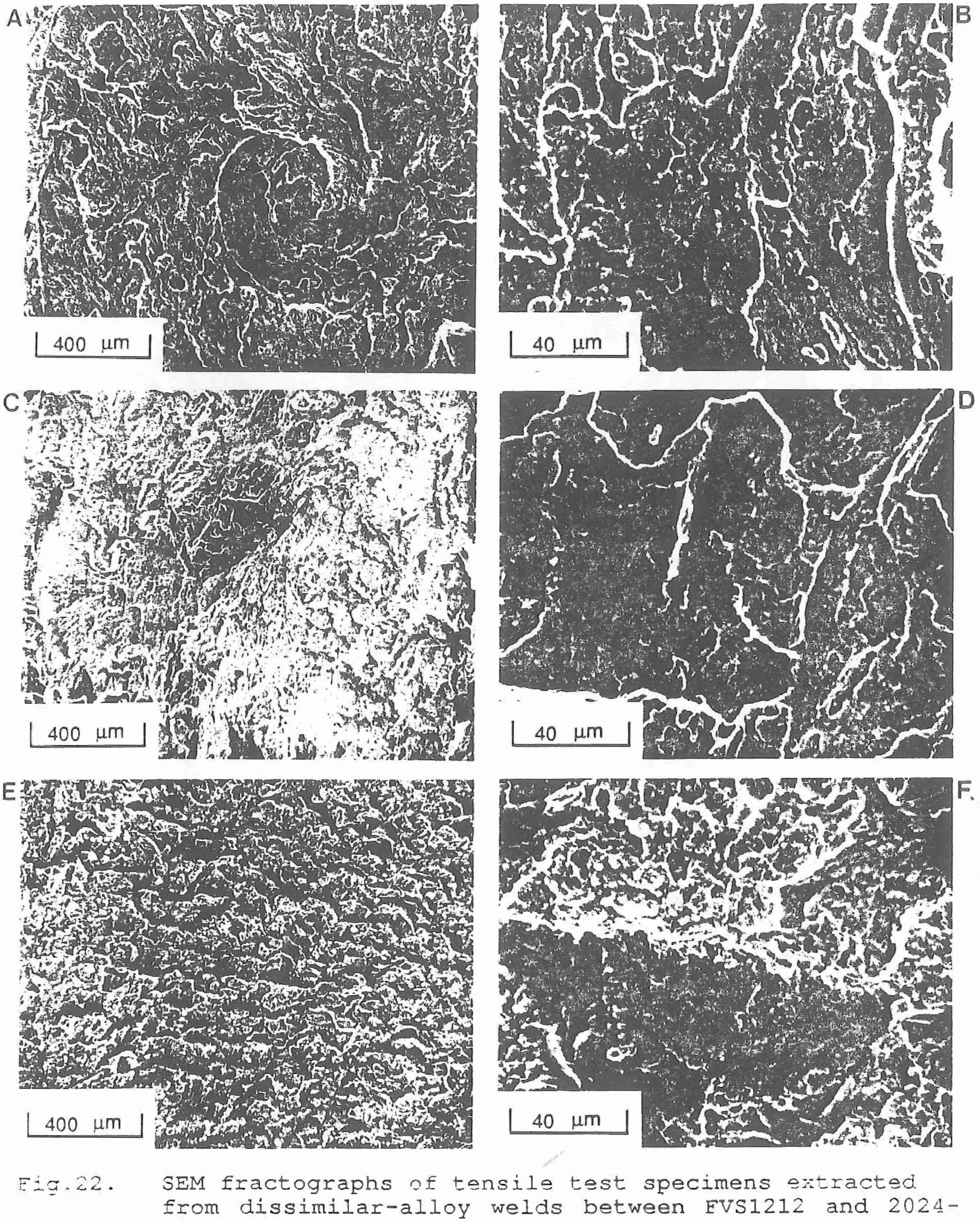

Fig.22. SEM fractographs of tensile test specimens extracted from dissimilar-alloy welds between FVS1212 and 2024-T351: (a,b) center of IFW produced with low axial force; (c,d) center of IFW produced with high axial force; (e,f) center of LFW.